Experimental Study on Deuterium Extraction from Liquid Pb-Li with the Vacuum Sieve Tray Technique for the European DEMO Fusion Reactor

Zur Erlangung des akademischen Grades einer

Doktorin der Ingenieurwissenschaften (Dr.-Ing.)

von der KIT-Fakultät für Maschinenbau des
Karlsruher Instituts für Technologie (KIT)
angenommene

Dissertation

von

Dipl.-Ing. Ester Diaz Alvarez

Tag der mündlichen Prüfung: 25.10.2021

Hauptreferent: Prof. Dr.-Ing. Robert Stieglitz

Korreferent: apl. Prof. Dr.-Ing. Leo Bühler

Kurzfassung

Das benötigte Tritium eines Fusionskraftwerks wird durch Neutronenbeschuss von Lithium im sogenannten *Breeding Blanket* (BB) erzeugt. Flüssige Konzepte von BB bestehen aus eutektischem Pb-Li. Das erzeugte Tritium wird aus dem flüssigen Metall bei dem *Tritium Extraction and Removal System* (TERS) extrahiert. Die *Vacuum Sieve Tray* (VST) Technologie wird für TERS für das europäische Demonstrationskraftwerk (DEMO) vorgeschlagen, welche eine Extraktionseffizienz von mindestens 80 % erfordert. Diese Technik besteht in der Erzeugung kleiner oszillierenden Tröpfchen, die in eine Vakuumkammer fallen.

Im Rahmen der vorliegenden Arbeit wurde eine mit Deuterium betriebene VST-Versuchsanlage aufgebaut. Um die Extraktioneffizienz zu bewerten wurden Versuche durchgeführt, die aus zwei Phasen bestehen. Zuerst wird Deuterium in das flüssige Metall (in einer oberen Kammer aus Edelstahl) gelöst und anschließend aus den fallenden Pb-Li-Tröpfchen (in einer unteren Edelstahlkammer unter Vakuum) extrahiert. Die Experimente wurden durch einen entwickelten fluiddynamischen Simulationscode und eine Hochgeschwindigkeitskamera, um die Größe und Bewegung der Flüssigmetalltröpfchen zu analysieren, unterstützt.

Die gemessene Menge gelöstes Deuteriums im Pb-Li beträgt $(8.9 \pm 1.5) \times 10^{-4}$ und $(4.4 \pm 1.4) \times 10^{-4}$ mol D_2 für Lösedrücke von 1000 bzw. 500 mbar. Diese Ergebnisse werden durch eine sorgfältige Auswertung des in die Struktur verlorenen Deuteriums bestimmt und entsprechen einer Sieverts-Konstanten von $(8.5 \pm 1.9) \times 10^{-3}\,\mathrm{mol_D\,m^{-3}\,Pa^{-0.5}}$.

Die Menge an D_2, die aus Tröpfchen mit einem Durchmesser von etwa 1.2 ± 0.2 mm innerhalb einer Fallhöhe von ≈ 0.5 m extrahiert wird, ist geringer als 8×10^{-6} mol. Dieses Ergebnis impliziert eine Extraktionseffizienz von ≤ 1.2 %, die wesentlich niedriger als der erwartete Wert ist, der auf der Diffusion von Deuterium zur Oberfläche der Tröpfchen beruht. Die erhaltenen Ergebnisse legen entweder einen Stoffübergangskoeffizienten von etwa $5 \times 10^{-12}\,\mathrm{m^2\,s^{-1}}$ oder einen oberflächenbegrenzten Extraktionsprozess nahe.

Abstract

The tritium needed to fuel a fusion power plant will be produced in the so-called Breeding Blanket (BB) by neutron bombardment of lithium. Liquid concepts of BB are composed of eutectic Pb-Li and rely on a Tritium Extraction and Removal System (TERS) to extract the generated tritium from the liquid metal. The Vacuum Sieve Tray (VST) technique is proposed as TERS for the European Demonstration power plant (DEMO), which requires a minimum extraction efficiency of 80 %. This technique consists in extracting the tritium dissolved in Pb-Li by generating small oscillating droplets, which fall in a vacuum chamber.

Within the present work, a VST experimental facility operated with deuterium has been assembled and qualified. Experiments consisting in dissolving deuterium into the liquid metal (in a stainless-steel upper chamber) and subsequently extracting it from the falling Pb-Li droplets (in a stainless-steel lower chamber under vacuum) have been carried out in order to evaluate the extraction efficiency. The experiments have been assisted with a developed fluid-dynamics simulation code and a high-speed camera to analyse the size and motion of the liquid-metal droplets.

The measured amount of deuterium dissolved into the Pb-Li is $(8.9 \pm 1.5) \times 10^{-4}$ and $(4.4 \pm 1.4) \times 10^{-4}$ mol of D_2 for dissolving pressures of 1000 and 500 mbar, respectively. These results have been determined with a careful evaluation of the deuterium lost into the structure and correspond to a Sieverts' constant of $(8.5 \pm 1.9) \times 10^{-3}\,\mathrm{mol_D\,m^{-3}\,Pa^{-0.5}}$.

The amount of D_2 extracted from droplets of about 1.2 ± 0.2 mm diameter within a falling height of ≈ 0.5 m is lower than 8×10^{-6} mol. This result implies an extraction efficiency of ≤ 1.2 %, which is substantially lower than the expected value relying on diffusion of deuterium towards the surface of the droplets. The obtained results suggest either a mass transfer coefficient of about $5 \times 10^{-12}\,\mathrm{m^2\,s^{-1}}$ or a surface-limited extraction process.

Contents

Acknowledgements

The work behind these pages has been a journey. A deep learning process involving not only acquiring scientific knowledge in every specific field that the PhD encounters, but also in overcoming situations, learning to trust that there are always solutions and, not less important, personal skills. I would like to thank all those who have been part of this PhD-journey, helping me to become a better person, more capable, more resilient and a scientist.

First, I would like to thank Prof. Robert Stieglitz for having accepted me as a PhD student, for his guidance, his constructive solutions in crucial moments, and for his careful review and feedback of the manuscript. I would also like to express my gratitude to Prof. Leo Bühler for kindly accepting being my Korreferent and his review of the thesis.

I would like to give special thanks to Dr. Uwe Besserer, who took over the supervision of this work during the second half of the PhD, for the support that he gave me to finish this doctorate.

This PhD journey would not have started without my first supervisor, Dr. Laëtitia Frances. I am honoured to have been your first PhD student. Thank you for believing in me, for your encouragement, for teaching me how to become a better writer, a better communicator and for providing me with the necessary tools to finish this work. I would also like to profoundly thank Dr. Rodrigo Antunes. Thank you for your unconditional support, for all the scientific and non-scientific discussions, which made me feel accompanied during long part of this journey. Laëtitia and Rodrigo, my deepest thanks to both of you for your feedback of the manuscript and for being there with more dedication than I could even ask for.

I would also like to thank Dr. Beate Bornschein for her guidance and practical hints in communication and planning/organisation during the PhD work, and together with Dr. Lutz Bornschein for their review of the thesis.

I would like to express my gratitude to Dr. András Bükki-Deme for the development of the LabVIEW software and to Alejandro Muñoz Ovalle for the CAD design of the facility. Laëtitia, Rodrigo, András, Alejandro and Matti thank you very much for the fun canteen and after-work hours. I would also like to deeply thank the TVT group. David Hillesheimer, Nancy Tuchscherer, Tobias Falke, To-

bias Weber, Joshua Kohpeiß, Albert Braun danke für eure Verfügbarkeit und eure unendliche Unterstützung mit der VST Anlage. Special thanks to Stefan Welte for his thorough support with the realisation of the setup and the technical challenges that were encountered along this project. Many thanks to Dr. Sebastian Mirz and Dr. Roland Gyuráki for their support with the high-speed camera and to Dr. Alexander Marsteller for his aid with rarefied-gas theory. Special thanks to Annette Heinzel for her assistance with the Pb-Li handling in crucial moments and corrosion tests and to Dr. Fumito Okino for sharing his experience and expertise with the VST technology. Many scientific and technical discussions were greatly helpful for the realisation of this project, for that I would like to thank Dr. Michael Sturm, Tiago Pomela, Cyra Neugebauer, Valentin Hermann, Dr. Sebastian Mirz and the PhD students and group leaders attendants of the TLK scientific seminars. As a whole, I would like to express my gratitude to my colleagues in the Tritium Laboratory Karlsruhe for creating the everyday support environment, which goes from short coffee-break talks to the good care that Eva Porter and Sylvia Krieger have taken of me (danke schön euch beiden).

My most profound and immeasurable gratitude goes to my strongest support system. Yurena, Clara, Cyra, Helena, Laura V. and Grecia. Thank you for the $\approx 8000\,\mathrm{h}$ accumulated whatsapp audios und Unterhaltungen, which are the secret of how I have managed it to the end of this PhD. Gracias chicas. Marc and Alberto, thank you for being there and your emotional support along the journey. Maria, Sebastian, Valentin, Santiago, Alex, Eider, Jone, Alexander, Katharina, Lena, Juri, Laura L., las Frauen, Jessica, Aaron, Jesi, Felix, Christian and others, that in a way or another have accompanied me during this time, rising up my motivation, good mood, empathizing, giving hints or just listening. Thank you all.

Finally, my deepest and special thanks go to my family, to whom I dedicate this manuscript. A mi madre, que ha sido mi sustento y gran ejemplo de superación; a mi hermano Ayoze, que me ha ayudado y escuchado desde los duros comienzos (con mecánica cuántica) de este viaje; a mi hermano Adrian, que siempre que hablamos me injecta dosis de motivación; a mi padre, que me ha apoyado y dado los recursos para ser independiente; a mi abuela Carmen, a la que estoy profundamente agradecida por la familia que ha sostenido y quien es mi mayor ejemplo de aprendizaje continuo; a mi tía Bea, que ha estado ahí en los momentos duros con cariño y comprensión; a mi tío Jaime, por su apoyo y aportaciones siempre claras y prácticas; a mi prima Silvia, porque sin ella no habría empezado mi aventura de fusión, y a todos y cada uno de mi familia. A mi familia de no-sangre, a Rita, a Karmele, a Prudencio, gracias por guiarme, escucharme, animarme. Gracias por estar ahí.

This work has been carried out within the framework of the EUROfusion Consortium and has received funding from the Euratom research and training programme 2014-2018 under grant agreement No 633053. The views and opinions expressed herein do not necessarily reflect those of the European Commission.

List of Acronyms

BB	Breeding Blanket
D	Deuterium
DCLL	Dual Coolant Lithium Lead
DEMO	DEMOnstration power plant
EH	Electrical Heater
FPP	Fusion Power Plant
GLC	Gas-Liquid Contactor
H	Hydrogen (protium)
HCLL	Helium Cooled Lithium Lead
HWMR	Heavy-Water-Moderated Reactor
LC	Lower Chamber
MARS	Mirror Advanced Reactor Study
MFC	Mass Flow Controller
MHD	Magnetohydrodynamics
PAV	Permeator Against Vacuum
P&ID	Pipe and Instrumentation Diagram
QMS	Quadrupole Mass Spectrometer
RAFM	Reduced Activation Ferritic/Martensitic
RG	Regenerable Getter
T	Tritium
TBR	Tritium Breeding Ratio
TERS	Tritium Extraction and Removal System
TLK	Tritium Laboratory Karlsruhe
UC	Upper Chamber
VST	Vacuum Sieve Tray
WCLL	Water Cooled Lithium Lead

List of Symbols

a	Characteristic length of a system (m)
A	Surface area (m^2)
A_d	2D Area of the droplet captured in one image (m^2), defined in eq. (4.13)
A_n	Cross-sectional area of the nozzle (m^2)
C	Atomic concentration ($mol_{H,D,T}\, l^{-1}$)
$C_{D\,[PbLi]}$	Atomic concentration of deuterium in Pb-Li ($mol_D\, l^{-1}$), defined in eq. (5.4)
d_d	Droplet diameter (mm), defined in eqs. (2.1), (4.13)
d_{lc}	Diameter of lower chamber (mm)
d_M	Molecular diameter (m)
d_n	Nozzle diameter (mm)
d_n^{eq}	Equivalent nozzle diameter (mm), defined in eq. (4.9)
d_{tray}	Diameter of the nozzle tray (m)
d_{uc}	Diameter of the upper chamber (mm)
$\mathcal{D}$	Diffusivity ($m^2\, s^{-1}$)
$\mathcal{D}_0$	Temperature-independent pre-exponential factor of diffusivity ($m^2\, s^{-1}$)
$E_{\mathcal{D}}$	Activation energy of diffusivity ($J\, mol^{-1}$)
$E_{\mathcal{P}}$	Activation energy of permeability ($J\, mol^{-1}$)
$E_{\mathcal{S}}$	Activation energy of solubility ($J\, mol^{-1}$)
f	Frequency of oscillation (s^{-1}), defined in eq. (2.2)
g	Gravitational acceleration ($m\, s^{-2}$)
h	Height (m)
h_c	Height of the centre of the window in the lower chamber (m)
h_{fall}	Falling height of the droplets (m)
h_{lc}	Height of the lower chamber (mm)
h_n	Height of the nozzle in the lower chamber (m)

$h_{\mathrm{PbLi(lc)}}$	Height of Pb-Li in the lower chamber (coordinate system: simulation, see Figure 4.1) (m)
$h_{\mathrm{PbLi(uc)}}$	Height of Pb-Li in the upper chamber (coordinate system: simulation, see Figure 4.1) (m)
$h'_{\mathrm{PbLi(lc)}}$	Height of Pb-Li in the lower chamber (coordinate system: experiments, see Figure 4.1) (m)
$h'_{\mathrm{PbLi(uc)}}$	Height of Pb-Li in the upper chamber (coordinate system: experiments, see Figure 4.1) (m)
h_{uc}	Height of the upper chamber (mm)
Δh_{st}	Standard height step in the simulation code VST-experiment (m)
J	Flux of diffusing atoms ($\mathrm{mol_{H,D,T}\,m^{-2}\,s^{-1}}$)
k_{B}	Boltzmann constant: $1.3806 \times 10^{-23}\,\mathrm{m^2\,kg\,s^{-2}\,K^{-1}}$
Kn	Knudsen number (-), defined in eq. (6.2)
$\bar{l}$	Mean free path (m), defined in eq. (6.3)
L	Length of a system, in the flux direction (m)
m_t	Mass of diffused substance at time t (kg)
m_∞	Mass of diffused substance at time ∞ (kg)
n	Amount of gas (general) (mol), defined in eq. (3.1)
$n_{1,2,3}$	Amount of gas in the different regions of the lower chamber shown in Figure 6.1 (mol); 1: upper half of the chamber, 2: lower half of the chamber, 3: flexible tube
$n_{\mathrm{D_2}}$	Amount of D_2 gas (mol)
$n_{\mathrm{D_2\,diss}}$	Amount of deuterium dissolved in the Pb-Li at the end of the dissolution phase ($\mathrm{mol_{D_2}}$); note that, in Chapter 5, it corresponds to $n_{\mathrm{D_2[PbLi]}}(t_{\mathrm{end}})$
$n_{\mathrm{D_2\,ext}}$	Amount of deuterium extracted ($\mathrm{mol_{D_2}}$)
$n_{\mathrm{D_2[PbLi]}}$	Amount of D_2 dissolved into the Pb-Li, evaluated at τ_{diss} (mol)
$n_{\mathrm{D_2[ss]}}$	Amount of D_2 lost through the stainless-steel walls during dissolution experiment, evaluated at τ_{diss} (mol)
$n_{\mathrm{D_2[ss*]}}$	Amount of D_2 lost through all the stainless-steel walls of the upper chamber during a permeation experiment (experiment with no Pb-Li), evaluated at τ_{diss} (mol)
N	Number of nozzles
N_{hex}	Number of hexagons in a tray with hexagonal nozzle configuration
p	Pressure of the gas (Pa or mbar)

$p_{1,2,3}$	Gas pressure at the different regions of the lower chamber shown in Figure 6.1 (mbar); 1: upper half of the chamber, 2: lower half of the chamber, 3: flexible tube
$p_{\mathrm{lc,\,ext}}$	Gas pressure in lower chamber during extraction phase (mbar)
p_{sensor}	In Chapter 6: pressure measured by the vacuum sensor (mbar)
p_{uc_0}	Initial gas pressure in the upper chamber during the extraction phase (mbar)
$p_{\mathrm{uc,\,diss}}$	Gas pressure in upper chamber during dissolution phase (mbar)
$p_{\mathrm{uc,\,ext}}$	Gas pressure in upper chamber during extraction phase (mbar)
p_{v}	Vapour pressure (Pa)
δp	Total fluid-dynamics pressure losses (mbar)
$\delta p_{\mathrm{c\text{-}p}}$	Pressure loss due to change in section chamber-to-pipe (mbar)
δp_{p}	Pressure loss due to friction along the pipe (mbar)
$\delta p_{\mathrm{p\text{-}n}}$	Pressure loss due to change in section pipe-to-nozzle (mbar)
δp_{v}	Pressure loss inside the valve (mbar)
$\mathcal{P}$	Permeability ($\mathrm{mol\,m^{-1}\,s^{-1}\,Pa^{-1/2}}$)
$\mathcal{P}_0$	Temperature-independent pre-exponential factor of permeability ($\mathrm{mol\,m^{-1}\,s^{-1}\,Pa^{-1/2}}$)
Q	Pb-Li volumetric flow ($\mathrm{m^3\,s}$)
R	Ideal gas constant: $8.314\,\mathrm{J\,K^{-1}\,mol^{-1}}$ or $83.14\,\mathrm{l\,mbar\,K^{-1}\,mol^{-1}}$
$\mathcal{S}$	Solubility or *Sieverts' constant* ($\mathrm{mol_D\,m^{-3}\,Pa^{-1/2}}$)
$\mathcal{S}_0$	Temperature-independent pre-exponential factor of solubility ($\mathrm{mol_D\,m^{-3}\,Pa^{-1/2}}$)
t	Time (s)
t_{fall}	Falling time of a droplet (s), defined in eq. (2.4)
$\bar{t}_{\mathrm{fall}}$	Average t_{fall} along the extraction experiment (s)
t_{sh}	Opening time of the shutter (of the high-speed camera) (s)
T	Temperature (K)
$T_{1,2,3,4}$	In Chapter 5: Temperature of the various wall sections of the upper chamber (K), as defined in Fig. 5.2, b; 1: upper flange, 2: upper part of the vertical wall, 3: lower part of the vertical wall, 4: lower flange
$T_{\mathrm{A,B,C,D,E}}$	Temperature of the various sections of the lower chamber (K), as shown in Fig. 6.1; A: top surface, B: middle of the chamber, C: surface of the Pb-Li, D: vacuum sensor, E: flexible tube
T_{Heater}	Temperature of the heater (K)
T_{PbLi}	Temperature of the Pb-Li (K)
v	Speed ($\mathrm{m\,s^{-1}}$)

v_{c}	Speed of the Pb-Li droplets at h_{c} in the lower chamber ($\mathrm{m\,s^{-1}}$)
v_{n}	Speed of Pb-Li at the exit of the nozzle ($\mathrm{m\,s^{-1}}$)
$\overline{v}_{\mathrm{n}}$	Average v_{n} along the extraction experiment ($\mathrm{m\,s^{-1}}$)
V	Volume ($\mathrm{m^3}$ or l)
$V_{\mathrm{gas(lc)}_{0,f}}$	Initial and final volume of gas, respectively, in the lower chamber during the extraction phase (l)
V_{lc}	Volume of the lower chamber (l)
$V_{\mathrm{PbLi(lc)}_{0,f}}$	Initial and final volume of Pb-Li, respectively, in the lower chamber during the extraction phase (l)
$V_{\mathrm{PbLi(uc)}_{0,f}}$	Initial and final volume of Pb-Li, respectively, in the upper chamber during the extraction phase(l). Note that $V_{\mathrm{PbLi(uc)}_0}$ also corresponds to the volume of Pb-Li in the upper chamber during dissolution
V_{uc}	Volume of the upper chamber (l)
x	Longitudinal coordinate, in the flux direction (m)
x_i	General variable (with $i = 1, 2...$)
y	Vertical coordinate, in the direction of the falling droplets (m)
δy	Vertical elongation of the falling droplets due to t_{sh} (m), defined in eq. (4.12)
δ	Rarefaction parameter (-), defined in eq. (6.4)
δ_{avg}	Average rarefaction parameter (-), defined in eq. (6.6)
ε	Thickness (mm)
η_{exp}	Experimental efficiency (- or %), defined in eq. (2.15)
η_{theo}	Theoretical efficiency (- or %), defined in eq. (2.3)
$\overline{\eta}_{\mathrm{theo}}$	Average η_{theo} along the extraction experiment (- or %)
μ	Dynamic viscosity (Pa s)
ν_{sh}	Speed of the shutter (of the high-speed camera) ($\mathrm{s^{-1}}$)
ρ	Density ($\mathrm{kg\,m^{-3}}$)
σ	Surface tension ($\mathrm{N\,m^{-1}}$)
τ_{ch}	Characteristic time of a diffusion process (s), defined in eq. (2.8)
τ_{diss}	Time to reach steady-state in the Pb-Li (s), obtained from the definition of τ_{ch} in eq. (2.8)
τ	Duration of the extraction experiment (s)
χ_{top}	Fraction of D_2 permeated through the top surfaces of upper chamber (lined blue in Figure 5.2, b) (%), defined in eq. (5.3)
Ψ^2	Dimensionless deviation function (-), used to evaluate the deviation between the fluid-dynamic simulation and the experimental results, defined in eq. (4.7)

Chapter 1

Introduction

1.1 Tritium self-sufficiency: a requisite in fusion reactors

Nuclear fusion has been investigated for decades with the aim to provide low-carbon baseload electricity, which is needed in a sustainable energy mix. Fusion Power Plants (FPPs), made of low-activation materials, will supply continuous electricity to the grid relying on the energy obtained from the fusion of light nuclei.

Among the possible fusion reactions, the one occurring between deuterium (^{2}H or D) and tritium (^{3}H or T) has, by far, the largest cross-section at the lowest temperature (maximum at about 60 keV $\approx 7{\times}10^8$ K), as shown in Figure 1.1. Therefore, the main stream of research in fusion is based on the D-T reaction:

$$\mathrm{D} + \mathrm{T} \longrightarrow {}^4\mathrm{He}\ (3.5\ \mathrm{MeV}) + \mathrm{n}\ (14.1\ \mathrm{MeV}). \tag{1.1}$$

Deuterium is widely available, with a relative abundance of 0.0115 at.% (related to the hydrogen content in fresh water) [1]. It can be obtained from the water of the oceans, by electrolysis. Tritium, however, is extremely rare in nature. The balance between its natural production (by cosmic rays) and its radioactive decay (around 5 % per year) results in a constant atomic concentration of 1×10^{-18} in natural hydrogen [2]. The primary sources of tritium are the fission Heavy-Water-Moderated Reactors (HWMRs), which produce $0.21{-}0.26\ \mathrm{kg_T/GWe/fpy}$. Currently, the available tritium inventory from HWMRs is about 60 kg [3]. However, a FPP of 1000 MWe is expected to consume 167.4 kg of tritium per year [4]. Therefore, a FPP would be only feasible if it produces its own tritium, which formulates one of the main challenges of the fusion research [5].

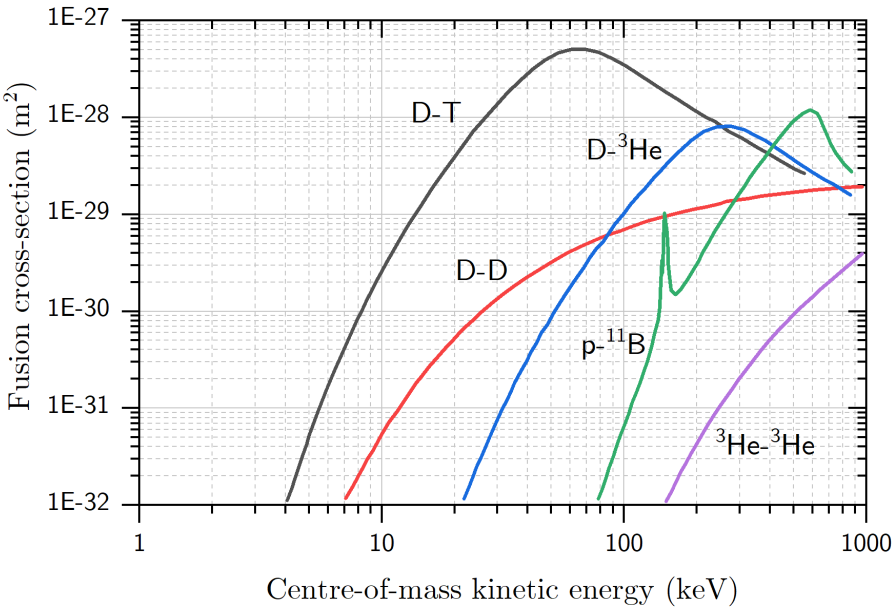

Figure 1.1: Cross-section of fusion reactions as a function of kinetic energy (from [6]). $1\,\mathrm{keV} \approx 1.2 \times 10^7\,\mathrm{K}$.

1.2 Tritium production in liquid breeding blankets

In a future FPP, tritium is generated relying on the bombardment of lithium atoms with the neutrons released from the fusion plasma (see equation (1.1)). Two reactions are possible [7]:

$$^6\mathrm{Li} + \mathrm{n} \longrightarrow \mathrm{T} + {}^4\mathrm{He} + 4.8\,\mathrm{MeV}, \tag{1.2}$$

$$^7\mathrm{Li} + \mathrm{n} \longrightarrow \mathrm{T} + {}^4\mathrm{He} + \mathrm{n} - 2.5\,\mathrm{MeV}. \tag{1.3}$$

For thermal and slow neutrons, equation (1.2) is the predominant reaction [8]. Thus, the lithium used in a FPP must be enriched with ^{6}Li (up to 90 % [9])[1].

Tritium production occurs in the so-called Breeding Blanket (BB), which is a wall module placed at the reactor, surrounding the fusion plasma (see Figure 1.2). The BB contains the enriched lithium and a neutron multiplier (e.g. Be or Pb) to improve the reaction yield. The breeding blanket has three main functions:

(i) It must shield the neutrons that come from the plasma in order to minimize the damage that they would cause to the reactor components, mainly the vacuum vessel and the superconducting magnets, which are components that cannot be replaced during the entire reactor lifetime.

[1] The natural abundance of ^{6}Li is 7.59 at.% [1]

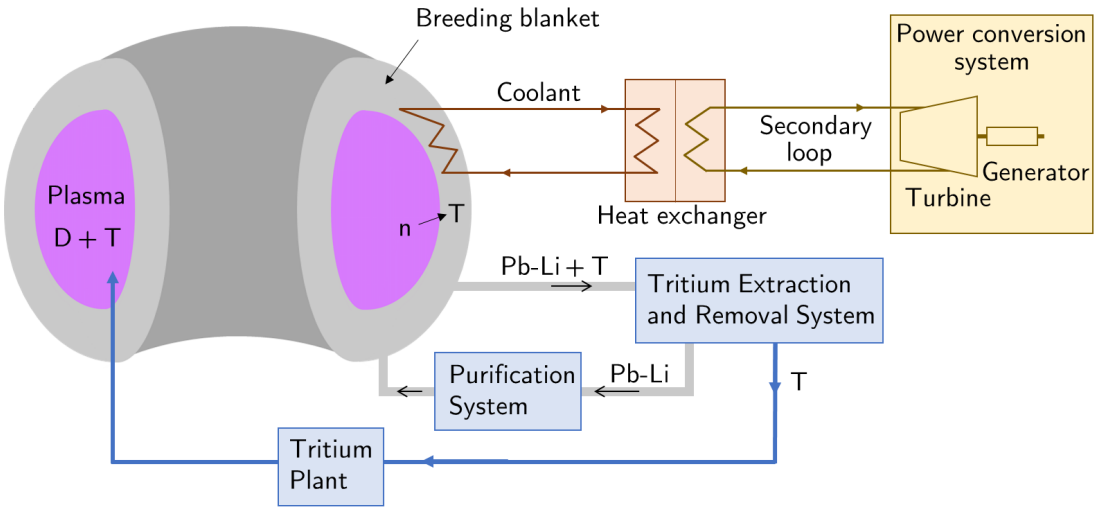

Figure 1.2: Basic scheme of a fusion power plant relying on a liquid breeding blanket.

(ii) By stopping the neutrons from the plasma, the BB also collects most of the energy from the fusion reactions. As seen in equation (1.1), the neutrons carry 80 % of the energy produced in the plasma[2]. This kinetic energy is converted into thermal energy in the BB, which is extracted from the blanket by the cooling system. In the heat exchanger, the heat of the coolant is transferred to a secondary loop (with typically water), in which steam is produced. At the power conversion system, the heat from the steam is transformed into electricity by means of turbine generators, as in a conventional power plant.

(iii) As mentioned above, the neutrons are also used to produce the tritium necessary to fuel the plasma. The tritium generated in the BB is recovered by the Tritium Extraction and Removal System (TERS) and processed in the tritium plant.

There are solid and liquid concepts of BB under research. Solid concepts are typically composed of pebbles of lithium ceramics (Li_4SiO_4 or Li_2TiO_3) and beryllium as neutron multiplier. Liquid BBs typically use an eutectic alloy of Pb-Li (15.8 at.% Li), relying on lead as neutron multiplier [10, 11]. The liquid breeders have several advantages compared to the solid ones: (i) it is easier to transport the breeder material outside the blanket for tritium recovery, as well as for maintenance (e.g. breeder replacement); (ii) the material is not damaged by neutron irradiation; (iii) tritium diffusivity is larger, which is important to extract the tri-

[2]The remaining 20 % of the fusion energy, carried by the helium nuclei, is normally recovered through the divertor. The divertor is an important component of the first wall, conceived to receive the exhaust particles from the plasma, from where they will be pumped out.

Table 1.1: Main characteristics of liquid breeding blanket concepts under research for the European DEMO [12–21].

Characteristic	HCLL	WCLL	DCLL
Coolant	He	H_2O	Pb-Li + He
Coolant temperature range (°C)	300 – 500	295 – 328	300 – 548
Pb-Li total mass flow ($kg\,s^{-1}$)	890	956	29 527
T concentration in Pb-Li ($mol_T\,m^{-3}$)	2×10^{-2}	4×10^{-2}	5.6×10^{-4}

tium from the BB, and (iv) they have higher thermal conductivity, which is essential for both cooling of the materials and the energy extraction. However, liquid breeders face several disadvantages: a continuously flowing liquid metal is subject to Magnetohydrodynamic (MHD) effects. They not only cause pressure losses in the BB loop, but also have to be electromagnetically isolated to prevent large-scale electric current circulation in the conducting structure material, which could lead to excessive Lorenz forces into the structure in case of a plasma disruption. In addition, the flowing Pb-Li at high temperature is highly corrosive.

Three concepts of liquid BB have been investigated for the European Demonstration power plant (DEMO), with designs based on different coolants (see main characteristics in Table 1.1). The Helium Cooled Lithium Lead (HCLL) and the Water Cooled Lithium Lead (WCLL) use the conventional concept, in which a coolant loop (helium or water, respectively) transfers the heat from the BB to the heat exchanger. In the Dual Coolant Lithium Lead (DCLL) concept, however, the Pb-Li itself is used as primary coolant and its loop passes through the heat exchanger (additionally, a helium loop is used to cool down the first wall and supporting structures). Because of that, a higher speed of the liquid metal is required in DCLL, with the consequent increased MHD effects and corrosion. In the frame of the European blanket design strategy for DEMO, the water cooling concept, WCLL, is regarded as the most promising and, thus, chosen as baseline. The HCLL concept is maintained as a back-up and DCLL is regarded as a more-advanced future solution [22].

The designers of the BBs and the tritium fuel cycle, as a whole, face a big challenge. The tritium inventory in the FPP has to be minimized due to safety regulations, but hydrogen isotopes present a high diffusivity through metals at the foreseen operation temperatures. This, in addition to the extremely low concentration of tritium in the Pb-Li, makes the development of a TERS with an excellent efficiency absolutely necessary.

However, the experimental research of TERS technologies is not straightforward.

Operating with Pb-Li and hydrogen isotopes requires an environment free of oxygen and water (i.e. good leak-tightness), high temperatures, and materials and equipment compatible with Pb-Li (due to galvanic corrosion). In addition, the solubility of hydrogen isotopes in eutectic Pb-Li is unknown: experimental values in literature show discrepancies of several orders of magnitude [23, 24]. Therefore, both qualifying an experimental facility and quantifying the hydrogen dissolved in the liquid metal to evaluate the extraction technologies is very challenging.

The minimum extraction efficiency currently considered for the dimensioning of the TERS of the European DEMO is 80 % [12, 25]. Different TERS technologies are under study to achieve this goal. However, none of them has been yet experimentally demonstrated to match this efficiency requirement. This work is focused on the investigation of one of the TERS technologies proposed for liquid BB: the Vacuum Sieve Tray (VST). This technique consists in inducing the formation of small Pb-Li droplets by letting the liquid metal fall in a vacuum chamber. The increased surface-to-volume ratio, in addition to a mass movement caused by oscillations of the droplets, likely facilitates the extraction of tritium, which is recovered by means of a pumping system.

1.3 Objectives and structure of this work

The present work is based on the development and experimental results of a small-scale VST facility operated with D_2 for the investigation of the extraction process of deuterium from the liquid metal. The experiment requires at first the dissolution of deuterium into the liquid metal and the quantification of the amount dissolved. This is a crucial step in the investigation, due to the unknown solubility of hydrogen in Pb-Li. Then, the evaluation of the extraction phase is divided into two distinct parts: the fluid dynamics of the falling droplets and the quantification of the gas extracted. Thus, with the information of gas dissolved and extracted and the Pb-Li fluid dynamics, the proposed model of extraction efficiency (shown in Section 2.2) can be assessed. Consequently, the potential of the technology for a reactor-scale VST-TERS can be evaluated.

The objectives of this thesis are defined as follows:

1. **Qualification of the experimental facility for dissolution of deuterium in Pb-Li and its extraction with the VST method**. This includes guaranteeing the satisfactory performance of the Pb-Li fluid dynamics and its monitoring: no solidification in the loop, formation of liquid jet and droplets, monitoring the level (volume) of Pb-Li in both dissolution and extraction chambers

and the fluid dynamics of the falling droplets.

2. **Simulation and experimental validation of the Pb-Li fluid dynamics**. Crucial parameters of the extraction model are the *falling time* and the *diameter of the droplets*. Theoretical assessment of the latter and simulations of the former shall be compared with experimental observations. Additionally, oscillations in the droplet shape must be observed in order to analyse their potential impact on the extraction efficiency.

3. **Evaluation of the deuterium dissolved in the Pb-Li**. A static method of dissolution is tested, relying on Sieverts' law. In addition to the assessment of the method, the quantification of deuterium dissolved includes the evaluation of the deuterium lost into the structure of the dissolution chamber.

4. **Assessment of the deuterium extracted**. This includes experiments with one nozzle (one line of falling droplets), performed under varying conditions of amount of deuterium dissolved and falling time.

5. **Evaluation of the extraction efficiency and assessment of the viability of the VST technique for further development**. The evaluation of the extracted deuterium and its relation to the fluid-dynamic parameters of interest allows to carry out a scale-up study and assess the feasibility of the technology for DEMO.

This thesis is structured as follows: Chapter 1 provides an introduction to the present work in the context of fusion and liquid breeding blankets. Chapter 2 covers the state of the art of the Vacuum Sieve Tray, among other technologies for tritium extraction from liquid Pb-Li. In this chapter, the literature and theoretical information required to understand the present work research is also provided.

In Chapter 3, the experimental facility is described and the experimental strategy (including matrix of experiments) is presented. The experimental results and their analysis are divided into three main blocks: Chapters 4, 5 and 6.

Chapter 4 is dedicated to the Pb-Li fluid dynamics. First, the code *VST-experiment* is presented (Section 4.2), which is used to simulate the fluid dynamics of one typical run. The experimental results are then fitted with the *VST-experiment* simulation. In Section 4.3, the fitting method is explained and the output Pb-Li volumes and uncertainties are given. The last part of the chapter (Section 4.4) discusses the observations and analysis of the droplets, where the results of the simulations are validated and the size and oscillations of the droplets are characterized.

Chapter 5 comprises the evaluation of deuterium dissolved in the Pb-Li during the dissolution phase. The analysis is based on a mass balance (explained in Section 5.1) evaluated at the time at which steady-state is reached. Section 5.3 shows the total amount of D_2 gas depleting in the gas volume of the chamber (diffused into Pb-Li and walls); then, Section 5.4 shows the evaluation of deuterium loss through the walls, and finally, Section 5.5 gives the resulting deuterium dissolved into the Pb-Li.

The amount of deuterium extracted is evaluated in Chapter 6. First, the gas accountancy method in the lower chamber is explained and validated (Section 6.1). Then, the evaluation of deuterium extracted in two representative runs is given (Section 6.2). Last, the obtained experimental extraction efficiency and its impact on the following steps of the research and on the viability of the technology for DEMO are discussed in Section 6.3.

In Chapter 7, the conclusions of the present work and perspectives based on the obtained results are summarized.

Chapter 2

The Vacuum Sieve Tray (VST) technique: tritium extraction from liquid Pb-Li

2.1 Techniques of tritium extraction from liquid Pb-Li. State of the art

Several Tritium Extraction and Removal System (TERS) technologies are under study for the liquid Breeding Blanket (BB) concepts of the European Demonstration power plant (DEMO). The current baseline is the Permeator Against Vacuum (PAV), which relies on the permeation properties of tritium through metals. The lithium-lead flows along membranes, through which the tritium permeates due to a partial pressure difference. On the permeate side the tritium is pumped out and routed to the tritium plant. Calculations show that a feasible size of a PAV-TERS for DEMO is expected to provide the required efficiency of 80 % [19, 26]. However, the technology is still under experimental demonstration. PAV demands membrane materials with high tritium permeability, as well as compatibility with Pb-Li due to corrosion (candidate materials are V, Nb and Ta) [27]. Additionally, because the partial pressure of tritium that will be dissolved in the lithium-lead is difficult to estimate, the level of vacuum needed at the permeate side to achieve the permeation is also unknown. If the tritium partial pressure is very low, forcing its permeation out of the Pb-Li may be technologically very challenging [19].

Other technologies are still under research, such as Gas-Liquid Contactors (GLCs), also named *packed columns*. A gas with low solubility in Pb-Li, typically helium or argon, flows in counter-current through the falling liquid metal. In this process, bubbles are formed and the gas acts as a carrier gas, extracting the tritium dissolved in the lithium-lead. A second step is needed to remove the tritium from the carrier gas. Experimental results have demonstrated extraction efficiencies from the Pb-Li up

to 30 – 31 % [28, 29], which may be improved by an optimization of the extraction loop and/or implementing a GLC cascade. This technology will be tested in the experimental reactor ITER, with a foreseen extraction efficiency of ≈ 44 % [30]. It should be clarified that the reported values of efficiency are evaluated at the lithium-lead and without including the next step of removing the tritium from the carrier gas. Although this efficiency is far from meeting the requirements, GLCs have the advantage above other techniques of being more mature and technologically proved.

Regenerable Getters (RGs) can also be used to extract tritium from Pb-Li. They rely on the affinity of tritium for some metals like vanadium. The liquid metal flows along solid getters, which trap the tritium in form of tritides (loading phase). Then the tritium can be released by heating the getters (regeneration phase). Even though this method exhibits high extraction efficiency, the disadvantage of not working in continuous mode has decreased the interest in this technology. Yet studies on the compatibility of getter materials with Pb-Li have been performed. Nevertheless, further research is still necessary, e.g. in the stability of the getter performance due to impurities [31–34].

A fourth extraction technique under consideration is the Vacuum Sieve Tray (VST). It consists in letting the Pb-Li fall through thin nozzles into a chamber under vacuum. The liquid metal falls in form of oscillating droplets that release the tritium gas, which is recovered with a pumping system. This method relies not only on a greater surface-to-volume ratio to increase the diffusion of tritium out of the liquid metal, but also on the convection of the Pb-Li in the falling droplets, which is likely to favour the release of tritium. Since the 1980s, the VST technology has been considered to extract tritium from liquid BB because of its simplicity [35]. In the last decade, VST extraction experiments (with deuterium) were performed at the University of Kyoto [36–38] reporting a coefficient of mass transfer which is two orders of magnitude greater than diffusion. The enhanced mass transfer has been explained by the mass movement of the Pb-Li induced by a cyclic deformation of the droplets while falling [38]. Based on the reported results, high extraction efficiencies would be expected and a VST-TERS for DEMO would match the required efficiency of 80 % [39].

2.2 VST functional principle and theoretical extraction efficiency

When the Pb-Li falls through a thin nozzle, it forms a liquid jet. Small perturbations intrinsic in the stream, in addition to the surface tension, originate the

so-called *Plateau-Rayleigh instability* [40, 41]. The radius of the liquid column fluctuates with increasing sinusoidal oscillations until a critical point is reached and the liquid jet breaks into droplets. The theoretical equivalent diameter of the formed droplets, d_d, is given by equation (2.1) as a function of the nozzle diameter, d_n (see Appendix A for mathematical derivation):

$$d_{\mathrm{d}} \simeq 1.89\, d_{\mathrm{n}}. \tag{2.1}$$

However, the falling droplets are not perfect spheres. Instead, their shape oscillates from an oblate to a prolate ellipsoid (in the ideal case). The fundamental frequency, f, of this oscillation in a liquid droplet falling in vacuum is described by [40, 42]:

$$f = \sqrt{\frac{8}{3}\frac{\sigma}{\pi\rho V}}, \tag{2.2}$$

where σ denotes the surface tension of the droplet, ρ its density and V its volume.

Inside the falling Pb-Li droplets, the tritium is dissolved in atomic form. The mass transport mechanisms that occur during the extraction process are:

1. Inside the droplet: mass transfer of the atomic tritium from the interior to the surface of the droplet by diffusion and convective transport of the liquid metal due to the droplet oscillations.

2. At the liquid-vacuum interface: recombination of the tritium atoms to form T_2 molecules and desorption from the liquid metal surface.

3. In the vacuum continuum: migration of the T_2 molecules inside the chamber in the vacuum phase and their recovery by the pumping system.

Since the mean free path of tritium molecules in the vacuum continuum is much larger than the one of tritium atoms inside the liquid metal, step 3 is not considered a limiting process in the tritium recovery. However, whether the migration inside the liquid or the recombination at the surface is the limiting process is a more complicated question. In the absence of literature data for recombination rates of hydrogen at liquid Pb-Li–vacuum interfaces, the approach followed is to assume that step 2 occurs faster than step 1. This assumption is based on the fact that the solubility of hydrogen atoms in Pb-Li is likely endothermic (see Figure 2.3, later in Section 2.3.3). In systems involving diatomic gases with endothermic solution, the recombination process during outgassing is exothermic. Therefore, these systems are typically bulk-controlled [43]. Then, step 1 is assumed to be the limiting process. Nevertheless, at the end of this research work, the experimental results can be evaluated to check this assumption.

Concerning the migration of tritium inside the droplet, extensive investigations have been performed in the field of liquid droplets falling in a liquid medium. Several models have been developed for mass extraction (see Appendix B). Depending on the droplet fluid dynamics, they can be divided into three categories: (i) droplets without internal circulation, treated as rigid spheres [44, 45], (ii) droplets with internal (laminar) circulation [44, 46], and (iii) oscillating droplets (typically with the formation of vortices leading to turbulent regimes) [47–49].

The mass extraction from droplets of types (ii) and (iii) was experimentally proved greater than the one from rigid droplets. The internal circulation in the droplets has been observed with trace impurities but it has not been yet fully understood. Some of the conclusions are: every system that exhibited oscillations showed deformed or completely damped circulation; the oscillations seem to be maintained by the vortex discharge behind the moving droplets; and the oscillations were not from full prolate to full obleate ellipsoids, but instead from nearly spherical to obleate form [50–54].

These conclusions were made for liquid-liquid systems and are most likely related to the friction resistance of the continuous phase. In the case of droplets falling in vacuum, the continuous phase would not impose friction forces. Therefore, the fluid dynamics in the droplets should be different and the described models do not perfectly apply. Due to the lack of investigation in liquid–vacuum systems, and for simplicity, a first approach to evaluate the extraction efficiency is to use the model of the rigid sphere, with a possible enhanced mass transfer due to internal movement of the Pb-Li.

From the mathematics of diffusion, a substance leaving (or entering) a sphere of diameter d_d, with diffusivity $\mathcal{D}$, during a time t, can be described by [45] (see Appendix B):

$$\eta_\mathrm{theo} = \frac{m_t}{m_\infty} = 1 - \frac{6}{\pi^2} \sum_{\mathrm{n}=1}^{\infty} \frac{1}{\mathrm{n}^2} \exp\left(\frac{-4\mathcal{D}\,\mathrm{n}^2\,\pi^2\,t}{d_\mathrm{d}^2}\right), \tag{2.3}$$

where m_t and m_∞ are the total mass of diffusing substance that has left (or entered) the sphere at time t and ∞, respectively, and n is the index of summation. In the application to VST, equation (2.3) describes the theoretical extraction efficiency of one droplet during its falling time, $t = t_\mathrm{fall}$, which is given by:

$$t_\mathrm{fall} = \frac{-v_\mathrm{n} + \sqrt{v_\mathrm{n}^2 + 2\,g\,h_\mathrm{fall}}}{g}, \tag{2.4}$$

where v_n is the initial speed of the droplet (at the exit of the nozzle), g is the gravitational acceleration and h_fall is the falling height.

Table 2.1: Values of diffusivity of deuterium in Pb-Li at 400 °C, mass transfer coefficient* reported in previous VST experiments at the same temperature; theoretical extraction efficiency, calculated with equation (2.3) for droplet diameter $d_{\mathrm{d}} = 1.2$ mm, initial droplet speed $v_{\mathrm{n}} = 4\ \mathrm{m\,s^{-1}}$, at two falling heights: $h_{\mathrm{fall}} = 0.5$, 5 m.

$\mathcal{D}$ $(\mathrm{m^2\,s^{-1}})$	η_{theo} $(h_{\mathrm{fall}} = 0.5\,\mathrm{m})$	η_{theo} $(h_{\mathrm{fall}} = 5\,\mathrm{m})$
1.23×10^{-9} [55]	6.5 %	15.6 %
5.04×10^{-9} [56]	12.8 %	30.2 %
3.4×10^{-7}* [37]	78.0 %	99.9 %

The extraction model based on a rigid sphere has been used in previous investigations of the VST technology [35, 37]. At the University of Kyoto, experiments were performed with deuterium and nozzle diameters between 0.4 – 1 mm. Using the rigid sphere model, presented in equation (2.3), they reported a mass transfer coefficient, which is two orders of magnitude greater than the diffusion coefficients available in literature. These results support the assumption that the extraction process from the droplets is bulk-controlled.

Table 2.1 shows diffusivity values of deuterium in Pb-Li at 400 °C, reported by Reiter [55] and Edao *et al.* [56], and the enhanced mass transfer coefficient obtained by Okino *et al.* [37]. Additionally, extraction efficiencies calculated with equation (2.3) are shown for two relevant scenarios, at experimental scale ($h_{\mathrm{fall}} = 0.5\,\mathrm{m}$) and at reactor scale ($h_{\mathrm{fall}} = 5\,\mathrm{m}$). The values displayed in Table 2.1 show that if the tritium extraction is only based on diffusivity and the volume-to-surface ratio of the droplet formation, the VST technique does not match the efficiency requirements for DEMO. However, if the internal movement of Pb-Li leads to a substantial enhancement of the mobility of tritium atoms, as reported in [37], the VST technique has a great potential for a reactor-scale TERS.

2.3 Transport of hydrogen in metals for experimental application

2.3.1 Conceptual background

The three isotopes of hydrogen are: protium (^{1}H or H), deuterium (^{2}H or D) and tritium (^{3}H or T). Since tritium is (β^-–decay) radioactive, at laboratory scale it is preferred to perform experiments with H and/or D and to prove the principle with T only in an advanced phase of the research. Additionally, since hydrogen is

a light (the lightest) element, it migrates easily through metals. The present work includes experiments with dissolution of deuterium into eutectic Pb-Li and its later extraction, both performed in stainless-steel (316L) chambers. Thus, the transport of hydrogen through metals has to be understood.

The first step in the interaction of hydrogen gas with a metal is the surface adsorption. The diatomic gas molecule can either be adsorbed via *van der Waals* forces (physisorption), or it can be attached to the metal surface by *chemical bonding* (chemisorption). If, in the latter, a dissociation of the hydrogen molecule is produced; then, the hydrogen atoms can enter the lattice and diffuse through the metal. The diffusion of the hydrogen atoms inside the metal is described by *Fick's laws of diffusion*:

$$J = -\mathcal{D}\,\frac{\partial C}{\partial x}, \tag{2.5}$$

$$\frac{\partial C}{\partial t} = \mathcal{D}\,\frac{\partial^2 C}{\partial x^2}, \tag{2.6}$$

where J is the flux of diffusing atoms ($\mathrm{mol_H\,m^{-2}\,s^{-1}}$), $\mathcal{D}$ is the diffusion coefficient ($\mathrm{m^2\,s^{-1}}$) and C is the atomic concentration ($\mathrm{mol_H\,m^{-3}}$). The diffusion flux is proportional to the gradient of concentration, as shown in equation (2.5).

At the beginning of the diffusion process, when hydrogen atoms start migrating into the metal, the concentration increases with time due to their accumulation. This non-stationary regime is described by equation (2.6).

In the general case of an instantaneous plane source of a diffusing substance, the concentration profile, obtained from (2.6), can be expressed as follows [45]:

$$C(x,t) = \frac{n}{2\sqrt{\pi\mathcal{D}t}}\exp\left(-\frac{x^2}{4\mathcal{D}t}\right), \quad \text{for } -\infty < x < +\infty \text{ and } t > 0, \tag{2.7}$$

where n is the total amount of substance (mol) inserted in the system at $x=0$, $t=0$, which diffuses in 1D into both directions $-\infty$ and $+\infty$. The characteristic time scale of the diffusion process, τ_{ch}, can be determined by maximising equation (2.7) over time at the position $x=L$:

$$\frac{\partial C(x=L,t)}{\partial t} = 0 \quad \longrightarrow \quad \tau_{\mathrm{ch}} = \frac{L^2}{2\mathcal{D}}, \tag{2.8}$$

where L is the length of the diffusion system. Note that the result is independent of the total mass of diffusing substance, and therefore it can be directly applied to a system with diffusing substance in only one direction ($0<x<L$), as is the case of a membrane with thickness L. Then, τ_{ch} can be used to estimate when the steady-state of the diffusion process inside the metal is achieved. (An alternative method to determine the characteristic time scale given in equation (2.8) is developed by [57].)

Steady-state is achieved once the metal is saturated with the diffusive substance. At this point, since no more atoms can be dissolved, the flux through the metal is stationary. The saturation is given by the solubility of the substance in the metal, which, in the case of a diatomic gas, is governed by *Sieverts' law*:

$$C = \mathcal{S}\sqrt{p}, \tag{2.9}$$

where p is the partial pressure in the gas phase (Pa) and $\mathcal{S}$ is the solubility coefficient ($\mathrm{mol_H\,m^{-3}\,Pa^{-1/2}}$), also called *Sieverts' constant*. Note that C refers to *atomic* concentration. The steady-state permeation flux is then calculated from equations (2.5) and (2.9), and can be written as:

$$J = \mathcal{P}\left(\sqrt{p_b} - \sqrt{p_a}\right)\frac{A}{L}, \tag{2.10}$$

where L is the thickness of the metal (in the permeation direction), A is the area of the surface and p_a and p_b are the partial pressures of the gas at both sides of the metal (note that the square-root dependency, from Sieverts' law, applies only to diatomic gases). $\mathcal{P}$ is the permeability constant ($\mathrm{mol\,m^{-1}\,s^{-1}\,Pa^{-1/2}}$), which is a function of the diffusivity and the solubility:

$$\mathcal{P} = \mathcal{D}\mathcal{S}. \tag{2.11}$$

All three rate coefficients, $\mathcal{P}$, $\mathcal{D}$ and $\mathcal{S}$, follow an Arrhenius dependency on temperature:

$$\mathcal{D} = \mathcal{D}_0\,\mathrm{e}^{-\frac{E_\mathcal{D}}{RT}}, \tag{2.12}$$

$$\mathcal{S} = \mathcal{S}_0\,\mathrm{e}^{-\frac{E_\mathcal{S}}{RT}}, \tag{2.13}$$

$$\mathcal{P} = \mathcal{P}_0\,\mathrm{e}^{-\frac{E_\mathcal{P}}{RT}}, \tag{2.14}$$

where $E_\mathcal{D}$, $E_\mathcal{S}$ and $E_\mathcal{P}$ are the corresponding activation energies and R is the ideal gas constant. The expressions shown in equations (2.12), (2.13) and (2.14) are characteristic of the diffusing substance and the metal, and are empirically obtained.

2.3.2 Diffusivity and permeability in stainless steel

Figure 2.1 shows diffusivity values of hydrogen (protium) and deuterium in stainless steel 316L. Additionally, Table 2.2 shows the coefficients of permeability of deuterium in stainless steel for similar temperature ranges. Both diffusion and permeation of hydrogen in steel are thermally activated processes, i.e. the corresponding activation energies are positives ($E_\mathcal{D}$ and $E_\mathcal{P}$ in equations (2.12) and (2.14)). Consequently, the diffusivity and permeability of hydrogen isotopes in stainless steel increase with temperature (as observed in Figure 2.1).

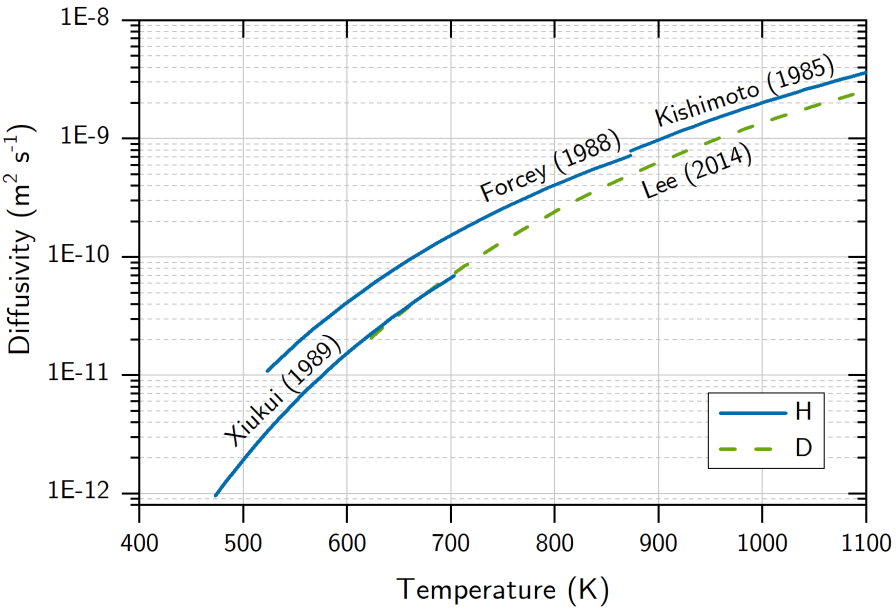

Figure 2.1: Diffusivity, $\mathcal{D}$, of hydrogen (H) and deuterium (D) in stainless steel 316L as a function of the temperature. [58, 60–62].

Table 2.2: Permeability coefficients, $\mathcal{P}_0$, and activation energies, $E_{\mathcal{P}}$, reported in literature for deuterium in stainless steel 316 [59] and 316L [58] for the given temperature ranges, T.

$\mathcal{P}_0$ (mol m m^{-2} s^{-1} Pa$^{-0.5}$)	$E_{\mathcal{P}}$ (J mol^{-1})	T (K)	Reference
3.54×10^{-7}	67300	623–973	[59]
4.56×10^{-7}	71200	623–1123	[58]

As a reference, the reported values for deuterium at 400 °C (which is the operation temperature of the setup) are: $\mathcal{D} = 4.73\times10^{-11}$ m^2 s^{-1}, reported by Lee *et al.* [58] and the permeability values $\mathcal{P} = 2.10\times10^{-12}$ mol m^{-1} s^{-1} Pa$^{-0.5}$ from Shiraishi *et al.* [59] and $\mathcal{P} = 1.35\times10^{-12}$ mol m^{-1} s^{-1} Pa$^{-0.5}$ from Lee *et al.* [58].

2.3.3 Diffusivity and solubility in eutectic Pb-Li

The lead-lithium alloy considered for the liquid breeding blankets is the eutectic mixture, which has the melting point at 235 °C [63]. The composition used as *eutectic* had been for years 17 at.% Li and 83 at.% Pb. However, there was a reassessment of the phase boundaries and the composition in the last studies has been updated to 15.7 at.% Li and 84.3 at.% Pb [64].

Table 2.3 shows the main temperature-dependent thermo-physical properties of the eutectic Pb-Li in its liquid form. At 400 °C, its density is 9720 kg m^{-3}, dynamic

viscosity: 1.5×10^{-3} Pa s, surface tension: 0.446 N m^{-1} and vapour pressure: 2.5×10^{-5} Pa.

Figure 2.2 shows the reported diffusivity values of hydrogen isotopes in Pb-Li as a function of the temperature. Note that the values reported for deuterium (D) by Edao *et al.* and Reiter at 400 °C are the ones given in Table 2.1. Similarly to the case of stainless steel, the diffusivity of hydrogen in Pb-Li also increases with temperature. However, in the case of Pb-Li, there is one order of magnitude scattering in the reported values. These deviations are presumably a consequence of the different measuring methods and setups (note that the experimental errors are not reported). Another possible reason for the scattered values is small variations in the composition of the Pb-Li used in the different experiments. However, since no verification of the Pb-Li composition is normally reported, it is not possible to

Table 2.3: Properties of eutectic Pb-Li (T in K) and range of application.

Parameter	Value	T (K)	Ref
Density, ρ (kg m^{-3})	$\rho = 1.052 \times 10^4 - 1.19\,T$	508–880	[65]
Dynamic viscosity, μ (Pa s)	$\mu = 1.87 \times 10^{-4} \exp\left(\frac{1400}{T}\right)$	521–900	[66]
Surface tension, σ (N m^{-1})	$\sigma = 0.52 - 1.1 \times 10^{-4}\,T$	520–1000	[65]
Vapour pressure, p_v (Pa)	$p_v = 1.5 \times 10^{10} \exp\left(\frac{-22900}{T}\right)$	550–1000	[65]

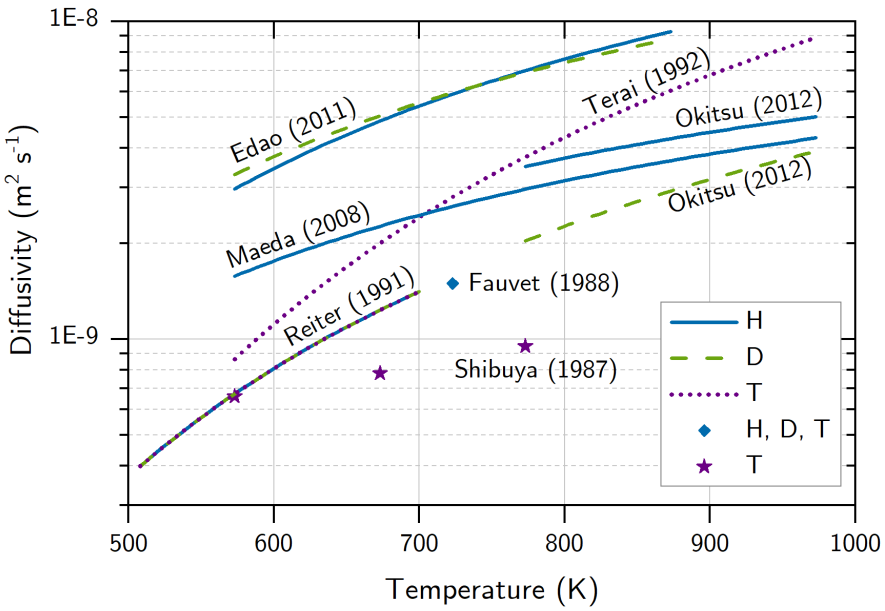

Figure 2.2: Diffusivity of hydrogen isotopes in eutectic Pb-Li as a function of the temperature. Experimental results from Terai *et al.* [67], Fauvet *et al.* [68], Reiter [55] and Shibuya *et al.* [69] were obtained with desorption methods; and results from Edao *et al.* [56], Maeda *et al.* [70] and Okitsu *et al.* [71] were obtained via permeation methods.

study the influence of the Pb-Li composition on the scattered values.

Nevertheless, comparing Figures 2.1 and 2.2, the diffusivity of hydrogen isotopes in Pb-Li is around two orders of magnitude larger than in stainless steel at similar temperatures. Therefore, when using stainless steel as a structural material for experiments involving dissolution/diffusion of hydrogen isotopes in Pb-Li, the gas lost into the structure has to be carefully quantified and considered in the results.

Figure 2.3 shows the Sieverts' constant reported for hydrogen isotopes in eutectic Pb-Li as a function of the temperature. Some solubility values increase with the temperature (see Aiello *et al.* [73], Maeda *et al.* [70], Chan *et al.* [75], Okitsu *et al.* [71]), while others show almost no dependency of the temperature (see Wu [74] and Reiter [55]). This could be due to slightly different compositions (Wu [74] tested various Pb-Li compositions and reported a transition from exothermal to endothermal dissolution that occurs at around 17 at.% Li).

Additionally, a scatter of two orders of magnitude is observed among the published solubility results. The large discrepancy among the values is currently under discussion. Possible reasons include: (i) the methodology used for each experimental

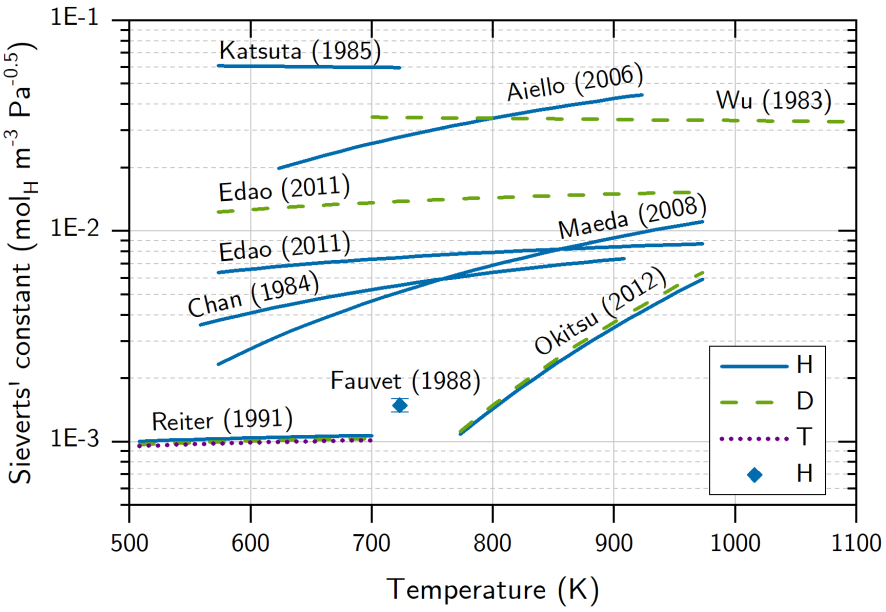

Figure 2.3: Solubility of hydrogen isotopes in eutectic Pb-Li as a function of the temperature. All values are experimentally obtained, except for the value reported for tritium, which is theoretically extrapolated. The results from Katsuta *et al.* [72], Fauvet *et al.* [68] and Reiter [55] were obtained with desorption methods; the values from Aiello *et al.* [73], Wu [74] and Chan *et al.* [75] were obtained with absorption methods; and the results from Edao *et al.* [56], Maeda *et al.* [70] and Okitsu *et al.* [71] were obtained via permeation methods.

result (i.e. absorption, desorption or permeation, shown in the caption of Figure 2.3); (ii) assumptions made in the determination (e.g. neglecting the permeation through the walls of the container), which could lead to large experimental errors, or (iii) variations in the fraction of lithium in the Pb-Li alloy (among the reported values, the Li concentration varies from 15.7 at.% to 17 at.%). Note that the great difference in atomic mass between Pb ($207.2\,\mathrm{g\,mol^{-1}}$) and Li ($6.94\,\mathrm{g\,mol^{-1}}$) leads to a mixture, which is very sensitive in atomic composition (in weight percentage, the fraction of Pb in the two mentioned eutectic mixtures is $\approx 99.32 - 99.38$ wt.%). Thus, the manufacturing of the alloy must be very finely done and later composition analyses to check the eutectic mixture are essential (which are normally not reported in the references shown in Figures 2.2 and 2.3).

The effect of fine variations in the Pb-Li eutectic composition in both diffusivity and solubility of hydrogen isotopes in the liquid alloy remains still unknown and is further discussed in the present work (in Sections 3.1.4, 5.6.1, 6.3.1).

2.4 The problem of the unknown solubility in Pb-Li

In the experimental research of TERS techniques for Pb-Li, typically two processes are needed: firstly, the hydrogen isotope, e.g. deuterium, is dissolved in the liquid metal and, secondly, it is extracted with the corresponding technique. Then, the extraction efficiency, η_{exp}, can be experimentally determined with the amount initially dissolved in the Pb-Li, $n_{\mathrm{D_2\,diss}}$, and the amount extracted, $n_{\mathrm{D_2\,ext}}$, as follows:

$$\eta_{\mathrm{exp}} = \frac{n_{\mathrm{D_2\,ext}}}{n_{\mathrm{D_2\,diss}}}. \tag{2.15}$$

Typically, the amount of deuterium dissolved, $n_{\mathrm{D_2\,diss}}$, can be evaluated using Sieverts' law (equation (2.9)). However, in the case of eutectic Pb-Li, as shown in Figure 2.3, there is a huge disagreement in the reported values of Sieverts' constant. Thus, the intrinsic challenge to assess the extraction efficiency, η_{exp}, is to precisely determine the quantity of deuterium dissolved in the liquid metal, $n_{\mathrm{D_2\,diss}}$. This is a critical issue, which affects all the technologies under research for the TERS of liquid breeding blanket concepts.

Since the amount of deuterium dissolved cannot be calculated with values of solubility, it has to be either directly measured or indirectly determined from experiments. Hydrogen sensors to measure the concentration of hydrogen isotopes in the liquid metal are under development, based on two different physical principles: permeation sensors [76, 77] and electrochemical sensors [78].

Permeation sensors consist in a hollow capsule immersed in the liquid lithium-lead, through which hydrogen permeates. In steady-state, the partial pressure of hydrogen in both the capsule and in the liquid metal equal each other. However, these sensors rely on the knowledge of the Sieverts' constant to determine the concentration of hydrogen. Thus, permeation sensors are reasonable to determine a concentration profile, but not to measure absolute values of concentration.

Electrochemical sensors consist of an electrode immersed in the liquid metal and a reference electrode immersed in an electrolyte with a known H-concentration. The potential difference between the two electrodes gives the relative hydrogen concentration. This principle allows measuring the concentration of hydrogen without relying on solubility values. However, electrochemical sensors are so far only available for pure liquid lithium or other lead eutectic alloys, such as Pb-Bi [78, 79].

Since there is currently no reliable method to directly measure the concentration of hydrogen inside the lithium-lead, in the present work, $n_{\mathrm{D_2\,diss}}$ is determined by means of a mass balance during the dissolution phase (discussed in Chapter 5), which requires to evaluate a set of secondary experimental data.

Chapter 3

The VST facility and experimental strategy

3.1 Description of the facility

An experimental facility, operated with D_2, was built at the Tritium Laboratory Karlsruhe (TLK) to investigate the Vacuum Sieve Tray (VST) technique. Its assembly and commissioning are part of the present work. The facility aims to meet two main objectives: (i) evaluation of the deuterium dissolution and VST extraction processes, (ii) using tritium and Pb-Li compatible components in order to test the functionality and gain know-how with the liquid metal for a future experimental set-up operated with tritium.

3.1.1 The Pb-Li loop

Figure 3.1 shows the Pb-Li loop, which consists of two chambers made of stainless steel (316L): the *upper chamber* (UC), in which the dissolution occurs, and the *lower chamber* (LC), in which the deuterium is extracted. The lower chamber has four ports: two with windows assembled, one with a flexible tube connected to the pumping system, and a last one that is sealed with a blind flange. The two chambers are connected by a short pipe with an automatic valve and ending in the nozzle (0.6 mm diameter), through which the Pb-Li falls to the lower chamber. Additionally, there is a transfer line to rise the Pb-Li back from the lower chamber to the upper chamber.

Seven independent heaters are installed along the Pb-Li loop to maintain the metal at the desired temperature. They consist of resistance wires and are covered by rock-wool and glass-fiber insulation. In the upper chamber, the heater is placed at the bottom surface, in order to force buoyant convection in the liquid and enhance the dissolution of deuterium. In the lower chamber, the heaters are placed at the top and bottom, since the windows (of borosilicate with kovar frame) withstand

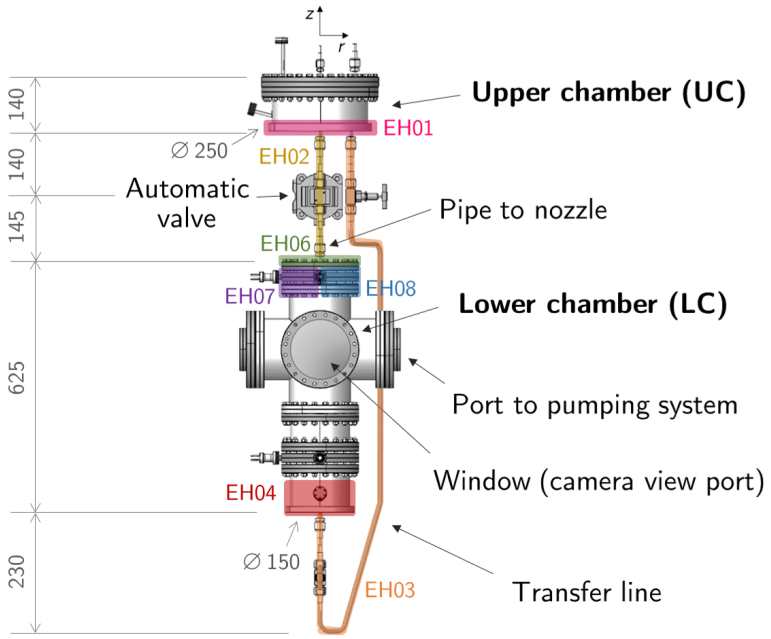

Figure 3.1: Pb-Li loop with main dimensions given in mm. The heated zones, to maintain the Pb-Li liquid, are divided by independent electrical heaters (EH). They are listed in Table 3.1 with their respective operation temperature.

Table 3.1: Operation temperature of the heaters in the Pb-Li loop.

Reference	Location	Temperature (°C)
EH01	Upper chamber	400
EH02	Short pipe (automatic valve)	435
EH03	Transfer line	450
EH04	Lower chamber (bottom)	360
EH06	Lower chamber (top flange)	455
EH07, EH08	Lower chamber (side-top)	445

a maximum of only 350 °C. The operation temperature of each heater is given in Table 3.1. The set temperatures of heaters EH02, EH06 and EH07 are higher than 400 °C to ensure the desired temperature at the nozzle (which cannot be directly covered by a heater). On the other hand, the Pb-Li in the lower chamber, heated by EH04, had to be maintained at 360 °C in order to limit the evaporation rate of Pb-Li, which slowly was covering the windows. The heater of transfer line, EH03, also had to be maintained at a higher temperature (than 400 °C) to avoid Pb-Li solidification in critical points (specifically at the valve HV204 at the outlet of the lower chamber).

3.1.2 Gas inlet, evacuation and analysis

The facility has three gas inlets: D_2, H_2 and Ar (the latter is also adapted to provide He or N_2, if necessary). Mainly D_2 is used for the dissolution experiments and Ar is used to lift the Pb-Li to the upper chamber by pressurization of the lower chamber. Occasionally, He is used for experimental tests that require an inert gas with low solubility in metals but similar thermal conductivity as D_2.

Figure 3.2 shows the experimental facility (note that the Pb-Li loop is covered by insulation). The evacuation of the two chambers is done via a pumping system, which consists of a turbo-molecular pump followed by a fore pump. To protect the turbo-molecular pump from possible Pb-Li vapours, a *cold trap* is placed at the inlet. The cold trap consists of several steel meshes, at room temperature, to condense any possible metal vapour.

Originally, the setup was designed to collect the extracted gas in a collecting tank, placed at the outlet of the fore pump (located behind the pump in Figure 3.2). However, during the commissioning phase, it was observed that the background gas collected with the pumping system was much larger than expected and the pressure in the collecting tank would easily exceed its maximum during an experiment. Additionally, tests were performed to determine the pumping efficiency (gas collected vs extracted) and no repeatability was demonstrated in the measurements. These results were explained by possible internal cavities in the pumping system that retain gas and release it slowly, acting as *virtual leaks*. Because of these two reasons, it was decided to measure the extracted gas directly in the lower chamber.

A Quadrupole Mass Spectrometer (QMS) is also assembled next to the collecting

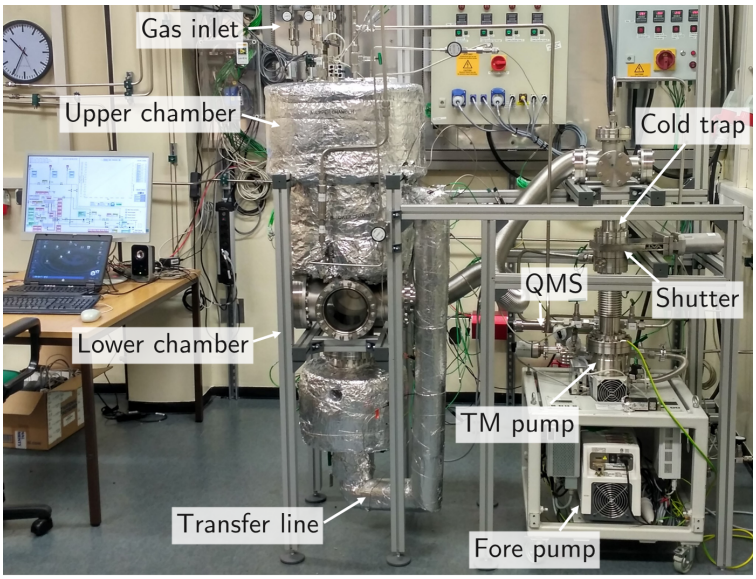

Figure 3.2: Laboratory configuration of the experimental setup.

tank, with connection to the chambers. It is used to analyse the composition of the gas (e.g. after the vacuum test in the upper chamber to identify if the background is due to leak or outgassing from previous experiments).

Monitoring and control of the experiment is realized via a LabVIEW program. The software records the experimental data with a minimum sampling time of 1 s and also has safety features to protect the QMS and vacuum sensors from high pressure.

3.1.3 Measuring devices and uncertainty assessment of the experimental data

3.1.3.1 Amount of gas and its uncertainty assessment

The deuterium dissolved in the Pb-Li is determined from the evolution of the amount of gas in the upper chamber. Likewise, the D_2 extracted is determined from the evolution of the amount of gas in the lower chamber. They are both calculated by means of the *ideal gas law*, which relates the amount of gas, n, in a closed volume, V, with its pressure, p, and temperature, T:

$$n = \frac{pV}{RT}, \tag{3.1}$$

where $R \simeq 83.14\,\mathrm{l\,mbar\,K^{-1}\,mol^{-1}}$ is the *ideal gas constant*. The assessment of the uncertainty is determined following the general equation for error propagation [80]:

$$\delta f(x_i)^2 = \sum_{i=1}^{N} \left(\frac{\partial f}{\partial x_i}\right)^2 \delta x_i^2, \tag{3.2}$$

in which f is a function of independent variables x_i (with $i = 1, ...N$), and δ denotes uncertainty. The application of equation (3.2) to (3.1) leads to:

$$\delta n = \sqrt{\left(\frac{\partial n}{\partial p}\right)^2 \delta p^2 + \left(\frac{\partial n}{\partial V}\right)^2 \delta V^2 + \left(\frac{\partial n}{\partial T}\right)^2 \delta T^2}. \tag{3.3}$$

In this section, the main characteristics of the measuring devices and a first assessment of the uncertainty calculations are presented. A few relevant examples (using similar conditions to the experiments performed, shown in Chapters 5 and 6) are considered to gain a first insight into the accuracy and limitations of the measured gas in both chambers. Further calculations of error handling and propagation are given in Appendix K.

3.1.3.2 Upper chamber

Figure 3.3 shows a cross section of the upper chamber with its main dimensions (in mm) and measuring devices. The chamber was designed with a large diameter to favour the dissolution of D_2 into the liquid Pb-Li (i.e. large gas–liquid interface). It has a sampling port (left of the figure) and a conic bottom in order to facilitate that all Pb-Li flows down to the lower chamber during the extraction experiment. It has a pressure sensor (RP010) located at a cold finger, since the sensor does not withstand the operation temperature of the chamber (400 °C), with a thermocouple (RT014) next to it to measure the temperature of the gas at the sensor. Additionally, there are four thermocouples (RT010, RT011, RT012, RT013) to measure the temperature of the gas in the chamber (when there is no Pb-Li). With Pb-Li, RT012 and RT013 are used to measure the temperature of the liquid metal and check its level (whose maximum is around 23 mm).

The main characteristics of the pressure sensor (RP010) are given in Table 3.2. The sensor has a full scale of 3 bar to cover the operation range of the experiments,

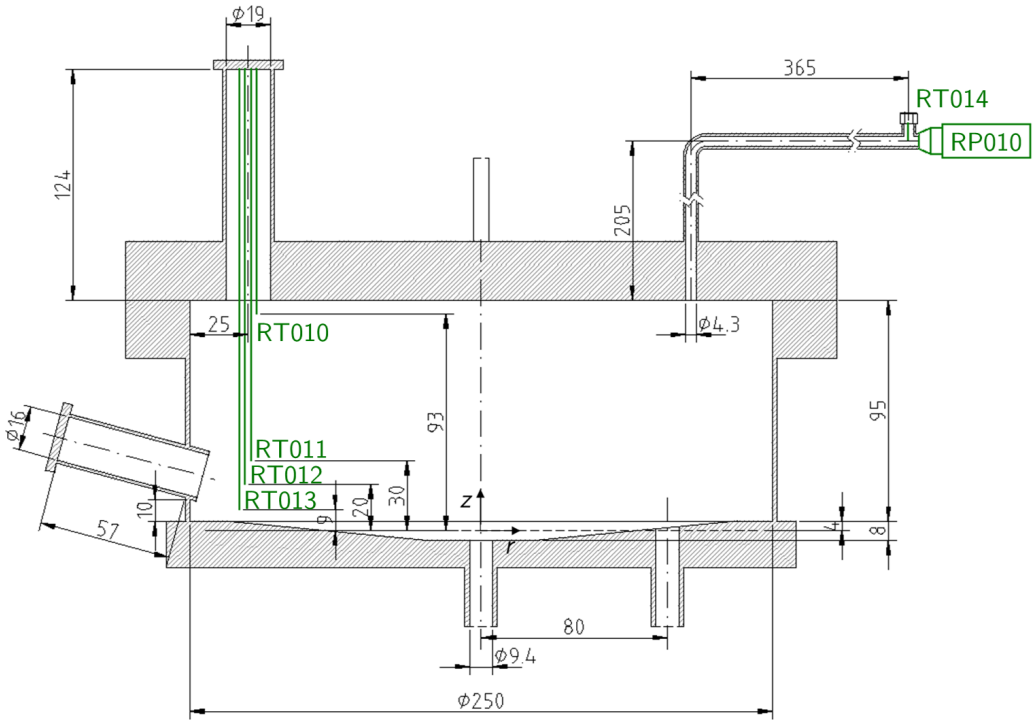

Figure 3.3: Cross section of the upper chamber with dimensions given in mm. RP010 is the pressure sensor, located at the cold finger. The thermocouple RT014 measures the temperature of the gas at the pressure sensor. The thermocouples RT010, RT011, RT012, RT013 measure the gas temperature in the chamber. Additionally, RT012 and RT013 measure the Pb-Li temperature (and level). The total volume of the upper chamber is 4.88±0.02 l.

Table 3.2: Main characteristics of the pressure sensor in upper chamber, RP010.

Parameter	Value
Model:	PTA227, EFE
Full Scale (F.S.):	3 bar
Non-linearity and hysteresis:	±0.016% F.S.: 0.48 mbar
Non-repeatability:	±0.02% F.S.: 0.60 mbar
Thermal zero and sensitivity shifts:	±0.02% F.S./°C: 0.60 mbar/°C
Maximum operating temperature:	125 °C

500–1500 mbar. However, since the variations of pressure during the dissolution phase are expected to be small (several millibar), the accuracy of the sensor has to be carefully regarded. From its sensitivity to variations of temperature shown in Table 3.2, the uncertainty in the pressure measurement can become, as an example, ±4.08 mbar for a variation of 5 °C. This is not admissible for the analysis of the experimental results. However, it has been observed that the variation of the sensor signal with the temperature of the sensor is linear (at constant pressure). Therefore, a calibration was done to improve the accuracy of the sensor. From this calibration, shown in Appendix G, a correction factor of -1.2 mbar/°C was obtained for the range $17.4-22.4$ °C. The measurements performed with the pressure sensor RP010 are corrected with this factor, which allows to have a more accurate pressure measurement and a constant minimized uncertainty of ±1.08 mbar (since the error due to temperature shifts can be neglected).

The total volume of the upper chamber is 4.88 ± 0.02 l (which was measured by combinations of gas expansions with a dedicated high-accuracy equipment [81]). However, the volume of the Pb-Li has to be measured/determined for each experiment. This is a limiting factor in the accuracy of the results, which affects both the total gas dissolved and its concentration. The volume of Pb-Li in the chamber can be determined with the three level thermocouples (RT011, RT012, RT013). The distance between them, 10 mm, is however too large, i.e. using them as level sensors results in an uncertainty of ±0.25 l of Pb-Li (which corresponds to ≈ ±7% and ≈ ±20%, relative to the volume of gas and Pb-Li, respectively). In order to improve this uncertainty, the code developed to simulate the fluid dynamics during the extraction phase has been used to determine the volume of Pb-Li by fitting the experimental results with simulations, as explained in Chapter 4. With this method, the uncertainty is minimized to $\pm 0.03 - 0.04$ l (which corresponds to ≈ ±1% and ≈ ±3%, relative to the volume of gas and Pb-Li, respectively).

Since the maximum Pb-Li height is expected to lie between RT011 and RT012, the temperature of the gas is measured with RT010 and RT011, when all the Pb-Li is in the upper chamber, and with RT010 and RT013, when there is no Pb-Li. The temperature of the gas is then calculated with equation (3.4), assuming that it is only due to radiation from top and bottom (*infinite*) surfaces with constant temperatures T_a and T_b, respectively (both in K), given by the corresponding above-mentioned thermocouples:

$$T = \sqrt[4]{\frac{T_a^4 + T_b^4}{2}}. \tag{3.4}$$

All the thermocouples are Ni-Cr K-type and have an uncertainty of $\pm 2.2\,^{\circ}\mathrm{C}$ or $\pm 0.75\,\%$ (in °C), whichever is greater. The uncertainty is propagated with equation (3.2).

Table 3.3 shows the uncertainty contributions for an example case (representative of the dissolution experiments). The value of n and its uncertainty are calculated with equations (3.1) and (3.3). The error from the volume ($\pm 1.2\,\%$) limits the global uncertainty of n (which is minimized to $\pm\,1.3\,\%$). During the dissolution experiments in the upper chamber, V is constant, T variations are within uncertainty (thus, T is effectively constant), and the variation of p is measured. I.e. the *detection limit* to measure the variation of the amount of gas (due to diffusion into the Pb-Li and walls) corresponds to 1.08 mbar, which has been minimized with the calibration of the pressure sensor.

In the treatment of the uncertainty, special attention is paid to the type of error. The uncertainty contribution from the pressure sensor is of *random* type or due to instrumental limitations. This type of error can be decreased by averaging values measured under the same conditions. On the other hand, the error contributions from volume and temperature are of the type *systematic* or *offset*. The type of uncertainty has been considered in the error propagation to avoid an overestimation (or underestimation) of the final uncertainty of the results.

Table 3.3: Uncertainty assessment of the amount of gas in the upper chamber for a typical example case.

Variable	Example value	Uncertainty	Type of uncert.
Gas pressure, p (mbar)	1000	1.08 (0.1 %)	random
Gas volume, V (l)	3.68	0.04 (1.2 %)	systematic
Gas temperature, T (°C)	380	2.85 (0.4 %, in K)	systematic
Amount of gas, n (mol)	6.78×10^{-2}	8.78×10^{-4} (1.3 %)	combined

3.1.3.3 Lower chamber

Figures 3.4 and 3.5 show the cross section of the lower chamber with its main dimensions (in mm) and its measuring devices. This chamber also has a sampling port and a conic bottom (similar to the upper chamber), as seen in Figure 3.5. It has assembled one pressure sensor (RP041) and two vacuum sensors (RP040 and RP042), all placed at cold fingers to protect them from the high temperatures (with RT042 measuring the gas temperature at the sensor RP041). Two thermocouples measure the temperature of the nozzle (RT040 and RT041) and RT043 measures the temperature of the gas at the top of the chamber. Eight thermocouples are placed at the bottom of the chamber to measure the level of the Pb-Li and its temperature.

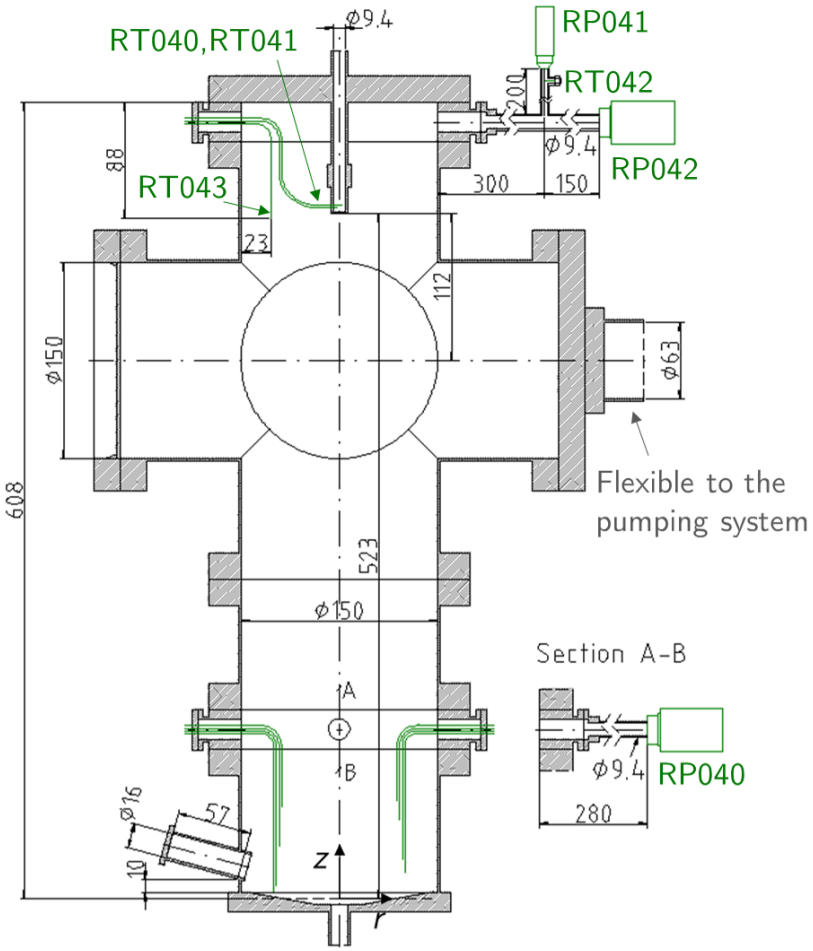

Figure 3.4: Cross section of the lower chamber with main dimensions given in mm. The pressure sensor RP041 and the vacuum sensors RP040 and RP042 are placed at cold fingers. RT042 measures the temperature of the gas at RP041. The thermocouples RT040 and RT041 measure the temperature of stainless-steel surface next to the nozzle, RT043 measures the temperature of the gas. See zoom of the bottom of the chamber in Figure 3.5. The total volume of the lower chamber is 27.3 ± 0.1 l (note that it includes the flexible down to the shutter valve, shown in Figure 3.2).

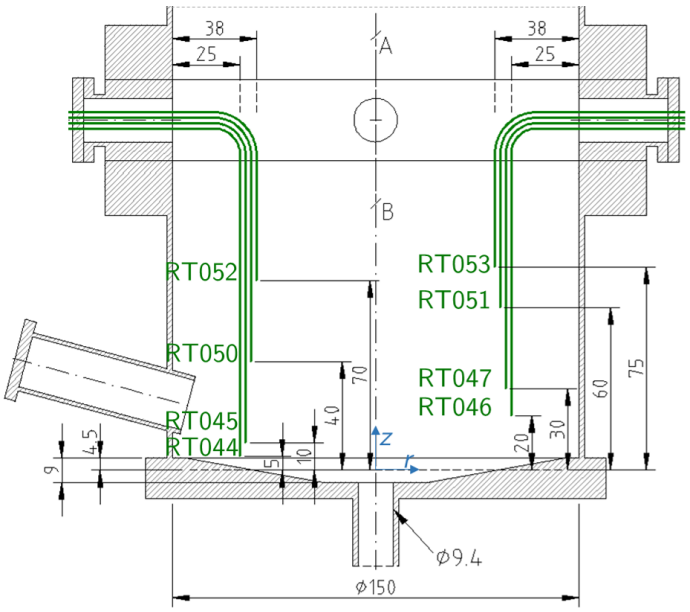

Figure 3.5: Cross section of the bottom of the lower chamber with dimensions given in mm. The eight thermocouples RT044, RT045, RT046, RT047, RT050, RT051, RT052, RT053 are placed at the given positions to detect the Pb-Li level and measure its temperature.

The total volume of the lower chamber is $27.3 \pm 0.1\,\mathrm{l}$ (which was measured with the method presented in [81], as in the upper chamber). During extraction, the Pb-Li level increases from RT044 to almost RT053 ($\approx 1.2\,\mathrm{l}$). Thus, applying *Boyle's law* (which describes a closed system at constant temperature: $p_1 V_1 = p_2 V_2$), the increase of pressure in the lower chamber due to *only* the change in volume of Pb-Li during the whole extraction experiment is $\approx 5\,\%$ (e.g. from 0.150 to 0.157 mbar). Therefore, if the amount of gas extracted from the droplets is in this range, the change in volume of the Pb-Li must be very finely assessed in the calculations in order to assess the amount of D_2 extracted. From the fluid-dynamics simulation, which fits the experimental results (explained in Chapter 4), the volume of Pb-Li in the chamber at every instant is obtained, with an uncertainty of $\pm 0.01 - 0.02\,\mathrm{l}$.

The temperature of the gas in the lower chamber is, however, a more intricate issue, due to its geometry and large temperature gradients. The top and bottom of the chamber are at 455 °C and 360 °C, respectively (see Table 3.1), the windows (middle of the chamber) are colder and the flexible tube is at room temperature. Therefore, for the evaluation of the amount of gas, the chamber is divided in three sub-volumes and equation (3.4) is used to determine the temperature of the regions with temperature gradient. The approach is further explained in Chapter 6.

The pressure sensor RP041 is similar to the one in the upper chamber (same characteristics as in Table 3.2). It is used to measure the pressure of argon when

Table 3.4: Characteristics of the vacuum sensors in lower chamber (F.S.: full scale, M.P.: measuring point)

Parameter	RP040	RP042
Model:	422, MKS	CTR100N, Leybold
Type:	cold cathode	capacitance diaphragm
Range (mbar):	$1.3\times10^{-11}-1.3\times10^{-2}$	$1.3\times10^{-3}-13.3$
Resolution:	2 significant digits	0.003% F.S.: 4×10^{-4} mbar
Accuracy:	±5% M.P.	±0.25% M.P.
Max. operating temperature:	250 °C	50 °C
Temperature effect on zero:	(-)	±0.005% F.S./°C
Gas dependency:	yes	no

transferring the Pb-Li to the upper chamber.

To measure the D_2 extracted from the Pb-Li during the extraction phase, two vacuum gauges are installed to cover a wide range of vacuum (from 1.3×10^{-11} to 13.3 mbar). Their main characteristics are given in Table 3.4. Due to the gradients of temperature in vacuum regime, the actual pressure inside the chamber has to be determined with rarefied gas theory (with the corresponding increase of uncertainty). This is explained in Chapter 6.

Table 3.5 shows a simplified assessment of the uncertainty contributions of p, V, T in the lower chamber for two relevant cases:

- Case #1: $p = 1.1\times10^{-3}$ mbar (read by the sensor RP040). The total amount of gas obtained is $n = (1.01 \pm 0.06)\times10^{-6}$ mol. This example is taken from the calculation of the beginning of run#13.

- Case #2: $p = 0.153$ mbar (measured by the sensor RP042). The total amount of gas obtained is $n = (1.21 \pm 0.08)\times10^{-4}$ mol. This example is taken from the calculation of the beginning of run#14.

As mentioned above, the total amount of gas is evaluated from the division into three sub-volumes. Thus, for simplicity, the p, V, T uncertainty values shown in Table 3.5 are averages from the three regions. With this, an overview of the contributions can be observed.

In both example cases, the major contribution to the uncertainty is given by the pressure. Specifically in case #2, the uncertainty of the pressure measurement is of ±0.4 %, but it is highly increased by the calculations due to the gas (transition) regime. The final relative uncertainty of n is very similar in the two cases. However,

Table 3.5: Uncertainty contributions of the amount of gas in the lower chamber for two example cases. Case #1: $p = 1.1\times10^{-3}$ mbar (RP040), $n = (1.01 \pm 0.06)\times10^{-6}$ mol; case #2 $p = 0.153$ mbar (RP042), $n = (1.21 \pm 0.08)\times10^{-4}$ mol.

Variable	Avg. relative uncertainty		Type of
	Case #1	Case #2	uncertainty
Gas pressure, p	±7.6%	±5.0%	random
Gas volume, V	±4.4%	±4.4%	systematic
Gas temperature, T	±1.4%	±1.4%	systematic
Total amount of gas, n	±5.7%	±6.2%	combined

the detection limit is very different: $\approx 6\times10^{-8}$ mol in case #1 and $\approx 8\times10^{-6}$ mol in case #2.

Additionally, the type of uncertainty (random vs systematic) and its treatment in the error propagation varies depending on the region. For example, in the gas region close to the Pb-Li, the volume and temperature of the gas vary. Therefore, the advantage normally intrinsic to systematic error (when subtracting two values) cannot be used. Appendix K is dedicated to the error propagation of the calculations.

3.1.4 Pb-Li used in the experiments

A total of 21.6 kg of eutectic mixture of Pb-Li (99.95% purity, 15.7 at.% Li) was supplied by the company CAMEX, spol. s r. o., Czech Republic, in form of ingots. From this amount, 15.10 kg of Pb-Li were inserted in the facility (which at 400 °C occupy 1.55 l). The surface of the ingots was cleaned mechanically with a file. Then, the ingots were weighted and introduced in the upper chamber. From the moment the upper chamber was closed until the first experiment, the Pb-Li was under evacuation during four weeks at 180 °C and the subsequent three weeks at 400–440 °C, with intermediate flushing of helium and argon during the commissioning of the setup. This procedure is assumed to have removed any possible oxides still present in the metal after the mechanical abrasion of its surface. Additionally, during the decommissioning of the facility (with all the Pb-Li solidified in the lower chamber), the upper chamber was opened and found clean and without any visual indication of oxides. This supports the assumption above.

The composition of the Pb-Li was analysed before and after the experimental campaign by the Chemical Analysis group in IAM-AWP, KIT, with inductively coupled plasma atomic emission spectroscopy (ICP-AES). The full results of the

Table 3.6: Comparison of the Pb-Li composition from samples taken before and after the experimental campaign. Only the main impurities are shown, for extended information see full analysis in Appendix E.

Element	Before (wt.%)	After (wt.%)
Pb	99.1	98.8
Li	0.490	0.592
Fe	< 0.0002	0.00103
Ni	< 0.0002	0.00422
Cu	< 0.0001	0.00130

analysis, which include Li, Ti, Cr, Mn, Fe, Ni, Cu, Zn, Ag, Sn, Sb, Pb and Bi, are given in Appendix E.

Table 3.6 shows the main results of the composition (in weight percentage) of the Pb-Li samples analysed before and after. The concentration of lithium was found to be inhomogeneous in the analysis of the first sample. Thus, the unexpectedly low concentration of initial lithium, 0.490 wt.% (corresponding to 12.9±0.6 at.% Li), is attributed to a not fully homogeneous mixture provided. Note that, given the low atomic concentration of Li and the large difference of atomic mass with respect to Pb, obtaining a homogeneous eutectic Pb-Li mixture is challenging. The final concentration of Li, 0.592 wt.% (15.2±0.2 at.%), which is assumed to be the real concentration, from a better homogenisation after the experimental campaign, is still lower than the expected one (15.7 at.%). This deviation from the composition reported by the manufacturer can be a consequence of the inhomogeneous Li concentration, since not all the Pb-Li acquired was used (6.5 kg were not inserted in the facility). Additionally, the experimental melting point, $\approx 238-240\,^{\circ}\mathrm{C}$, is in agreement with the atomic concentration 15.2 at.% Li, from the Pb-Li phase diagram reported by Hubberstey *et al.* [64].

It is important to note that a small deviation in the atomic concentration of lithium (and inhomogeneity) seems to be a common issue in the manufacturing of eutectic Pb-Li. E.g., the lithium fraction in a batch of eutectic Pb-Li previously provided by another manufacturer was analysed to be 18.4 ± 0.6 at.%. Frequent small deviations in composition are attributed to the very small mass fraction of lithium in the eutectic mixture (≈0.62 wt.% Li), which shows the importance of analysing the composition of the Pb-Li (and its homogeneity) to be used in an experimental campaign.

The Pb-Li was in liquid state inside the setup during six months (at 360–400 °C).

The appearance of impurities in the composition is due to the dissolution of elements from the structural metals in contact with the Pb-Li caused by a difference of chemical potential between the solid and the liquid metals [13] [1]. Fe and Ni are from the chambers and pipes, made of stainless steel 316L (traces of Cr and Mn also appeared, not shown in Table 3.6), and the dissolved Cu is from the gaskets used.

3.2 Experimental procedure

A typical run consists in the following steps (summarised in Table 3.7): First, the Pb-Li is transferred to the upper chamber (UC) through the transfer line. For that, the lower chamber (LC) is pressurized with argon (up to ≈ 1 bar), which has a negligible solubility in Pb-Li [83, 84].

Once the Pb-Li is in the UC, its volume is measured (step #2) by injecting a known amount of argon in the upper chamber, estimated with the mass flow controller. This method is used to double check the simulations performed in Chapter 4, which provide a higher accuracy. Similarly, the volume of Pb-Li in UC is also measured after the extraction (step #8).

Step #3 consists in setting the operation temperature of the experiment (given in Table 3.1) very slowly (1 °C/min) to avoid fast expansions or contractions of the metals that can lead to air leaks at the connections. Once the UC is thermalised,

Table 3.7: Steps of a typical experiment (UC: upper chamber, LC: lower chamber).

Step	Duration
#1: Transfer Pb-Li to UC	20 min
#2: Measure Pb-Li volume in UC	10 min
#3: Thermalisation operation temperature	6 h
#4: Vacuum test in UC	16 h
#5: Gas analysis with QMS and evacuation UC	1 h
#6: D_2 dissolution in Pb-Li	48 h
#7: D_2 extraction in LC	30 min
#8: Measure Pb-Li volume in UC	10 min
#9: Bake-out and evacuation of the setup	4 days

[1] Electronegativity values of the elements shown in Table 3.6 are Li: 2.65 V, Pb: 3.9 V, Fe: 4.93 V, Ni: 5.35 V, Cu: 4.6 V [82]. The potential difference between the Pb-Li and the structure elements causes the electrochemical corrosion.

a vacuum test is performed (step #4), which consists in monitoring the pressure increase in the closed chamber (during 16 h) previously evacuated. This test is crucial to control the initial state of the Pb-Li and chamber before the dissolution. In addition, the small amount of gas resulting from the vacuum test is analysed with the QMS to determine if it is from a leak or outgassing of D_2 (remaining in the metals from the previous experiment). The result of this vacuum test must be similar for all the experiments (and below the uncertainty or detection limit) to ensure that they are comparable.

The dissolution phase (step #6) consists in inserting D_2 in the UC up to a given pressure and, with the chamber closed, recording the pressure decrease and temperature during 48 h. The duration of this phase has been chosen to be long enough to ensure steady state.

The extraction phase (step #7) starts by recording pressure and temperature in the closed lower chamber during at least 40 min to evaluate the background. This is performed in parallel with the end of the dissolution phase in the upper chamber, so that the droplets start falling right after 48 h dissolution. In the upper chamber, the D_2 gas left from dissolution phase remains in the chamber to maintain the concentration of D inside the Pb-Li during the extraction phase. In some experiments (runs #15, #17 and #18, see Table 3.8), the gas pressure in the upper chamber has to be increased to vary (decrease) the falling time of the droplets. This is done by adding Ar in the UC, so that the partial pressure of D_2 does not change. Then, the automatic valve is opened and the falling Pb-Li droplets are recorded with the high-speed camera. Pressure and temperature are monitored until the last droplet of Pb-Li falls and gas from the upper chamber enters the lower chamber (which is seen by a sudden increase of the pressure in the LC).

When the experiment finishes, the upper chamber is slowly set to the bake-out temperature (440 °C) and the whole setup is evacuated during 4 days in order to release the deuterium trapped in the metal walls of all structures (step #9).

3.3 Experimental matrix

Pressure and temperature are the two main parameters that can be varied in the experiments. The temperature has a major influence in the diffusion of deuterium in metals, affecting (i) the amount of deuterium permeated through the walls, (ii) the deuterium dissolved in the Pb-Li and (iii) the deuterium extracted from it. Additionally, the volume, the viscosity, and the surface tension of the liquid Pb-Li have a dependency on temperature (see Table 2.3), which affects its fluid dynamics. There-

fore, in order to limit the degrees of freedom of the research in the first campaign, the temperature of the liquid metal, T_{PbLi}, is kept constant for all the experiments.

The partial pressure of D_2 during the dissolution phase, $p_{\mathrm{uc,\,diss}}$, influences directly the amount of deuterium dissolved into the Pb-Li (described by Sieverts' law in equation (2.9)). However, during the extraction phase, the total pressure of the gas in the upper chamber, $p_{\mathrm{uc,\,ext}}$, affects the speed of the falling liquid metal and, thus, the falling time of the droplets. As stated above, this pressure is adjusted by adding argon in the UC (before the extraction) in runs #15, #17 and #18.

Table 3.8 shows the matrix of experiments performed during the experimental campaign. $p_{\mathrm{uc,\,diss}}$ and $p_{\mathrm{uc,\,ext}}$ are varied to separate the two effects: (i) the amount of deuterium dissolved and (ii) the droplets falling time, respectively.

The optimization of the experimental matrix was crucial because of two main reasons: firstly, the Pb-Li was slowly condensing at the windows, which results in the loss of visibility over time that impedes the recording of the droplets with the high-speed camera. Secondly, the high temperatures in addition to the presence of Pb-Li can worsen the conditions of the setup over time. This was learned from a previous campaign, in which increasing leakages were found after several switches of temperature (between operation temperature and bake-out). In addition, some valves were damaged after a prompt solidification of the Pb-Li due to a safety shutdown of the heaters. The setup had to be rebuilt after an eruption due to the reaction of Pb-Li to an air-leak through the damaged valve. This experience

Table 3.8: Experimental matrix. $p_{\mathrm{uc,\,diss}}$: gas pressure during dissolution phase (D_2), $p_{\mathrm{uc,\,ext}}$: gas pressure in the upper chamber during extraction (D_2+Ar), $p_{\mathrm{lc,\,ext}}$: initial gas pressure in the lower chamber during extraction, T_{PbLi}: temperature of the Pb-Li.
In grey: experiments without D_2.

Run	$p_{\mathrm{uc,\,diss}}$ (mbar)	$p_{\mathrm{uc,\,ext}}$ (mbar)	$p_{\mathrm{lc,\,ext}}$ (mbar)	T_{PbLi} (°C)
Run#12	-	(He) 500	10^{-3}	400
Run#13	1000	1000	10^{-3}	400
Run#14	1000	1000	0.15	400
Run#15	1000	1500	0.15	400
Run#16	-	(Ar) 1000	10^{-3}	400
Run#17	500	1000	0.15	400
Run#18	500	1500	0.15	400
Run#19	1000	1000	0.15	400
Run#20	-	(He) 1000	(He) 0.15	400

shows how sensitive the handling of the liquid metal is and the need to optimise the campaign to obtain the most valuable results in the least time possible.

The experimental matrix was optimized to vary $p_{\mathrm{uc,\,diss}}$ and $p_{\mathrm{uc,\,ext}}$ between two values: 500 vs 1000 mbar and 1000 vs 1500 mbar, respectively. These values have been chosen to be as high as possible in order to minimize the uncertainty of the results. Since the falling time also varies during one run, the relation between the falling time and the extraction efficiency is also investigated throughout each run.

The extraction phase of run#13 was performed with the lower chamber initially evacuated. Due to the unexpected small amount of deuterium extracted, for the next runs it was decided to strategically record the background with a given initial amount of D_2 (see Chapter 6). Therefore, run#14 was performed under the same conditions of run#13 (deuterium dissolved and falling time), for their results to be comparable.

The last experiment, run#19, is a repetition of run#14 to prove the repeatability of the experiments, and to check that there is no variation in the results over time (after several weeks of operation of the facility).

Table 3.8 also shows three experiments marked in grey (runs #12,#16 and #20), which were carried out without D_2, using either Ar or He, which have negligible solubility in Pb-Li [83, 84]. Run#12 was performed to test the fluid dynamics of the Pb-Li and to prove that the configuration of the high-speed camera and the extra light used to record the droplets were adequate to obtain analysable frames (e.g. without blurry effect due to the falling speed). Run#16 and run#20 were necessary to check the evolution of pressure and temperature in the lower chamber only due to the falling Pb-Li (with no extraction).

In order to evaluate the amount of deuterium dissolved in the Pb-Li, the amount that is lost through the walls of the upper chamber has to be considered. For that, several experiments were done in the upper chamber without Pb-Li, summarized in Table 3.9. They are referred to as *permeation experiments*, whereby the gas lost into the walls is measured (no Pb-Li). This is to differentiate them from the *dissolution phase* of the runs shown in Table 3.8, which are performed under similar conditions, but with Pb-Li (they are later also called *dissolution experiments*).

Previous tests were performed with helium, to achieve the closest temperature profile of the gas and chamber with and without Pb-Li. Helium was used due to its similar heat conductivity to the one of D_2 and to maintain the metals free from the hydrogen isotope. From these tests, it was found that the temperature of the heater needs to be set at $411 - 411.5\,^{\circ}\mathrm{C}$, depending on the gas pressure, when there is no Pb-Li (see Table 3.9).

Table 3.9: Permeation experiments in upper chamber. $p_{\mathrm{uc,\,diss}}$: pressure of D_2 (similar to dissolution phase), T_{heater}: temperature of the heater EH#01

Experiment	$p_{\mathrm{uc,\,diss}}$ (mbar)	T_{heater} (°C)
Perm#24	1000	411.5
Perm#25	1000	411.5
Perm#26	500	411

The permeation experiments not only had to be performed under the same conditions of pressure and temperature as the dissolution phase, but also complying with similar evacuation and bake-out times. Therefore, the steps shown in Table 3.7 were mimicked, i.e. each experiment took, as a whole, one week. This procedure was used to prove that the defined bake-out time is enough to remove the D_2 from the walls to obtain repeatable measurements. For this reason, the permeation experiments were performed previous to the main experiments, and the first one was at the highest pressure and repeated (perm#24 = perm#25).

3.4 Experimental requirements and technical limitations

The main experimental requirements and technical limitations of the facility are summarised into the following points:

- Since hydrogen is a combustible gas (it reacts exothermically with oxygen under certain conditions of relative concentration), the facility must be leak-tight. Following regulations of the laboratory, the leak rate at each connection has been checked to be $\leqslant 10^{-9}\,\mathrm{mbar\,l\,s^{-1}}$.

- Every section of the Pb-Li loop must be above the melting temperature (235 °C) in order to prevent its solidification. However, the heaters cannot exceed the maximum allowed temperature of the loop components (450 and 500 °C).

- The upper chamber is designed to maximise the contact surface of the liquid metal with the D_2 gas to favour dissolution.

- In the lower chamber, the extraction efficiency increases with the droplet falling height (see equations (2.3) and (2.4)). However, the height of the chamber is limited by the Pb-Li transfer between experiments. In order to avoid using a

liquid metal pump, the Pb-Li is lifted to the upper chamber by gas pressurization of the lower chamber. The limit is set by the maximum pressure allowed in a *non-pressurized* facility: 1.5 bar. From Bernoulli equation (shown in next chapter, equation (4.1)), the maximum Pb-Li elevation height is $\approx 1.57\,\mathrm{m}$. Considering the geometry of the facility and a margin of safety (to allow for flexibility in case of experiments with a larger Pb-Li volume), the effective maximum droplet falling height in the lower chamber is $\approx 0.53\,\mathrm{m}$.

– In both dissolution and extraction phases, the pressure must be monitored. However, since the pressure and vacuum sensors do not withstand the high temperatures required for the Pb-Li, they had to be placed in a distant, cooler, position.

– Additionally, the pressure sensor in the dissolution chamber must be able to measure small variations of pressure ($\sim 1\,\mathrm{mbar}$) at high absolute values ($\sim 1\,\mathrm{bar}$). This has been achieved by means of a calibration of the sensor.

– The use of a high-speed camera to record the falling droplets is necessary to analyse their size, shape and dynamic evolution. A minimum of 50 000 fps (frames per second) is required to provide acceptable uncertainty of the size of the droplets, due to blurring effect (later discussed in Section 4.4). For the camera and the needed extra light (required to compensate for the short opening time of the shutter), the extraction chamber is designed to have two windows.

– Lastly, the evaporation of Pb-Li (which is a function of pressure and temperature) in the lower chamber must be minimized to avoid damaging the turbo-molecular pump with Pb-Li vapours and their condensation on the windows that impedes visibility into the chamber. The former has been prevented by installing a cold trap and the latter has been controlled by maintaining the Pb-Li in the lower chamber at a maximum temperature of 360 °C.

Chapter 4

Pb-Li fluid dynamics: simulation and experimental results

4.1 Strategy to evaluate the fluid dynamics

4.1.1 Influence of the fluid dynamics on the extraction efficiency and its evaluation strategy

The fluid dynamics of the falling Pb-Li droplets have a great impact on the extraction efficiency. The model of a stagnant droplet, shown in equation (2.3), is regarded as a first approach due to its simplicity.

$$\eta_{\mathrm{theo}} = 1 - \frac{6}{\pi^2} \sum_{\mathrm{n}=1}^{\infty} \frac{1}{\mathrm{n}^2} \exp\left(\frac{-4\mathcal{D}\,\mathrm{n}^2\,\pi^2\,t_{\mathrm{fall}}}{d_{\mathrm{d}}^2}\right) \tag{2.3*}$$

In addition, an enhancement of the efficiency due to mass movement of the Pb-Li in the droplets can be evaluated. The extraction efficiency should be influenced by:

(i) the *droplet falling time*, t_{fall}, which is the finite time that the deuterium atoms have to leave the droplet;

(ii) the *droplet diameter*, d_{d}, which establishes the volume-to-surface ratio of the liquid metal medium and the maximum distance that each D atom needs to navigate to exit the droplet;

(iii) *mass movement of the Pb-Li*, such as oscillations of the droplet shape or internal circulation of the fluid within the droplet, which can enhance the migration of the deuterium atoms towards the droplet surface.

The *falling time* depends on the falling height, h_{fall}, and the speed of the Pb-Li at the exit of the nozzle, v_{n}, as shown in equation (2.4), $t_{\mathrm{fall}} = (-v_{\mathrm{n}} + \sqrt{v_{\mathrm{n}}^2 + 2\,g\,h_{\mathrm{fall}}})/g$. The falling height, h_{fall}, decreases during the experiment, since the height of Pb-Li

in the lower chamber, $h_{\mathrm{PbLi(lc)}}$, increases with the falling liquid metal. The speed of the Pb-Li at the exit of the nozzle (see Figure 4.1) is obtained by the *Bernoulli equation*, which describes the conservation of energy between two points in a flowing liquid, as follows:

$$\rho g h_1 + p_1 + \frac{1}{2}\rho v_1^2 \;=\; \rho g h_2 + p_2 + \frac{1}{2}\rho v_2^2 + \delta p, \tag{4.1}$$

where h_1 and h_2 are the heights of the fluid at the points 1 and 2, respectively; v_1 and v_2 are the speeds of the fluid at the given points; ρ is the density of the fluid; g the gravitational acceleration; p_1 and p_2 are the pressures at the given points, and the term δp includes all the pressure losses between 1 and 2.

The continuity equation of the incompressible flow in the upper chamber leads to:

$$Q = A_1 v_1 = A_2 v_2, \tag{4.2}$$

where Q is the Pb-Li flow rate, and A_1 and A_2 are the cross-sectional areas at the points 1 and 2. As shown in Figure 4.1, in the present case, 1 is at the surface of Pb-Li in the UC and 2 is at the exit of the nozzle in the LC. Since $A_1/A_2 \sim 10^5$, the speed of Pb-Li at the top surface, v_1, can be neglected in equation (4.1). Likewise, during the experiments, the ratio of gas pressure is $p_1/p_2 \geq 10^3$, thus p_2 can also be neglected. Therefore, equation (4.1) can be simplified to:

$$\rho g h_{\mathrm{PbLi(uc)}} + p_{\mathrm{uc}} - \frac{1}{2}\rho v_{\mathrm{n}}^2 - \delta p = 0. \tag{4.3}$$

The first term of equation (4.3) corresponds to the hydrostatic pressure, the second to the gas (*static*) pressure, the third to the dynamic pressure and the fourth corresponds to the pressure losses. The pressure losses, δp, include friction losses at the walls of the pipe (δp_{p}), losses due to change in section (chamber to pipe, $\delta p_{\mathrm{c\text{-}p}}$, and pipe to nozzle, $\delta p_{\mathrm{p\text{-}n}}$), and losses inside the valve (δp_{v}):

$$\delta p = \delta p_{\mathrm{c\text{-}p}} + \delta p_{\mathrm{p}} + \delta p_{\mathrm{v}} + \delta p_{\mathrm{p\text{-}n}}. \tag{4.4}$$

The calculation of the various pressure losses is shown in Appendix F.

v_{n}, h_{fall} and, thus, t_{fall} vary throughout one experiment, and are simulated with the code described in Section 4.2. v_{n} is also experimentally determined from the frames recorded with the high-speed camera (see Section 4.4).

The expected *droplet diameter*, d_{d}, as a function of the nozzle diameter is given by equation (2.1), $d_{\mathrm{d}} \simeq 1.89\, d_{\mathrm{n}}$. In the typical case of a non-perfectly-spherical droplet, d_{d} is the equivalent diameter of a sphere of the same volume. The size of the droplets is experimentally determined from the frames recorded with the high-speed camera. Additionally, the evolution of the droplet shape due to oscillations can be inferred from the frames. The results are described in Section 4.4.

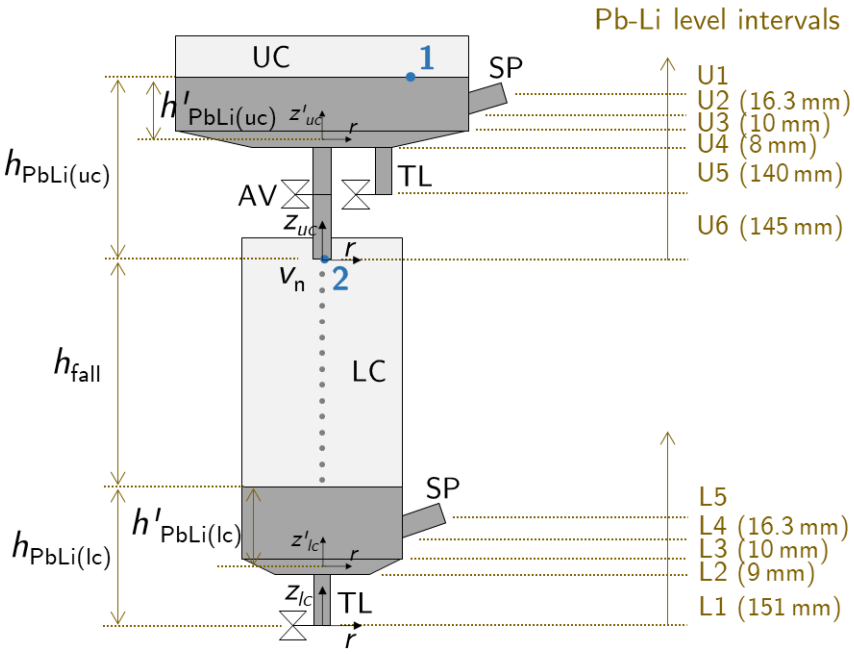

Figure 4.1: Scheme of the geometry and fluid-dynamics variables used in the simulation (geometrical parameters are not scaled). UC: upper chamber, LC: lower chamber, AV: automatic valve, TL: transfer line, SP: sampling port. $h'_{\mathrm{PbLi(uc)}}$ and $h'_{\mathrm{PbLi(lc)}}$ show the heights of Pb-Li in the same coordinate system as the experimental results (same as Figures 3.3, 3.5). On the right, the Pb-Li level intervals U_i and L_i (with their absolute magnitudes) are used in the code to determine the Pb-Li level in each chamber (step (iv) in Figure 4.2).

4.1.2 Determination of the Pb-Li volume for analysis of the experimental data

The amounts of gas both dissolved and extracted (into and from the Pb-Li) are determined with the volume of the gas in the respective chamber. Therefore, as explained in Section 3.1.3, an accurate determination of the volume of the Pb-Li in both chambers during the experiments is necessary. This is done by fitting the experimental results (i.e. data from Pb-Li level thermocouples and duration of the run) with simulations. The description of the method and the results are given in Section 4.3.

4.2 Code *VST-experiment*: simulation of fluid dynamics

A code to simulate the fluid dynamics of the Pb-Li during one experiment has been developed in Matlab. It is based on the principles of a previous simulation

Table 4.1: Inputs and outputs of the code VST-experiment. $f(t)$ specifies that the variable f evolves with time.

Inputs	Outputs
Nozzle diameter, d_{n}	Pb-Li volumetric flow, $Q(t)$
Initial gas pressure in UC, p_{uc_0}	Pb-Li pressure losses, $\delta p(t)$
Pb-Li temperature, T_{PbLi}	Gas pressure in UC, $p_{\mathrm{uc}}(t)$
Initial volume in UC, $V_{\mathrm{PbLi(uc)}_0}$	Pb-Li height in UC, $h_{\mathrm{PbLi(uc)}}(t)$
Final volume in UC, $V_{\mathrm{PbLi(uc)}_f}$	Pb-Li height in LC, $h_{\mathrm{PbLi(lc)}}(t)$
Standard height step (similar to *time step*), Δh_{st}	Pb-Li speed at exit of the nozzle, $v_{\mathrm{n}}(t)$
	Extraction efficiency, $\eta(t)$
	Duration of the experiment, τ

tool [39], which was developed with a different geometry and objectives.

The present code, adapted to the experimental setup used in this work, is used to simulate the height of the Pb-Li in both chambers, the speed at the exit of the nozzle and, with these, to compute the theoretical extraction efficiency. It includes the geometrical parameters of the facility: heights/lengths, diameters and surface roughness of chambers, pipes and nozzle; as well as the conic bottom of both chambers (designed to prevent Pb-Li adherences) and the position and dimensions of the sampling ports. Figure 4.1 shows, schematically, the geometry of the chambers. On the right, different intervals are depicted, attending to the changes in geometry. They are used by specific functions to determine the height of Pb-Li in each chamber (with the Pb-Li volume inside the chamber as input).

Table 4.1 summarizes the inputs and outputs of the code. The main inputs are the initial gas pressure in the upper chamber, p_{uc_0}, the temperature of the Pb-Li, T_{PbLi}, and the initial volume of the liquid metal in the upper chamber, $V_{\mathrm{PbLi(uc)}_0}$. With these inputs and the geometry of the setup, the code computes the height of Pb-Li in both chambers and all fluid-dynamics parameters necessary to determine the falling time at one time step (i.e. one iteration). Then, the time step is recalculated and the next iteration is computed. One iteration of calculations (at time $t = t_i$) consists in the following steps (see scheme in Figure 4.2):

(i) Equation (4.3) is solved by an iterative method in order to obtain the Pb-Li flow that exits the nozzle, $Q_i = v_{\mathrm{n}_i} A_{\mathrm{n}}$, and its speed v_{n_i}.

(ii) With v_{n_i} and the falling height computed in the previous iteration, $h_{\mathrm{fall}_{i-1}}$, the falling time, t_{fall_i}, is calculated with equation (2.4).

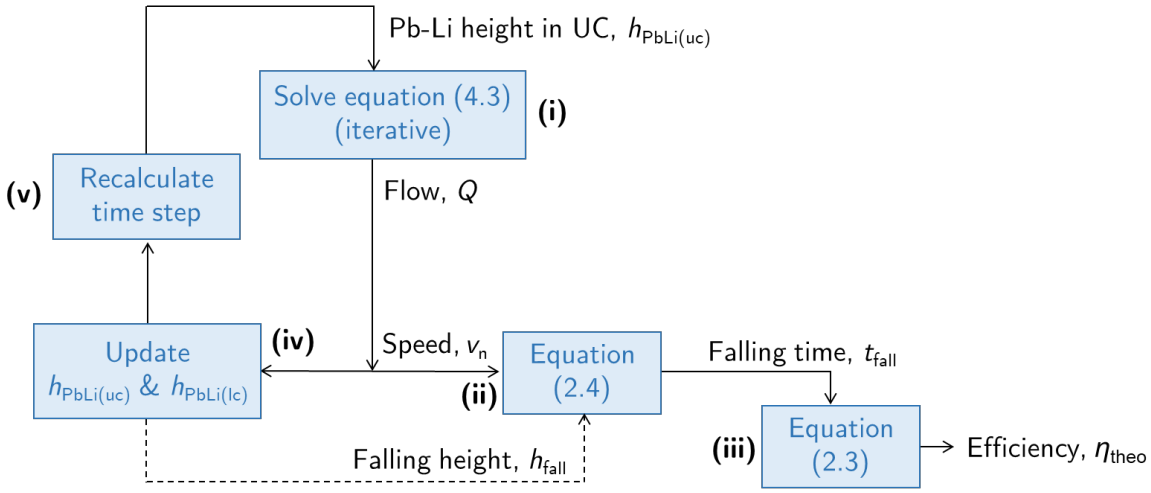

Figure 4.2: Calculations during one iteration of the code. Dashed line means it updates in the next iteration.

(iii) The extraction efficiency, η_{theo_i}, is computed with equation (2.3), with the calculated t_{fall_i}, the droplet diameter, d_{d}, obtained with equation (2.1) and the diffusion coefficient reported by [37] ($\mathcal{D} = 3.4 \times 10^{-7}\,\mathrm{m^2\,s^{-1}}$).

(iv) The volume of Pb-Li that is transferred from the upper chamber to the lower chamber, ΔV_i, is calculated with the current time step, Δt_i, as follows:

$$\Delta V_i = Q_i \Delta t_i. \tag{4.5}$$

Then, the Pb-Li volumes in both chambers are updated and the heights $h_{\mathrm{PbLi(uc)}_i}$ and $h_{\mathrm{PbLi(lc)}_i}$ are recalculated with two specific functions, attending to the different geometry sections (intervals) in Figure 4.1.

(v) The effect of ΔV_i in the accuracy of the simulation depends on the interval in which the Pb-Li surface lies. For example, a better accuracy (smaller ΔV_i) is needed when $h_{\mathrm{PbLi(uc)}_i}$ is in the tube than when it is inside the chamber (see intervals U5 and U3 in Figure 4.1). Therefore, the time step is recalculated at the end of every iteration in order to optimize accuracy vs computing time. The new time step is determined with:

$$\Delta t_{i+1} = \min \left(\frac{\Delta h_{\mathrm{st}}\, A_{\mathrm{PbLi}_j}}{Q_i} \right)_{j=\mathrm{uc,\,lc}}, \tag{4.6}$$

where A_{PbLi_j} is the area of the Pb-Li surface in each of the chambers ($j = \mathrm{uc}, \mathrm{lc}$) and Δh_{st} is the so-called *standard height step*, which is given as input when running the simulation. Similar to the concept of *time step* in a simulation tool, Δh_{st} corresponds to the desired (maximum) change in Pb-Li height for each iteration. A typical value used for Δh_{st} is 0.2 mm.

The program ends when the Pb-Li volume in the upper chamber reaches the given input value: *final volume in upper chamber*, $V_{\mathrm{PbLi(uc)}_f}$. If this value is zero, the program ends when all the Pb-Li has fallen into the lower chamber.

Figure 4.3 shows the terms of the Bernoulli equation (4.3) for a typical example case in which the initial pressure in the upper chamber is 1000 mbar. The figure shows the magnitude of the different terms acting in the resulting speed of the Pb-Li. First, it is worth to note the proportion of the pressure losses due to change of section at the nozzle ($\delta p_{\mathrm{p\text{-}n}}$). This is relevant for the dimensioning of a scaled-up VST extraction system: the larger the pressure drop (slower falling droplets), the higher the efficiency.

In the simulated case, the Pb-Li level in the upper chamber decreases down to the tube of the nozzle (interval U5 in Figure 4.1) after 16 min. Hence the hydrostatic pressure and, consequently, the speed at the exit of the nozzle (and dynamic pressure term) decrease much faster in the last 40 s.

The two terms favouring the Pb-Li falling (positive terms in equation (4.3)) are the gas pressure (p_{uc}) and the hydrostatic pressure ($\rho g h_{\mathrm{PbLi(uc)}}$). The hydrostatic pressure (given by the Pb-Li height) is similar for all the experiments. Therefore, the gas pressure in the UC is the experimental variable that is used in the experimental

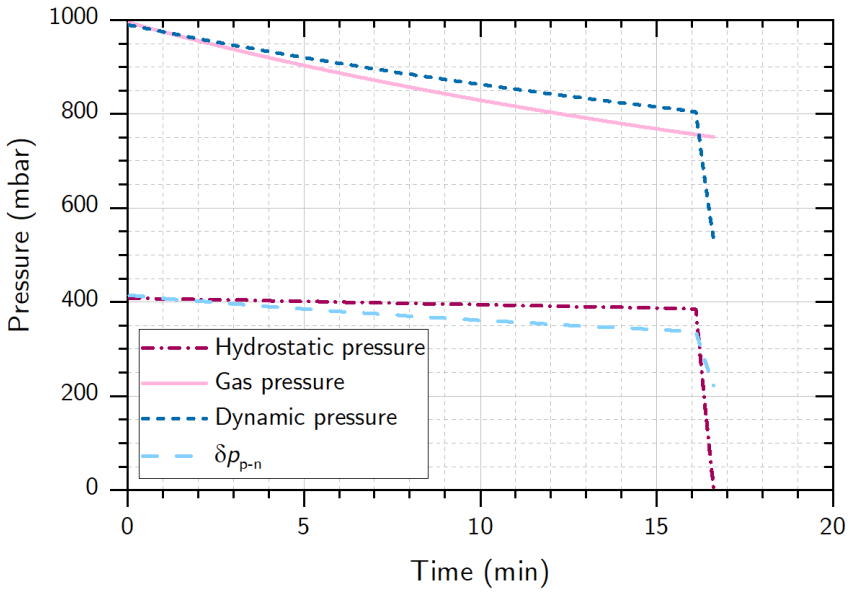

Figure 4.3: Terms of Bernoulli equation (4.3) simulated with $d_{\mathrm{d}} = 0.6\,\mathrm{mm}$, $p_{\mathrm{uc}_0} = 1000\,\mathrm{mbar}$, $T_{\mathrm{PbLi}} = 400\,^{\circ}\mathrm{C}$, $V_{\mathrm{PbLi(uc)}_0} = 1.2\,\mathrm{l}$, $V_{\mathrm{PbLi(uc)}_f} = 0\,\mathrm{l}$, $\Delta h_{\mathrm{st}} = 0.2\,\mathrm{mm}$. The terms corresponding to hydrostatic pressure ($\rho g h_{\mathrm{PbLi(uc)}}$) and gas pressure ($p_{\mathrm{uc}}$) favour the Pb-Li fall, while the dynamic pressure ($\frac{1}{2}\rho v_{\mathrm{n}}^2$) and pressure loss due to cross-sectional area change at the nozzle ($\delta p_{\mathrm{p\text{-}n}}$) oppose it. The rest of the pressure losses (in equation (4.4)) are $< 10^{-1}$ mbar.

campaign to vary the speed of the Pb-Li at the exit of the nozzle, v_n.

Table 4.2 shows simulated results for the two values of initial gas pressure (p_{uc_0}) defined in the experimental matrix (Table 3.8), 1500 and 1000 mbar. Since 1500 mbar is the maximum pressure allowed in the facility, the first row also corresponds to the experimental limit of the setup. The last row shows the percentage variation expected between the two sets of experiments: the falling time of the droplets is expected to increase by 13 % and the extraction efficiency should increase by 4 %, when decreasing p_{uc_0} from 1500 to 1000 mbar.

Figure 4.4 shows the evolution of v_n and h_{fall} during the simulated example case ($p_{uc_0} = 1000$ mbar). Since both parameters decrease over time, the falling time remains almost constant during the experiment (until $t = 16$ min), as shown in Fig-

Table 4.2: Simulated results for the two experimental values of gas pressure in UC (with $d_d = 0.6$ mm, $T_{PbLi} = 400\,°C$, $V_{PbLi(uc)_0} = 1.2$ l, $V_{PbLi(uc)_f} = 0$ l, $\Delta h_{st} = 0.2$ mm, and $\mathcal{D}$ from [37]). $\overline{v}_n$, $\overline{t}_{fall}$ and $\overline{\eta}_{theo}$ are the average speed at the exit of the nozzle, falling time and extraction efficiency, respectively, along the experiment and τ its duration.

p_{uc_0} (mbar)	$\overline{v}_n$ (m s^{-1})	$\overline{t}_{fall}$ (s)	$\overline{\eta}_{theo}$ (%)	τ (min)
1500	4.92	0.091	76 %	14.3
1000	4.24	0.103	79 %	16.6
difference:	-14%	13%	4%	16%

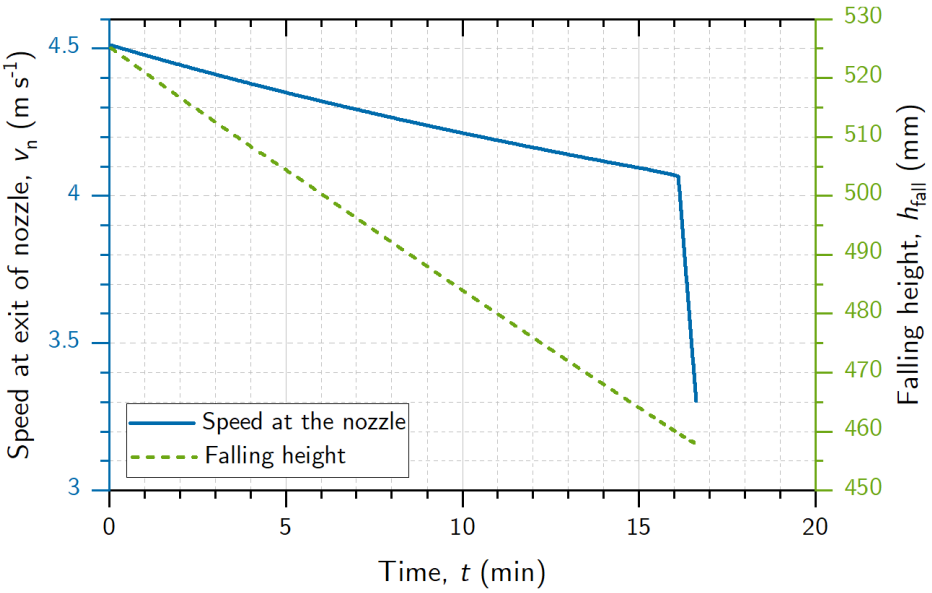

Figure 4.4: Speed at the exit of the nozzle and falling height simulated for the example case of $p_{uc_0} = 1000$ mbar, $T_{PbLi} = 400\,°C$, $V_{PbLi(uc)_0} = 1.2$ l and $V_{PbLi(uc)_f} = 0$ l.

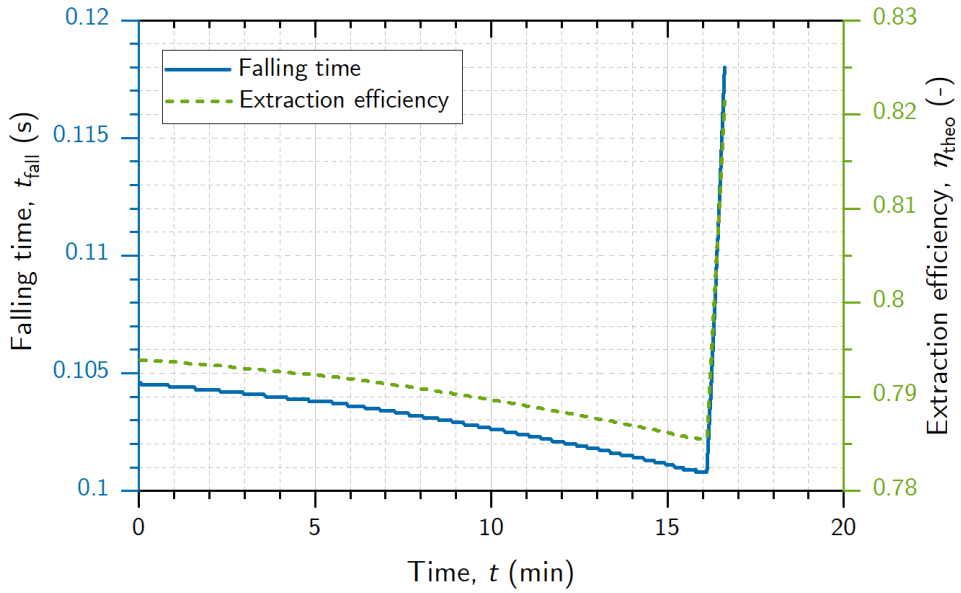

Figure 4.5: Falling time and extraction efficiency simulated for the example case of $p_{uc_0} = 1000\,\text{mbar}$, $T_{PbLi} = 400\,°C$, $V_{PbLi(uc)_0} = 1.2\,l$ and $V_{PbLi(uc)_f} = 0\,l$.

ure 4.5. Only at the end of the experiment t_{fall} increases, because the droplets are substantially slower (Pb-Li level in UC is within the pipe: intervals U5–U6 in Figure 4.1).

Figure 4.5 also shows the theoretical extraction efficiency. As expected from equation (2.3), it follows a similar tendency to the falling time. It is important to note that, even if at the end of the experiment the extraction efficiency increases drastically (due to the slower droplets), this does not influence much the average (integrated) efficiency during the whole experiment: $\overline{\eta}_{theo} = 79\,\%$, from Table 4.2. This is due to that the last portion of Pb-Li falling (after $t = 16\,\text{min}$) corresponds to a very small volume ($\approx 2.5\,\%$ of the total volume).

4.3 Fitting experimental results with simulation

4.3.1 Method

As previously shown in Table 4.1, the initial and final volumes of Pb-Li in the upper chamber are inputs of the *VST-experiment* code, used to simulate the fluid dynamics. However, in practice, the initial volume is not accurately known. In addition, occasionally, some Pb-Li was observed to remain in the upper chamber at the end of the experiment (e.g. run#14).

Therefore, the method used to obtain accurate simulations (that describe the actual experimental results) and to determine accurately the Pb-Li volumes is to fit

the experimental data with the *VST-experiment* code.

The experimental data from the extraction runs used to fit the experiments with the simulation are:

- The time at which the Pb-Li reaches each *level thermocouple* in the upper and lower chambers: $t(h'_{\mathrm{PbLi(uc)}} = h'_i)$ and $t(h'_{\mathrm{PbLi(lc)}} = h'_j)$, with i, j being the level thermocouples in the respective chamber (shown in Figures 3.3 and 3.5) [1].

- The total duration of the experiment, τ. It starts when the first Pb-Li droplets fall and it ends when the gas from the upper chamber enters the lower chamber (right after the last droplet falls).

The variables to be optimized with the fitting procedure are:

- The equivalent nozzle diameter, $d_{\mathrm{n}}^{\mathrm{eq}}$. This variable is restricted to $\leq 0.6\,\mathrm{mm}$. It allows the possibility of a partial decrease of the nozzle cross-section due to some solidification.

- The initial volume of Pb-Li in the upper chamber, $V_{\mathrm{PbLi(uc)}_0}$. From the experiments, this is only known with a large uncertainty (given by the distance between the level thermocouples). $V_{\mathrm{PbLi(uc)}_0}$ is necessary for the analysis of the dissolution phase.

- The final volume of Pb-Li in the upper chamber, $V_{\mathrm{PbLi(uc)}_f}$. This variable is normally zero (since all the Pb-Li should fall to the lower chamber). It is specifically added to the fitting procedure of run#14, in which some Pb-Li remained in the upper chamber.

A scheme of the functions involved in the fitting procedure is shown in Figure 4.6. It works as follows:

(i) An initial guess of the variables d_{n}, $V_{\mathrm{PbLi(uc)}_0}$ and $V_{\mathrm{PbLi(uc)}_f}$ is given to the *optimize* function. This is a minimization function, which iteratively runs the function *deviations* until the difference between the output value, Ψ^2, from two iterations is below the convergence criterion of 10^{-4}.

(ii) The function *deviations* contains the experimental values to fit: the time at which the Pb-Li has reached each thermocouple and the duration of the experiment, as mentioned above. It also contains the initial gas pressure, p_{uc_0}, and

[1] Note that the prime in h' and h'_{PbLi} denotes the coordinate system starting at the base of the chambers (see Figure 4.1).

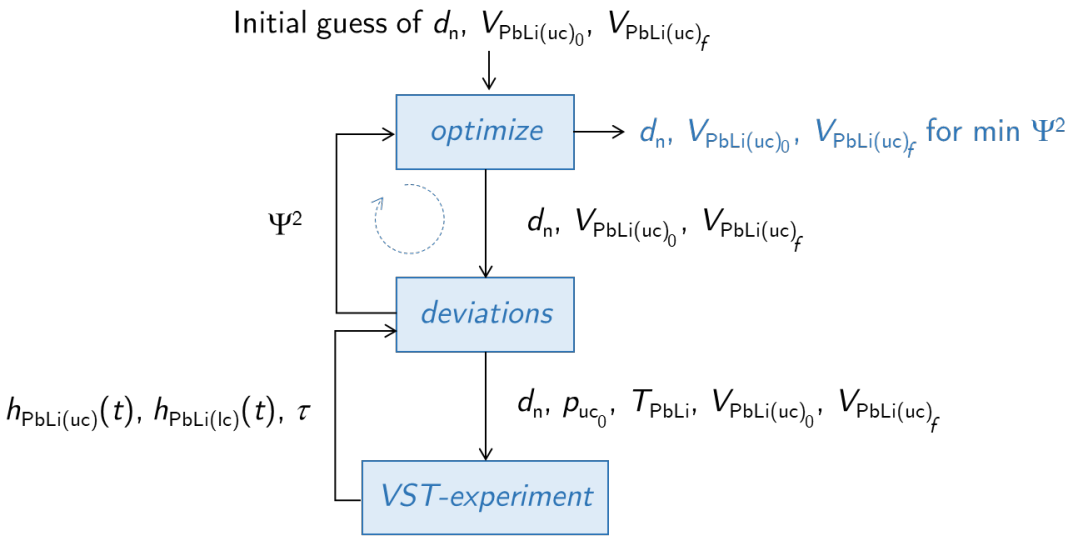

Figure 4.6: Scheme of the functions used to fit the experimental data with the simulation.

Pb-Li temperature, T_{PbLi}. The output of the function *deviations* is the value of Ψ^2 given by equation (4.7), which is a dimensionless measurement of the deviations between the experimental and simulated parameters to be fitted:

$$\Psi^2 = f_1 \sum_{i=1}^{N} \left(h'^{\mathrm{exp}}_{\mathrm{PbLi(uc)}_i} - h'^{\mathrm{sim}}_{\mathrm{PbLi(uc)}_i} \right)^2 + f_2 \sum_{j=1}^{M} \left(h'^{\mathrm{exp}}_{\mathrm{PbLi(lc)}_j} - h'^{\mathrm{sim}}_{\mathrm{PbLi(lc)}_j} \right)^2 + \\ + f_3 \left(\tau^{\mathrm{exp}} - \tau^{\mathrm{sim}} \right)^2 .. \tag{4.7}$$

The superscripts 'exp' and 'sim' refer to the experimental and simulated values, respectively, the counters i and j correspond to the level thermocouples in the upper and lower chambers, respectively, (depicted in Figures 3.3 and 3.5) and the weighting factors are functions of the experimental error of the parameters, as follows:

$$f_1 = \left(\frac{1}{\delta h'^{\mathrm{exp}}_{\mathrm{PbLi(uc)}}} \right)^2, \qquad f_2 = \left(\frac{1}{\delta h'^{\mathrm{exp}}_{\mathrm{PbLi(lc)}}} \right)^2, \qquad f_3 = \left(\frac{1}{\delta \tau^{\mathrm{exp}}} \right)^2, \tag{4.8}$$

where the symbol δ denotes the uncertainty of the variable.

(iii) The function *deviations* obtains the simulated values by calling the code *VST-experiment* (explained in Section 4.2) with the corresponding inputs.

The output values of the function *optimize* (shown in blue, in Figure 4.6): d_n, $V_{\mathrm{PbLi(uc)}_0}$ and $V_{\mathrm{PbLi(uc)}_f}$ correspond to the scenario in which the simulation matches best the experimental results (minimum deviations). Therefore, they are later used as inputs of *VST-experiment* to simulate the corresponding run.

4.3.2 Results from simulation: Pb-Li volume and falling time

Figure 4.7 shows the resulting fitting curve for run#13 of the Pb-Li level in both chambers. The experimental data, depicted with dark-blue symbols, correspond to the experimental results (at which time the Pb-Li reached each thermocouple). The error bars are given by the uncertainty of the position of the thermocouples. The light-blue curves show the evolution of the Pb-Li height simulated with *VST-experiment* with the values obtained from the fitting procedure.

After all the Pb-Li falls into the LC, gas from the UC passes through the nozzle and enters the LC. Thus, the rapid pressure increase in the LC is an indication that all the Pb-Li has fallen. This was the case for all the runs, except for run#14, in which some Pb-Li remained in the UC. Therefore, the fitting procedure for run#14 includes the variable $V_{\mathrm{PbLi(uc)}_f}$. For the rest of the runs, $V_{\mathrm{PbLi(uc)}_f}$ is set to zero and only d_n, $V_{\mathrm{PbLi(uc)}_0}$ is included in the fitting.

Table 4.3 shows the experimental parameters (initial pressure in the upper chamber, p_{uc_0}, and duration of the run, τ) and the results of the fitting procedure for all runs. Unexpectedly, the duration of run#14 is 30 % longer than the one of run#13, while they are performed under the same conditions: similar initial gas pressure and volume of Pb-Li in the upper chamber. This is likely originated by a partial obstruction of the nozzle due to some solidification at the nozzle during run#14, which is supported by the observations with the high-speed camera: while the droplets in run#13 follow a well defined vertical line, the droplets of run#14 tend to deviate

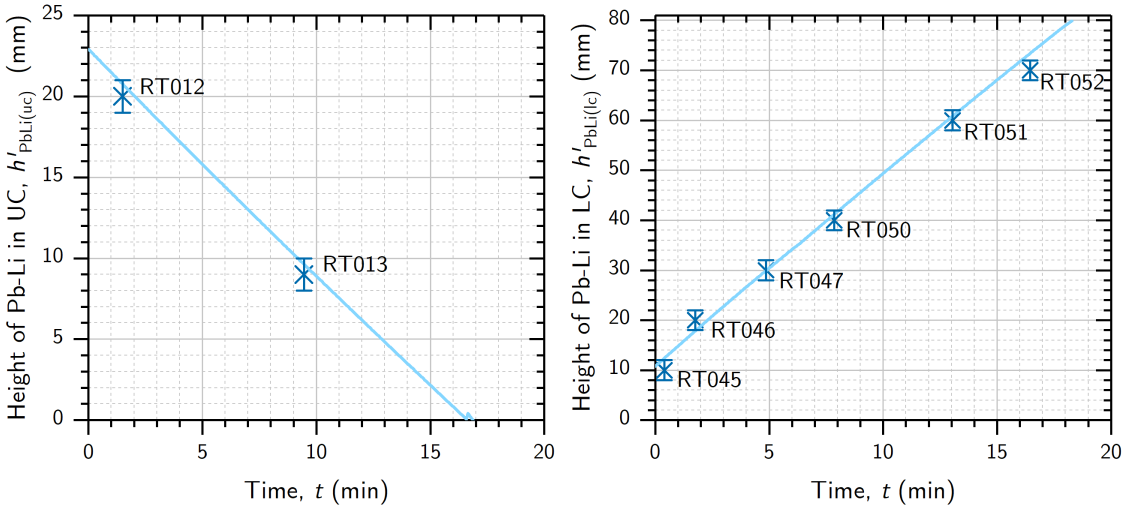

Figure 4.7: Evolution of Pb-Li height in the upper chamber (left) and the lower chamber (right) during run#13. Experimental data (data points) and simulation (solid line) with input values from fitting: $d_\mathrm{n} = 0.59\,\mathrm{mm}$, $V_{\mathrm{PbLi(uc)}_0} = 1.23\,\mathrm{l}$ ($p_{\mathrm{uc}_0} = 939.7\,\mathrm{mbar}$, $T_{\mathrm{PbLi}} = 400\,^\circ\mathrm{C}$, $V_{\mathrm{PbLi(uc)}_f} = 0\,\mathrm{l}$).

Table 4.3: Experimental parameters: initial pressure in UC, p_{uc_0}, and duration of the experiment, τ; and results from fitting procedure: equivalent nozzle diameter, $d_{\mathrm{n}}^{\mathrm{eq}}$, initial and final volume of Pb-Li in UC, $V_{\mathrm{PbLi(uc)}_0}$ and $V_{\mathrm{PbLi(uc)}_f}$. Runs with no dissolution, extraction of deuterium marked in grey.

Run	p_{uc_0} (mbar)	τ (min)	$d_{\mathrm{n}}^{\mathrm{eq}}$ (mm)	$V_{\mathrm{PbLi(uc)}_0}$ (l)	$V_{\mathrm{PbLi(uc)}_f}$ (l)
Run#12	491.6	34.0	0.50	1.37	-
Run#13	939.7	18.2	0.59	1.23	-
Run#14	933.4	26.0	0.46	1.18	0.09
Run#15	1454.0	15.6	0.57	1.20	-
Run#16	940.0	17.7	0.59	1.20	-
Run#17	939.8	17.3	0.59	1.19	-
Run#18	1452.5	19.7	0.52	1.24	-
Run#19	937.0	19.1	0.58	1.25	-
Run#20	1022.0	18.6	0.57	1.20	-

and no straight (vertical) line is observed (see Figure 4.9). This effect is also observed to a small extent in runs #12 and #18. For this reason, the diameter of the nozzle has been included as a variable in the fitting procedure (instead of constant $d_{\mathrm{n}} = 0.6\,\mathrm{mm}$). Therefore, the column $d_{\mathrm{n}}^{\mathrm{eq}}$ in Table 4.3 shows the equivalent diameter of a (non-circular) nozzle cross-section A_{n}, defined as follows:

$$A_{\mathrm{n}} = \frac{\pi}{4}(d_{\mathrm{n}}^{\mathrm{eq}})^2. \tag{4.9}$$

Note that the initial volume of Pb-Li in the UC, $V_{\mathrm{PbLi(uc)}_0}$, corresponds to the Pb-Li in the UC during the dissolution phase. Thus, the values shown in Table 4.3 are the ones used in the calculations of deuterium dissolved in Chapter 5.

Table 4.4 shows the deviations parameter Ψ^2 (defined in equation (4.7)), which is a direct quantification of the quality of the fits. The first three columns (terms h'_{uc}, h'_{lc} and τ) correspond to the three terms of equation (4.7), which added to each other result in Ψ^2. They show that the fits adapt very well to the total duration of the experiments (τ), while the major contribution of the deviations are from matching the level thermocouples (see example run#13 in Figure 4.7).

Table 4.4 also shows the deviation of the fitting curves (simulation vs experiment) in the two axes: $\Delta\tau$ is the deviation in the duration (x-axis in Figure 4.7), and $\mathrm{std}(h'_{\mathrm{PbLi}})$ is the standard deviation of the height of Pb-Li (y-axis in Figure 4.7). $\mathrm{std}(h'_{\mathrm{PbLi}})$ is calculated for the total amount of thermocouples in both chambers

Table 4.4: Results from function *deviation* with the inputs from Table 4.3: the three terms of equation (4.7) and Ψ^2; the deviation in duration of the experiment: $\Delta\tau = \tau^{\text{exp}} - \tau^{\text{sim}}$; and standard deviation of the height of Pb-Li, $\text{std}(h'_{\text{PbLi}})$, calculated with equation (4.10).

Run	Term h'_{uc} (-)	Term h'_{lc} (-)	Term τ (-)	Ψ^2 (-)	$\Delta\tau$ (s)	$\text{std}(h'_{\text{PbLi}})$ (mm)
Run#12	1.46	2.29	0.03	3.78	1.7	1.23
Run#13	1.00	6.06	0.26	7.33	5.1	1.90
Run#14	5.22	3.36	0.01	8.59	-1.1	1.63
Run#15	1.93	10.25	0.87	13.07	9.5	2.48
Run#16	2.06	8.24	0.67	10.97	8.2	2.24
Run#17	0.97	6.40	0.41	7.79	6.4	1.95
Run#18	0.99	6.17	0.42	7.58	6.5	1.91
Run#19	3.08	4.71	0.26	8.05	5.1	1.77
Run#20	6.90	4.37	0.15	11.42	3.8	1.87

($n=8$) with:

$$\text{std}(h'_{\text{PbLi}}) = \sqrt{\frac{\sum_{j=1}^{n}(h'^{\,\text{exp}}_{\text{PbLi}_j} - h'^{\,\text{sim}}_{\text{PbLi}_j})^2}{n-1}}. \tag{4.10}$$

Since the deviation of τ is very small for all runs ($\Delta\tau \leq 0.85\%$), the deviation in time (x-axis) has been neglected in the calculation of the uncertainty. Therefore, the uncertainty of the Pb-Li height has been calculated from the $\text{std}(h'_{\text{PbLi}})$ as follows:

$$\delta h'_{\text{PbLi}} = \frac{\text{std}(h'_{\text{PbLi}})}{\sqrt{n}}. \tag{4.11}$$

The resulting uncertainty of the Pb-Li height for each run, $\delta h'_{\text{PbLi}}$, is given in Table 4.5. When multiplying these values by the cross-section area of the chambers, the uncertainty of the Pb-Li volume in each chamber is obtained: $\delta V_{\text{PbLi(uc)}}$ and $\delta V_{\text{PbLi(lc)}}$. These uncertainties, given in Table 4.5, are used in the calculations of the following chapters.

From the fitting results shown in Tables 4.3 and 4.5, the volume of Pb-Li in the upper chamber during the dissolution phase is known with an uncertainty between $2.4-3.6\,\%$ for all runs. This is one order of magnitude smaller than the experimental uncertainty, calculated with the distance between the level thermocouples shown in Figure 3.3 ($\delta V_{\text{PbLi(uc)}} = 0.25\,\text{l}$). In the lower chamber (extraction phase), most important is the improvement of the uncertainty in the falling height (inversely proportional to the Pb-Li height). The experimental uncertainty varies between $\pm 2.5-10\,\text{mm}$ (distance between thermocouples in Figure 3.5 is $5-20\,\text{mm}$).

Thus, with the simulations, this uncertainty has been also improved by one order of magnitude (see $\delta h'_{\mathrm{PbLi}}$ values in Table 4.5).

Figure 4.8 shows the falling time of all the extraction experiments, obtained from the fitting procedure (values from Table 4.3). The runs depicted in solid lines share a similar gas pressure in the upper chamber: $p_{\mathrm{uc}_0} \approx 1000\,\mathrm{mbar}$. In these runs, the droplets fall more slowly than in the runs depicted in dashed lines, in which $p_{\mathrm{uc}_0} \approx 1500\,\mathrm{mbar}$. At the end of each experiment, there is normally a rapid increase of the falling time, due to the last portion of Pb-Li that is in the tube (note that

Table 4.5: Resulting uncertainties used in the calculations of deuterium dissolved and extracted (Chapters 5 and 6).

Run	$\delta h'_{\mathrm{PbLi}}$ (mm)	$\delta V_{\mathrm{PbLi(uc)}}$ (l)	$\delta V_{\mathrm{PbLi(lc)}}$ (l)
Run#12	0.4	0.02	0.01
Run#13	0.7	0.03	0.01
Run#14	0.6	0.03	0.01
Run#15	0.9	0.04	0.02
Run#16	0.8	0.04	0.01
Run#17	0.7	0.03	0.01
Run#18	0.7	0.03	0.01
Run#19	0.6	0.03	0.01
Run#20	0.7	0.03	0.01

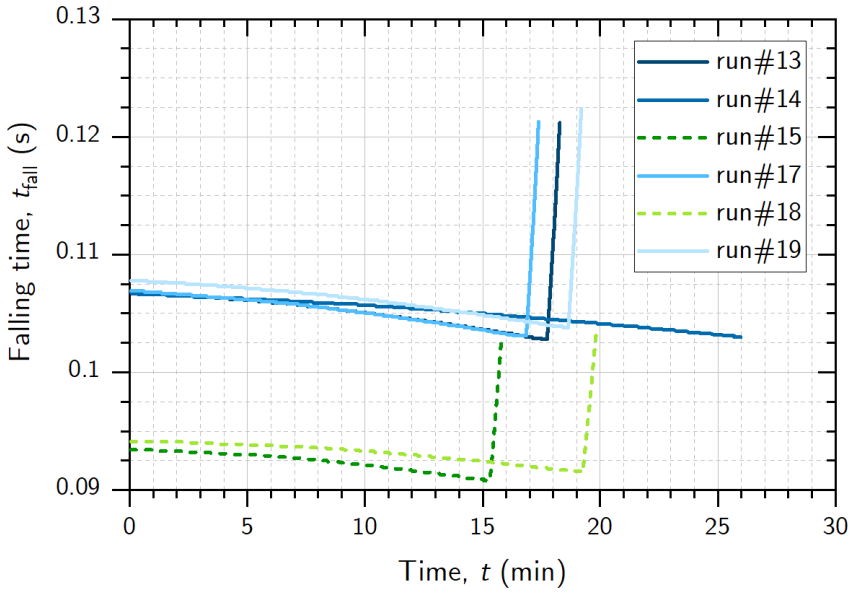

Figure 4.8: Falling time simulated with the values shown in Table 4.3. Runs starting at $p_{\mathrm{uc}_0} \approx 1000\,\mathrm{mbar}$ are depicted with solid lines and $p_{\mathrm{uc}_0} \approx 1500\,\mathrm{mbar}$ with dashed lines.

inside the tube, the Pb-Li level and, consequently, the hydrostatic pressure decrease much faster). In the case of run#14, this effect is not seen because the experiment stops before all the Pb-Li falls (the Pb-Li level in the UC does not reach the tube).

4.4 Observations with high-speed camera

4.4.1 Overview

A high-speed camera, Memrecam HX-3 (with software HXLink SP-642), has been used to record the falling droplets. For each run, shots of duration $\sim 10^{-1}$ s are taken every minute. A LED module of 9 W (with an intermediate diffuser) is used to light the lower chamber from the window opposite to the camera, to maximize the contrast of the droplets. The camera can take up to 1.3×10^6 fps (frames per second). However, in practice, the maximum frequency of the frames and, more specifically, the opening of the shutter are limited by the amount of light.

From equations (2.1), $d_\mathrm{d} \simeq 1.89\, d_\mathrm{n}$, and (2.2), $f = \sqrt{8\sigma/(3\pi\rho V)}$, the expected droplet diameter and expected oscillation frequency (for a nozzle diameter of 0.6 mm) are 1.134 mm and 196 Hz, respectively. Therefore, 2000 fps are sufficient to analyse the possible oscillations. The opening time of the shutter, t_sh, however, is restricted to a shorter time, in order to minimize the blurring (elongation) effect of the captured droplets in the falling direction (an example is given in Appendix H). The relation between the blurring effect and the speed of the shutter is calculated as follows: The displacement of a droplet, δy, which is falling with speed v, during the time that the shutter is open t_sh, is given by:

$$\delta y = v\, t_\mathrm{sh} = \frac{v}{\nu_\mathrm{sh}}, \tag{4.12}$$

where ν_sh is the shutter speed (expressed in s^{-1}). For example, the image of a droplet falling at $v = 4\,\mathrm{m\,s^{-1}}$ and recorded at $\nu_\mathrm{sh} = 50\mathrm{k\,s^{-1}}$ is elongated by 0.08 mm (7 % of its diameter). The elongation δy is considered during the analysis of the images as a correction in the determination of the size (diameter), and as a source of error in the determination of the speed.

In the experiments, the shutter speed of the frames has been varied from 10k to $100\mathrm{k\,s^{-1}}$. The maximum shutter speed used during each run is given by the light inside the chamber, which was decreasing with every run due to the progressive condensation of Pb-Li at the windows. This can be observed in Figure 4.9, which shows frames of runs #13 (a), #14 (b) and #17 (c), all taken at $50\mathrm{k\,s^{-1}}$. The three runs are done under the same conditions (similar gas pressure in the upper chamber).

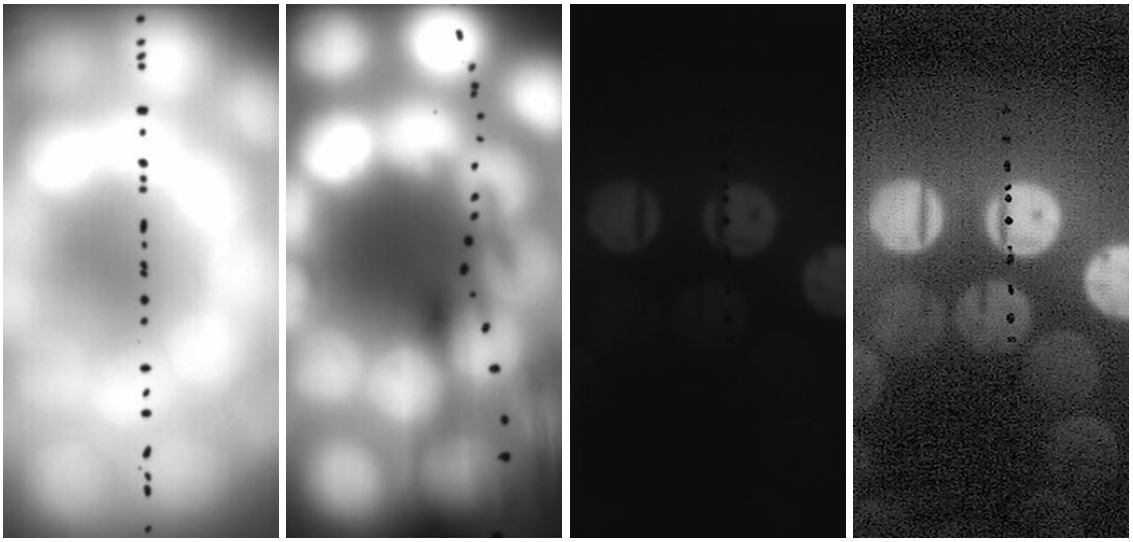

(a) Run#13 **(b)** Run#14 **(c)** Run#17 **(d)** Enhanced (c)

Figure 4.9: Frames of falling liquid Pb-Li droplets taken with $\nu_{\mathrm{sh}} = 50\mathrm{k\,s^{-1}}$. (d) is a modified version of the frame (c), after increasing the *gain*, *gamma* and *enhance* of the picture.

However, while in runs #13 and #17 (see enhanced picture (d)) the droplets fall following a vertical line, in run #14 the droplets fall at varying angles. This indicates that in run#14, the Pb-Li is not passing through an orifice with perfect vertical walls. This observation, in combination with the longer duration of the experiment, as shown in Table 4.3, suggests that there is some partial obstruction of the nozzle in run#14 (for example, some small particle or solidification at the nozzle), which also increases the pressure losses. This should decrease the size and speed of the falling droplets, which are analysed in the following sections (4.4.2 and 4.4.3).

For the analysis of the frames, a pixel-to-mm conversion is used, which is based on pictures taken of a ruler placed in the center of the chamber (more information in Appendix H). The obtained conversion factor is $7.047 \pm 0.205\,\mathrm{px\,mm^{-1}}$ (for the focal length of 43.2 cm, measured from the base of the camera to the center –z-axis– of the lower chamber). The given uncertainty is calculated for ± 1 cm in the normal direction to the picture plane, due to possible deflection of the droplet chain.

4.4.2 Droplet diameter and oscillations

The formation of a liquid jet that breaks into droplets has been confirmed for the runs #12 and #14 and assumed to exist for the rest of the runs. Therefore, the theoretical droplet diameter and oscillations is estimated from the Plateau-Rayleigh instability shown in Section 2.2.

The size of the droplets has been analysed with the image-processing software *ImageJ*. With this program, the 2D area of each droplet in one frame is obtained (only the droplets that present enough contrast with respect to the background). If there are some areas wrongly identified (e.g. two droplets identified as one object, or areas corresponding to the darker background at the top and bottom of the frame), they are manually removed from the analysis. Then, the diameter of the droplet, d_d, is calculated with

$$A_\mathrm{d} = \frac{\pi}{4} d_\mathrm{d}(d_\mathrm{d} + \delta y), \qquad d_\mathrm{d} = \frac{-\delta y + \sqrt{\delta y^2 + \frac{16}{\pi} A_\mathrm{d}}}{2}, \tag{4.13}$$

where A_d is the 2D area identified as one droplet and δy is the elongation due to the shutter speed defined by equation (4.12). By this approach, the derived diameter, d_d, assumes radial axis-symmetry.

Figure 4.10 shows the droplet diameter distribution for a sample of $n = 206$ droplets from run#13. The mean droplet diameter is 1.18 ± 0.15 mm. The uncertainty includes the error due to sharpness of the picture (± 2 px), the error of the distance camera–droplets (± 1 cm) and the statistical error ($\mathrm{std}/\sqrt{n}$). The result is in accordance with the theoretical diameter, calculated with equation (2.1), 1.134 mm.

In addition, the size of about 200 droplets per run has been analysed for the runs #12 and #14. The rest of the runs are not considered for this analysis, due to net picture quality arguments (not enough contrast between droplets and background). Figure 4.11 shows the resulting droplet diameter as a function of the equivalent

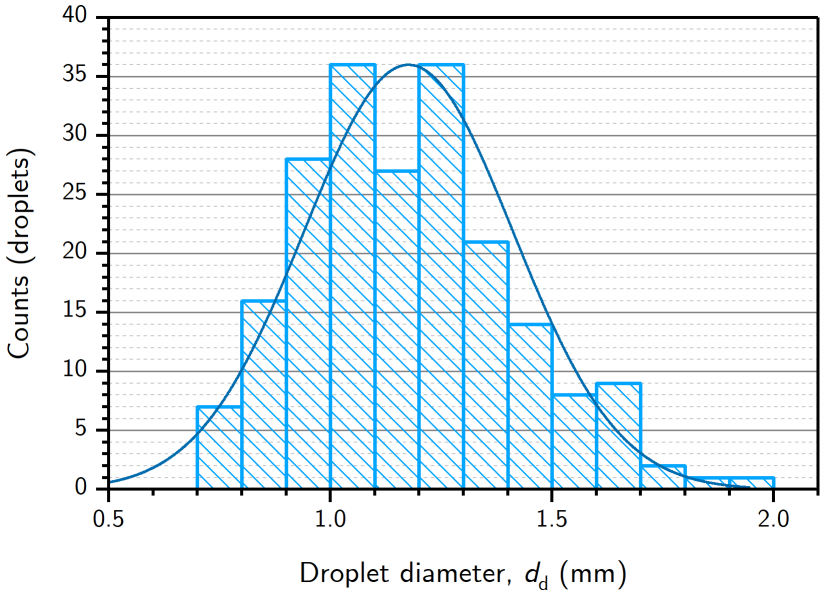

Figure 4.10: Distribution of the equivalent droplet diameter evaluated with a sample of 206 droplets from run#13. Mean value: 1.18 mm, std: 0.24 mm.

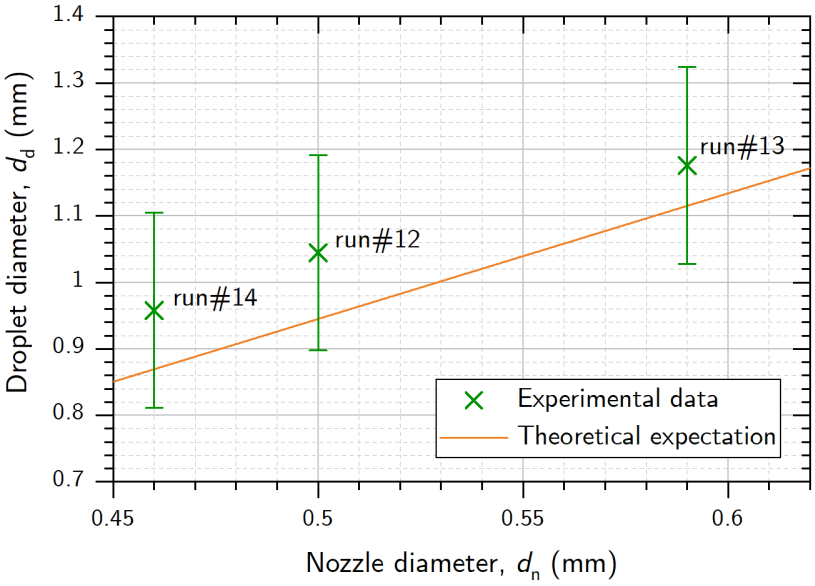

Figure 4.11: Relation between the diameter of the droplets obtained with the analysis of the HS-camera frames and the diameter of the nozzle obtained from simulation (data points); theoretical relation from equation (2.1) (solid line).

nozzle diameter shown in Table 4.3 (data points). The expected droplet diameter, calculated with equation (2.1), $d_\mathrm{d} \simeq 1.89\, d_\mathrm{n}$, is depicted with a solid line. The experimental data seem to match the theoretical expectations: (i) the agreement between data points and theoretical curve is within error bars and (ii) without considering the error bars, an increasing tendency of the droplet diameter with the nozzle diameter is observed, which is due to that smaller average droplets are originated from orifices with smaller cross-sectional area.

During the analysis of the frames, it has been observed that some droplets coalesce along their falling path. This effect has been observed for two, three and sometimes even four droplets. They start falling as single small droplets and end their path as one bigger droplet. This phenomenon occurs due to a slightly different initial speed from the droplet formation at the liquid jet in combination with a short distance between them. The existence of merging droplets explains that the obtained mean value of droplet diameter (Figures 4.10 and 4.11) is consistently larger than the one theoretically evaluated.

Additionally, a variation of the shape of the droplets is observed in all cases. Oscillations from oblate to prolate shape are commonly recognized and, sometimes, the observed movement indicates an additional rotation of the droplet. As an example, Figure 4.12 shows the shape oscillation of one droplet during 6 ms. The oblate shape in (a) turns spherical (b), then prolate (d), spherical (f) and oblate again (g). From the evaluation of the ratio d_y/d_x (vertical diameter/horizontal di-

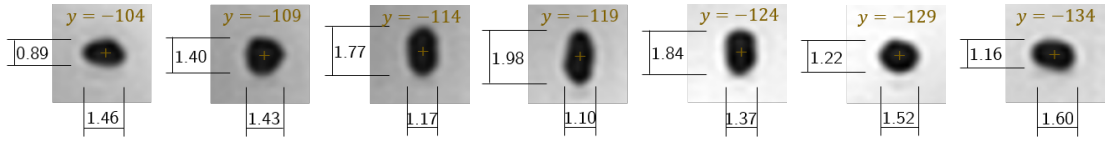

(a) 0 ms **(b)** 1 ms **(c)** 2 ms **(d)** 3 ms **(e)** 4 ms **(f)** 5 ms **(g)** 6 ms

Figure 4.12: Shape evolution of one droplet (extracted from run#13) during 6 ms. Dimensions and the vertical position, y, are given in mm. The vertical position is given with reference to the nozzle ($y = 0$). Frames taken with opening of the shutter $\nu_{\mathrm{sh}} = 50\mathrm{k\,s^{-1}}$.

ameter), it is observed that a full cycle (oblate-prolate-oblate) completes in almost 6 ms. With the equivalent diameter of the droplet, $d_{\mathrm{d}} = 1.37 \pm 0.15$ mm, and its volume, $V = 1.34 \pm 0.44\,\mathrm{mm}^3$, the theoretical frequency of oscillation is calculated with equation (2.2) to be is 170.3 Hz (one oscillation period: 5.87 ms). Thus, the oscillation observed in Figure 4.12 (≈ 6 ms) is in agreement with the fundamental frequency of oscillation described by the Plateau-Rayleigh instability theory.

4.4.3 Droplet speed

The speed of the droplets was analysed with the manual tracking option of *ImageJ*. Runs #13–#19 [2] were analysed at $t = 1$ and 15 min. Each sample consists of 50 droplets, whose position was evaluated in four consecutive frames. Only droplets close to the center of the chamber (in horizontal line with the camera) were analysed, in order to minimize the error produced by the angle of observation. The resulting average speed of each sample (evaluated at the center of the chamber), v_{c}, was extrapolated to the speed at the nozzle, v_{n}, with:

$$v_{\mathrm{n}} = \sqrt{v_{\mathrm{c}}^2 - 2(h_{\mathrm{n}} - h_{\mathrm{c}})g}, \tag{4.14}$$

where $(h_{\mathrm{n}} - h_{\mathrm{c}})$ is the distance between the nozzle and the center of the chamber, and g is the gravitational acceleration.

Table 4.6 shows the resulting speed at the nozzle, v_{n}, for each sample (see columns 'Experiment'). The uncertainty of the values includes the accuracy of the tracking point (±2–8 px, depending on the quality of the frame), the error due to elongation ($\delta y = 0.04 - 0.47$ mm), the error of the distance camera–droplets (±1 cm) and the statistical error ($\mathrm{std}/\sqrt{n}$). The columns 'Simulation' show the simulated speed at

[2] Unlike the analysis of the droplet diameter, image processing of the frames was not considered to influence the results of the evaluation of the speed, since the position of each droplet was evaluated at its center.

Table 4.6: Speed at the exit of the nozzle, v_n. 'Experiment': experimental values obtained from the analysis of the frames; 'Simulation': values simulated with the inputs of Table 4.3; 'Deviation': difference between the simulated and experimental values.

Run	v_n at $t = 1\,\text{min}$ $(\text{m}\,\text{s}^{-1})$			v_n at $t = 15\,\text{min}$ $(\text{m}\,\text{s}^{-1})$		
	Experiment	Simulation	Deviation	Experiment	Simulation	Deviation
Run#13	4.72 ± 0.37	4.39	0.33	4.38 ± 0.37	4.02	0.36
Run#14	3.97 ± 0.41	4.38	0.41	3.74 ± 0.41	4.14	0.40
Run#15	5.41 ± 0.37	5.13	0.28	4.68 ± 0.37	4.64	0.04
Run#17	4.69 ± 0.72	4.37	0.32	4.35 ± 0.71	4.02	0.33
Run#18	5.33 ± 0.68	5.13	0.20	4.82 ± 0.68	4.72	0.10
Run#19	4.64 ± 0.66	4.37	0.27	4.25 ± 0.67	4.03	0.22

the given time with the inputs from Table 4.3. As shown at the columns 'Deviation' (difference between the experimental and simulated values), the agreement between the experimental results and the simulation is within the experimental error. Additionally, the deviation remains within 1–11% of the experimental value. With this, the simulation code and the fitting method presented in the previous sections of this chapter are validated.

In conclusion, the code *VST-experiment* predicts the fluid dynamics, including the speed of the droplets, their falling time and monitoring of the volume of Pb-Li in both chambers with a high accuracy. Moreover, the droplet diameter has been measured and high-frequency oscillations of the droplets shape are observed. The frequencies extracted correspond to those predicted and observed in other experiments. Thus, all essential fluid-dynamics parameters to evaluate the extraction efficiency are confirmed by the experiments.

Chapter 5

Evaluation of the amount of deuterium dissolved

5.1 Methodology

During the dissolution phase, the amount of gas D_2 initially inserted in the upper chamber decreases with time due to its diffusion into the liquid Pb-Li and stainless-steel walls, as shown in Figure 5.1 (a). At steady state, the amount of deuterium dissolved in the Pb-Li, $n_{D_2[PbLi]}$, cannot be calculated with the Sieverts' law (equation (2.9)), since the solubility of D_2 in Pb-Li is uncertain (literature values disagree by several orders of magnitude). Therefore, in the present work, the amount of deuterium dissolved in the Pb-Li is determined with a mass balance evaluated at the gas phase, as follows:

$$-\Delta n_{D_2} = n_{D_2[ss]} + n_{D_2[PbLi]}, \tag{5.1}$$

where $-\Delta n_{D_2}$ refers to the variation of D_2 in the gas phase in the upper chamber, as shown in Figure 5.1 (b); $n_{D_2[ss]}$ is the amount of D_2 lost through the stainless steel, and $n_{D_2[PbLi]}$ is the amount of D_2 dissolved into the Pb-Li [1].

The amount of deuterium dissolved in the Pb-Li, $n_{D_2[PbLi]}$, is determined following four main steps:

(i) Evaluation of the time at which steady state is reached inside the Pb-Li (τ_{diss}). This is considered as the dissolution time, since after τ_{diss} the Pb-Li is saturated (i.e. the net flux is zero: atoms that enter the liquid metal, also leave it through the lower walls). Therefore, the mass balance to determine the deuterium

[1] Note that, although deuterium enters a metal in atomic form, in this work all the quantities and/or calculations are generally expressed in moles of D_2, in order to avoid confusion. This is also convenient since all experimental evaluations are made within the gas phase.

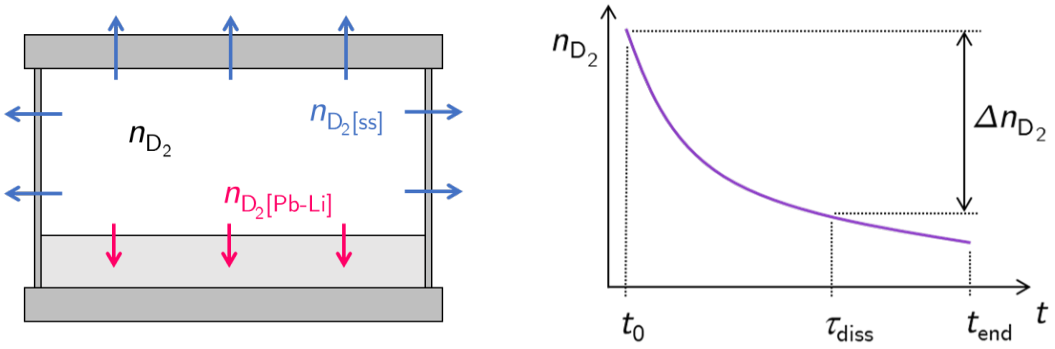

(a) Scheme of dissolution phase

(b) Evolution of gas D_2 in the chamber

Figure 5.1: Scheme of the dissolution phase in the upper chamber. (a) Amount of D_2 gas in the chamber (n_{D_2}); deuterium lost through the stainless steel ($n_{D_2[ss]}$); deuterium dissolution into the Pb-Li ($n_{D_2[PbLi]}$). (b) Schematic evolution in time of D_2 gas in the chamber, with $-\Delta n_{D_2}$ being the total amount of gas that has entered the metals until τ_{diss}.

dissolved has to be evaluated at τ_{diss}. This approach assumes that before τ_{diss} no D_2 (or negligible amount) escapes the liquid metal, since it is considered to be dissolved.

(ii) Evaluation of the total amount of gas lost into the metals until τ_{diss} (Δn_{D_2}). With the evolution of pressure and temperature of the gas inside the chamber and its volume, the curve $n_{D_2}(t)$, as in Figure 5.1 (b), is obtained with the ideal gas law (equation (3.1)). Δn_{D_2} is the difference between the initial point $n_{D_2}(t_0)$ and $n_{D_2}(\tau_{diss})$.

(iii) Evaluation of the amount of gas permeated through the walls ($n_{D_2[ss]}$). It consists in the following intermediate steps:

(a) Experimental determination of the D_2 that permeates through the whole chamber under the same conditions of p and T but without any liquid Pb-Li, as depicted in Figure 5.2 (a). For this purpose, three permeation experiments (with no Pb-Li) are performed. Note that the obtained amount $n_{D_2[ss^*]}$ is marked with an asterisk to denote permeated *through all the walls* (in order to differentiate it from $n_{D_2[ss]}$, which denotes permeation *only through the Pb-Li–free walls*).

(b) With the dimensions of the chamber, the thicknesses of the walls and their temperature profile, as shown in Figure 5.2 (b), the percentage of deuterium permeated through the upper surfaces (shown in lined blue patterns), corresponding to the Pb-Li–free walls, is theoretically calcu-

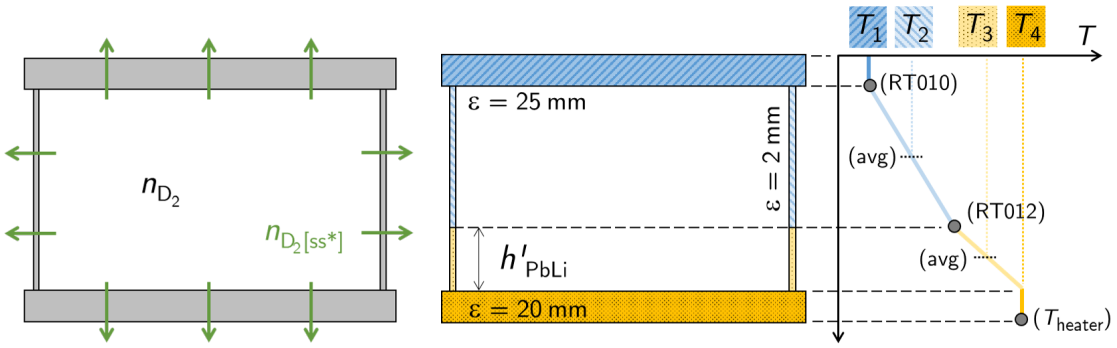

(a) Permeation experiment **(b)** Wall temperature and thickness in calculations

Figure 5.2: Schemes of the upper chamber used in the determination of D_2 permeated through the steel walls. (a) Scheme of permeation experiment (without Pb-Li). $n_{D_2[ss*]}$ denotes the deuterium that permeates through all the walls. (b) Scheme of the temperature profile used in the theoretical calculation of the fraction of D_2 that permeates through the upper walls (shown in lined blue patterns). The walls surfaces covered by Pb-Li during a dissolution experiment are shown in dotted yellow patterns. ε denotes thickness.

lated using the literature data of permeability for stainless steel.

(c) The theoretical percentage from the above point (b) applied to the experimental total value $n_{D_2[ss*]}$ from (a) gives the amount of D_2 that permeates through the Pb-Li–free walls in the dissolution experiments, $n_{D_2[ss]}$.

(iv) Determination of the amount of deuterium dissolved in the Pb-Li ($n_{D_2[PbLi]}$), with equation (5.1).

The simplified version of the chamber, a cylinder as shown in Figure 5.2, is used to facilitate the calculations of permeation. This assumption neglects the sampling port and feedthroughs, which are mainly in the coldest part of the chamber (e.g. the tube of the pressure sensor is at room temperature, thus, the permeation through it is several orders of magnitude lower than through the heated surfaces).

The next sections show the results of the above-mentioned steps. The colours of the figures are in accordance with the schemes shown in Figures 5.1 and 5.2 to facilitate visual association.

5.2 Evaluation of the dissolution time (τ_{diss})

The dissolution time, defined as the time to reach steady state (τ_{diss}) in the Pb-Li, is evaluated with equation (2.8), $\tau_{ch} = L^2 / 2\mathcal{D}$, assuming the atoms of deuterium only diffuse in the vertical direction, $L = h'_{PbLi(uc)}$ (note that $h'_{PbLi(uc)} \approx 22$ mm, while

Table 5.1: Height of Pb-Li in the upper chamber during dissolution ($h'_{\mathrm{PbLi(uc)}}$) and dissolution time (τ_{diss}) calculated with equation (2.8) and diffusivity $\mathcal{D} = 3.14{\times}10^{-9}\,\mathrm{m^2\,s^{-1}}$.

Run	$h'_{\mathrm{PbLi(uc)}}$ (mm)	τ_{diss} (min, (h))
Run#13	22.9 ± 0.7	1392 (23.2)
Run#14	21.9 ± 0.6	1274 (21.2)
Run#15	22.3 ± 0.9	1320 (22.0)
Run#17	22.1 ± 0.7	1297 (21.6)
Run#18	23.1 ± 0.7	1417 (23.6)
Run#19	23.1 ± 0.6	1417 (23.6)

the diameter of the chamber $d_{\mathrm{uc}} = 250\,\mathrm{mm}$). The value of diffusivity used is an average between the values in literature for deuterium at 400 °C (see reported by Edao *et al.* [56] and Reiter [55] in Figure 2.2): $\mathcal{D} = 3.14 \times 10^{-9}\,\mathrm{m^2\,s^{-1}}$. The results are shown in Table 5.1. Note that the values vary from each other due to the small variations of the Pb-Li height in each run. The calculations shown in the following sections are evaluated at τ_{diss}, since afterwards no more deuterium is assumed to be dissolved into the Pb-Li.

It must be highlighted that, within the frame of this work, simulations have been performed using the diffusion equations to evaluate the deuterium dynamics through the Pb-Li and stainless-steel walls of the chamber. However, the theoretical results are not conclusive to evaluate the deuterium dissolved in the Pb-Li, given the broad combination of values of diffusivity and solubility in stainless steel and Pb-Li available in literature. For this reason, in this work the amount of deuterium dissolved is experimentally evaluated with a mass balance at τ_{diss}.

5.3 Amount of D_2 gas decrease during dissolution (Δn_{D_2}): diffused into both Pb-Li and steel walls

Figure 5.3 shows the evolution of pressure, p, and temperature, T, of the gas in the upper chamber during the dissolution phase of run#13, as an example. p decreases due to diffusion into the Pb-Li and the stainless-steel walls. Additionally, its slope decreases with time as the concentration of deuterium increases in the liquid and the walls. At around $\tau_{\mathrm{diss}} = 1392\,\mathrm{min}$ (steady state in the Pb-Li) the pressure tends to a constant decrease. Note that the saturation of the top flange is estimated to take longer than $10^3\,\mathrm{h}$ (evaluated with $\mathcal{D}$ from Figure 2.1 and equation (2.8)).

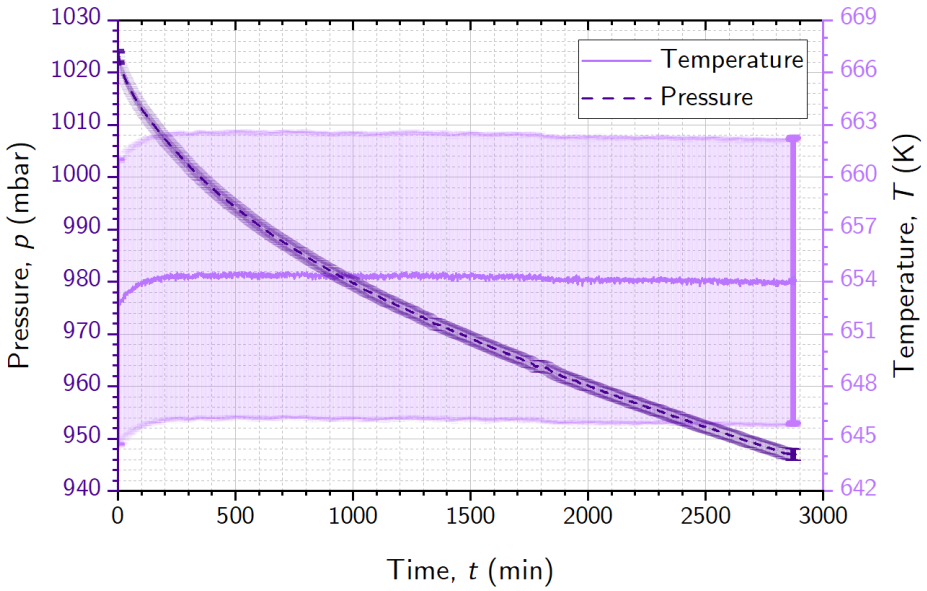

Figure 5.3: Temporal evolution of gas pressure (p) and gas temperature (T) measured during the dissolution phase in run#13.

Therefore, steady state is not reached in the entire stainless-steel walls during the experiment. Furthermore, it is important to note that, even when the metals are fully saturated, the gas pressure continues decreasing due to permeation. Then, a *pseudo* steady state is continuously (slightly) varying in time.

The values of initial pressure, p_0, and the pressure decrease until τ_{diss}, $-\Delta p$, of all runs are shown in Table 5.2. Each experimental value of p is determined with an average over 10 data points (corresponding to 10 s and 10 min of recorded data, at t_0 and τ_{diss} respectively).

The gas temperature, T, is calculated with equation (3.4), $T = \sqrt[4]{(T_a^4 + T_b^4)/2}$, with T_a and T_b being the experimental values from thermocouples RT010 and RT012 (at the top of the chamber and surface of Pb-Li, respectively, see Figure 3.3). The thermalization of the gas takes around 4 h after its injection into the chamber, as seen in Figure 5.3. However, since the variation in temperature is only of 1.5 – 2 K (in all runs), in comparison with the uncertainty (about ±8 K), the temperature is considered constant during the whole experiment. The average value (during each run) is given in Table 5.2.

The volume of the gas, V_{gas}, is calculated by subtracting the volume of the upper chamber (4.88 ± 0.02 l) and the volume of the Pb-Li (Tables 4.3 and 4.5). The resulting values of V_{gas} are given in Table 5.2. Note that V_{gas} remains constant during each dissolution phase.

With the presented values of p, T and V, the amount of gas is computed using the ideal gas law (equation (3.1)). Figure 5.4 shows the resulting curve for run#13.

Table 5.2: Experimental values during dissolution phase: initial pressure of the gas (p_0), pressure variation until τ_{diss} ($-\Delta p$), average temperature of the gas (T), volume of the gas (V_{gas}), amount of gas diffused into the liquid metal and the steel walls until τ_{diss} ($-\Delta n_{\text{D}_2}$).

Run	p_0 (mbar)	$-\Delta p$ (mbar)	T (K)	V_{gas} (l)	$-\Delta n_{\text{D}_2}$ (mol)
Run#13	1023.4 ± 1.1	52.3 ± 1.5	654.1 ± 8.2	3.65 ± 0.04	$(3.51 \pm 0.12) \times 10^{-3}$
Run#14	1025.2 ± 1.1	46.7 ± 1.5	652.8 ± 8.2	3.70 ± 0.03	$(3.18 \pm 0.12) \times 10^{-3}$
Run#15	1023.4 ± 1.1	50.0 ± 1.5	651.7 ± 8.1	3.68 ± 0.05	$(3.39 \pm 0.12) \times 10^{-3}$
Run#17	514.4 ± 1.1	29.6 ± 1.5	651.9 ± 8.1	3.69 ± 0.04	$(2.02 \pm 0.11) \times 10^{-3}$
Run#18	516.0 ± 1.1	30.5 ± 1.5	652.4 ± 8.1	3.64 ± 0.04	$(2.05 \pm 0.11) \times 10^{-3}$
Run#19	1026.1 ± 1.1	56.2 ± 1.5	653.5 ± 8.2	3.63 ± 0.04	$(3.76 \pm 0.12) \times 10^{-3}$

The uncertainty is calculated with equation (3.3), which includes the errors in p, T and V, resulting in $\pm 1.6\,\%$ (with respect to the absolute value n). One may observe in Figure 5.4 that, since the rate of decrease is very small (n decreases throughout the experiment in only $\approx 7.6\,\%$, with respect to its initial value), the uncertainty of the measurements seem to be relatively large. Nevertheless, it should be noted that about $93\,\%$ of the total error corresponds to the uncertainty of V and T, which are considered constant during each experiment and, thus, reflect on offset error. The amount of gas lost until τ_{diss}, $-\Delta n$, is calculated as follows:

$$-\Delta n = (n_0 - n_{\text{f}}) = \frac{(p_0 - p_{\text{f}})V}{RT} = \frac{-\Delta p V}{RT}\,. \tag{5.2}$$

The resulting values of $-\Delta n$ are given in Table 5.2. The obtained uncertainties are in the range of $3.2 - 5.4\,\%$. The experimental data of all runs and the error calculations are given in Appendix I and K, respectively.

The results shown in Table 5.2 can be divided into two groups (separated by the dotted lines): the runs starting at $p_0 \approx 1000\,\text{mbar}$ (runs#13, #14, #15 and #19) and the runs at $p_0 \approx 500\,\text{mbar}$ (runs#17 and #18). Runs#13, #14, #15 and #19 present similar results, although vary slightly from each other due to minor deviations in the experimental p, V, T conditions. Run#17 and run#18 present smaller values of $-\Delta n$, due to their lower dissolving pressure ($p_0 \approx 500\,\text{mbar}$). The similar results obtained for similar initial conditions (of p, V, T) show the repeatability of the experiments. From the total variation of the amount of D_2 ($-\Delta n_{\text{D}_2}$), the fraction lost into the walls ($n_{\text{D}_2[\text{ss}]}$) and the fraction dissolved into the Pb-Li ($n_{\text{D}_2[\text{PbLi}]}$) are evaluated in the next sections.

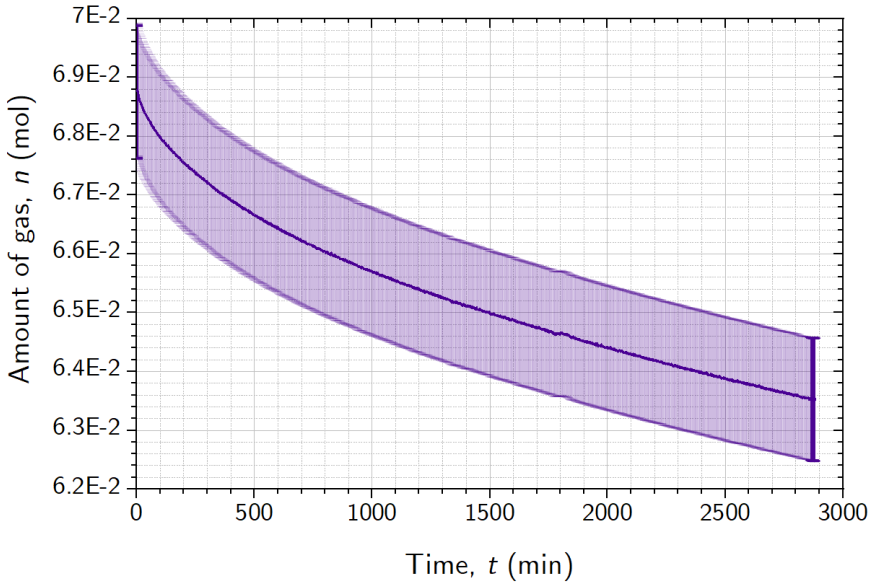

Figure 5.4: Temporal evolution of amount of gas in the upper chamber (gas phase) measured during the dissolution phase in run#13.

5.4 Evaluation of D_2 lost through the walls ($n_{D_2[ss]}$)

5.4.1 Permeation experiments

Previous to the runs performed with Pb-Li, three permeation experiments have been done in the upper chamber with two main objectives: (i) to test the repeatability of the process, i.e. to check that the bake-out time is enough to unload the walls of deuterium to start the next experiment, and (ii) to determine experimentally how much deuterium diffuses through the walls of the chamber.

The permeation experiments consist in reproducing the same process of the dissolution phase, but without Pb-Li in the upper chamber. This includes the same conditions of pressure, temperature and duration. All the steps from a typical run (including a four-day evacuation period, a vacuum test, etc., as shown in Table 3.7) are also followed, except for transferring the Pb-Li between chambers (steps #01 and #07). With this, the times of evacuation and the corresponding temperatures are respected and repeatability is evaluated.

Figure 5.5 shows the evolution of pressure and temperature of the gas during the first permeation experiment, perm#24. The temperature of the gas is calculated with equation (3.4), $T = \sqrt[4]{(T_a^4 + T_b^4)/2}$, in which the temperature of the top surface, T_a, is given by the thermocouple RT010 (see Figure 3.3) and the bottom surface, T_b, is determined from the average between RT013 and the temperature of the heater. In Figure 5.5, it is observed that the variation of temperature is about 2.5 K, far below the uncertainty ($\approx \pm 8$ K). This also applies to the other two permeation

experiments. Thus, the temperature is treated as constant, as in the calculations of the previous section.

Figure 5.6 shows the evolution of amount of D_2 in the gas phase (determined with the ideal gas law) during the permeation experiment perm#24 and its repetition, perm#25. The agreement between the results shows that for the maximum amount of gas ($p_0 \approx 1000\,\text{mbar}$), the deuterium remaining in the walls from the previous experiment is negligible in comparison with the experimental uncertainty. Hence,

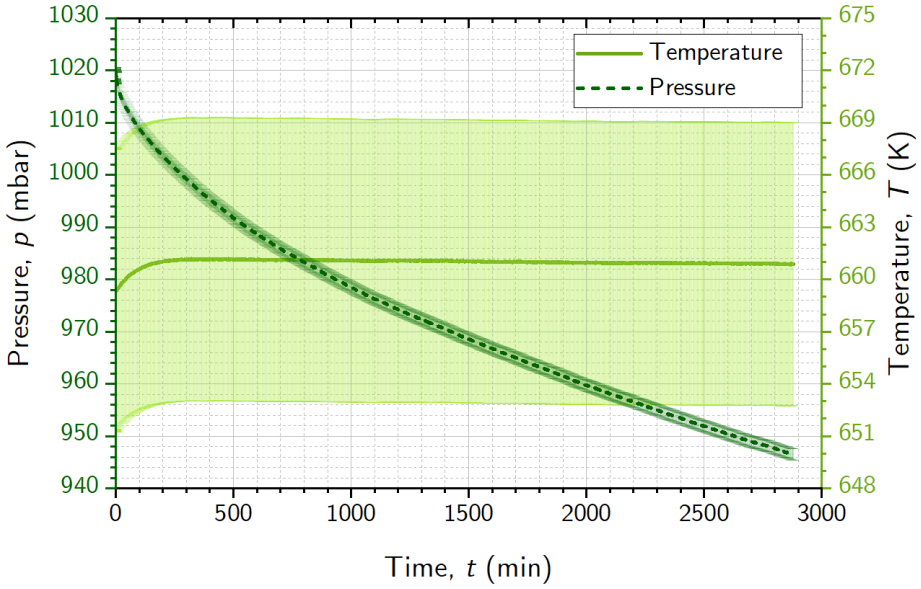

Figure 5.5: Temporal evolution of gas pressure (p) and gas temperature (T) measured during the permeation experiment perm#24.

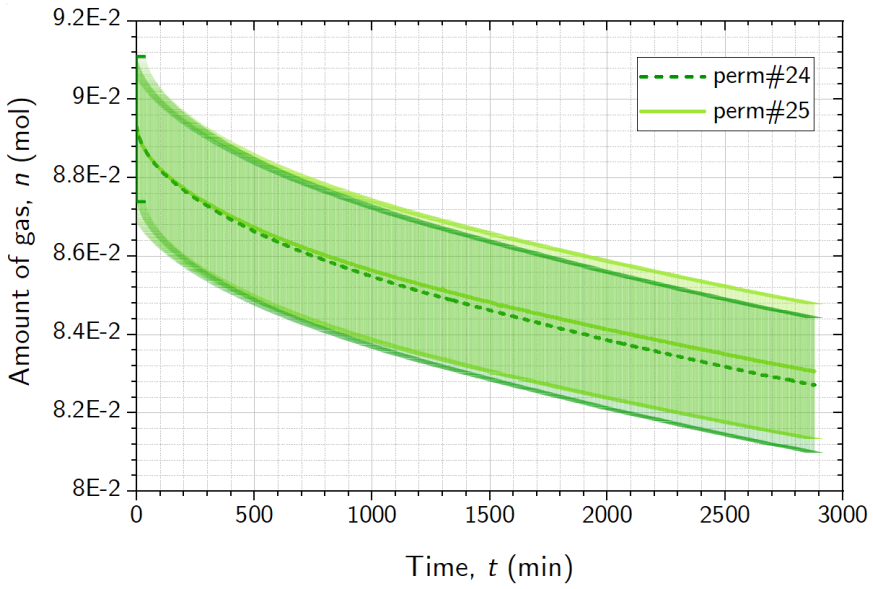

Figure 5.6: Temporal evolution of amount of gas in the upper chamber (gas phase) measured during the permeation experiments perm#24 and perm#25.

the bake-out time and temperature are proved to be sufficient.

For the second objective, it is important that the conditions of temperature in the chamber *with* and *without* Pb-Li are as close as possible. With that purpose, previous tests have been performed with helium to adjust the set point of the heater. Helium is selected because its solubility in metals is negligible (to avoid contamination of the walls) and its thermal conductivity is similar to the one of deuterium. From those tests, the set-point temperature of the heater has been defined as 411 °C and 411.5 °C for the permeation experiments at $p_0 \approx 500$ and 1000 mbar, respectively (in contrast with 400 °C for the dissolution runs).

Figure 5.7 shows the temperature profile of the permeation experiments (no Pb-Li), in green, and the dissolution runs (with Pb-Li), in purple, at $p_0 \approx 1000$ mbar. As seen in the figure, the profiles cannot be exactly the same with and without Pb-Li. Nevertheless, the following temperature values should be as close as possible between the permeation and dissolution runs:

(a) **Effective temperature of the gas**: The temperature of the gas in the region between RT012 and RT010, calculated with equation (3.4), for perm#24 and perm#26 is 653.1 ± 8.1 K and 654.3 ± 8.1 K, respectively. This is consistent with the temperature of the gas in all the dissolution runs, shown in Table 5.2.

(b) **Temperature of the stainless-steel walls**: The temperature of the Pb-Li–free surfaces, filled with lined blue patterns in Figure 5.2 (b), should be similar

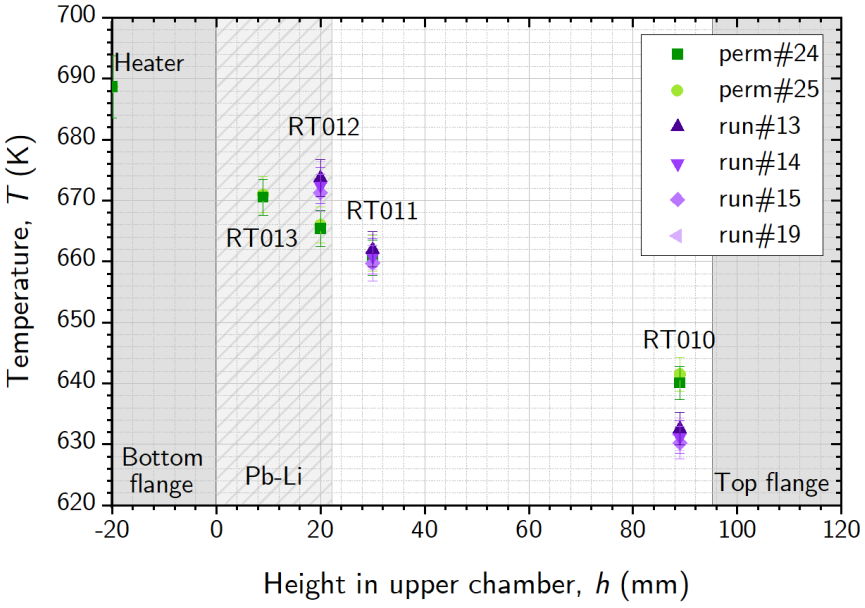

Figure 5.7: Experimental values of temperature recorded in the upper chamber (average values) during permeation experiments (no Pb-Li) and dissolution runs (with Pb-Li) at $p_0 \approx 1000$ mbar.

in both the permeation and dissolution experiments to be able to evaluate the amount of deuterium that escapes through the walls.

The temperature of the upper wall, T_2, is the average between RT010 and RT012. The maximum difference of T_2 between the permeation experiments (perm#24 and perm#26) and the corresponding dissolution runs is: $< 2\,\mathrm{K}$ for experiments at 1000 mbar and $< 3\,\mathrm{K}$ for the ones at 500 mbar. These differences are $< 0.5\,\%$ and within error bars.

The temperature of the top flange, T_1, is given by RT010. The difference of T_1 between the permeation experiments and their corresponding dissolution runs, $\leq 9.9\,\mathrm{K}$, is larger than the experimental uncertainties, $\approx 2.8\,\mathrm{K}$. This is due to the different temperature profiles (with and without Pb-Li). Thus, T_1 cannot be adjusted without sacrificing the values of T_2. The top flange is, however, the stainless-steel surface through which the least deuterium permeates due to its low temperature and large thickness. Therefore, the compromise adopted is to enlarge the error bars of T_1 of the permeation experiments in the calculations, up to $\pm 9.9\,\mathrm{K}$. (See all values of T_1 and T_2 in Appendix I.)

After verifying that the temperatures (gas and stainless steel) of the permeation experiments and the dissolution runs are equivalent, it is concluded that the permeation experiments are valid to evaluate the amount of deuterium lost through the Pb-Li–free steel walls.

Table 5.3 shows the main results of the permeation experiments: initial gas pressure, p_0, variation of pressure, $-\Delta p$, temperature of the gas, T, and variation of amount of gas, $n_{\mathrm{D_2[ss^*]}}$, evaluated at τ_{diss} of runs#13 and #17. $n_{\mathrm{D_2[ss^*]}}$ is determined with equation (5.2), as in the previous section. In this case, this variation corresponds to the amount of gas that permeates through all the walls of the upper chamber. The resulting values of $n_{\mathrm{D_2[ss^*]}}$ for perm#24 and perm#26 have an

Table 5.3: Experimental values of the two permeation experiments used in the calculations. As example, only the values determined for (a) run#13 and (b) run#17 are given in this table. Initial pressure of the gas (p_0), pressure variation until τ_{diss} ($-\Delta p$), average temperature of the gas (T_{gas}), and variation of amount of gas until τ_{diss} ($n_{\mathrm{D_2[ss^*]}}$), i.e. diffused into all the walls of the chamber.

Experiment	p_0 (mbar)	$-\Delta p$ (mbar)	T_{gas} (K)	$n_{\mathrm{D_2[ss^*]}}$ (mol)
Perm#24	1019.5 ± 1.08	48.9 ± 1.5 (a)	660.9 ± 8.1	$(4.28 \pm 0.16) \times 10^{-3}$ (a)
Perm#26	521.9 ± 1.08	29.2 ± 1.5 (b)	661.2 ± 8.1	$(2.55 \pm 0.14) \times 10^{-3}$ (b)

uncertainty of 3.7 % and 5.6 %, respectively.

Comparing the results of Tables 5.2 (runs#13 and #17) and 5.3, the gas lost during the permeation experiments ($n_{D_2[ss^*]}$) is larger than the gas lost during the dissolution runs ($-\Delta n_{D_2}$). This is because during the permeation experiments there is a larger gas–metal interface (light dotted yellow in Figure 5.2 (b)), due to the absence of Pb-Li. Additionally, the surface normally covered by Pb-Li (all dotted yellow in Figure 5.2 (b)) is at a higher temperature, due to the adjusted temperature of the heater during the permeation experiments.

In the next section, the gas that permeates only through the upper surfaces, $n_{D_2[ss]}$, (lined blue in Figure 5.2 (b)) is calculated.

5.4.2 Determination of permeation through the Pb-Li–free walls ($n_{D_2[ss]}$)

This step consists in a theoretical calculation of deuterium permeation through the different surfaces of the chamber. For this purpose, a simplified version of the upper chamber is used (as shown in Figure 5.2). The total permeation surface is divided into various sections corresponding to different temperatures and thicknesses. The vertical wall is additionally divided into two sections as a function of the height of Pb-Li in each run. Table 5.4 shows a summary of the values used in the calculations related to run#13. The geometrical values are taken as exact, except for the divided area of the vertical wall, which carries the uncertainty propagated from the height of Pb-Li.

Table 5.5 shows the calculations performed for run#13. They consist in the following: (i) The upper and lower walls are divided with the Pb-Li height of run#13. (ii) The theoretical permeation through each section is calculated with the two values of permeability shown in Table 2.2 and equations (2.10), $J = \mathcal{P}\left(\sqrt{p_b} - \sqrt{p_a}\right) A/L$, and (2.14), $\mathcal{P} = \mathcal{P}_0 \exp(-E_{\mathcal{P}}/RT)$, and with the experimental temperatures and

Table 5.4: Surface area (A), thickness (ε) and temperature (T) of the four sections of perm#24 using the height of Pb-Li of run#13.

Section	A (m^2)	ε (mm)	T (K)
Upper flange	0.049	25	640.1 ± 9.9
Upper wall	0.057 ± 0.002	2	652.7 ± 2.0
Lower wall	0.018 ± 0.001	2	677.0 ± 2.9
Lower flange	0.049	20	688.7 ± 5.1

Table 5.5: Theoretical calculations of D_2 permeated in perm#24 during 1392 min, with the permeability values, $\mathcal{P}$, given in Table 2.2. The division between upper and lower walls is done using the Pb-Li height from run#13. Fractions of D_2 permeated through the "in–run#13–Pb-Li–free" surfaces (blue) and "in–run#13–Pb-Li–covered" surfaces (yellow) are also given.

Section	Amount of D_2 permeated (mol) with $\mathcal{P}$ from [59]:		with $\mathcal{P}$ from [58]:	
Upper flange	$(6.0 \pm 1.2) \times 10^{-5}$	(61±3)%	$(3.7 \pm 0.8) \times 10^{-5}$	(60±4)%
Upper wall	$(1.10 \pm 0.05) \times 10^{-3}$		$(6.9 \pm 0.3) \times 10^{-4}$	
Lower wall	$(5.7 \pm 0.3) \times 10^{-4}$	(39±2)%	$(3.7 \pm 0.2) \times 10^{-4}$	(40±2)%
Lower flange	$(1.8 \pm 0.2) \times 10^{-4}$		$(1.2 \pm 0.1) \times 10^{-4}$	
Total	$(1.91 \pm 0.07) \times 10^{-3}$		$(1.21 \pm 0.04) \times 10^{-3}$	

pressure of perm#24 during the τ_{diss} of run#13 (1392 min). The fraction of deuterium permeated through the upper surfaces is given in blue, and the deuterium permeated through the lower surfaces, in yellow (as depicted in Figure 5.2 (b)). The quantity of interest of these results is (iii) the percentage of D_2 permeated through the top surfaces, $\approx 60\,\%$ (later used as χ_{top} in equation (5.3)).

The results obtained with the two theoretical values of permeability ($\mathcal{P}$ from [59] and [58]) are similar, since (i) the absolute values are in the same order of magnitude and (ii) the relative values are in accordance with each other. In comparison, the experimental result of perm#24, shown in Table 5.3 ($(4.28 \pm 0.16) \times 10^{-3}$ mol), is also within the same order of magnitude, although slightly larger. This difference is because the theoretical calculations refer to steady state (and, therefore, the fluxes are smaller). It is assumed that in non-steady state the relative fraction of atoms through the different surfaces is conserved. This assumption is based on the use of the same geometry, temperature and material, and on the similarity between the experimental and theoretical absolute values.

The fraction of deuterium permeated through the upper surfaces, χ_{top}, is taken as the average between the two theoretical results (blue percentages in Table 5.5), e.g., for run#13, $\chi_{top} = (60 \pm 2)\%$. Then, the total amount of deuterium that permeates through the Pb-Li–free walls during the dissolution runs, $n_{D_2[ss]}$, is calculated as follows:

$$n_{D_2[ss]} = \chi_{top}\ n_{D_2[ss^*]}, \tag{5.3}$$

with $n_{D_2[ss^*]}$ being the amount of deuterium lost during the corresponding perme-

Table 5.6: Experimental value of gas diffused through all the walls in the corresponding permeation experiment ($n_{D_2[ss^*]}$); theoretical fraction of deuterium diffused through the upper surfaces (χ_{top}); gas diffused through the Pb-Li–free walls ($n_{D_2[ss]}$), calculated with equation (5.3). All values are evaluated at the corresponding τ_{diss}.

Run	$n_{D_2[ss^*]}$ (mol)	χ_{top}	$n_{D_2[ss]}$ (mol)
run#13	$(4.3 \pm 0.2) \times 10^{-3}$	$(60 \pm 2)\%$	$(2.6 \pm 0.1) \times 10^{-3}$
run#14	$(4.1 \pm 0.2) \times 10^{-3}$	$(61 \pm 2)\%$	$(2.5 \pm 0.1) \times 10^{-3}$
run#15	$(4.2 \pm 0.2) \times 10^{-3}$	$(61 \pm 3)\%$	$(2.6 \pm 0.1) \times 10^{-3}$
run#17	$(2.6 \pm 0.1) \times 10^{-3}$	$(62 \pm 3)\%$	$(1.57 \pm 0.07) \times 10^{-3}$
run#18	$(2.6 \pm 0.1) \times 10^{-3}$	$(61 \pm 2)\%$	$(1.60 \pm 0.09) \times 10^{-3}$
run#19	$(4.3 \pm 0.2) \times 10^{-3}$	$(60 \pm 2)\%$	$(2.6 \pm 0.1) \times 10^{-3}$

ation experiment. Table 5.6 shows the summary of the results for all runs, which have a relative uncertainty of $\pm 4-6\,\%$. As expected, the values of $n_{D_2[ss]}$ are very similar among all runs with the same initial pressure, since the conditions of temperature and surface of the metals are almost identical (the largest difference between them is due to τ_{diss}, which is different for every experiment).

5.5 Evaluation of deuterium dissolved in the Pb-Li ($n_{D_2[PbLi]}$)

The amount of deuterium dissolved in the Pb-Li, $n_{D_2[PbLi]}$, is determined with the mass balance presented in equation (5.1) ($-\Delta n_{D_2} = n_{D_2[ss]} + n_{D_2[PbLi]}$) and the obtained values of $-\Delta n_{D_2}$ and $n_{D_2[ss]}$ shown in Tables 5.2 and 5.6, respectively. The resulting values of $n_{D_2[PbLi]}$ are given in the first column of Table 5.7. At this point, it is noteworthy to observe the fractions of gas involved in the mass balance, by comparing the obtained results. From the total amount of gas that has decreased during each dissolution experiment at τ_{diss} ($-\Delta n_{D_2}$), only $21-31\,\%$ is dissolved into the Pb-Li ($n_{D_2[PbLi]}$), while $69-79\,\%$ is lost through the stainless-steel walls ($n_{D_2[ss]}$). This shows the importance of an appropriate evaluation of the gas lost through the walls due to permeation in the accountancy of deuterium dissolved.

Additionally, the average concentration of atomic deuterium in the Pb-Li, $C_{D\,[PbLi]}$, is calculated with:

$$C_{D\,[PbLi]} = 2\,\frac{n_{D_2[PbLi]}}{V_{PbLi}}. \tag{5.4}$$

In the case of run#13, the resulting amount of deuterium dissolved at τ_{diss} is

Table 5.7: Amount of deuterium dissolved in the Pb-Li at τ_{diss} ($n_{\text{D}_2[\text{PbLi}]}$) evaluated with the mass balance (eq. (5.1)); amount of deuterium dissolved in the Pb-Li evaluated at t_{end} ($n_{\text{D}_2[\text{PbLi}]}(t_{\text{end}})$) with eq. (5.5); average atomic concentration of deuterium in the Pb-Li evaluated at t_{end} ($C_{\text{D}\,[\text{PbLi}]}(t_{\text{end}})$), and obtained Sieverts' constant ($\mathcal{S}$).

Run	$n_{\text{D}_2[\text{PbLi}]}$ (mol)	$n_{\text{D}_2[\text{PbLi}]}(t_{\text{end}})$ (mol)	$C_{\text{D}\,[\text{PbLi}]}(t_{\text{end}})$ ($\text{mol}_\text{D}\,\text{l}^{-1}$)	$\mathcal{S}$ (mol m^{-3} $\text{Pa}^{-0.5}$)
run#13	$(9.3 \pm 1.5)\times10^{-4}$	$(9.2 \pm 1.5)\times10^{-4}$	$(1.5 \pm 0.3)\times10^{-3}$	$(9.7 \pm 1.6)\times10^{-3}$
run#14	$(6.8 \pm 1.5)\times10^{-4}$	$(6.7 \pm 1.5)\times10^{-4}$	$(1.1 \pm 0.3)\times10^{-3}$	$(7.4 \pm 1.7)\times10^{-3}$
run#15	$(8.2 \pm 1.6)\times10^{-4}$	$(8.1 \pm 1.6)\times10^{-4}$	$(1.4 \pm 0.3)\times10^{-3}$	$(8.8 \pm 1.7)\times10^{-3}$
run#17	$(4.5 \pm 1.3)\times10^{-4}$	$(4.4 \pm 1.3)\times10^{-4}$	$(7 \pm 2)\times10^{-4}$	$(6.8 \pm 2.0)\times10^{-3}$
run#18	$(4.5 \pm 1.4)\times10^{-4}$	$(4.4 \pm 1.4)\times10^{-4}$	$(7 \pm 2)\times10^{-4}$	$(6.5 \pm 2.1)\times10^{-3}$
run#19	$(1.2 \pm 0.2)\times10^{-3}$	$(1.2 \pm 0.2)\times10^{-3}$	$(1.9 \pm 0.3)\times10^{-3}$	$(1.2 \pm 0.2)\times10^{-2}$

$(9.3 \pm 1.5)\times10^{-4}\,\text{mol}_{\text{D}_2}$, and the average concentration is $(1.5 \pm 0.3)\times10^{-3}\,\text{mol}_\text{D}\,\text{l}^{-1}$. However, from $\tau_{\text{diss}} = 23.2\,\text{h}$ until the end of the dissolution phase ($t_{\text{end}} = 48\,\text{h}$), the pressure of D_2 continues decreasing, from 971.1 to 946.9 mbar. Assuming perfect mixing, the impact of the pressure decrease (from τ_{diss} to t_{end}) on the concentration of deuterium in the Pb-Li is evaluated with the following relation:

$$\frac{n_{\text{D}_2[\text{PbLi}]}(t_{\text{end}})}{n_{\text{D}_2[\text{PbLi}]}(\tau_{\text{diss}})} = \frac{C_{\text{D}\,[\text{PbLi}]}(t_{\text{end}})}{C_{\text{D}\,[\text{PbLi}]}(\tau_{\text{diss}})} = \frac{\sqrt{p_{\text{D}_2}(t_{\text{end}})}}{\sqrt{p_{\text{D}_2}(\tau_{\text{diss}})}}, \tag{5.5}$$

from Sieverts' law, assuming constant solubility. In the example case of run#13, from equation (5.5), the deuterium dissolved at $t_{\text{end}} = 48\,\text{h}$ is $\approx 98.7\,\%$ of the amount evaluated at τ_{diss}.

The results calculated at the end of each dissolution experiment (t_{end}) with equation (5.5) are given in Table 5.7. Both, $n_{\text{D}_2[\text{PbLi}]}(t_{\text{end}})$ and $C_{\text{D}\,[\text{PbLi}]}(t_{\text{end}})$, have a relative uncertainty of $\pm 13 - 32\,\%$. The runs with similar dissolving pressure have similar $n_{\text{D}_2[\text{PbLi}]}(t_{\text{end}})$ and $C_{\text{D}\,[\text{PbLi}]}(t_{\text{end}})$.

The consistency between runs under different dissolving pressures is evaluated with Sieverts' law. With the assumption that steady state is reached in the Pb-Li at τ_{diss}, the concentration in the two sets of experiments (at 1000 mbar and at 500 mbar), assuming a linear concentration profile, follows the relation:

$$\frac{C_{\text{D}\,[\text{PbLi}]}(p_{\text{D}_2} \approx 500\text{mbar})}{C_{\text{D}\,[\text{PbLi}]}(p_{\text{D}_2} \approx 1000\text{mbar})} \approx \sqrt{0.5}, \tag{5.6}$$

which is obtained from substituting the approximate dissolving pressure values of the two sets of runs into Sieverts' law ($C = \mathcal{S}\sqrt{p}$).

The average concentration of the experiments at $p_0 \approx 1000\,\mathrm{mbar}$ is $(1.5 \pm 0.3) \times 10^{-3}\,\mathrm{mol_D\,l^{-1}}$. Therefore, from equation (5.6), the expected concentration for the runs at $p_0 \approx 500\,\mathrm{mbar}$ is $(1.0 \pm 0.2) \times 10^{-3}\,\mathrm{mol_D\,l^{-1}}$. This approximate value is in accordance with the results of runs#17 and #18 shown in Table 5.7.

Furthermore, the solubility coefficient, $\mathcal{S}$, is evaluated with the experimental results. Note that the Sieverts' constant is referred to the (maximum) concentration at the liquid–gas interface. Since the Pb-Li height is small, and under the assumptions that (i) the liquid metal is saturated with deuterium and (ii) there is no convection, the concentration profile is assumed linear in the vertical direction. Therefore, the solubility coefficient, $\mathcal{S}$, is determined with Sieverts' law ($C = \mathcal{S}\sqrt{p}$), the dissolving pressure at t_{end} and the concentration at the interface liquid–gas, i.e. twice the average concentration. The resulting values of $\mathcal{S}$ are given in Table 5.7 and are depicted in Figure 5.8 for comparison with the literature values already shown in Figure 2.3. The presented results are in the same range as the values reported by Edao *et al.* [56] and Chan *et al.* [75].

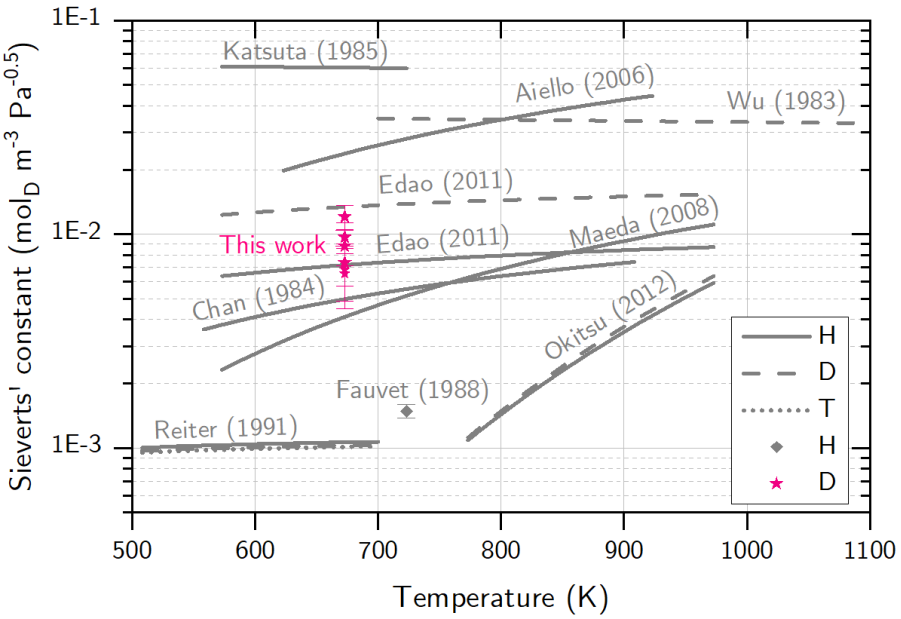

Figure 5.8: Experimental results of equivalent solubility coefficient from all dissolution runs obtained in this work (star data points in magenta); solubility coefficients of hydrogen isotopes in eutectic Pb-Li from literature (in grey) [55, 56, 68, 70–75].

5.6 Discussion of the obtained results in the scope of fusion

5.6.1 Solubility of deuterium in Pb-Li and effect of the alloy composition

In this work, solubility values of deuterium in Pb-Li have been obtained taking into account the diffusion of deuterium through the walls and with a careful uncertainty evaluation. The obtained values are consistent with each other (following the dependency on the dissolving pressure from Sieverts' law) and with literature data. However, it must be remarked that the lithium content of the alloy used is 15.2 ± 0.2 at.% Li and during the experimental campaign some impurities have been dissolved into the mixture. Therefore, the obtained results cannot be directly transferred to fusion applications without special care. This may be common to other experiments with Pb-Li, as it is discussed subsequently.

The solubility of hydrogen in Pb-Li increases with the atomic fraction of lithium in the alloy, as reported by Chan *et al.* [75]. They tested the solubility of hydrogen (protium) in different mixtures of Pb-Li, varying the concentration of lithium from 20 at.% to 90 at.% (which, unfortunately, does not cover the eutectic composition). Extrapolating their results, the solubility of H in a Pb-Li mixture with 17 at.% Li is ≈ 10 % larger than the one in a mixture of 15.7 at.% Li (at 673 K). This deviation, which is already considerable, could be expected in the works related to liquid breeding blankets since one of the two above Li concentrations is typically used [2].

Moreover, as stated in Section 3.1.4, the composition of the Pb-Li used in the present work differs from the one reported by the manufacturer: 15.2 ± 0.2 at.% instead of 15.7 at.%, which is attributed to an inhomogeneous distribution of the lithium atoms in the alloy. In the experimental works reporting solubility values for H and/or D in the literature (Figure 5.8), no verification of the composition of the Pb-Li is normally reported, i.e. only the eutectic mixture given by the manufacturer is provided. Thus, as stated in [65], there is a possibility that the fraction of Li is partially responsible for the discrepancy of the solubility values reported in the literature. In addition, final analyses with possible impurities are not reported either.

In the perspectives of liquid breeding blankets, experimental studies have been performed to test the corrosion of proposed structural materials (ferritic-martensitic

[2] Note that the eutectic mixture was formerly attributed to 17 at.% Li and, after a reassessment of the phase boundaries by Hubberstey *et al.* [64], the eutectic definition was updated to 15.7 at.% Li.

steels) caused by Pb-Li at operation temperatures and relevant speeds, which have led to non-negligible corrosion rates ($30-370\,\mu\mathrm{m\,y^{-1}}$) [85–91]. However, the consequences of the dissolved impurities in the liquid metal still need to be investigated.

All in all, given the small amount of lithium present in the eutectic Pb-Li mixture (15.7 – 17 at.% Li, 0.62 – 68 wt.% Li) and the corrosive nature of the alloy, in relative terms, the variation of composition between alloys from different batches used in different experiments, as well as the evolution of composition over time in a liquid breeding blanket, may be significant. Thus, the influence of the atomic fraction of lithium in the Pb-Li and the presence of impurities on the solubility (and diffusivity) of hydrogen isotopes should be investigated in the range of fusion applications.

5.6.2 Mobility of deuterium in Pb-Li and stainless steel in the perspectives of fusion

Regarding the dissolution experiments of the present work, the amount of deuterium lost through the 316L stainless-steel walls represents $\approx 69-79\,\%$ of the total gas decrease, $-\Delta n_{\mathrm{D_2}}$ (into Pb-Li and walls of the chamber). Even though the Pb-Li has been at a higher temperature than the steel walls, the relative amount of gas (mol/surface area) lost through the walls is 1–1.7 times larger than the dissolution into the Pb-Li. This shows that the permeation of hydrogen isotopes through stainless-steel containers or pipes is, not only far from being negligible, but larger than the permeability of hydrogen isotopes in Pb-Li at similar temperatures [3]. This can have consequences on both experimental works and fusion reactors using Pb-Li as discussed hereunder.

On the one hand, the gas lost through the structure may have an impact on the disagreement of the results shown in Figure 5.8, depending on the methodology used and the assumptions made in each experiment. For example, desorption methods (used by Reiter [55], Fauvet *et al.* [68] and Katsuta *et al.* [72]) underestimate the solubility, while absorption methods (used by Chan *et al.* [75], Aiello *et al.* [73] and Wu [74]) lead to an overestimation of the solubility, if the gas lost into the structure is not accurately estimated (in both methods). Even though this argumentation is not conclusive (since different structural materials are used in the various setups and e.g. both Katsuta *et al.* and Reiter used desorption methods and reported very distant solubility values), it is possible that an underestimation of the gas lost through the structure may be partially responsible for the substantial difference

[3] Note that permeability is the combination of diffusivity and solubility, as shown in equation (2.11): $\mathcal{P} = \mathcal{D}\mathcal{S}$

of the results. Thus, the gas lost through the structure must be very carefully regarded, e.g. as performed here, in the experiments concerning the interaction of hydrogen isotopologues with Pb-Li, including the research of TERS techniques for liquid breeding blankets.

On the other hand, the large mobility of the hydrogen isotopes in steel-based structural materials in a fusion reactor is a critical issue [92, 93], since the whole tritium inventory must be limited and the recovery of tritium to fuel the plasma must be maximized [25, 94]. Structural materials under investigation for DEMO are Reduced Activation Ferritic/Martensitic (RAFM) steels, such as EUROFER [95]. These steels present hydrogen permeability and diffusivity one and two orders of magnitude, respectively, higher than stainless steel 316L [96] (used in this work). Thus, in order to restrict the diffusion of tritium into the structure, the development of robust tritium-permeation-barrier (in addition to anti-corrosion) coatings is crucial for DEMO [13, 97–106].

Chapter 6

Evaluation of the amount of deuterium extracted

6.1 Methodology

The main steps of the extraction phase are the following:

(i) Evacuation of the chamber: the lower chamber is evacuated between experiments for approximately six days down to $\sim 10^{-4} - 10^{-3}$ mbar.

(ii) Inserting deuterium (only runs#14–#19): a certain amount of D_2 (≈ 0.15 mbar) is set as the background pressure. This step does not apply to run#13, in which the background measurement starts with the chamber evacuated.

(iii) Recording background: with the lower chamber completely closed, the pressure and temperature are recorded during a minimum of 40 min.

(iv) Deuterium extraction: the automatic valve is opened and the Pb-Li droplets fall in the lower chamber. The gas pressure and temperature recorded are used to evaluate the amount of deuterium extracted from the Pb-Li.

The evolution of the amount of gas in the lower chamber (both during measurement of background and D_2 extraction) is computed with the ideal gas law (equation (3.1)), with the pressure, temperature and volume of the gas. However, the configuration of the chamber complicates the evaluation of the temperature and pressure of the gas. The geometry of the lower chamber (as seen in Figures 3.2 and 3.4) consists of a six-way cross (to facilitate the placement of windows) attached to a 1.5-m flexible tube, a smaller six-way cross, cold trap and small pipe lines all conforming one closed volume (down to the shutter valve). Additionally, the main body of the chamber (almost fully covered with insulation material) has heaters on

its top and bottom surfaces (up to 455°C, to maintain the Pb-Li liquid), but the flexible tube is at room temperature.

Thus, in order to treat its geometry and temperature gradients, the lower chamber is divided into three regions, as shown in Figure 6.1. The amount of gas in each region is calculated separately and the total gas is the summation of all three contributions as follows:

$$n = n_1 + n_2 + n_3. \tag{6.1}$$

being n_1, n_2 and n_3 the amount of gas determined in each one of the three regions. The evaluation of the temperature, pressure and volume of the gas in each region is explained in the following sections. Then, the validation of the methodology is shown with the analysis of a control experiment (run#20).

6.1.1 Evaluation of the gas temperature

The temperature of the various sections depicted in Figure 6.1 is evaluated as follows:

– **Section A:** The temperature of this section corresponds to the one of the heater EH06. During runs#13–#14: $T_A = 445 \pm 3.3\,°C$, and during runs#15–#20: $T_A = 455 \pm 3.4\,°C$.

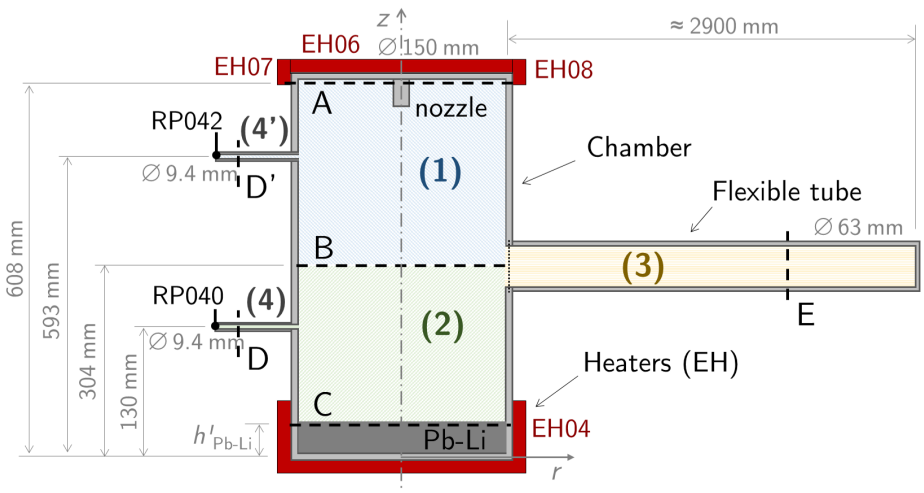

Figure 6.1: Simplified scheme of the lower chamber divided into three regions. (1) and (2): upper and lower halves of the six-way cross, respectively; (3): flexible tube and line ending at shutter valve; (4) and (4') cold fingers to the vacuum sensors, RP040 and RP042, respectively. EH: electric heaters. A, B, C, D, D', E: sections at which the temperature is evaluated. Note that the scheme is a simplification of the geometry shown in Figures 3.2 and 3.4.

– **Section B:** The temperature is obtained from an average of seven measurements at various points of the metal surface along Section B. $T_B = 56.7 \pm 5.8\,°C$. This temperature is much lower than the one of sections A and C because of the absence of insulation to protect the windows from high temperature (see Figure 3.2).

– **Section C:** This section corresponds to the Pb-Li surface. Therefore, it moves upwards when the Pb-Li level increases. Its temperature is obtained from a linear fit with the measurements of the level thermocouples (RT044-047, RT050-053). It varies over time and it is specifically calculated for each experiment.

– **Sections D and D':** The temperature at the vacuum sensors is given by RT042, placed at the cold finger next to the vacuum sensor RP042.

– **Section E:** The region (3) is at room temperature. Its value is taken as the average between RT014 and RT054.

The temperatures of the gas in regions (1) and (2), in Figure 6.1, are calculated with equation (3.4), $T = \sqrt[4]{(T_a^4 + T_b^4)/2}$, and the temperatures of the corresponding upper and lower sections (A–B and B–C, respectively). The temperature of region (3) is the one of section E.

6.1.2 Evaluation of the gas pressure

Since the vacuum sensors are placed at a cold finger, an evaluation at a microscopic level is performed to verify if the pressure is constant along the whole volume or if there is a pressure gradient to take into consideration (with respect to the measured value).

In this evaluation, two experiments are initially considered: run#13 (in which $p \approx 10^{-3}\,\text{mbar}$) and run#14 ($p \approx 0.15\,\text{mbar}$) as a representative of the rest of the runs performed at the same p conditions.

First, the gas regime is characterized by means of the *Knudsen number*, Kn, with the following definition [107]:

$$\text{Kn} = \frac{2\bar{l}}{\sqrt{\pi}a}, \tag{6.2}$$

in which a is the characteristic length of the system (e.g. pipe radius) and $\bar{l}$ is the mean free path of the gas molecules, defined as:

$$\bar{l} = \frac{k_B T}{\sqrt{2}\pi p d_M^2}, \tag{6.3}$$

where k_B is the Boltzmann constant, T is the temperature of the gas, p its pressure, and d_M is the molecular diameter. In the present calculations, the kinetic diameter of D_2 is assumed to be equal to the one of H_2: $d_M = 2.89 \times 10^{-10}$ m [108].

From the Knudsen number, the gas regime is characterized as follows: $Kn < 0.01$ corresponds to *viscous regime*, $0.5 > Kn > 0.01$ to *transition regime* (or *Knudsen regime*), and $Kn > 0.5$ to *molecular regime* [107].

Table 6.1 shows the evaluation of $\bar{l}$ and Kn at the different regions of the lower chamber in runs #13 and #14. In run#13 ($p \approx 10^{-3}$ mbar), the gas regime in the whole chamber is molecular ($Kn > 0.5$). In run#14 ($p \approx 0.15$ mbar), the gas in the chamber is within the transition regime ($0.01 < Kn < 0.5$). Since Kn in regions 1, 2, 3 is very close to the viscous limit, an approximation is applied in this case, which simplifies the calculations. In both runs, the pressure in the different regions must be determined with rarefied gas theory, since the gas flow in the cold fingers (at the vacuum sensors) is either in molecular or transition regime.

For that, the *rarefaction parameter*, δ, defined as follows, is first calculated:

$$\delta = \frac{1}{Kn}. \tag{6.4}$$

The pressure in one region (j), in relation with the pressure of a contiguous region (i) is calculated with equation (6.5), which describes a typical case scenario in rarefied gas theory [107]. In this scenario, two vessels (i and j) under vacuum are connected by a capillary. In this capillary a so-called *thermomolecular pressure effect* occurs: molecules flow from one vessel to another due to the thermal creep, which creates a pressure gradient with a consequent opposite flow. The relation between pressure and temperature in the two vessels is described by:

$$p_j = p_i \left(\frac{T_j}{T_i} \right)^{\gamma}, \tag{6.5}$$

where the parameter γ depends on the rarefaction parameter in the capillary. In the present case, equation (6.5) is applied to evaluate the pressure inside the chamber at

Table 6.1: Mean free path ($\bar{l}$), Knudsen number (Kn) and gas regime evaluated for the two representative cases: run#13 ($p \approx 10^{-3}$ mbar) and run#14 ($p \approx 0.15$ mbar).

Region	d (mm)	run#13			run#14		
		$\bar{l}$ (mm)	Kn (-)	Regime	$\bar{l}$ (mm)	Kn (-)	Regime
(1) top LC	150	227	3.4	molecular	1.5	0.02	≈ viscous
(2) bottom LC	150	202	3.0	molecular	1.3	0.02	≈ viscous
(3) flexible	63	110	3.9	molecular	0.7	0.03	≈ viscous
(4), (4') cold finger	9.4	112	26.9	molecular	0.7	0.18	transition

the region where the cold finger is physically connected (i.e. 1 or 2 for the cold fingers 4' and 4, respectively). Additionally, equation (6.5) is also used to relate contiguous regions (e.g. 1–2 and 1–3), based on the principle that the thermomolecular pressure effect is not intrinsically related to the existence of a capillary, but to the gas flow regime (and its characteristic rarefaction parameter).

Between the different regions in the lower chamber, the temperature difference $T_i - T_j$ and thermal gradients are large, with a consequent non-linear thermomolecular pressure effect. Therefore, an approximated γ is determined with an average rarefaction parameter, δ_{avg}, defined as follows (as suggested in Section III of reference [109]):

$$\delta_{\text{avg}} = \delta_i \frac{p_{\text{avg}}}{p_i} \frac{T_i}{T_{\text{avg}}} = \delta_i \frac{1 + (T_j/T_i)^{\gamma}}{1 + (T_j/T_i)}. \tag{6.6}$$

Then, the calculation of γ is performed following the instructions of Section II of reference [109].

Table 6.2 shows the resulting parameters for the example case of a pressure read by the sensor RP040 of 1.00×10^{-3} mbar (relevant scenario in run#13). The first column (δ) shows the rarefaction parameter in each region calculated with equation (6.4). The second column ($i \rightarrow j$) shows from which region (i) are the calculations made. For example, the pressure in region 2 (bottom of the lower chamber) is calculated directly with the values from region 4 (cold finger), since the cold finger is directly connected to region 2. The last column shows the resulting pressure in each region. As seen in the table, for this case scenario, a 38 % deviation is obtained between the pressure in the top of the chamber and the pressure read by the sensor. Note that, in comparison with the intrinsic uncertainty of the vacuum sensor RP040 ($\pm$ 6−14 % for the range covered throughout run#13), such deviation is substantial and has to be considered. These calculations vary with p and T, thus,

Table 6.2: Evaluation of pressure in example case 1: pressure read by the sensor RP040 (at the cold finger (4)) $1.00{\times}10^{-3}$ mbar. Rarefaction parameter calculated for each region (δ); direction of the calculation ($i \rightarrow j$: from region i to j); average rarefaction parameter (δ_{avg}) calculated with equation (6.6); coefficient γ between regions i, j (γ_{ij}) calculated following Section II of ref. [109], and pressure (p) calculated with equation (6.5).

Region	δ (-)	$i \rightarrow j$	δ_{avg} (-)	γ_{ij} (-)	p (mbar)
(1) top LC	0.29	2→1	0.3	0.38	1.38×10^{-3}
(2) bottom LC	0.33	4→2	0.03	0.47	1.32×10^{-3}
(3) flexible	0.25	2→3	0.4	0.37	1.05×10^{-3}
(4) cold finger	0.04	(-)	(-)	(-)	1.00×10^{-3}

Table 6.3: Evaluation of pressure in example case 2: pressure read by the sensor RP042 (at the cold finger (4')) 0.150 mbar. Rarefaction parameter calculated for each region (δ); direction of the calculation ($i \rightarrow j$: from region i to j); average rarefaction parameter (δ_{avg}) calculated with equation (6.6); coefficient γ between regions i, j (γ_{ij}) calculated following Section II of ref. [109], and pressure (p) calculated with equation (6.5).

Region	δ (-)	$i \rightarrow j$	δ_{avg} (-)	γ_{ij} (-)	p (mbar)
(1) top LC	43.9	4→1	4.36	0.09	0.158
(2) bottom LC	49.6	(=1)	(-)	(-)	0.158
(3) flexible	38.1	(=1)	(-)	(-)	0.158
(4') cold finger	5.6	(-)	(-)	(-)	0.150

they are performed throughout the experiment.

Table 6.3 shows the results for a case scenario of $p = 0.150$ mbar at the vacuum sensor RP042, which is representative for runs #14–#20. In this case, the pressure in regions 2 and 3 is assumed equal to the pressure in region 1, due to the approximation to viscous regime in these three regions. In this scenario, the resulting pressure in the chamber deviates about 6 % from the value measured by the sensor. Note that the vacuum sensor RP042 has an intrinsic error of ±0.4 %. Thus, a 6 % deviation is also noticeable. The calculations (which vary with p and T) are performed along the whole extraction experiment(s).

An estimated error from the evaluation of the pressure in regions 1, 2, 3 with the presented method is added. This error attempts to include the deviation from the real value due to the linearisation of the rarefaction parameter. This deviation is greater for larger δ and it is estimated based on results in [109]. From this estimation, the uncertainty of the pressure is increased in ≈ 5 % of the absolute value in runs#14–#20, and ≈ 0.7 %, 0.7 % and 1.1 % in regions 1, 2 and 3, respectively, in run#13.

Extended information regarding rarefied gas theory and the model used in this chapter can be found in the dedicated Appendix C and in references [107] (Chapter 5), [110] (Chapters 10, 11) and [109].

6.1.3 Evaluation of the gas volume

The total volume of the chamber is $V_{\text{lc}} = 27.30 \pm 0.14$ l. In order to apply the ideal gas law to each of the three regions, the volume of each of them is estimated as follows:

Table 6.4: Initial and final volumes of Pb-Li in the lower chamber during the extraction phase (determined with simulation, see Section 4.3).

Run	$V_{\mathrm{PbLi(lc)}_0}$ (l)	$V_{\mathrm{PbLi(lc)}_f}$ (l)
run#13	0.19 ± 0.01	1.42 ± 0.01
run#14	0.21 ± 0.01	1.37 ± 0.01
run#15	0.20 ± 0.02	1.39 ± 0.02
run#17	0.18 ± 0.01	1.37 ± 0.01
run#18	0.12 ± 0.01	1.34 ± 0.01
run#19	0.10 ± 0.01	1.35 ± 0.01
run#20	0.13 ± 0.01	1.34 ± 0.01

- **Region (3)**: This volume, which includes the flexible, a six-way cross and the cold trap, is calculated from its geometry, resulting in $V_3 = 9.2 \pm 0.6\,\mathrm{l}$.

- **Region (1)**: This volume correspond to half of the chamber body. Therefore, it is calculated by subtracting the volume of region (3) from the total volume, V_{lc}, and dividing it into two. It results in $V_1 = 9.1 \pm 0.3\,\mathrm{l}$. Note that $V_1 = V_2$ when there is no Pb-Li.

- **Region (2)**: The volume of the gas in this region varies throughout one experiment, since the volume of Pb-Li increases with the falling droplets. It is calculated with $V_2 = V_1 - V_{\mathrm{PbLi\ (lc)}}$, where the volume of the Pb-Li, $V_{\mathrm{PbLi\ (lc)}}$, is simulated with the code (discussed in Chapter 4) for each run. As a reference, Table 6.4 shows the initial and final volumes of Pb-Li in the lower chamber during each run.

6.1.4 Experimental validation of the method with run#20

Run#20 is performed under the same conditions as run#14 ($\approx 1000\,\mathrm{mbar}$ in the upper chamber and $\approx 0.15\,\mathrm{mbar}$ in the lower chamber), but with helium instead of D_2 in both upper and lower chambers. I.e. run#20 is a control experiment, with no gas extraction. Its experimental results are analysed to validate the plausibility of the methodology to determine the amount of D_2 extracted, which is described in this section.

Figure 6.2 shows the evolution of pressure, p, in the lower chamber (evaluated from experimental results as explained in 6.1.2) and the volume of the gas, V. At time $t = 0$, the automatic valve opens, i.e. the data before ($t < 0$) correspond to

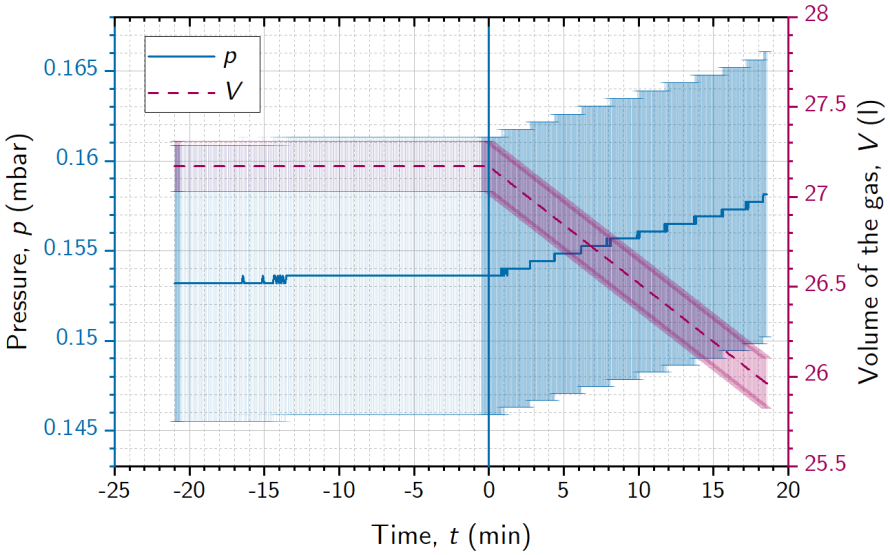

Figure 6.2: Temporal evolution of pressure and volume of helium measured in the lower chamber during the control experiment run#20. The steps in the pressure curve are due to the resolution of the vacuum sensor RP042 (4×10^{-4} mbar).

the volume and pressure of the background He with the chamber completely closed. During $t>0$, Pb-Li droplets are falling in the lower chamber, leading to a decrease of the gas volume in the chamber. The last data points shown in the graph correspond to the instant before all the Pb-Li falls and the gas from the upper chamber enters the lower chamber. The pressure increases after $t=0$ essentially due to the change in volume, since He is not absorbed by the metals (steel walls or liquid Pb-Li) and the change in temperature is very slight (T is constant in regions 1 and 3 and its variation in region 2 throughout one experiment is of $\approx 6\,\mathrm{K}$; thus, its net effect is negligible). The relative error of the pressure is $\approx\pm 5\,\%$ and the one of the volume $\approx\pm 0.5\,\%$.

Figure 6.3 shows the evolution of the gas in the chamber, determined with the methodology previously explained in Section 6.1.2. The relative uncertainty is $\approx\pm 6\,\%$. This figure shows the expected results: the amount of helium remains constant during the experiment. Therefore, it serves as a verification of the methodology. This means that the considerations taken in the calculations, as a whole (determination of pressure, temperature, volume, and division in three regions), are proved reliable to evaluate the extraction experiments in relative terms (comparing evolution over time).

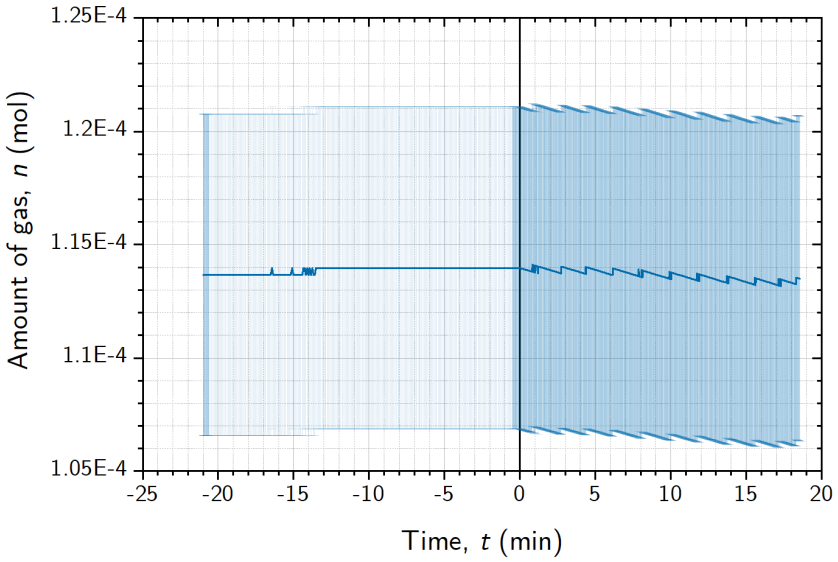

Figure 6.3: Temporal evolution of amount of helium in the lower chamber measured during the control experiment run#20.

6.2 Evaluation of D_2 extracted

6.2.1 Analysis of extraction run#13

Run#13 is the first extraction run of the experimental campaign. Figure 6.4 shows the evolution of pressure and gas volume in the lower chamber during the extraction experiment, performed at the background pressure $\sim 10^{-3}$ mbar. The four solid blue curves show the pressure measured by the vacuum sensor (p_{sensor}) and the pressure calculated for the three regions (p_1, p_2, p_3).

In this run, the lower chamber is evacuated until $t \approx -24$ min, at a constant pressure of $p \approx 1.2 - 1.6 \times 10^{-3}$ mbar (see constant p curves in Figure 6.4). At $t \approx -24$ min the chamber is closed and the background (increasing) pressure is recorded. At $t = 0$ min the automatic valve is opened and Pb-Li droplets start falling into the lower chamber. Consequently, the volume of the gas in the lower chamber (dashed curve), which is constant during the background recording ($t < 0$), decreases after $t = 0$. Additionally, the increase in pressure after $t = 0$ is greater than before ($t < 0$), due to the change in gas volume and D_2 extraction from the droplets. The temperature variation of the gas in region 2 is only $(545.0 - 538.6) \pm 9$ K, while in the other regions is constant (as explained in section 6.1.1).

Figure 6.5 shows the temporal evolution of the total amount of gas in the chamber (solid curve). The background is evaluated by performing a linear fit to the slope of the data points (with data sets of 2 min) between $-24 < t < 0$ min, which has the

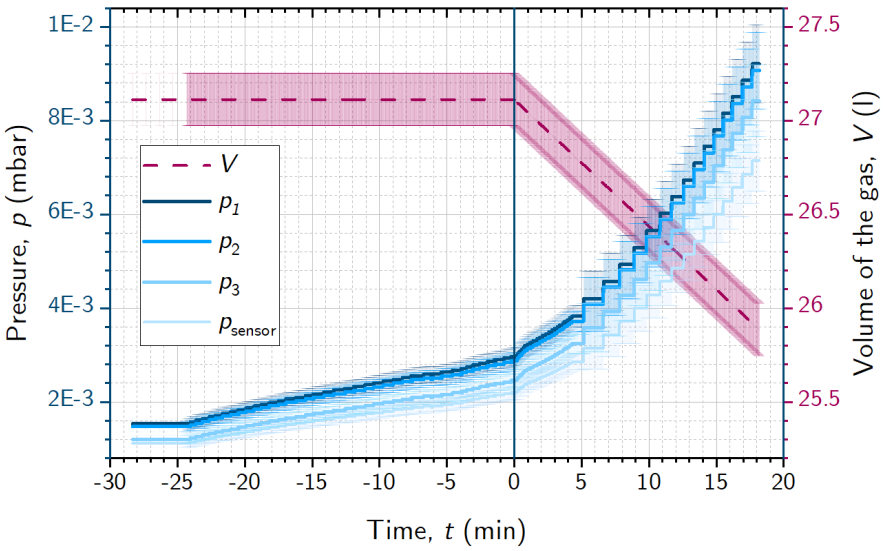

Figure 6.4: Temporal evolution of gas pressure measured at the sensor and in regions 1, 2 and 3, and gas volume in the lower chamber during extraction run#13. The steps in the pressure curve are due to the resolution of the vacuum sensor RP040 (two significant digits).

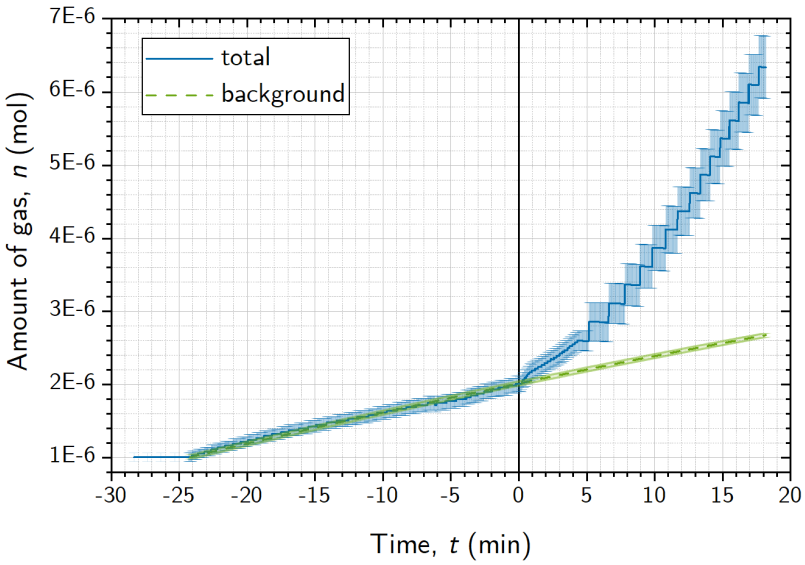

Figure 6.5: Temporal evolution of the amount of gas measured in the lower chamber during the extraction run#13 and evaluation of the background.

form:

$$\frac{\delta n}{\delta t} = -2.50 \times 10^{-10} t + 3.86 \times 10^{-8}, \tag{6.7}$$

with n in mol and t in min. The resulting background curve for run#13, shown in Figure 6.5 (dashed curve), is the integration of equation (6.7) throughout the experiment. The uncertainty assigned to the background curve is calculated with the standard deviation of the residuals, which is $\pm 2.76 \times 10^{-8}$ mol.

Subtracting the background curve from the total amount of gas, the evolution of D_2 extracted is obtained ($n_{D_2\,ext}$), which is presented in Figure 6.6. As expected, during $t<0$ the deuterium extracted equals zero and after the Pb-Li starts falling, the amount of D_2 extracted increases.

The extraction per unit volume of falling Pb-Li ($n_{D_2\,ext}/V_{PbLi}$) is also presented in Figure 6.6 (dashed curve). This is calculated dividing the extraction rate ($mol\,min^{-1}$) by the flow of Pb-Li ($l\,min^{-1}$) along the experiment (for $t>0$). $n_{D_2\,ext}/V_{PbLi}$ increases over time due to two reasons:

(i) The speed of the droplets decreases due to the reduction of the hydrostatic pressure in the upper chamber with time, as discussed in Chapter 4 (see example in Figure 4.4). Thus, the extraction time increases.

(ii) The concentration of deuterium inside the Pb-Li droplets increases due to the concentration profile in the upper chamber (concentration of deuterium is maximum at the upper layers, i.e. the last droplets).

In order to analyse the contribution of the two parameters, (i) and (ii), they must be separated. For this purpose, the results of runs #15 and #17 are needed, since they vary the speed of the droplets and concentration, respectively, while keeping the other parameter constant with respect to run#13. Nevertheless, the effect of (ii) is foreseen to be the most significant, since the variation of concentration profile is expected to be much larger than the variation in speed of the droplets.

At the end of run#13 ($t=18\,min$) the total amount of D_2 extracted is $(3.7\pm0.4)\times10^{-6}\,mol$ (see solid curve in Figure 6.6). From Table 5.7 (in the previous

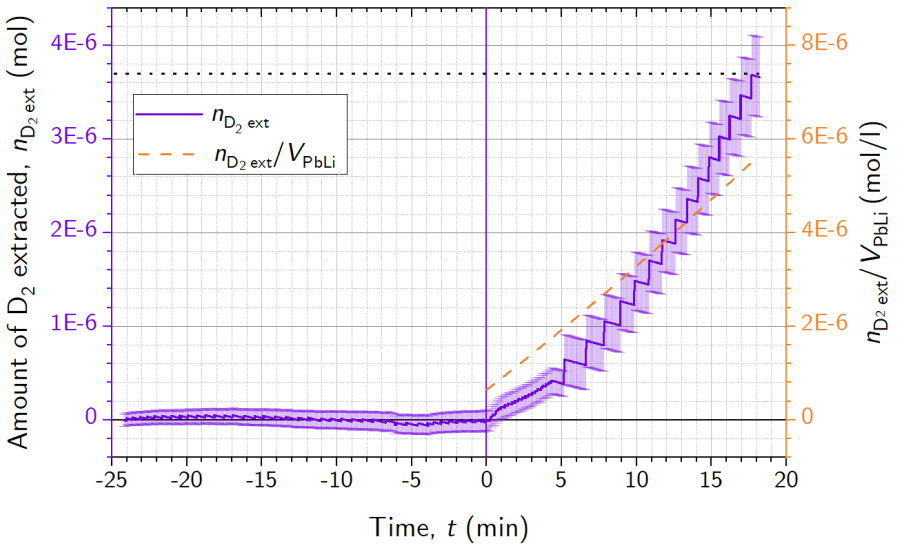

Figure 6.6: Evolution of the gas extracted in the lower chamber during run#13 (left y-axis) and amount of D_2 extracted per unit volume of Pb-Li (right y-axis).

chapter), the total amount of D_2 dissolved in run#13 is $(9.2 \pm 1.5) \times 10^{-4}$ mol. Thus, the obtained extraction efficiency over the whole experiment is 0.40 % ($\pm$ 0.08 %). This is much less than the extraction efficiency expected for only diffusion inside the droplets, $\approx 6.5 - 12.8$ % (see Table 2.1). This result gives rise to two possible explanations:

- The limiting process of deuterium extraction from the droplets is not the diffusion (or mass transfer inside the liquid phase), but the recombination at the liquid–vacuum interface (surface of the droplets).
- At the experimental conditions (high temperature, chamber previously evacuated and slow rate of gas extracted), a non-negligible amount of deuterium released from the droplets might be absorbed at the walls of the lower chamber. In this case, the measured extracted gas and, thus, the obtained efficiency is underestimated.

In order to dismiss the latter possibility, a new approach is applied in the following experiment, run#14.

6.2.2 Analysis of extraction run#14

Here, the experimental procedure is modified by inserting an initial amount of D_2 in the chamber right before recording the background. With this strategy, two objectives are targeted:

(i) The walls of the chamber are already loaded with deuterium (at the given D_2 pressure) by the time at which the extraction starts, minimizing the amount of D_2 extracted from the droplets that is lost through the walls.

(ii) The background measurement includes intrinsically the effect of the D_2 flux lost at the walls (which is expected to decrease with the loading of the walls).

The amount of deuterium initially injected in the lower chamber is set to 10 % of the total amount of deuterium dissolved. This corresponds approximately to the expected amount of gas extracted in the case that diffusion inside the droplets is the main and limiting process of the extraction. Therefore, run#14 is a repetition of run#13, but with the calculated starting partial pressure of D_2 in the chamber, $p \approx 0.15$ mbar.

Figure 6.7 shows the evolution of pressure and volume of the gas in the lower chamber during the extraction run#14. The pressure in regions 1, 2, 3 is calculated with the method explained in Section 6.1.2. Note that the uncertainty ($\approx 5\%$) is

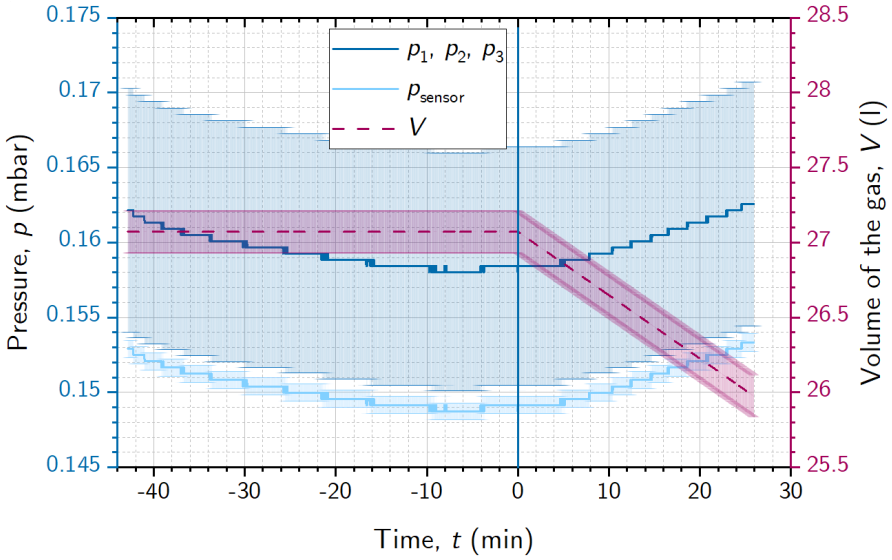

Figure 6.7: Temporal evolution of gas pressure measured at the sensor and in regions 1, 2 and 3, and gas volume in the lower chamber during the extraction run#14. The steps in the pressure curve are due to the resolution of the vacuum sensor RP042 ($4{\times}10^{-4}$ mbar).

much larger than in run#13 due to two factors: (i) the measuring vacuum sensor is different (RP042), due to the pressure operation range; and (ii), as explained in Section 6.1.2, the rarefaction parameter is in a range that increases substantially the error of the pressure evaluation.

The background pressure is measured during 40 min in order to saturate the walls and have enough data to analyse the curve. During this time, the pressure of the gas decreases due to the permeation of deuterium through the walls. At the beginning the curve is steeper and then the slope decreases gradually, due to the dissolution of the deuterium into the stainless steel. Between $-4 < t < 0$ min, the pressure increases slightly (≈ 0.002 mbar) due to some technical problems encountered with the valve opening and Pb-Li falling through the nozzle. The experiment is considered to start at $t = 0$ min, when the Pb-Li droplets fall continuously and this small jump is corrected later during the analysis. After $t = 0$ min, the volume of the gas decreases and the pressure increases due to the droplets falling and consequent D_2 extraction. This experiment ends (at $t = 26$ min) when no more droplets fall, although still a small amount of Pb-Li remains in the upper chamber (as explained in Chapter 4).

Figure 6.8 shows the evolution of amount of gas in the chamber calculated as explained in Section 6.1. The background is evaluated (in the range $-43 < t < -4$ min) following a similar methodology as in run#13. The slopes along the curve are evaluated with linear fits applied to 8 min-data sets. Then, a double exponential

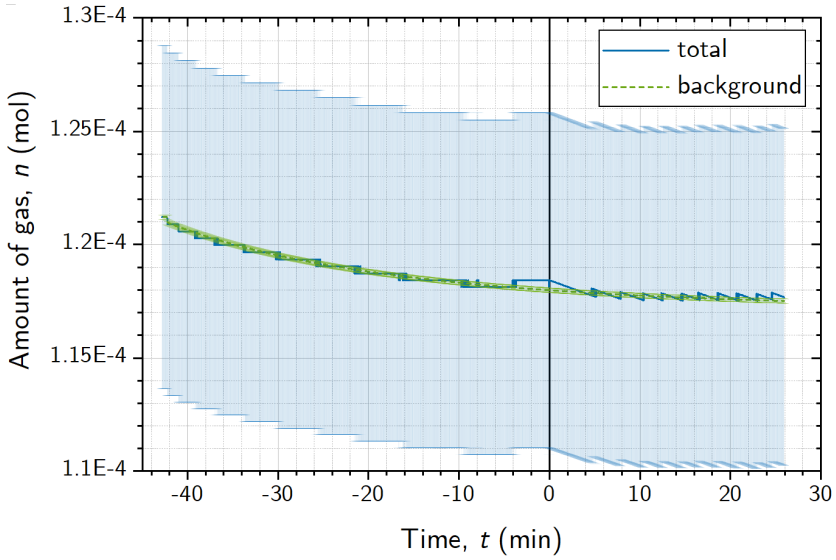

Figure 6.8: Temporal evolution of the amount of gas measured in the lower chamber during the extraction run#14 and evaluation of background.

fit is performed to the slopes, which has the form:

$$\frac{\delta n}{\delta t} = A\exp(Bt) + C\exp(Dt), \tag{6.8}$$

with $A = -1.67{\times}10^{-9}\,\mathrm{mol\,min^{-1}}$, $B = -8.35{\times}10^{-2}\,\mathrm{min^{-1}}$, $C = -2.61{\times}10^{-8}\,\mathrm{mol\,min^{-1}}$ and $D = -3.19\times10^{-2}\,\mathrm{min^{-1}}$. The resulting background curve for run#14 (dashed curve in Figure 6.8), is the integration of equation (6.8) along the experiment. The error associated to the fit is given by the standard deviation of the residuals: $\pm9.7\times10^{-8}\,\mathrm{mol}$.

Figure 6.9 shows the amount of D_2 extracted, obtained by subtracting the two curves of Figure 6.8 and correcting the jump at $t = -4\,\mathrm{min}$. As seen in the figure, no measurable amount of gas is extracted.

By comparing the uncertainty of Figure 6.9 ($\pm7.7\times10^{-6}\,\mathrm{mol}$) with the small amount of D_2 extracted in run#13 ($(3.7\pm0.4)\times10^{-6}\,\mathrm{mol}$), both results can be considered consistent.

Two main conclusions are obtained from the results of runs #13 and #14:

(i) The D_2 lost through the walls does not have an important effect on the gas accountancy for relevant amounts of deuterium extracted, since the resulting extraction efficiency is similar for the two runs (no considerably higher extraction obtained during run#14). Additionally, Figure 6.8 shows that $2.2{\times}10^{-6}\,\mathrm{mol}$ of D_2 are lost at the walls during 20 min of background measurement. This corresponds to a possible deviation of only 0.3 % (in absolute terms) in the resulting efficiency, which is negligible for accepted values of extraction efficiency.

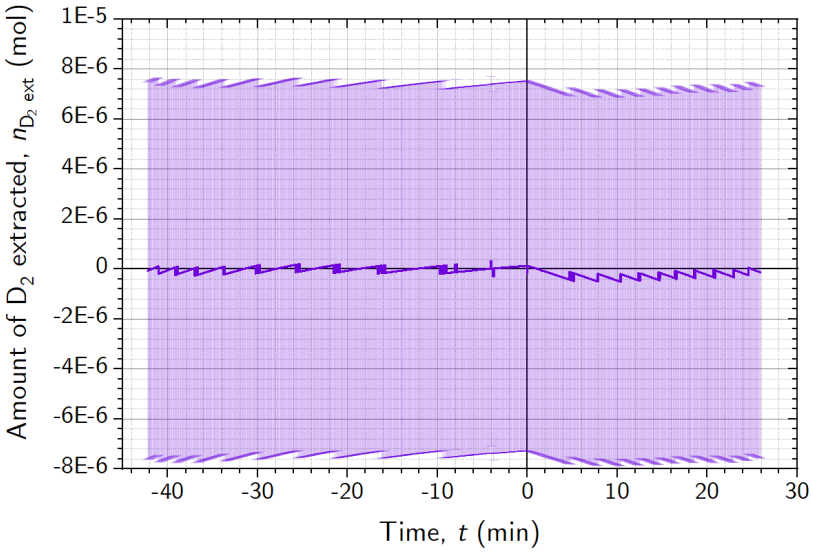

Figure 6.9: Temporal evolution of the gas extracted in the lower chamber during run#14.

(ii) The computed extraction efficiency in both runs is $\leq 1.2\%$. This maximum value is computed for a maximum extraction in run#14 equal to the uncertainty (7.7×10^{-6} mol).

The analysis of the following extraction runs (#15, #17, #18, #19) gives similar results as run#14.

6.3 Discussion on extraction efficiency

6.3.1 Comparison of the extraction efficiency with expectations

Extraction efficiency values have been obtained with a careful uncertainty evaluation and taking into account:

- Mechanical cleaning of the Pb-Li and long bake-out period before the experimental campaign to avoid oxides.
- Composition analysis before and after the experiments to check the fraction of lithium and examine the appearance of impurities.
- Careful tracking of the Pb-Li volume in both dissolution and extraction phases with simulations fitting experiments.
- Ensure periods of evacuation to unload the walls of the setup and achieve repeatability, with a dedicated vacuum test before each experiment.

– Evaluation of the deuterium dissolved in the Pb-Li with a mass balance, instead of relying on values of solubility.

– Assessment of the deuterium lost due to permeation through the stainless-steel walls of the chamber during the dissolution phase.

– Evaluation of the deviation of the pressure reading in the extraction chamber due to large gradients of temperature in molecular and transition regimes.

– Loading of the walls of the lower chamber with deuterium at the expected pressure to minimize the gas absorbed by the walls during extraction.

With all these considerations, repeatable results have been obtained. However, the resulting extraction efficiency ($< 1.2\,\%$) is much lower than the initial expectations ($\approx 6.5 - 12.8\,\%$, computed with diffusivity values [55, 56], and $\approx 78\,\%$, computed with the expected enhanced mass transfer reported by [37]).

The measured low extraction efficiency can be attributed to several reasons: (a) the diffusion coefficient of D in Pb-Li is lower than the values reported in literature; (b) the extraction model is not adequate to reproduce the mobility of the deuterium atoms inside the droplet bulk; (c) the recombination of deuterium atoms at the droplet surface is the limiting process in the extraction mechanism. These aspects are individually discussed hereafter.

(a) For an extraction efficiency of $0.4\,\%$ (as obtained during run#13), the mass transfer coefficient of deuterium in the droplets is calculated to be[1]: $5{\times}10^{-12}\,\mathrm{m^2\,s^{-1}}$. This value is three orders of magnitude lower than the diffusion coefficients reported in literature (see Table 2.1). Additionally, internal mass movement of Pb-Li inside the falling droplets is presumed, as seen with the high-speed camera that the droplets rotate and oscillate. This mass movement, which is most likely turbulent (see more information in Appendix B), increases the mass transfer of the deuterium atoms inside the droplets. Therefore, the corresponding diffusivity of deuterium in liquid Pb-Li should be even smaller than the obtained value $5{\times}10^{-12}\,\mathrm{m^2\,s^{-1}}$ (at $\approx 400\,^{\circ}\mathrm{C}$). The reason for a diffusivity lower than the values reported in the literature may originate from a different composition of the Pb-Li, since both Reiter [55] ($1.23 \times 10^{-9}\,\mathrm{m^2\,s^{-1}}$) and Edao *et al.* [56] ($5.04 \times 10^{-9}\,\mathrm{m^2\,s^{-1}}$) used higher concentrations of lithium: 16.6 at.% and 17 at.%, respectively, whereas 15.2 ± 0.2 at.% is used in the present work. Note that the diffusivity values increase with the fraction of lithium. As discussed in Section 5.6, the amount of lithium might have a substantial influence

[1] Value calculated with equation (2.3), average values of run#13: $d_d = 0.0012\,\mathrm{m}$, $h_{\mathrm{fall}} = 0.49\,\mathrm{m}$, $v_{\mathrm{n}} = 3.8\,\mathrm{m\,s^{-1}}$, and $n = 500$ (large number of terms, n, is required for accuracy at low efficiencies).

in the properties of the eutectic Pb-Li, since Li is the main responsible for the chemical activity of the alloy [65]. Therefore, further investigation is still needed into the effect of fine variations of the lithium fraction on the physical-chemical Pb-Li properties, at the concentrations of interest (eutectic mixture).

(b) The extraction model describes a substance diffusing towards the surface of a perfect sphere. Since the shape of the droplets is not perfectly spherical and changing in time, the model is taken as an approximation. It is assumed that the average path of the dissolved deuterium atoms to the surface of the droplet equals the case of a perfect sphere, since droplets have an ellipsoid shape oscillating between obleate and prolate. Under this assumption, the only effect of the oscillations in the model is an increased mobility (larger $\mathcal{D}$) due to the mass movement of the Pb-Li. In any case, the spherical shape maximises the path of a deuterium atom to the closest point of the droplet surface. This means that if the model approximation may deviate from reality, it would never overestimate the efficiency (in a bulk-controlled mechanism).

(c) Based on the results from previous work on the VST technique (which reported an enhanced mass transfer coefficient inside the droplets [37]), a bulk-controlled extraction mechanism is assumed in the approach of this study. I.e. the migration of deuterium atoms towards the droplet surface by means of diffusion has been assumed the slowest process. This assumption is also supported by the endothermic solubility of hydrogen isotopes in Pb-Li (see Figure 2.3). When the solubility of a diatomic gas in a metal has a positive enthalpy, the dissociation process at the surface of the metal is endothermic. Correspondingly, the recombination process during outgassing is exothermic, which means that it happens rapidly. Therefore, in general terms, the extraction of hydrogen dissolved in Pb-Li should be naturally a bulk-controlled process. However, since the obtained extraction efficiency is one order of magnitude lower than expected, the possibility of a surface-limited extraction process under the tested conditions must be considered.

Specific research of surface- vs bulk-controlled processes is found in the field of membrane technology, including metal–vacuum systems with diatomic gases [43, 111–115]. However, in liquid metal–vacuum systems, and more specifically Pb-Li, the research is scarce. Therefore, calculations to evaluate which is the limiting process in the present work is not possible without a big degree of uncertainty.

Shipilevsky and Glebovsky [43] showed theoretically that at low concentrations (under a critical number of dissolved monolayers), even in systems with endothermic solubility, kinetics can be limited by recombination. In the case of droplets falling in vacuum, the deuterium atoms dissolved migrate radially outwards. Then, there are two extreme options: (i) the recombination rate is very slow (thus, the process is

surface-controlled) and (ii) recombination and desorption happens very fast (then, the concentration gradient inside the bulk decreases towards the surface). In option (ii), the extraction process, which starts as bulk-controlled, can lead to a point in which it turns into surface-controlled. Supporting the explanation of a surface-controlled extraction, Kinjo *et al.* [116] performed experiments of hydrogen recovery from liquid Pb-Li with Ar/H_2 bubbling (GLC technique). They reported that at low concentrations the hydrogen transfer from the liquid to the gas phase is not in the diffusion-limiting regime.

In conclusion, two hypotheses are proposed to explain the obtained results: either the diffusivity is much lower than expected (explained by a different composition of the liquid metal) or the extraction process is surface-controlled at the experimental conditions, i.e. concentration of deuterium dissolved and temperature.

As mentioned before, the obtained extraction efficiency is much lower than the one expected from the most recent results on VST, published by Okino *et al.* in 2013 [37], wherein they reported an enhanced mass transport coefficient, $3.4 \times 10^{-7}\,\mathrm{m^2\,s^{-1}}$ (two orders of magnitude larger than the diffusivity reported by Reiter, $1.23 \times 10^{-9}\,\mathrm{m^2\,s^{-1}}$ [55]). This enhanced mass transport has increased the expectations of the VST technique, which has been foreseen to reach theoretical extraction efficiencies of 99 % for a falling height of 5 m, as shown in Table 2.1.

However, the efficiency obtained in the present work is in agreement with previous experiments reported by Okino *et al.* in 2012 [36]. They performed experiments of deuterium extraction from Pb-Li with one nozzle of 1 mm diameter under similar conditions of dissolving pressure ($10^2 - 10^3$ mbar) and temperature ($400 - 500\,^{\circ}\mathrm{C}$). The reported extraction was one order of magnitude lower than the expected one with the diffusivity reported by Reiter in [55]. Similarly, in the present work, the extraction efficiency of run#13 is 0.4 %, while the expected efficiency with the diffusivity reported by Reiter is ≈ 6.5 % (see Table 2.1). It remains unclear why a greater mass transfer was obtained in [37], where similar experimental conditions were used.

6.3.2 Application of VST to fusion

A sensitivity study based on the obtained experimental results has been conducted to evaluate whether physical parameters compensate for such a small diffusivity. For this study, a diffusion-limited extraction process with $\mathcal{D} = 5{\times}10^{-12}\,\mathrm{m^2\,s^{-1}}$ (as the above-mentioned option a) is considered. The parameters evaluated are (i) the VST chamber height, (ii) the nozzle diameter and (iii) the Pb-Li speed at the nozzle, which can be adjusted by varying the number of nozzles considering a fixed operation Pb-Li flow of the breeding blanket.

Figure 6.10 shows the extraction efficiency calculated with equation (2.3), as a function of the falling height, h_{fall}, for different droplet diameters, d_{d}.

$$\eta_{\mathrm{theo}} = 1 - \frac{6}{\pi^2} \sum_{\mathrm{n}=1}^{\infty} \frac{1}{\mathrm{n}^2} \exp\left(\frac{-4\mathcal{D}\,\mathrm{n}^2\,\pi^2\,t_{\mathrm{fall}}}{d_{\mathrm{d}}^2} \right) \tag{2.3*}$$

Note that the falling time, t_{fall}, depends on h_{fall} and the speed of the Pb-Li at the exit of the nozzles, v_{n}. To simplify the study, the calculations are done for a reference value of $v_{\mathrm{n}} = 4\,\mathrm{m\,s^{-1}}$ (solid lines in the figure) and the scenario with highest efficiency is reproduced decreasing v_{n} by one order of magnitude (shown as dashed line). The biggest droplet diameter considered (1.2 mm) is similar to d_{d} in the present experimental work. It is observed that even decreasing d_{d} by one order of magnitude ($d_{\mathrm{d}} = 0.1\,\mathrm{mm}$), the theoretical extraction efficiency does not exceed 20 % for falling heights lower than 20 m.

Additionally, Table 6.5 provides more information of the dimensions required for the scenarios depicted in Figure 6.10. The nozzle diameter, d_{n}, is calculated with equation (2.1), $d_{\mathrm{d}} \simeq 1.89\,d_{\mathrm{n}}$. The total number of nozzles, N, is determined with the Pb-Li flow reported for the breeding blanket WCLL, $956\,\mathrm{kg\,s^{-1}}$ [18] at 400 °C (with $Q = N A_{\mathrm{n}} v_{\mathrm{n}}$). The dimensioning of the diameter of the nozzle tray, d_{tray}, assumes one single circular tray with hexagonal configuration of nozzles [2], as used

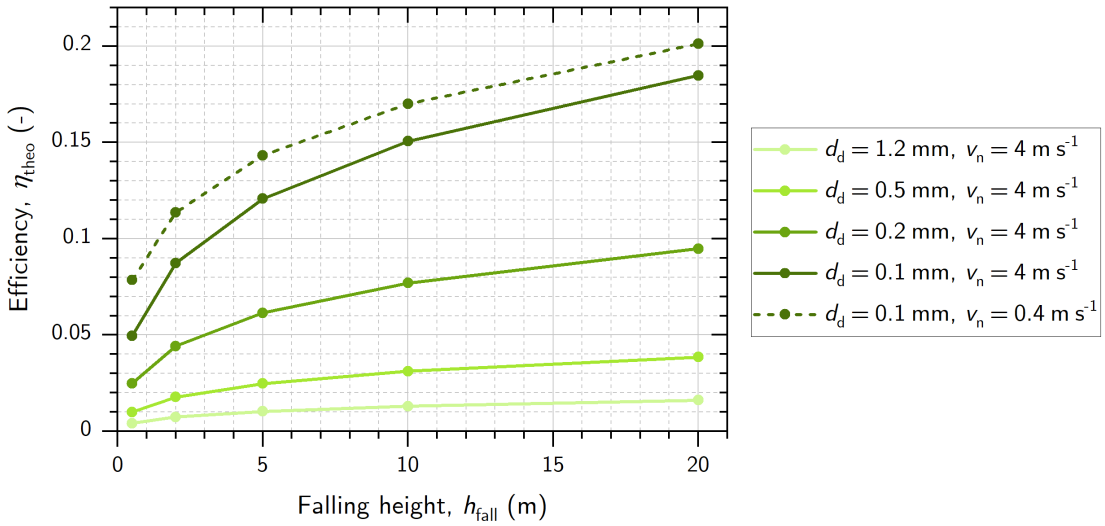

Figure 6.10: Extraction efficiency calculated with equation (2.3) and $\mathcal{D} = 5 \times 10^{-12}\,\mathrm{m^2\,s^{-1}}$ as a function of the falling height (h_{fall}) and droplet diameter (d_{d}). Solid lines represent cases calculated with speed at the exit of the nozzle $v_{\mathrm{n}} = 4\,\mathrm{m\,s^{-1}}$ and dashed line, $v_{\mathrm{n}} = 0.4\,\mathrm{m\,s^{-1}}$.

[2] For the dimensioning of the tray, the number of hexagons, N_{hex}, is calculated with the number of nozzles, N, as follows: $N = 3\,N_{\mathrm{hex}}^2 + 3\,N_{\mathrm{hex}} + 1$.

Table 6.5: Droplet diameter (d_d), nozzle diameter (d_n), speed at the nozzle (v_n), total number of nozzles (N) and diameter of the nozzle tray (d_tray), corresponding to the five cases depicted in Figure 6.10, calculated for a Pb-Li flow of $956\,\mathrm{kg\,s^{-1}}$ (WCLL [18]).

d_d (mm)	d_n (mm)	v_n ($\mathrm{m\,s^{-1}}$)	N (nozzles)	d_tray (m)
1.2	0.6	4	77,663	3.2
0.5	0.3	4	447,337	7.7
0.2	0.1	4	2,795,857	19.3
0.1	0.05	4	11,183,427	38.6
0.1	0.05	0.4	111,834,272	122.1

in reference [39], with a distance between nozzles of 10 mm. The last two rows presented in Table 6.5 (with $d_\mathrm{d} = 0.1\,\mathrm{mm}$) correspond to the two highest extraction efficiencies depicted in Figure 6.10. They show that, in addition to $h_\mathrm{fall} \approx 20\,\mathrm{m}$, 0.05 mm-diameter nozzles and a sieve tray diameter of $38.6 - 122.1\,\mathrm{m}$ are needed to achieve extraction efficiency values close to 20 %. Given this low value, various stages need to be considered to achieve the requirements of DEMO ($\geq 80\,\%$ [12, 25]). In the case of $d_\mathrm{d} = 0.1\,\mathrm{mm}$, $v_\mathrm{n} = 4\,\mathrm{m\,s^{-1}}$, $h_\mathrm{fall} = 20\,\mathrm{m}$ and $d_\mathrm{tray} = 38.6\,\mathrm{m}$, the theoretical efficiency of one stage is about $\eta_\mathrm{theo} = 18.5\,\%$ (see darkest solid curve in Figure 6.10). In this case, eight stages are required to reach a net extraction efficiency of 80.5 % and match the requirements of DEMO.

As mentioned before, this scaling-up study is based on the assumption that the extraction process of the present experimental results is diffusion-limited (the above-mentioned option a). If, on the contrary, the extraction process is surface-limited (option c), more investigation is needed to understand under which conditions (i.e. concentration of deuterium, temperature of the Pb-Li, size of the droplets, pressure at the vacuum phase) the extraction process changes to a bulk-controlled regime. Because, only in this regime the advantage of a possible mass transfer enhancement due to Pb-Li movement can be profited and the VST extraction technique could be promising for DEMO.

Chapter 7

Conclusions and perspectives

The European Demonstration power plant (DEMO) needs a Tritium Extraction and Removal System (TERS) with high extraction efficiency ($\geq 80\,\%$) to recover the tritium produced in the Breeding Blanket (BB) in order to limit the tritium losses to the structure and to maximise the availability of the tritium produced. However, to the best knowledge of the author, there are very few works in the European fusion community that have experimentally studied the extraction of hydrogen isotopes from Pb-Li. One of the main reasons is the complications that are intrinsic to an experimental setup operating with liquid Pb-Li (in addition to hydrogen isotopes). I.e. the compatibility of materials due to the corrosive properties of the liquid metal and the high temperatures required, which also increase the permeation of hydrogen through the metal structural materials. Furthermore, the solubility of hydrogen isotopes in Pb-Li is practically unknown, since literature shows two orders of magnitude of scattered values, which adds considerable uncertainties in the design of the experimental setups and analysis of the results. This whole picture complicates substantially the quantification of hydrogen dissolved in the liquid metal, which is needed for the experimental research of the TERS technologies. Previous results on Vacuum Sieve Tray (VST) showed an enhanced mobility of deuterium leaving the Pb-Li droplets, which was attributed to the oscillation of their shape [37, 38]. According to these data, extraction efficiencies above 80 % are expected with a compact setup [39], making the VST technique a promising candidate for DEMO.

During the present work, an experimental VST facility operated with deuterium is assembled and qualified. This setup consists of two main chambers: an upper chamber, where the dissolution of D_2 is established (at 500 to 1000 mbar), and a lower chamber to extract D_2 from the falling droplets under vacuum (≤ 0.15 mbar). The functionality of the setup to perform experiments of dissolution and extraction is demonstrated.

A code to simulate the fluid dynamics of a VST extraction experiment (e.g. evo-

lution of Pb-Li volume in both chambers, falling time of the droplets) is developed in MATLAB. The code is validated using image analysis of the falling droplets recorded with a high-speed camera. Experimental data (from Pb-Li level thermocouples and the total duration of the Pb-Li falling) are used to fit each run with the simulations and, with this, to obtain an accurate accountancy of the Pb-Li volume in the upper and lower chambers.

The existence of a liquid jet at the outlet of the nozzle is observed with a high-speed camera, which confirms that the droplet formation occurs in the Plateau-Rayleigh instability regime. In addition, shape oscillations of the droplets, at $\approx$ 170 Hz, are observed as predicted by the Plateau-Rayleigh theory. Image analysis of the droplets with ImageJ is used to measure the diameter of the droplets and their falling speed. The average diameter of the droplets is 6 % larger than the one predicted by the Plateau-Rayleigh theory, which is explained by the coalescence of some droplets along their falling path. The measured speed is in agreement with the simulations.

For the dissolution of deuterium into the Pb-Li in the upper chamber, a static method is pursued relying on the Sieverts' law. The amount of deuterium dissolved is determined with a mass balance evaluated at the time at which steady state for dissolution into the Pb-Li is achieved ($\approx$ 22 h). The measured amount of deuterium dissolved into the Pb-Li is $(8.9 \pm 1.5) \times 10^{-4}$ and $(4.4 \pm 1.4) \times 10^{-4}$ mol of D_2 for dissolving pressures of 1000 and 500 mbar, respectively. The average concentration of atomic deuterium dissolved in the Pb-Li, at the same dissolving pressures, is $(1.5 \pm 0.3) \times 10^{-3}$ and $(7 \pm 2) \times 10^{-4}$ $\mathrm{mol_D\,l^{-1}}$. These results are coherent with Sieverts' law and are in the same range as the solubility values given by Edao *et al.* and Chan *et al.* [56, 75]. The obtained values of solubility are determined taking into account deuterium permeation through the walls of the chamber (often not considered in the literature) and for a known composition of Pb-Li (15.2 ± 0.2 at.% Li).

The extraction experiments are performed with one nozzle of 0.6 mm diameter and a falling height of ≈ 0.5 m. The total amount of D_2 extracted is lower than 8×10^{-6} mol for each of all six experiments. The obtained extraction efficiency is ≤ 1.2 %, which is around one order of magnitude lower than the expected efficiency relying on diffusion of deuterium towards the surface of the droplets (i.e. without enhanced mobility due to oscillation of the droplets).

Using the diffusion-limited model, such low extraction efficiencies suggest that the mass transfer coefficient responsible for the mobility of deuterium towards the droplet surface is only about 5×10^{-12} $\mathrm{m^2\,s^{-1}}$. In this case, the diffusion coefficient must be more than three orders of magnitude smaller than the values reported by

Reiter and Edao *et al.* [55, 56].

Another explanation for the low extraction efficiency is that the limiting process of the extraction is not the migration of atoms towards the surface of the droplets, but their recombination at the interface. Theoretical and experimental works have demonstrated that at low concentrations, it is possible that the outgassing of hydrogen from the liquid Pb-Li can be surface-limited [43, 116].

A sensitivity analysis of the VST dimensioning parameters is conducted based on the obtained extraction results and assuming a diffusion-limited model. It shows that, for the Pb-Li flow of the breeding blanket WCLL ($956\,\mathrm{kg\,s^{-1}}$ [13]), eight stages with VST towers of 20 m height and 38.6 m diameter (with 10^7 nozzles of 0.05 mm diameter) are needed to reach an extraction efficiency exceeding 80 %.

Further research is required on the interaction of hydrogen isotopes with Pb-Li. This includes the dependency of solubility and diffusivity on the composition of the alloy, i.e. atomic fraction of lithium and presence of impurities. If the properties of eutectic Pb-Li are highly sensitive to its composition (which could be one explanation for the huge scattering in solubility values), it could be possible that the obtained extraction results (limited by a low mass-transfer coefficient, $\approx 5{\times}10^{-12}\,\mathrm{m^2\,s^{-1}}$) may be improved by e.g. varying the fraction of Li. This research is essential, not only in regard to VST as tritium extraction technique, but also in the prospect of eutectic Pb-Li as tritium breeder for DEMO. If the presence of impurities, or small changes in the ratio of lithium, produce drastic variations in the properties of the liquid metal, it may be challenging to control its chemistry with the Pb-Li purification system planned for EU-DEMO [13].

Moreover, further investigation is needed into the outgassing process of hydrogen from Pb-Li at the low concentrations expected in the breeder $\approx 2{\times}10^{-5}\,\mathrm{mol_T\,l^{-1}}$ [16] and the conditions under which the extraction process is limited by diffusion or recombination. This is crucial for the development of TERS techniques relying on mass transport through an interface, such as VST (liquid–vacuum), GLC (liquid–gas and recovery from the carrier gas) or PAV (liquid–solid–vacuum).

Bibliography

[1] Rosman, K. J. R. & Taylor, P. D. P. Isotopic compositions of the elements 1997 (Technical Report). *Pure and Applied Chemistry* **70,** 217–235. doi:10.1351/pac199870010217 (1998).

[2] Tanabe, T. *Tritium: Fuel of Fusion Reactors.* 1st ed. ISBN: 978-4-431-56458-4 (Springer, Tokyo, 2017).

[3] Kovari, M., Coleman, M., Cristescu, I. & Smith, R. Tritium resources available for fusion reactors. *Nuclear Fusion* **58,** 026010. doi:10.1088/1741-4326/aa9d25 (2018).

[4] Abdou, M. *Overview of the Tritium Fuel Cycle and Conditions for Tritium Fuel Self- Sufficiency and Other Tritium Issues* (4th IAEA DEMO Programme Workshop, Karlsruhe, Germany, 2016). https://nucleus.iaea.org/sites/fusionportal/Technical%20Meeting%20Proceedings/4th%20DEMO/website/talks/November%2015%20Sessions/Abdou.pdf. Last accessed on 08/07/2021.

[5] *European Research Roadmap to the Realisation of Fusion Energy* (EUROfusion, 2018). https://www.euro-fusion.org/eurofusion/roadmap/. Last accessed on 08/07/2021.

[6] Atzeni, S. & Meyer-ter-Vehn, J. *The Physics of Inertial Fusion: Beam Plasma Interaction, Hydrodynamics, Hot Dense Matter.* 1st ed. ISBN: 0-19-856264-0 (Oxford University Press, New York, 2004).

[7] Tosti, S. & Ghirelli, N. *Tritium in Fusion: Production, Uses and Environmental Impact.* 1st ed. ISBN: 978-1-62417-270-0 (Nova Science Publishers Inc., New York, 2013).

[8] Jacobs, D. G. *Sources of tritium and its behaviour upon release to the environment. AEC Critical Review Series.* TID-24635 (Oak Ridge National Laboratory, Tennessee, 1968). doi:10.2172/4799828.

[9] Giegerich, T., Battes, K., Schwenzer, J. C. & Day, C. Development of a viable route for lithium-6 supply of DEMO and future fusion power plants. *Fusion Engineering and Design* **149,** 111339. doi:10.1016/j.fusengdes.2019.111339 (2019).

[10] Raffray, A. R., Akiba, M., Chuyanov, V., Giancarli, L. & Malang, S. Breeding blanket concepts for fusion and materials requirements. *Journal of Nuclear Materials* **307-311,** 21–30. doi:10.1016/S0022-3115(02)01174-1 (2002).

[11] Boccaccini, L. V., Giancarli, L., Janeschitz, G., Hermsmeyer, S., Poitevin, Y., Cardella, A. & Diegele, E. Materials and design of the European DEMO blankets. *Journal of Nuclear Materials. Proceedings of the 11th International Conference on Fusion Reactor Materials (ICFRM-11) Kyoto, Japan 7-12 December 2003* **329-333,** 148–155. doi:10.1016/j.jnucmat.2004.04.125 (2004).

[12] Cismondi, F., Spagnuolo, G. A., Boccaccini, L. V., Chiovaro, P., Ciattaglia, S., Cristescu, I., Day, C., Del Nevo, A., Di Maio, P. A., Federici, G., *et al.* Progress of the conceptual design of the European DEMO breeding blanket, tritium extraction and coolant purification systems. *Fusion Engineering and Design* **157,** 111640. doi:10.1016/j.fusengdes.2020.111640 (2020).

[13] Utili, M., Bassini, S., Boccaccini, L. V., Bühler, L., Cismondi, F., Del Nevo, A., Eboli, M., DiFonzo, F., Hernandez, T., Wulf, S., *et al.* Status of Pb-16Li technologies for European DEMO fusion reactor. *Fusion Engineering and Design* **146,** 2676–2681. doi:10.1016/j.fusengdes.2019.04.083 (2019).

[14] Cismondi, F., Boccaccini, L. V., Aiello, G., Aubert, J., Bachmann, C., Barrett, T., Barucca, L., Bubelis, E., Ciattaglia, S., Del Nevo, A., *et al.* Progress in EU Breeding Blanket design and integration. *Fusion Engineering and Design* **136,** 782–792. doi:10.1016/j.fusengdes.2018.04.009 (2018).

[15] Aiello, G., Aubert, J., Jonqueres, N., Li Puma, A., Morin, A. & Rampal, G. Development of the Helium Cooled Lithium Lead blanket for DEMO. *Fusion Engineering and Design. Proceedings of the 11th International Symposium on Fusion Nuclear Technology-11 (ISFNT-11) Barcelona, Spain, 15-20 September 2013* **89,** 1444–1450. doi:10.1016/j.fusengdes.2013.12.036 (2014).

[16] Farabolini, W. *et al.* Tritium control modelling for a helium cooled lithium–lead blanket of a fusion power reactor. *Fusion Engineering and Design* **81,** 753–762. doi:10.1016/j.fusengdes.2005.07.018 (2006).

[17] Del Nevo, A., Arena, P., Caruso, G., Chiovaro, P., Di Maio, P., Eboli, M., Edemetti, F., Forgione, N., Forte, R., Froio, A., *et al.* Recent progress in developing a feasible and integrated conceptual design of the WCLL BB in EUROfusion project. *Fusion Engineering and Design* **146,** 1805–1809. doi:10.1016/j.fusengdes.2019.03.040 (2019).

[18] Del Nevo, A., Martelli, E., Agostini, P., Arena, P., Bongiovi, G., Caruso, G., Di Gironimo, G., Di Maio, P. A., Eboli, M., Giammusso, R., *et al.* WCLL breeding blanket design and integration for DEMO 2015: status and perspectives. *Fusion Engineering and Design. Proceedings of the 29th Symposium on Fusion Technology (SOFT-29) Prague, Czech Republic, September 5-9 2016* **124,** 682–686. doi:10.1016/j.fusengdes.2017.03.020 (2017).

[19] Garcinuño, B., Rapisarda, D., Antunes, R., Utili, M., Fernández-Berceruelo, I., Sanz, J. & Ibarra, A. The tritium extraction and removal system for the DCLL-DEMO fusion reactor. *Nuclear Fusion* **58,** 095002. doi:10.1088/1741-4326/aacb89 (2018).

[20] Rapisarda, D., Fernandez, I., Palermo, I., Gonzalez, M., Moreno, C., Ibarra, A. & Mas de les Valls, E. Conceptual Design of the EU-DEMO Dual Coolant Lithium Lead Equatorial Module. *IEEE Transactions on Plasma Science* **44,** 1603–1612. doi:10.1109/TPS.2016.2561204 (2016).

[21] Urgorri, F. R., Moreno, C., Carella, E., Castellanos, J., Del Nevo, A. & Ibarra, A. Preliminary System Modeling for the EUROfusion Water Cooled Lithium Lead Blanket. *Fusion Science and Technology* **71,** 444–449. doi:10.1080/15361055.2016.1273712 (2017).

[22] Federici, G., Boccaccini, L. V., Cismondi, F., Gasparotto, M., Poitevin, Y. & Ricapito, I. An overview of the EU breeding blanket design strategy as an integral part of the DEMO design effort. *Fusion Engineering and Design* **141,** 30–42. doi:10.1016/j.fusengdes.2019.01.141 (2019).

[23] Utili, M., Ciampichetti, A., Aiello, A., Ricapito, I., Agostini, P., Desideri, F. & Liger, K. Design of a multipurpose laboratory scale apparatus for the investigation of hydrogen isotopes in PbLi and permeation technologies. *Fusion Engineering and Design* **87,** 1342–1346. doi:10.1016/j.fusengdes.2012.03.013 (2012).

[24] Pozio, A., Carewska, M., Santucci, A. & Tosti, S. Behaviour of hydrogenated lead–lithium alloy. *International Journal of Hydrogen Energy* **42,** 1053–1062. doi:10.1016/j.ijhydene.2016.08.166 (2017).

[25] Demange, D., Boccaccini, L. V., Franza, F., Santucci, A., Tosti, S. & Wagner, R. Tritium management and anti-permeation strategies for three different breeding blanket options foreseen for the European Power Plant Physics and Technology Demonstration reactor study. *Fusion Engineering and Design. Proceedings of the 11th International Symposium on Fusion Nuclear Technology-11 (ISFNT-11) Barcelona, Spain, 15-20 September 2013* **89,** 1219–1222. doi:10.1016/j.fusengdes.2014.04.028 (2014).

[26] D'Auria, V., Dulla, S., Ravetto, P., Savoldi, L., Utili, M. & Zanino, R. Tritium Extraction from Lithium-Lead in the EU DEMO Blanket Using Permeator Against Vacuum. *Fusion Science and Technology* **71,** 537–543. doi:10.1080/15361055.2017.1291252 (2017).

[27] Garcinuño, B., Rapisarda, D., Fernández-Berceruelo, I., Jiménez-Rey, D., Sanz, J., Moreno, C., Palermo, I. & Ibarra, A. Design and fabrication of a Permeator Against Vacuum prototype for small scale testing at Lead-Lithium facility. *Fusion Engineering and Design* **124,** 871–875. doi:10.1016/j.fusengdes.2017.02.060 (2017).

[28] Alpy, N., Terlain, A. & Lorentz, V. Hydrogen extraction from Pb–17Li: results with a 800 mm high packed column. *Fusion Engineering and Design* **49-50,** 775–780. doi:10.1016/S0920-3796(00)00461-0 (2000).

[29] Utili, M., Aiello, A., Laffi, L., Malavasi, A. & Ricapito, I. Investigation on efficiency of gas liquid contactor used as tritium extraction unit for HCLL-TBM Pb-16Li loop. *Fusion Engineering and Design. Proceedings of the 12th International Symposium on Fusion Nuclear Technology (ISFNT-12) Jeju Island, Korea, 14-18 September 2015* **109-111,** 1–6. doi:10.1016/j.fusengdes.2016.03.067 (2016).

[30] Ricapito, I., Calderoni, P., Poitevin, Y., Aiello, A., Utili, M. & Demange, D. Tritium Processing for the European Test Blanket Systems: Current Status of the Design and Development Strategy. *Fusion Science and Technology* **67,** 543–546. doi:10.13182/FST14-T75 (2015).

[31] Gräbner, H., Feuerstein, H. & Oschinski, J. Compatibility of metals and alloys in liquid Pb-17Li at temperatures up to 650 °C. *Journal of Nuclear Materials* **155-157,** 702–704. doi:10.1016/0022-3115(88)90399-6 (1988).

[32] Feuerstein, H., Gräbner, H. & Horn, S. Extraction of tritium from molten Pb-17Li by use of solid getters. *Fusion Technology 1990. Proceedings of the 16th Symposium on Fusion Technology, London, U.K., 3-7 September 1990* 646–649. doi:10.1016/B978-0-444-88508-1.50113-4 (1991).

[33] Feuerstein, H., Gräbner, H., Oschinski, J., Beyer, J., Horn, S., Hörner, L. & Santo, K. *Compatibility of 31 Metals, Alloys and Coatings with Static Pb-17Li Eutectic Mixture.* FZKA–5596 (Forschungszentrum Karlsruhe GmbH Technik und Umwelt, Germany, 1995). doi:10.5445/IR/270038128.

[34] Reimann, J. & Feuerstein, H. Gettering and/or cold trapping for tritium recovery from a self-cooled Pb-17Li blanket. *Fusion Technology 1990. Proceedings of the 16th Symposium on Fusion Technology, London, U.K., 3–7 September 1990.* 752–756. doi:10.1016/B978-0-444-88508-1.50135-3 (1991).

[35] Donohue, M. L. & Price, M. E. *Mirror Advanced Reactor Study (MARS). Final report. Volume 1-B. Commercial fusion electric plant* UCRL-53480-Vol.1B (Lawrence Livermore National Lab., CA (USA), 1984). doi:10.2172/6332189.

[36] Okino, F., Noborio, K., Yamamoto, Y. & Konishi, S. Vacuum sieve tray for tritium extraction from liquid Pb–17Li. *Fusion Engineering and Design. 10th International Symposium on Fusion Nuclear Technology (ISFNT-10) Portland, Oregon, USA, 11-16 September 2011* **87,** 1014–1018. doi:10.1016/j.fusengdes.2012.02.071 (2012).

[37] Okino, F., Noborio, K., Kasada, R. & Konishi, S. Enhanced Mass Transfer of Deuterium Extracted from Falling Liquid Pb-17Li Droplets. *Fusion Science and Technology* **64,** 543–548. doi:10.13182/FST12-546 (2013).

[38] Okino, F., Noborio, K., Kasada, R. & Konishi, S. Deuterium Transport Prediction in Oscillating Liquid Pb-17Li Droplet. *Fusion Science and Technology* **64,** 549–551. doi:10.13182/FST13-A19151 (2013).

[39] Mertens, M. A. J., Demange, D. & Frances, L. Model and simulation of a vacuum sieve tray for T extraction from liquid PbLi breeding blankets. *Fusion Engineering and Design* **112,** 541–547. doi:10.1016/j.fusengdes.2016.05.038 (2016).

[40] Strutt, J. W. On the capillary phenomena of jets. *Proceedings of the Royal Society of London* **29,** 71–97. doi:10.1098/rspl.1879.0015 (1879).

[41] Rapp, B. E. *Microfluidics: Modeling, Mechanics and Mathematics.* 1st ed. ISBN: 978-1455731411 (William Andrew, Elsevier, Oxford, 2016).

[42] Lamb, H. *Hydrodynamics.* 6th ed. ISBN: 978-0-486-60256-1 (Dover Publications Inc., New York, 2009).

[43] Shipilevsky, B. M. & Glebovsky, V. G. Competition of bulk and surface processes in the kinetics of hydrogen and nitrogen evolution from metals into vacuum. *Surface Science* **216,** 509–527. doi:10.1016/0039-6028(89)90392-0 (1989).

[44] Kumar, A. & Hartland, S. Correlations for prediction of mass transfer coefficients in single drop systems and liquid–liquid extraction columns. *Chemical Engineering Research and Design* **77,** 372–384. doi:10.1205/026387699526359 (1999).

[45] Crank, J. *The Mathematics of Diffusion.* 2nd ed. ISBN: 0-19-853344-6 (Oxford University Press, London, 1975).

[46] Kronig, R. & Brink, J. C. On the theory of extraction from falling droplets. *Applied Scientific Research* **2,** 142. doi:10.1007/BF00411978 (1951).

[47] Handlos, A. E. & Baron, T. Mass and heat transfer from drops in liquid-liquid extraction. *AIChE Journal* **3,** 127–136. doi:10.1002/aic.690030121 (1957).

[48] Rose, P. M. & Kintner, R. C. Mass transfer from large oscillating drops. *AIChE Journal* **12,** 530–534. doi:10.1002/aic.690120325 (1966).

[49] Angelo, J. B., Lightfoot, E. N. & Howard, D. W. Generalization of the penetration theory for surface stretch: Application to forming and oscillating drops. *AIChE Journal* **12,** 751–760. doi:10.1002/aic.690120423 (1966).

[50] Calderbank, P. H. & Korchinski, I. J. O. Circulation in liquid drops: (A heat-transfer study). *Chemical Engineering Science* **6,** 65–78. doi:10.1016/0009-2509(56)80012-2 (1956).

[51] Johnson, A. I. & Hamielec, A. E. Mass transfer inside drops. *AIChE Journal* **6,** 145–149. doi:10.1002/aic.690060128 (1960).

[52] Licht, W. & Pansing, W. F. Solute transfer from single drops in liquid-liquid extraction. *Industrial and Engineering Chemistry* **45,** 1885–1896. doi:10.1021/ie50525a023 (1953).

[53] Skelland, A. H. P. & Wellek, R. M. Resistance to mass transfer inside droplets. *AIChE Journal* **10,** 491–496. doi:10.1002/aic.690100416 (1964).

[54] Heertjes, P. M., Holve, W. A. & Talsma, H. Mass transfer between isobutanol and water in a spray-column. *Chemical Engineering Science* **3,** 122–142. doi:10.1016/0009-2509(54)80017-0 (1954).

[55] Reiter, F. Solubility and diffusivity of hydrogen isotopes in liquid Pb-17Li. *Fusion Engineering and Design* **14,** 207–211. doi:10.1016/0920-3796(91)90003-9 (1991).

[56] Edao, Y., Noguchi, H. & Fukada, S. Experiments of hydrogen isotope permeation, diffusion and dissolution in Li–Pb. *Journal of Nuclear Materials. Proceedings of 14th International Conference on Fusion Reactor Materials (ICFRM-14) Sapporo, Japan, 10-11 September 2009* **417,** 723–726. doi:10.1016/j.jnucmat.2010.12.126 (2011).

[57] Carr, E. J. Characteristic time scales for diffusion processes through layers and across interfaces. *Physical Review E* **97,** 042115. doi:10.1103/PhysRevE.97.042115 (2018).

[58] Lee, S. K., Yun, S.-H., Joo, H. G. & Noh, S. J. Deuterium transport and isotope effects in type 316L stainless steel at high temperatures for nuclear fusion and nuclear hydrogen technology applications. *Current Applied Physics* **14,** 1385–1388. doi:10.1016/j.cap.2014.08.006 (2014).

[59] Shiraishi, T., Nishikawa, M., Yamaguchi, T. & Kenmotsu, K. Permeation of multi-component hydrogen isotopes through austenitic stainless steels. *Journal of Nuclear Materials* **273,** 60–65. doi:10.1016/S0022-3115(99)00018-5 (1999).

[60] Xiukui, S., Jian, X. & Yiyi, L. Hydrogen permeation behaviour in austenitic stainless steels. *Materials Science and Engineering: A* **114,** 179–187. doi:10.1016/0921-5093(89)90857-5 (1989).

[61] Forcey, K. S., Ross, D. K., Simpson, J. C. B. & Evans, D. S. Hydrogen transport and solubility in 316L and 1.4914 steels for fusion reactor applications. *Journal of Nuclear Materials* **160,** 117–124. doi:10.1016/0022-3115(88)90038-4 (1988).

[62] Kishimoto, N., Tanabe, T., Suzuki, T. & Yoshida, H. Hydrogen diffusion and solution at high temperatures in 316L stainless steel and nickel-base heat-resistant alloys. *Journal of Nuclear Materials* **127,** 1–9. doi:10.1016/0022-3115(85)90056-X (1985).

[63] Pascual, L., Barrena, M. I., De Salazar, J. M. G., Soria, A., Fernandez, M., Conde, E. & Quinones, J. Production of different eutectic Pb-Li alloys in Spain. *Fusion Eng. Des.* **89,** 1269–1273. doi:10.1016/j.fusengdes.2014.03.062 (2014).

[64] Hubberstey, P., Sample, T. & Barker, M. G. Is Pb-17Li really the eutectic alloy? A redetermination of the lead-rich section of the Pb-Li phase diagram ($0.0 < x_{\mathrm{Li}}(\mathrm{at.}\%) < 22.1$). *Journal of Nuclear Materials* **191-194.** Special issue *Fusion Reactor Materials Part A*, 283–287. doi:10.1016/S0022-3115(09)80051-2 (1992).

[65] Mas de les Valls, E., Sedano, L. A., Batet, L., Ricapito, I., Aiello, A., Gastaldi, O. & Gabriel, F. Lead–lithium eutectic material database for nuclear fusion technology. *Journal of Nuclear Materials* **376,** 353–357. doi:10.1016/j.jnucmat.2008.02.016 (2008).

[66] Schulz, B. Thermophysical properties of the Li(17)Pb(83)alloy. *Fusion Engineering and Design* **14,** 199–205. doi:10.1016/0920-3796(91)90002-8 (1991).

[67] Terai, T., Nagai, S., Yoneoka, T. & Takahashi, Y. Diffusion coefficient of tritium in molten lithium-lead alloy ($Li_{17}Pb_{83}$) under neutron irradiation at elevated temperatures. *Journal of Nuclear Materials* **187,** 247–253. doi:10.1016/0022-3115(92)90504-E (1992).

[68] Fauvet, P. & Sannier, J. Hydrogen behaviour in liquid 17Li83Pb alloy. *Journal of Nuclear Materials* **155,** 516–519. doi:10.1016/0022-3115(88)90301-7 (1988).

[69] Shibuya, Y., Aida, M., Fujii, Y. & Okamoto, M. Isothermal release of tritium from neutron-irradiated Li17Pb83. *Journal of Nuclear Materials* **150,** 286–291. doi:10.1016/0022-3115(87)90006-7 (1987).

[70] Maeda, Y., Edao, Y., Yamaguchi, S. & Fukada, S. Solubility, diffusivity, and isotopic exchange rate of hydrogen isotopes in Li-Pb. *Fusion Science and Technology* **54,** 131–134. doi:10.13182/FST54-131 (2008).

[71] Okitsu, H., Edao, Y., Okada, M. & Fukada, S. Analysis of diffusion and dissolution of two-component hydrogen (H+D) in lead lithium. *Fusion Engineering and Design* **87,** 1324–1328. doi:10.1016/j.fusengdes.2012.03.004 (2012).

[72] Katsuta, H. *et al.* Hydrogen solubility in liquid Li17Pb83. *Journal of Nuclear Materials* **133-134,** 167–170. doi:10.1016/0022-3115(85)90127-8 (1985).

[73] Aiello, A., Ciampichetti, A. & Benamati, G. Determination of hydrogen solubility in lead lithium using sole device. *Fusion Engineering and Design* **81,** 639–644. doi:10.1016/j.fusengdes.2005.06.364 (2006).

[74] Wu, C. The solubility of deuterium in lithium-lead alloys. *Journal of Nuclear Materials* **114,** 30–33. doi:10.1016/0022-3115(83)90069-7 (1983).

[75] Chan, Y. C. & Veleckis, E. A thermodynamic investigation of dilute solutions of hydrogen in liquid Li-Pb alloys. *Journal of Nuclear Materials* **123,** 935–940. doi:10.1016/0022-3115(84)90198-3 (1984).

[76] Ciampichetti, A., Zucchetti, M., Ricapito, I., Utili, M., Aiello, A. & Benamati, G. Performance of a hydrogen sensor in Pb–16Li. *Journal of Nuclear Materials. Proceedings of the 12th International Conference on Fusion Reactor Materials (ICFRM-12) Santa Barbara, California, USA, 7-12 December 2015* **367-370,** 1090–1095. doi:10.1016/j.jnucmat.2007.03.250 (2007).

[77] Candido, L., Utili, M., Zucchetti, M., Ciampichetti, A. & Calderoni, P. Development of advanced hydrogen permeation sensors to measure Q2 concentration in lead-lithium eutectic alloy. *Fusion Engineering and Design. Proceedings of the 29th Symposium on Fusion Technology (SOFT-29) Prague, Czech Republic, 5-9 September 2016* **124,** 735–739. doi:10.1016/j.fusengdes.2017.05.012 (2017).

[78] Holstein, N., Krauss, W., Konys, J. & Nitti, F. S. Development of an electrochemical sensor for hydrogen detection in liquid lithium for IFMIF-DONES. *Fusion Engineering and Design. Proceedings of the 30th Symposium on Fusion Technology (SOFT-30) Giardini Naxos, Italy, 16-21 September 2018* **146,** 1441–1445. doi:10.1016/j.fusengdes.2019.02.100 (2019).

[79] Konys, J., Muscher, H., Voß, Z. & Wedemeyer, O. Oxygen measurements in stagnant lead–bismuth eutectic using electrochemical sensors. *Journal of Nuclear Materials* **335,** 249–253. doi:10.1016/j.jnucmat.2004.07.018 (2004).

[80] IPM, IEC, IFCC, ILAC, ISO, IUPAC, IUPAP & OI. *Evaluation of measurement data – Guide to the expression of uncertainty in measurement.* JCGM 100:2008 GUM 1995 with minor corrections. http://www.bipm.org/utils/common/documents/jcgm/JCGM_100_2008_E.pdf (2008). Last accessed on 21/11/2021.

[81] Köllő, Z., Alecu, C. G. & Moosmann, H. A new method to measure small volumes in tritium handling facilities, using p-V measurements. *Fusion Science and Technology* **60,** 972–975. doi:10.13182/FST11-A12578 (2011).

[82] Miedema, A. R. The electronegativity parameter for transition metals: Heat of formation and charge transfer in alloys. *Journal of the Less Common Metals* **32,** 117–136. doi:10.1016/0022-5088(73)90078-7 (1973).

[83] Shpil'rain, E. E., Skovorod'ko, S. N. & Mozgovoi, A. G. The solubility of inert gases in liquid-metal heat-transfer agents. *High Temperature* **38,** 384–388. doi:10.1007/BF02755996 (2000).

[84] Shpil'rain, E. E., Skovorod'ko, S. N. & Mozgovoi, A. G. The solubility of helium and argon in liquid lead, bismuth, and their eutectic alloy at high temperatures. *High Temperature* **45,** 127–130. doi:10.1134/S0018151X07010129 (2007).

[85] Benamati, G., Fazio, C. & Ricapito, I. Mechanical and corrosion behaviour of EUROFER 97 steel exposed to Pb–17Li. *Journal of Nuclear Materials* **307,** 1391–1395. doi:10.1016/S0022-3115(02)00990-X (2002).

[86] Glasbrenner, H., Konys, J., Röhrig, H. D., Stein-Fechner, K. & Voss, Z. Corrosion of ferritic–martensitic steels in the eutectic Pb–17Li. *Journal of Nuclear Materials* **283,** 1332–1335. doi:10.1016/S0022-3115(00)00322-6 (2000).

[87] Chakraborty, P., Kumar, N. N., Krishna, N. S., Maheshwari, N. K., Bysakh, S., Bose, A., Kain, V. & Tewari, R. Effect of oxide layer and the duration of exposure on the liquid metal corrosion mechanism of RAFM steel in molten Pb-Li. *Corrosion Science* **183,** 109321. doi:10.1016/j.corsci.2021.109321 (2021).

[88] Borgstedt, H. U., Frees, G. & Peric, Z. Material compatibility tests with flowing Pb17Li eutectic. *Fusion Engineering and Design* **17,** 179–183. doi:10.1016/0920-3796(91)90054-T (1991).

[89] Sannier, J., Broc, M., Flament, T. & Terlain, A. Corrosion of austenitic and martensitic stainless steels in flowing Pb17Li alloy. *Fusion Engineering and Design* **14,** 299–307. doi:10.1016/0920-3796(91)90013-G (1991).

[90] Broc, M., Flament, T., Fauvet, P. & Sannier, J. Corrosion of austenitic and martensitic stainless steels in flowing 17Li83Pb alloy. *Journal of Nuclear Materials* **155,** 710–714. doi:10.1016/0022-3115(88)90401-1 (1988).

[91] Tortorelli, P. F. & DeVan, J. H. Corrosion of ferrous alloys exposed to thermally convective Pb-17 at% Li. *Journal of Nuclear Materials* **141,** 592–598. doi:10.1016/0022-3115(86)90059-0 (1986).

[92] Nakamura, H., Sakurai, S., Suzuki, S., Hayashi, T., Enoeda, M., Tobita, K. & DEMO Plant Design Team. Case study on tritium inventory in the fusion DEMO plant at JAERI. *Fusion Engineering and Design* **81,** 1339–1345. doi:10.1016/j.fusengdes.2005.10.009 (2006).

[93] Humrickhouse, P. W. & Merrill, B. J. Tritium aspects of the fusion nuclear science facility. *Fusion Engineering and Design* **135,** 302–313. doi:10.1016/j.fusengdes.2017.04.099 (2018).

[94] Abdou, M., Riva, M., Ying, A., Day, C., Loarte, A., Baylor, L., Humrickhouse, P., Fuerst, T. F. & Cho, S. Physics and technology considerations for the deuterium–tritium fuel cycle and conditions for tritium fuel self sufficiency. *Nuclear Fusion* **61,** 013001. doi:10.1088/1741-4326/abbf35 (2021).

[95] Lindau, R., Möslang, A., Rieth, M., Klimiankou, M., Materna-Morris, E., Alamo, A., Tavassoli, A.-A., Cayron, C., Lancha, A.-M., Fernandez, P., *et al.* Present development status of EUROFER and ODS-EUROFER for application in blanket concepts. *Fusion Engineering and Design* **75,** 989–996. doi:10.1016/j.fusengdes.2005.06.186 (2005).

[96] Esteban, G. A., Peña, A., Legarda, F. & Lindau, R. Hydrogen transport and trapping in ODS-EUROFER. *Fusion Engineering and Design* **82,** 2634–2640. doi:10.1016/j.fusengdes.2007.02.002 (2007).

[97] Utili, M., Bassini, S., Cataldo, S., Di Fonzo, F., Kordac, M., Hernandez, T., Kunzova, K., Lorenz, J., Martelli, D., Padino, B., *et al.* Development of anti-permeation and corrosion barrier coatings for the WCLL breeding blanket of the European DEMO. *Fusion Engineering and Design* **170,** 112453. doi:10.1016/j.fusengdes.2021.112453 (2021).

[98] Houben, A., Rasiński, M., Gao, L. & Linsmeier, C. Tungsten nitride as tritium permeation barrier. *Nuclear Materials and Energy* **24,** 100752. doi:10.1016/j.nme.2020.100752 (2020).

[99] Wulf, S.-E., Krauss, W. & Konys, J. Long-term corrosion behavior of Al-based coatings in flowing Pb–15.7 Li, produced by electrochemical ECX process. *Nuclear Materials and Energy* **16,** 158–162. doi:10.1016/j.nme.2018.06.019 (2018).

[100] Muñoz, P., Hernández, T., Garcıa-Cortés, I., Sánchez, F., Maira, A., Iadicicco, D., Vanazzi, M., Utili, M., Di Fonzo, F. & Moroño, A. Radiation effects on deuterium permeation for PLD alumina coated Eurofer steel measured

during 1.8 MeV electron irradiation. *Journal of Nuclear Materials* **512,** 118–125. doi:10.1016/j.jnucmat.2018.10.008 (2018).

[101] Carmona Gazquez, M., Bassini, S., Hernandez, T. & Utili, M. Al_2O_3 coating as barrier against corrosion in Pb-17Li. *Fusion Engineering and Design* **124,** 837–840. doi:10.1016/j.fusengdes.2017.03.070 (2017).

[102] Xiang, X., Wang, X., Zhang, G., Tang, T. & Lai, X. Preparation technique and alloying effect of aluminide coatings as tritium permeation barriers: A review. *International Journal of Hydrogen Energy* **40,** 3697–3707. doi:10.1016/j.ijhydene.2015.01.052 (2015).

[103] Konys, J., Aiello, A., Benamati, G. & Giancarli, L. Status of tritium permeation barrier development in the EU. *Fusion Science and Technology* **47,** 844–850. doi:10.13182/FST05-A791 (2005).

[104] Aiello, A., Ciampichetti, A. & Benamati, G. An overview on tritium permeation barrier development for WCLL blanket concept. *Journal of Nuclear Materials* **329,** 1398–1402. doi:10.1016/j.jnucmat.2004.04.205 (2004).

[105] Hollenberg, G. W., Simonen, E. P., Kalinin, G. & Terlain, A. Tritium/hydrogen barrier development. *Fusion Engineering and Design* **28,** 190–208. doi:10.1016/0920-3796(95)90039-X (1995).

[106] Perujo, A. & Forcey, K. S. Tritium permeation barriers for fusion technology. *Fusion Engineering and Design* **28,** 252–257. doi:10.1016/0920-3796(95)90045-4 (1995).

[107] *Wutz Handbuch Vakuumtechnik.* 11th ed. German (ed Jousten, K.) ISBN: 978-3-8348-1745-7 (Springer Vieweg, Wiesbaden, 2012).

[108] Ismail, A. F., Khulbe, K. & Matsuura, T. *Gas Separation Membranes: Polymeric and Inorganic.* 1st ed. ISBN: 978-3-319-01094-6 (Springer International Publishing, Cham, 2015).

[109] Sharipov, F. Rarefied gas flow through a long tube at any temperature ratio. *Journal of Vacuum Science & Technology A* **14,** 2627–2635. doi:10.1116/1.579991 (1996).

[110] Sharipov, F. *Rarefied Gas Dynamics: Fundamentals for Research and Practice.* 1st ed. ISBN: 978-3-527-41326-3 (Wiley-VCH Verlag GmbH and Co. KGaA, Weinheim, 2016).

[111] Redhead, P. A. Hydrogen in vacuum systems: An overview. *AIP Conference Proceedings* **671,** 243–254. doi:10.1063/1.1597372 (2003).

[112] Pisarev, A. Hydrogen gas-driven permeation through the membrane with asymmetric surface conditions. *Journal of Membrane Science* **335,** 51–57. doi:10.1016/j.memsci.2009.02.041 (2009).

[113] Doyle, B. L. A simple theory for maximum H inventory and release: a new transport parameter. *Journal of Nuclear Materials* **111,** 628–635. doi:10.1016/0022-3115(82)90277-X (1982).

[114] Pick, M. A. & Sonnenberg, K. A model for atomic hydrogen-metal interactions — application to recycling, recombination and permeation. *Journal of Nuclear Materials* **131,** 208–220. doi:10.1016/0022-3115(85)90459-3 (1985).

[115] Richards, P. M. Surface-limited hydrogen release and uptake in metals. *Journal of Nuclear Materials* **152,** 246–258. doi:10.1016/0022-3115(88)90333-9 (1988).

[116] Kinjo, M., Fukada, S., Katayama, K., Edao, Y. & Hayashi, T. Experiment on recovery of hydrogen isotopes from Li17Pb83 blanket by liquid-gas contact. *Fusion Science and Technology* **71,** 520–526. doi:10.1080/15361055.2017.1293426 (2017).

[117] Fitzpatrick, R. *Theoretical fluid mechanics.* 1st ed. ISBN: 78-0-7503-1552-4 (IOP Publishing Ltd., Bristol, 2017).

[118] Bush, J. W. M. *18.357 Interfacial Phenomena, lecture notes* (Massachusetts Institute of Technology: MIT OpenCourseWare, 2010). https://ocw.mit.edu/courses/mathematics/18-357-interfacial-phenomena-fall-2010/lecture-notes/. Last accessed on 08/07/2021.

[119] Schroeder, R. R. & Kintner, R. C. Oscillations of drops falling in a liquid field. *AIChE Journal* **11,** 5–8. doi:10.1002/aic.690110105 (1965).

[120] Hager, W. H. *Wastewater Hydraulics: Theory and Practice.* 2nd ed. ISBN: 978-3-642-11382-6 (Springer-Verlag, Heidelberg, 2010).

[121] Chen, N. H. An explicit equation for friction factor in pipe. *Industrial and Engineering Chemistry Fundamentals* **18,** 296–297. doi:10.1021/i160071a019 (1979).

[122] Zigrang, D. J. & Sylvester, N. D. A Review of Explicit Friction Factor Equations. *Journal of Energy Resources Technology* **107,** 280–283. doi:10.1115/1.3231190 (1985).

[123] Benedict, R. P., Carlucci, N. A. & Swetz, S. D. Flow losses in abrupt enlargements and contractions. *Journal of Engineering for Power* **88,** 73–81. doi:10.1115/1.3678482 (1966).

[124] Shankar Subramanian, R. *CH330: Transfer Process Fundamentals, lecture notes* (Department of Chemical and Biomolecular Engineering, Clarkson University, 2014). https://web2.clarkson.edu/projects/subramanian/ch330/notes/index.html. Last accessed on 08/07/2021.

Appendix A

Plateau-Rayleigh Instability

A.1 Introduction

When a liquid falls through a thin circular nozzle, a liquid jet is formed. The inertia of the liquid tends to keep the column compact (in form of a cylinder), while the acceleration due to gravity slightly elongates the stream (shrinking the column). Small intrinsic perturbations (that can be represented by sinusoidal components) are always present. Some of them will naturally decrease and disappear, while others will grow. Additionally, the *surface tension* in a liquid is generated by inter-molecular cohesive forces. The molecules close to the interface experience an unbalanced cohesive force towards the interior of the liquid, which makes the interface to contract energetically favourable.

The increasing perturbations under the presence of the surface tension generate the *Plateau-Rayleigh instability*. A critical point is reached when the amplitude of the perturbation equals the radius of the stream and the liquid column breaks into droplets (achieving a lower energy state).

A.2 Mathematical description of Plateau-Rayleigh Instability. Derivation of the droplet diameter

Given a falling liquid column of radius R_0, density ρ, surface tension σ, the pressure jump, Δp, across its surface is described by the *Young-Laplace equation* (A.1). This jump is proportional to the surface tension and the curvature of the surface ($\mathbf{n}$ is the inward-directed surface unity vector).

$$\Delta p = \sigma \ \nabla \cdot \mathbf{n}. \tag{A.1}$$

Assuming zero external pressures, the pressure inside the column, p_0, is given

by:

$$p_0 = \frac{\sigma}{R_0}. \tag{A.2}$$

The *Navier-Stokes equation*, neglecting the gravitational force and any other external forces, has the general form:

$$\frac{\partial \mathbf{u}}{\partial t} + (\mathbf{u} \cdot \nabla)\mathbf{u} = -\frac{1}{\rho}\nabla p + \nu \cdot \nabla^2 \mathbf{u}, \tag{A.3}$$

where $\mathbf{u}$ is the velocity of the fluid and ν is its kinematic viscosity; and the *continuity equation* (mass conservation) follows:

$$\nabla \cdot \mathbf{u} = 0. \tag{A.4}$$

We can consider a perturbation on the surface of the stream with the form:

$$\widetilde{R} = R_0 + \epsilon\, e^{\omega t + ikz}, \tag{A.5}$$

where the amplitude of the perturbation $\epsilon \ll R_0$, ω is the growth rate, and k is the wave number in the z-direction (vertical). The wavelength is $\lambda = 2\pi/k$. Being $\widetilde{u_r}$ and $\widetilde{u_z}$ the radial and axial components of the perturbation velocity, and $\widetilde{p}$ the perturbation pressure; when substituting them into the Navier-Stokes equation (A.3), the terms corresponding to (i.e. that are in the order of) the perturbation yield:

$$\frac{\partial \widetilde{u_r}}{\partial t} = -\frac{1}{\rho}\frac{\partial \widetilde{p}}{\partial r}, \tag{A.6}$$

$$\frac{\partial \widetilde{u_z}}{\partial t} = -\frac{1}{\rho}\frac{\partial \widetilde{p}}{\partial z}. \tag{A.7}$$

And substituting in (A.4), the continuity equation takes the form:

$$\frac{\partial \widetilde{u_r}}{\partial r} + \frac{\widetilde{u_r}}{r} + \frac{\partial \widetilde{u_z}}{\partial z} = 0. \tag{A.8}$$

The perturbation terms of the form shown in equations (A.9) can be substituted in equations (A.6), (A.7) and (A.8) and result in the momentum equations (A.10) and (A.11) and the continuity equation (A.12).

$$\widetilde{u_r} = R(r)\, e^{\omega t + ikz}, \quad \widetilde{u_z} = Z(r)\, e^{\omega t + ikz}, \quad \widetilde{p} = P(r)\, e^{\omega t + ikz}, \tag{A.9}$$

$$\omega R = -\frac{1}{\rho}\frac{dP}{dr}, \tag{A.10}$$

$$\omega Z = -\frac{ik}{\rho}P, \tag{A.11}$$

$$\frac{dR}{dr} + \frac{R}{r} + ikZ = 0. \tag{A.12}$$

From equations (A.10), (A.11) and (A.12), we can obtain the differential equation for R(r):

$$r^2 \frac{d^2R}{dr^2} + r\frac{dR}{dr} - \left(1 + (kr)^2\right) R = 0. \tag{A.13}$$

This is a modified Bessel equation of order 1, whose general solution can be expressed in terms of the so-called modified Bessel functions:

$$R(r) = CI_1(kr) + C'K_1(kr), \tag{A.14}$$

where $I_1(kr)$ and $K_1(kr)$ are modified Bessel functions of the first and second kind, respectively, and C and C' are arbitrary constants. The function of second kind $K_1(kr) \to \infty$ when $r \to 0$; thus, the general solution can be expressed as:

$$R(r) = CI_1(kr). \tag{A.15}$$

From equations (A.10) and (A.15) we can obtain the pressure $P(r)$ by using the Bessel function identity $I_0'(\xi) = I_1(\xi)$:

$$P(r) = -\frac{\omega\rho C}{k} I_0(kr). \tag{A.16}$$

In order to continuing solving the problem, two boundary conditions are applied: (i) equation (A.17) shows the kinematic condition at the surface and (ii) (A.18) sets the normal stress balance on the surface.

$$\frac{\partial \widetilde{R}}{\partial t} = \tilde{u} \cdot n \simeq \widetilde{u_r}, \tag{A.17}$$

$$p_0 + \widetilde{p} = \sigma \, \nabla \cdot n. \tag{A.18}$$

From equations (A.15) and (A.17), we obtain:

$$C = \frac{\epsilon\omega}{I_1(kR_0)}. \tag{A.19}$$

If the curvature in (A.18) is expressed as $\nabla \cdot n = (1/R_1 + 1/R_2)$, where R_1 and R_2 are the principal radii of the curvature of the stream surface derived from (A.5):

$$\frac{1}{R_1} = \frac{1}{R_0 + \epsilon \, e^{\omega t + ikz}} \simeq \frac{1}{R_0} - \frac{\epsilon}{R_0^2} \, e^{\omega t + ikz}, \qquad \frac{1}{R_2} = \epsilon k^2 \, e^{\omega t + ikz}, \tag{A.20}$$

their substitution in (A.18) yields:

$$p_0 + \widetilde{p} = \frac{\sigma}{R_0} - \frac{\epsilon\sigma}{R_0^2}(1 - k^2R_0^2) \, e^{\omega t + ikz}. \tag{A.21}$$

Then, substituting p_0 from (A.2) into (A.21), the perturbation in pressure is described by:

$$\widetilde{p} = -\frac{\epsilon\sigma}{R_0^2}(1 - k^2R_0^2) \, e^{\omega t + ikz}. \tag{A.22}$$

Now, from (A.16), (A.19) and (A.22), the *dispersion relation* is obtained:

$$\omega^2 = \frac{\sigma}{\rho R_0^3} kR_0 \frac{I_1(kR_0)}{I_0(kR_0)}(1 - k^2 R_0^2). \tag{A.23}$$

The maximization of equation (A.23) yields:

$$kR_0(\omega_{\max}) \simeq 0.697. \tag{A.24}$$

Therefore, the fastest grow rate occurs for the following wavelength of the perturbation:

$$\lambda_{\max} \simeq 9.02 R_0, \tag{A.25}$$

and the liquid jet is estimated to break up at the following characteristic time:

$$t_{\text{breakup}} \simeq 2.91 \sqrt{\frac{\rho R_0^3}{\sigma}}. \tag{A.26}$$

In order to predict the characteristic diameter of the forming droplets, the volume of one wavelength of the stream ($\pi R_0^2 \lambda_{max}$) is equalled to the volume of one spherical droplet ($4/3\pi R_d^3$). With this, the equivalent diameter of the droplet formed from the instability, d_d, is obtained as a function of the diameter of the nozzle, d_0.

$$d_{\text{d}} \simeq 1.89 d_0. \tag{A.27}$$

A.3 Droplet oscillation

The falling droplets are not perfect spheres. Instead, their shape oscillates from oblate to prolate form. The frequency of oscillation of a liquid droplet (dispersed medium) falling in another medium (continuum) is described by [42]:

$$f = \frac{1}{\pi} \sqrt{\frac{2\sigma}{d_{\text{d}}^3} \frac{n(n+1)(n-1)(n+2)}{(n+1)\rho_{\text{d}} + n\rho_{\text{c}}}}, \tag{A.28}$$

where σ is the surface tension, ρ_{d} and ρ_{c} are the densities of the dispersed phase and continuum, respectively. The fundamental or first mode of oscillation, $n = 2$, is the only one observed experimentally. Therefore, the frequency of oscillations of a liquid droplet of volume V_{d} falling in vacuum ($\rho_{\text{c}} \to 0$) is:

$$f = \sqrt{\frac{8}{3} \frac{\sigma}{\pi \rho_{\text{d}} V_{\text{d}}}}. \tag{A.29}$$

References: [40–42, 117–119].

Appendix B

Models of extraction from falling droplets

B.1 Introduction

The mass extraction from droplets in liquid-liquid systems has been extensively investigated, which can be divided into three categories: (i) droplet without internal circulation treated as rigid spheres, (ii) droplets with internal laminar circulation, and (iii) fully oscillating droplets. Oscillating drops show a far greater rate of transfer than any other type [48].

In the absence of investigation performed for liquid droplets falling in vacuum, the models developed for a liquid continuum are reviewed in the following sections. The extrapolation to vacuum can be estimated by assuming zero resistance or zero density in the continuous phase. However, the shape of an oscillating droplet in a medium with resistance is different from its behaviour in vacuum. Therefore, it has to be noted that the extraction in vacuum cannot be not perfectly extrapolated from these models.

B.2 Stagnant droplets. Diffusion in a sphere

Droplets without internal circulation can be represented as rigid spheres. Then, the extraction rate can be derived from mathematics of diffusion in a perfect sphere [45]. The radial diffusion of a substance, in spherical coordinates, is described by equation (B.1), where C is the concentration of the substance, $\mathcal{D}$ the diffusion coefficient, t the given time and r the radial position:

$$\frac{\partial C}{\partial t} = \mathcal{D}\left(\frac{\partial^2 C}{\partial r^2} + \frac{2}{r}\frac{\partial C}{\partial r}\right). \tag{B.1}$$

The solution of equation (B.1) can be simplified by substituting $u = Cr$:

$$\frac{\partial u}{\partial t} = \mathcal{D}\left(\frac{\partial^2 u}{\partial r^2}\right). \tag{B.2}$$

Given a sphere of radius a, with an initial distribution $C(r, t = 0) = f(r)$ and a constant concentration $C(r = a, t) = C_a$ at the surface, the non-steady case can be evaluated as follows:

$$r = 0, \qquad t > 0, \qquad u = 0.$$

$$r = a, \qquad t > 0, \qquad u = aC_a.$$

$$0 < r < a, \qquad t = 0, \qquad u = rf(r).$$

If the sphere is initially at a uniform concentration $C(r, t = 0) = C_0$ and the surface concentration is maintained constant at C_a, the solution (at time = t) becomes:

$$\frac{C(r,t) - C_0}{C_a - C_0} = 1 + \frac{2a}{\pi r} \sum_{n=1}^{\infty} \frac{(-1)^n}{n} \sin\left(\frac{n\pi r}{a}\right) \exp\left(\frac{-\mathcal{D}\, n^2\, \pi^2\, t}{a^2}\right). \tag{B.3}$$

Integrating over r, the total amount of diffusing substance leaving (or entering) the sphere is given by equation (B.4), in which m_t and m_∞ are the total mass of substance that have left (or entered) the sphere at time t and ∞, respectively:

$$\frac{m_t}{m_\infty} = 1 - \frac{6}{\pi^2} \sum_{n=1}^{\infty} \frac{1}{n^2} \exp\left(\frac{-\mathcal{D}\, n^2\, \pi^2\, t}{a^2}\right). \tag{B.4}$$

B.3 Droplet with internal laminar circulation

In liquid-liquid systems, the extraction from droplets with internal circulation currents (caused by the viscous forces between the two fluids) has been found greater than in stagnant droplets. The rate of extraction, derived from convection (assuming laminar circulation) and diffusion, follows [46]:

$$\frac{m_t}{m_\infty} = 1 - \frac{3}{8} \sum_{n=1}^{\infty} A_n^2 \exp\left(-\lambda_n \frac{16\,\mathcal{D}\, t}{a^2}\right), \tag{B.5}$$

where the first approximate eigenvalues and coefficients are $\lambda_1 \simeq 1.678$, $\lambda_2 \simeq 9.83$, $A_1 \simeq 1.32$, $A_2 \simeq 0.73$ [46].

However, the assumption of laminar circulation is only valid for small Reynolds numbers. In many cases this means that the size of the droplet has to be remarkably reduced. In reality, it is much more common to have turbulent regimes inside the droplets. And in those cases, this model cannot be applied. Note that in the present work: $\rho \approx 9720\,\mathrm{kg\,m^{-3}}$, $v \approx 4\,\mathrm{m\,s^{-1}}$, $d \approx 1.2 \times 10^{-3}\,\mathrm{m}$, $\mu \approx 1.5 \times 10^{-3}\,\mathrm{kg\,m^{-1}\,s^{-1}}$. Thus, $\mathrm{Re} = \rho v d/\mu \approx 31100$ (turbulent regime).

B.4 Oscillating droplets

In order to account for the oscillations of the droplets and internal turbulent circulation patterns, a first approach was proposed by Handlos and Baron [47]. This model includes tangential motion due to internal circulation and random radial motion due to eddy diffusivities in liquid droplets falling in a liquid medium:

$$\frac{m_t}{m_\infty} = 1 - 2\sum_{n=1}^{\infty} A_n^2 \exp\left(-\frac{\lambda_n\, v\, t}{128\left(1+\frac{\mu_D}{\mu_C}\right) d}\right), \tag{B.6}$$

where v is the speed of the droplet, t is the falling time, d is the diameter of the droplet, μ_C and μ_D are the continuous and disperse phase dynamic viscosity, and A_n and λ_n are the coefficients and eigenvalues of the series. This model can clearly not be extrapolated to vacuum, in which $\mu_C \to 0$.

Rose and Kintner [48] observed that the droplets do not oscillate fully from obleate to prolate shape (likely due to the resistance of the continuum). Therefore, they developed another model with oscillations from spherical to obleate ellipse, and assuming all the resistance to transfer (in both media) in a thin zone near the surface. The model is described by:

$$\begin{aligned}\frac{m_t}{m_\infty} = 1 - \exp\Bigg[-\frac{2\pi\mathcal{D}_E}{V}\int_{t_0}^{t_f}\frac{1}{f_1(t)}\Bigg(\left(\frac{3V}{4\pi(a_0+a_p\mid\sin\omega' t\mid)^2}\right)^2 \\ \frac{1}{2\alpha}\ln\frac{1+\alpha}{1-\alpha} + (a_0+a_p\mid\sin\omega' t\mid)^2\Bigg)dt\Bigg],\end{aligned} \tag{B.7}$$

with:

$$\alpha^2 = \frac{(a_0+a_p\mid\sin\omega' t\mid)^2 - \left(\frac{3V}{4\pi(a_0+a_p|\sin\omega' t|)^2}\right)}{(a_0+a_p\mid\sin\omega' t\mid)^2}, \tag{B.8}$$

where V is the volume of the droplet, a_0 is the initial radius, a_p is the amplitude, $\omega' = 0.5\omega$, with ω being the frequency of oscillation, and the effective diffusivity $\mathcal{D}_E$ = (fraction of resistance in dispersed phase) $\cdot\, \mathcal{D}_D$ + (fraction of resistance in continuous phase) $\cdot\, \mathcal{D}_C$. This model (B.7) seems to adjust better to experimental results than the previously proposed (B.6). However, the complexity of the integral, with the undefined $f_1(t)$ makes its application more inaccessible.

Angelo *et al.* [49] proposed another approach for oscillating droplets based on the surface-time relation:

$$S(\tau) = S_0(1+\epsilon\sin^2\tau), \tag{B.9}$$

where S is the area of the time-dependent surface, S_0 is the characteristic reference area for constant surface, ϵ is a dimensionless amplitude factor, and $\tau = t/t_0$ is a dimensionless time variable, with t_0 being a characteristic constant time of the

system. For one cycle of oscillation, $\tau = \pi$, the predicted mass transfer coefficient follows:

$$K_D = \sqrt{\frac{4\,\mathcal{D}_{AD}\,\omega\,(1+\epsilon_0)}{\pi}}\left(\frac{1}{1+m\sqrt{\frac{\mathcal{D}_{AD}}{\mathcal{D}_{AC}}}}\right), \tag{B.10}$$

where the subscripts A, D, C and 0 refer to solute, disperse phase, continuous phase and interface, respectively, so that $\mathcal{D}_{AD}$ is the diffusivity of the solute inside the droplet, ω is the frequency of oscillation, $\epsilon_0 = \epsilon + 3/8\epsilon^2$, and $m = (\rho_{A0} - \rho_A^*)_D/(\rho_{A0} - \rho_{A\infty}^*)_C$. For liquid droplets falling in vacuum, $\mathcal{D}_{AC} \to \infty$, then:

$$K_D = \sqrt{\frac{4\,\mathcal{D}_{AD}\,\omega\,(1+\epsilon_0)}{\pi}}. \tag{B.11}$$

B.5 Discussion

Several authors have performed experiments with liquid-liquid systems in order to verify the existent theoretical models [44, 50–54]. The internal circulation in the droplets has been observed with trace impurities but it has not been fully understood. It has been observed that every system that exhibits oscillations shows deformed or completely damped circulation. It has also been found that the oscillations are maintained by the vortex discharge behind the moving droplets. Additionally, the oscillations are not from full prolate to full obleate ellipsoids.

These conclusions have been made for liquid-liquid systems and are most likely related to the resistance of the continuous phase. In the case of droplets falling in vacuum, the continuous phase would not impose resistance (no friction forces). Therefore, the behaviour may be different and the described models do not perfectly apply. Due to the lack of investigation in liquid-vacuum systems, and for simplicity, a first approach to evaluate the efficiency is to use the model of the perfect rigid sphere. Based on that model, the mass transfer can be assessed and compared to known values of diffusivity, in order to quantify enhancement due to droplet oscillations and internal circulation of the liquid.

Appendix C

Rarefied gas

C.1 Characterization of a gas regime

The *mean free path* of the gas molecules in a gas is generally defined as:

$$\bar{l} = \frac{k_{\mathrm{B}} T}{\sqrt{2}\pi p d_{\mathrm{M}}^2}, \tag{C.1}$$

where k_{B} is the Boltzmann constant, T is the temperature of the gas, p is its pressure, and d_{M} is the molecular diameter.

In the categorization of a rarefied gas is, however, the concept of *equivalent free path* used [107]:

$$\ell = \frac{\mu c_{\mathrm{p}}}{p}, \tag{C.2}$$

where μ is the viscosity and c_{p} is the most probable speed of the particles. The viscosity is given by:

$$\mu = \frac{1}{2}\rho \bar{c} \bar{l} = \frac{4p\bar{l}}{\pi \bar{c}}, \tag{C.3}$$

with $\bar{c}$ being the average speed of the molecules:

$$\bar{c} = \sqrt{\frac{8k_{\mathrm{B}}T}{\pi m_{\mathrm{M}}}} = \sqrt{\frac{8p}{\pi \rho}}, \tag{C.4}$$

where m_{M} is the mass of one molecule. The most probable speed is given by:

$$c_{\mathrm{p}} = \sqrt{\frac{2k_{\mathrm{B}}T}{m_{\mathrm{M}}}} = \sqrt{\frac{2p}{\rho}}. \tag{C.5}$$

With the definitions given above [107], substituting into equation (C.2), the relation between ℓ and $\bar{l}$ is:

$$\ell = \frac{2\bar{l}}{\sqrt{\pi}}. \tag{C.6}$$

The flow regime is normally characterized by the Knudsen number, which is defined as:

$$\mathrm{Kn} = \frac{\ell}{a}, \tag{C.7}$$

where a is the characteristic dimension of a system (e.g. in the case of a pipe, a would be its radius). $\mathrm{Kn} < 0.01$ corresponds to *viscous regime*, $0.5 > \mathrm{Kn} > 0.01$ to *transition regime* (or *Knudsen regime*), and $\mathrm{Kn} > 0.5$ to *molecular regime* [107].

Additionally, the *rarefaction parameter* is defined as:

$$\delta = \frac{ap}{\mu c_{\mathrm{p}}} = \frac{a}{\ell}. \tag{C.8}$$

Therefore, the above classification can also be done in terms of the rarefaction parameter: $\delta \gg 1$ denotes a viscous regime, while $\delta \ll 1$ corresponds to a molecular regime (as inversely proportional to Kn).

C.2 Capillary connecting two vessels

In the example case of a capillary connecting two vessels (1 and 2) under vacuum at different temperatures, two opposing effects occur: molecules move from one vessel to the other (cold to hot) due to the so-called *thermal creep*. As a consequence, a pressure gradient occurs, resulting in a counter flow. This phenomenon is called *thermomolecular pressure effect*. When the temperature difference is small, the relation between the pressure in both vessels can be described by the general case:

$$\frac{p_2}{p_1} = \left(\frac{T_2}{T_1}\right)^{\gamma}, \tag{C.9}$$

where the coefficient γ has the general form:

$$\gamma = \frac{Q_T}{Q_P}, \tag{C.10}$$

with Q_T and Q_P being coefficients related to the two counter flows in the capillary, due to thermal creep and pressure gradient, respectively:

$$Q = -Q_P v + Q_T \tau, \quad \text{with} \;\; v = \frac{a}{p}\frac{dp}{dx}, \; \tau = \frac{a}{T}\frac{dT}{dx}. \tag{C.11}$$

In equation (C.11), Q is the *reduced flow rate* along the capillary and x is the longitudinal coordinate. Both coefficients, Q_T and Q_P, are dependent on the local Knudsen number (or rarefaction parameter) and for small temperature and pressure differences are constant along the capillary.

In the case of a large temperature ratio between the two vessels (T_2/T_1) and large temperature gradient in the capillary, the thermomolecular pressure effect is not linear (neither are Q_T and Q_P). The coefficient γ can then be obtained from a linear theory approximation using an average rarefaction parameter calculated with:

$$\delta_{\mathrm{avg}} = \delta_1 \frac{p_{\mathrm{avg}}}{p_1}\frac{T_1}{T_{\mathrm{avg}}} = \delta_1 \frac{1 + (T_2/T_1)^{\gamma}}{1 + (T_2/T_1)}. \tag{C.12}$$

Then,

$$\gamma_{\text{avg}} = \frac{Q_T(\delta_{\text{avg}})}{Q_P(\delta_{\text{avg}})}, \tag{C.13}$$

This approximation is only valid for small values of δ_1 (molecular regime), since for large values of δ_1 the deviation between the real value and the linear approximation increases considerably.

The calculation of the coefficients Q_P and Q_T can be performed as explained in reference [109].

References: [107, 109, 110].

Appendix D

Experimental facility

D.1 Summary of main characteristics

The aim of this section is to summarize the main characteristics of the elements conforming the experimental facility. For reference, see the P&I diagram in Figure D.1.

D.1.1 Subassemblies and volumes

Table D.1 shows a summary of the main subassemblies and their volumes. The column 'delimitations' shows the valves defining the closed volume (see Figure D.1).

Several volumes have been determined with the high-accuracy setup described in [81] before the final assembly. Others have been determined with the facility already assembled by gas expansion from other subassemblies with previously known volumes.

Table D.1: Volumes of the subassemblies. Their delimitations are given by the valves that close the volume (see Figure D.1). The method used for the determination: (1) with specific facility shown in [81], (2) through gas expansion from another subassembly already measured with [81].

Subassembly	Volume (ml)	Delimitations	Method
Collecting tank	151.8 ± 0.5	HV430, HV440	(1)
Inlet line Ar	84 ± 1	HV201, HV042, HV043, HV050	(2)
Inlet line D_2	64 ± 1	HV041, HV042, HV480, HV060, HV050	(2)
Lower Chamber (LC)	$27\,301 \pm 142$	AV114, HV230, HV340, HV204, HV201	(1)
Transfer line	120.9 ± 0.4	HV104, HV204	(1)
Upper Chamber (UC)	$4\,879 \pm 20$	HV050, SV110, HV120, AV114, HV104	(1)

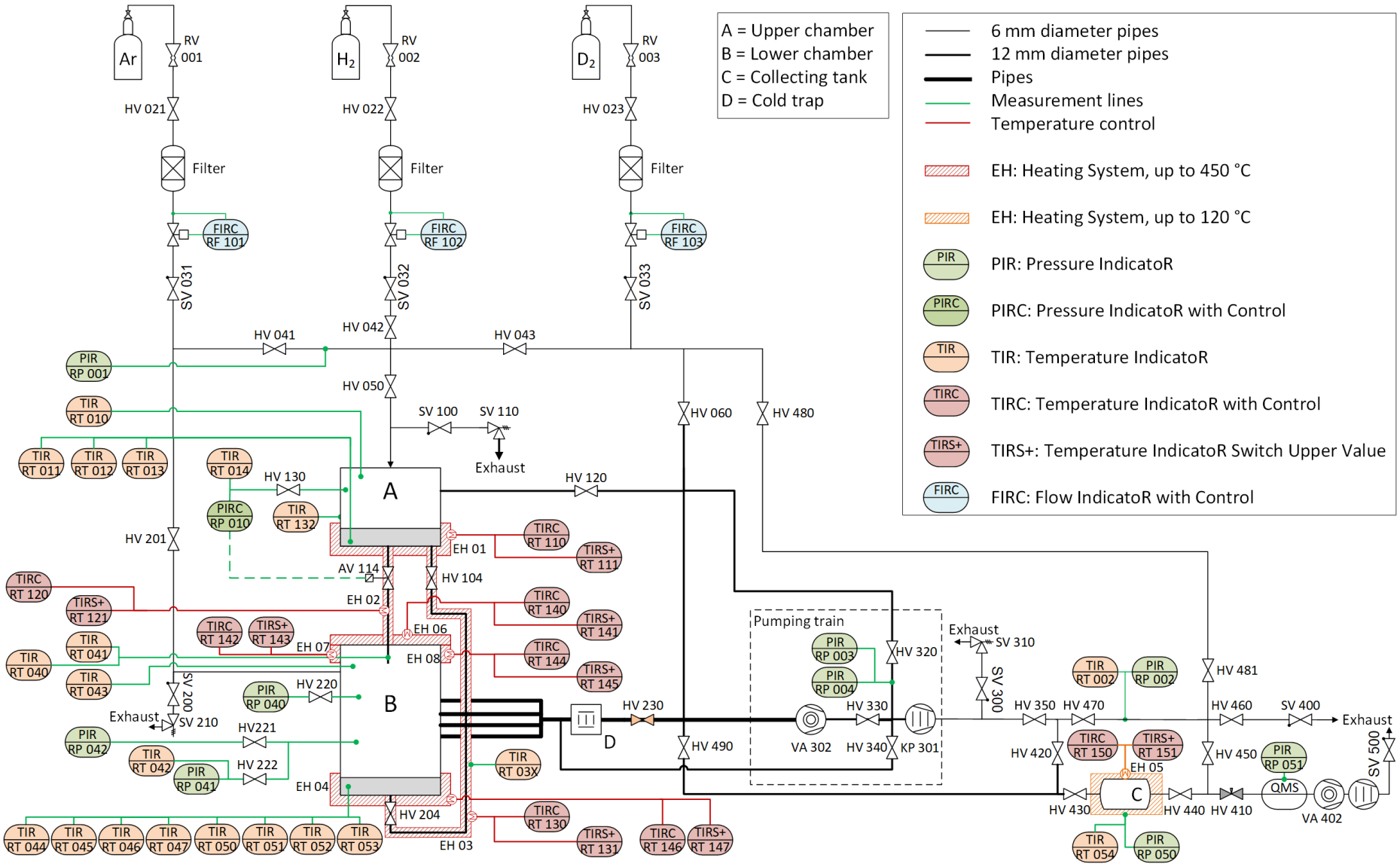

Figure D.1: P&I diagram of the experimental facility.

D.1.2 Pressure sensors

The pressure sensors installed at the facility are the model PTA227 from the company EFE. They have been selected because of its resistance to high temperature (although limited to 125 °C) and tritium compatibility (in views of testing them for a future tritium facility). Tables D.2 and D.3 show the pressure sensors installed in the facility and their main characteristics.

Table D.2: Pressure sensors installed at the facility, their full scale (F.S.) and the non-linearity and hysteresis combined ($\delta p_{\text{n-l\&h}}$) from calibration by manufacturer.

Sensor	Location	F.S. (mbar)	$\delta p_{\text{n-l\&h}}$ (mbar)
RP001	Inlet line	3000	±0.90
RP002	Collecting line	3000	±0.45
RP004	Pumping train	3000	±0.69
RP010	Upper chamber	3000	±0.48
RP041	Lower chamber	3000	±0.90
RP050	Collecting tank	1000	±0.75

Table D.3: Characteristics common to all pressure sensors shown in Table D.2.

Parameter	Value
Model:	PTA227, EFE
Non-repeatability:	±0.02% F.S.
Thermal zero and sensitivity shifts:	±0.02% F.S./°C
Max. operating temperature:	125 °C

D.1.3 Vacuum sensors

There are four vacuum sensors installed at the facility, as given in Table D.4. Sensors RP003 and RP051 are of the model PKR 251 from the company Pfeiffer. They have mainly a safety function and are used more in a qualitative manner in the operation of the facility, since they have a large measuring range but also large uncertainty. The vacuum sensors installed in the lower chamber, however, are used in the analysis of the experimental results. Their main characteristics are given in Table 3.4.

Table D.4: Vacuum sensors installed at the facility.

Sensor	Location	Range (mbar)
RP003	Pumping train	$5\times10^{-9} - 1000$
RP040	Lower chamber	$1.3\times10^{-11} - 1.3\times10^{-2}$
RP042	Lower chamber	$1.3\times10^{-3} - 13.3$
RP051	QMS ionization chamber	$5\times10^{-9} - 1000$

D.1.4 Temperature sensors

The thermocouples installed in the facility are of Ni-Cr K-type. Their uncertainty is 2.2 °C or 0.75 % (in °C), whichever is greater, of type offset. Their functionality is divided into three categories:

(i) Thermocouples with control and safety functions. Each heater has one control thermocouple that regulates the functioning with a given set point, and a safety thermocouple which shuts down the heater if a certain temperature is exceeded.

(ii) Temperature measurement of the gas, Pb-Li or metal surface.

(iii) Measurement of the Pb-Li level. These thermocouples are located at a certain position and show that the Pb-Li reaches (leaves) that level with a sudden increase (decrease) of the temperature.

The same thermocouple can also have several functions, for example the level thermocouples in the upper chamber are used to measure not only the level of Pb-Li, but also its temperature or the temperature of the gas when there is no Pb-Li. Table D.5 shows a list of the thermocouples of the categories (ii) and (iii).

D.1.5 Mass flow controllers

There are three Mass Flow Controllers (MFCs), model GF80 from the company Brooks Instruments, located at the gas feeding lines. Table D.6 shows their main characteristics. The occasional input of helium and nitrogen is done through the argon inlet line, so there is no dedicated MFC calibrated for these gases.

D.1.6 Quadrupole Mass Spectrometer

The facility has a quadrupole mass spectrometer (QMS) installed, used to analyse the composition of the gas after the vacuum tests. This permits to determine if there

Table D.5: List of temperature sensors with their location and function: measurement of gas temperature (T_g), metal-surface temperature (T_s), Pb-Li temperature (T_{PbLi}) or Pb-Li level (h_{PbLi}).

Sensor	Location	Measurement
RT010	Upper chamber	T_g
RT011, RT012, RT013	Upper chamber	h_{PbLi}, T_g, T_{PbLi}
RT014	Upper chamber (RP010)	T_g
RT132	Upper chamber (outer surface)	T_s
RT040, RT041	Lower chamber (nozzle)	T_s
RT043	Lower chamber	T_g
RT044–047, RT050–053	Lower chamber	h_{PbLi}, T_g, T_{PbLi}
RT042	Lower chamber (RP041)	T_g
RT133–137	Transfer line (outer surface)	T_s
RT002	Collecting pipe	T_g
RT054	Collecting tank	T_g

Table D.6: Main characteristics of the mass flow controllers. F.S.: full scale, S.P.: set point.

Parameter	RF001	RF002	RF003
Fluid:	Ar	H_2	D_2
Maximum flow rate ($l\,min^{-1}$):	5.0	2.0	2.0
Minimum flow rate ($l\,min^{-1}$):		2% F.S.	
Flow accuracy ($l\,min^{-1}$):	±1% S.P. (35–100%), ±0.35% F.S. (2–35%)		
Temperature range (°C):	5–50	5–50	5–50
Response time (s):	<1	<1	<1

Table D.7: Main characteristics of the QMS detector.

Parameter	Value
Mass range (amu):	1–100
Lowest detectable partial pressure (hPa):	10^{-14}
Maximum operating pressure (hPa):	1×10^{-4}
Operating temperature of the analyser (°C):	150
Operating temperature of the electronics (°C):	0–40

is outgassing from previous experiments or if there is any leakage (air entering the facility).

The detector model is PrismaPlus QMG 220M with C-SEM detector from the company Pfeiffer. Its main characteristics are given in Table D.7.

D.1.7 Other equipment

In each of the three gas feeding lines there is an ultrahigh-purity *gas filter*. They have a maximum flow rate of 30 $\mathrm{l\,min^{-1}}$ and maximum working pressure of 30 bar.

A *cold trap* is installed at the inlet of the main pumping train to protect the turbo-molecular pump from possible Pb-Li vapours. It consists of several layers of metallic grid at room temperature (cold in comparison with the Pb-Li melting point). Any possible Pb-Li vapour is able to condense at the grid before reaching the pumping train.

The main *pumping train* consists of a turbo-molecular pump and a fore pump (VA302 and KP301 respectively in the P&I diagram, Figure D.1). Table D.8 shows their main characteristics.

Table D.8: Characteristics of the main pumping train.

Parameter	Value
Turbo-molecular pump (model: HiPace 80, Pfeiffer)	
Rotation speed (RPM):	90000
Pumping speed for He ($\mathrm{l\,s^{-1}}$):	58
Pumping speed for H_2 ($\mathrm{l\,s^{-1}}$):	48
Maximum inlet pressure for N_2 (mbar):	22
Fore pump (model: ACP 15, Pfeiffer)	
Pumping speed ($\mathrm{l\,s^{-1}}$):	3.88
Maximum continuous inlet pressure (mbar):	1 013

Appendix E

Pb-Li composition analysis

E.1 Information referring to the Pb-Li used in the experimental campaign

The Pb-Li used in the experiments shown in this document was supplied by the company CAMEX, spol. s r. o. 21.6 kg of the eutectic lead-lithium alloy with 15.7 at% of lithium, with a reported purity of 99.95%, were provided in the form of ingots. From the obtained Pb-Li, 15.1 kg have been used for the experiments. Two composition analyses have been performed at the Institute for Applied Materials (IAM-AWP), Karlsruhe Institute of Technology (KIT):

(i) The first test was performed before the experimental campaign, with a sample extracted from of the Pb-Li provided at the same time of the insertion of the alloy into the facility.

(ii) After the experimental campaign, all the Pb-Li was solidified in the lower chamber. The second composition test was performed during the decommissioning of the facility, with two samples of the Pb-Li taken from the top surface and bottom (transfer line under the lower chamber).

Figures E.1 and E.2 show the results of the two composition analyses. The values shown for each sample are the average among three tests performed at different positions of each sample. In all analyses, inhomogeneity in the lithium and impurities content is reported.

The first analysis (in Figure E.1) shows a considerable reduction of the Li content (0.490 wt.%) with respect to the ordered eutectic mixture (0.620 wt.% Li). This is attributed to the inhomogeneity of the mixture. In the analyses performed after the experimental campaign (shown in Figure E.2), the average lithium content ($\approx$ 0.592 wt.% Li, average between 0.621 and 0.563 wt.%) increases with respect to the first analysis due to a better homogenization of the Pb-Li alloy during the ex-

Analysennr.			834 / 2019		
Bezeichnung			Probe 1 (13.11.2019)		
Parameter	Einheit	BG	MW	SD	±
Li	Massen (%)	0.069	0.490	0.034	0.010
Ti	Massen (%)	0.00004	< 0,00004	-	-
Cr	Massen (%)	0.0001	< 0,0001	-	-
Mn	Massen (%)	0.00002	< 0,00002	-	-
Fe	Massen (%)	0.0002	< 0,0002	-	-
Ni	Massen (%)	0.0002	< 0,0002	-	-
Cu	Massen (%)	0.0001	< 0,0001	-	-
Zn	Massen (%)	0.0002	< 0,0002	-	-
Ag	Massen (%)	0.0006	< 0,0006	-	-
Sn	Massen (%)	0.0003	< 0,0003	-	-
Sb	Massen (%)	0.0006	< 0,0006	-	-
Pb	Massen (%)	4.0	99.1	0.1	-
Bi	Massen (%)	0.0006	0.0061	0.0001	-
Summe	Massen (%)		99.5961		

BG: Bestimmungsgrenze; MW: Mittelwert; SD: Standardabweichung; ±: Messungenauigkeit

Figure E.1: Results of the composition analysis of the Pb-Li inserted in the facility (13/11/2019), performed at the Institute for Applied Materials (IAM-AWP) at the Karlsruhe Institute of Technology (KIT). BG: detection limit (from German *Bestimmungsgrenze*), MW: average value (from German *Mittelwert*), SD: standard deviation, ±: uncertainty of the measurement.

perimental campaign. However, the lithium fraction is still lower than the eutectic one. This is presumably because not all the Pb-Li batch (21.6 kg) has been used in the experiments, but 15.1 kg. This in addition to the Li inhomogeneity inside the alloy is assumed to be the reason for the low lithium content.

Furthermore, impurities (such as Fe, Ni, Cr, Cu) are found in the analyses after the experimental campaign. These are due to the dissolution of structural elements (from the stainless-steel structure and Cu gaskets) into the liquid Pb-Li. The impurities have to be considered because their presence may influence the solubility and mobility of deuterium inside the liquid metal, e.g. acting as a deuterium trap.

Analysennr.			751 / 2020			752 / 2020		
Bezeichnung			Probe 1			Probe 2		
Parameter	Einheit	BG	MW	SD	±	MW	SD	±
Li	Massen (%)	0.017	0.621	0.002	0.013	0.563	0.011	0.012
Ti	Massen (%)	0.00002	< 0,00002		-	< 0,00002		-
Cr	Massen (%)	0.00004	0.0002	0.0001	0.00004	0.0004	0.0004	0.00008
Mn	Massen (%)	0.00002	0.00008	0.00004	0.00002	0.00003	0.00003	0.00001
Fe	Massen (%)	0.00004	0.00011	0.00005	0.00003	0.00195	0.00177	0.00049
Ni	Massen (%)	0.00004	0.00344	0.00051	0.00034	0.00500	0.00030	0.00050
Cu	Massen (%)	0.00005	0.00091	0.00021	0.00009	0.00169	0.00006	0.00017
Zn	Massen (%)	0.00004	< 0,00004		-	< 0,00004		-
Ag	Massen (%)	0.0005	< 0,0005		-	< 0,0005		-
Sn	Massen (%)	0.0005	< 0,0005		-	< 0,0005		-
Sb	Massen (%)	0.0001	< 0,0001		-	< 0,0001		-
Pb	Massen (%)	1.8	98.8	0.1	-	98.8	0.2	-
Bi	Massen (%)	0.0002	0.0085	0.0035	-	0.0020	0.0001	-
Summe	Massen (%)		99.4342			99.3741		

BG: Bestimmungsgrenze; MW: Mittelwert; SD: Standardabweichung; ±: Messungenauigkeit

Figure E.2: Results of the composition analysis of the Pb-Li after the experimental campaign (19/08/2020), performed at the Institute for Applied Materials (IAM-AWP) at the Karlsruhe Institute of Technology (KIT). The sample 1 (Probe 1) was extracted from the surface of the Pb-Li and the sample 2 (Probe 2) was taken from the Pb-Li inside the transfer line, at the bottom of the lower chamber. BG: detection limit (from German *Bestimmungsgrenze*), MW: average value (from German *Mittelwert*), SD: standard deviation, ±: uncertainty of the measurement.

Appendix F

Pb-Li fluid-dynamics simulations

F.1 Calculation of pressure losses in upper chamber

F.1.1 The Bernoulli equation

The flow of Pb-Li exiting the nozzle is calculated by applying Bernoulli equation in two points: (1) the surface of the Pb-Li in the upper chamber and (2) the exit of the nozzle:

$$\rho g h_1 + p_1 + \frac{1}{2}\rho v_1^2 \;=\; \rho g h_2 + p_2 + \frac{1}{2}\rho v_2^2 + \delta p. \qquad (4.1^*)$$

Bernoulli equation describes the energy conservation between two points in a liquid using a simplified stream filament theory. It consists of the following terms (here given in units of pressure):

- The dynamic pressure ($\frac{1}{2}\rho v^2$): is the kinetic energy per unit volume of the fluid. It accounts for the pressure difference due to different speeds between the two points.
- The hydrostatic pressure ($\rho g h$): is the pressure exerted in a point of the fluid in equilibrium by the column of fluid above it due to gravity.
- The static pressure (p): is the pressure at the given point associated not with its motion, but with its state. In this case, it equals the pressure of the second medium at the given point (i.e. $p_1 =$ gas pressure in the upper chamber, $p_2 =$ gas pressure in the lower chamber).
- The pressure losses (δp): This term accounts for the irreversible losses along the way between the two points.

As explained in Section 4.1, the speed at the surface, v_1, and the pressure in the lower chamber, p_2, can be neglected.

F.1.2 Pressure losses

The pressure losses, δp, that occur to the Pb-Li along its way until exiting the nozzle are: friction losses at the walls of the pipe (δp_{p}), losses due to change in section (chamber to pipe, $\delta p_{\mathrm{c\text{-}p}}$, and pipe to nozzle, $\delta p_{\mathrm{p\text{-}n}}$), and losses inside the valve (δp_{v}). They are depicted in Figure F.1.

$$\delta p = \delta p_{\mathrm{c\text{-}p}} + \delta p_{\mathrm{p}} + \delta p_{\mathrm{v}} + \delta p_{\mathrm{p\text{-}n}}. \tag{4.4*}$$

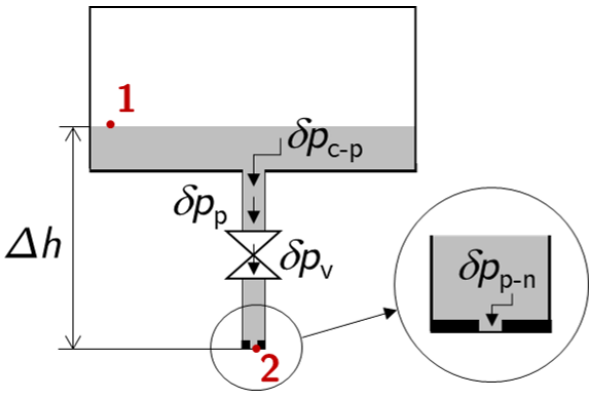

Figure F.1: Scheme of pressure losses.

F.1.2.1 Pressure loss due to cross-sectional area changes

The losses due to a contraction of the cross section (i) from chamber to pipe ($\delta p_{\mathrm{c\text{-}p}}$) and (ii) from pipe to nozzle ($\delta p_{\mathrm{p\text{-}n}}$) are calculated with the following equation:

$$\delta p_{i-j} = K_{ij}\rho\frac{v_j^2}{2} = K_{ij}\rho\frac{Q^2}{2A_j^2}\,, \quad \text{with } K_{ij} = 0.42\left(1-\frac{A_j}{A_i}\right) = 0.42\left(1-\frac{D_j^2}{D_i^2}\right), \tag{F.1}$$

where v is the speed, ρ is the Pb-Li density, Q is flow, A is cross-sectional area and D is diameter, attending to the corresponding section (i being the larger cross section: chamber or pipe, and j being the downstream smaller cross section: pipe or nozzle). K_{ij} is the loss coefficient relative to the ratio between the two changing cross-sectional areas.

F.1.2.2 Pressure loss due to friction

The losses due to friction, also called *viscous pressure losses*, along the pipe (δp_{p}) are calculated as follows:

$$\delta p_p = f_{\mathrm{D}}\frac{L_{\mathrm{p}}}{D_{\mathrm{p}}}\rho\frac{v_{\mathrm{p}}^2}{2} = f_{\mathrm{D_p}}\frac{L_{\mathrm{p}}}{D_{\mathrm{p}}}\rho\frac{Q^2}{2A_{\mathrm{p}}^2}, \tag{F.2}$$

where L is the length of the pipe or nozzle, correspondingly, and f_{D} is the *Darcy friction factor*, which is calculated differently for laminar and turbulent flows. Therefore, first, the *Reynolds number*, Re, has to be calculated:

$$\mathrm{Re} = \frac{\rho}{\mu} v D = \frac{\rho}{\mu} \frac{Q}{A} D, \tag{F.3}$$

where ρ is the density of the liquid and μ is its dynamic viscosity.

For laminar regime (when $\mathrm{Re} < 2300$), the Darcy friction factor is calculated with:

$$f_{\mathrm{D}} = \frac{64}{\mathrm{Re}}. \tag{F.4}$$

For turbulent flow ($\mathrm{Re} > 2300$)[1], the Darcy friction factor is calculated with the *Colebrook-White equation*:

$$\frac{1}{f_{\mathrm{D}}} = -2 \log \left(\frac{\varepsilon}{3.7D} + \frac{2.51}{\mathrm{Re}\sqrt{f_{\mathrm{D}}}} \right), \tag{F.5}$$

where ε is the roughness of the surface of the corresponding tube (pipe or nozzle). This equation is solved using the *Serghide's solution approximation*, as follows:

$$A = -2 \log \left(\frac{\varepsilon}{3.7D} + \frac{12}{\mathrm{Re}} \right), \tag{F.6}$$

$$B = -2 \log \left(\frac{\varepsilon}{3.7D} + \frac{2.51A}{\mathrm{Re}} \right), \tag{F.7}$$

$$C = -2 \log \left(\frac{\varepsilon}{3.7D} + \frac{2.51B}{\mathrm{Re}} \right), \tag{F.8}$$

$$\frac{1}{f_{\mathrm{D}}} = A - \frac{(B-A)^2}{C - 2B + A}. \tag{F.9}$$

In the current work, typical values of Reynolds number within the pipe are: $\mathrm{Re_p} \approx 400 - 1000$ (laminar).

F.1.2.3 Pressure loss in the valve

The pressure loss when the liquid passes through the valve is calculated with the following equation:

$$\delta p_{\mathrm{v}} = K_{\mathrm{v}} \rho \frac{v_{\mathrm{p}}^2}{2} = K_{\mathrm{v}} \rho \frac{Q^2}{2A_{\mathrm{p}}^2}, \tag{F.10}$$

where K_{v} is the loss coefficient given by the manufacturer of the valve, and the index p denotes characteristics corresponding to the pipe.

[1] For the purpose of simplification, $\mathrm{Re} = 2300$ is commonly used as the delimiting value between laminar and turbulent regimes. However, this is not an exact number (instead, there is a so-called *transition regime*). If the Reynolds number is close to this value, the flow must be further studied. But this is not the case in the simulations performed in the current work.

F.1.2.4 Pressure losses in the case of several nozzles

The simulation code *VST-experiment* is also adapted to the case of simulating a multi-nozzle array, with N nozzles. In this case, the Pb-Li flow through one nozzle is Q/N.

The pressure loss due to change in section is defined by equation (F.1), independently of the shape of the cross section of the nozzle (or its perimeter). Therefore, the area of all the nozzles is taken as a whole in the coefficient $K_{\text{p-n}}$, as follows:

$$\delta p_{\text{p-n (multi-nozzle)}} = K_{\text{pn}} \rho \frac{Q^2}{2(NA_{\text{n}})^2} \ , \quad \text{with } K_{\text{pn}} = 0.5 \left(1 - \frac{NA_{\text{n}}}{A_{\text{p}}}\right) \tag{F.11}$$

References of this section (F.1): [120–124].

F.2 Results of fitting simulations to the experiments

As an extension of Section 4.3.2 (Chapter 4), Figures F.2–F.9 show the resulting fitting curves for all runs (#12–#20) of the Pb-Li level in both chambers. The experimental data, depicted in dark blue, correspond to the experimental results (at which time the Pb-Li reaches each thermocouple). The light-blue curves show the evolution of the Pb-Li height simulated with the code *VST-experiment* with the values obtained from the fitting procedure (explained in Section 4.3). The error bars are given by the uncertainty of the position of the thermocouples. Two of the thermocouples in the lower chamber, RT044 and RT053, are removed from the fitting process because, in all runs, the Pb-Li is initially above the former and does not reach the latter.

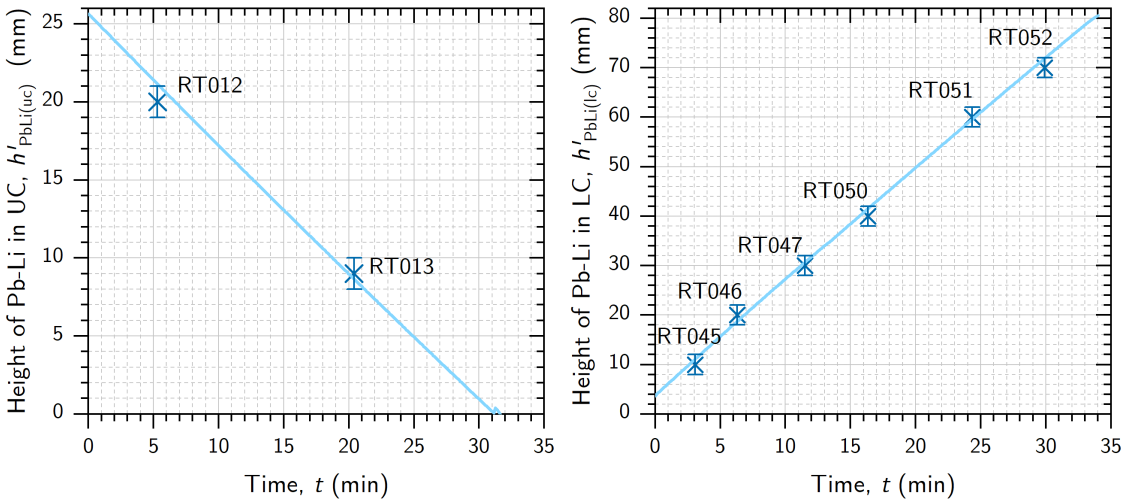

Figure F.2: Temporal evolution of Pb-Li height in the upper chamber (left) and the lower chamber (right) during run#12. Experimental data (dark blue) and simulation (light blue) with input values from fitting: $d_{\mathrm{n}} = 0.50\,\mathrm{mm}$, $V_{\mathrm{PbLi(uc)}_0} = 1.37\,\mathrm{l}$ ($p_{\mathrm{uc}_0} = 491.6\,\mathrm{mbar}$, $T_{\mathrm{PbLi}} = 400\,^{\circ}\mathrm{C}$, $V_{\mathrm{PbLi(uc)}_f} = 0\,\mathrm{l}$).

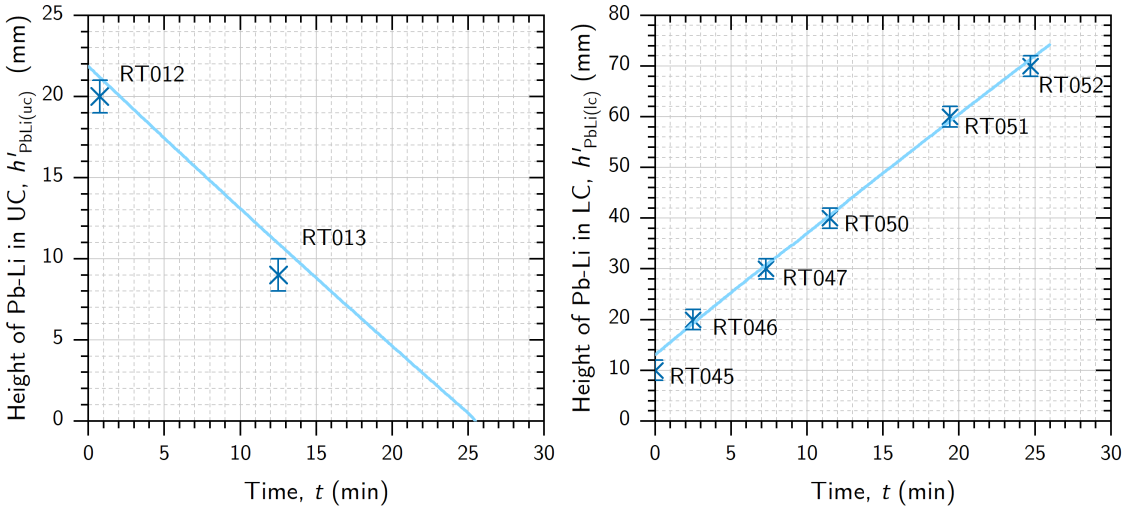

Figure F.3: Temporal evolution of Pb-Li height in the upper chamber (left) and the lower chamber (right) during run#14. Experimental data (dark blue) and simulation (light blue) with input values from fitting: $d_{\mathrm{n}} = 0.46\,\mathrm{mm}$, $V_{\mathrm{PbLi(uc)}_0} = 1.18\,\mathrm{l}$, $V_{\mathrm{PbLi(uc)}_f} = 0.09\,\mathrm{l}$ ($p_{\mathrm{uc}_0} = 933.4\,\mathrm{mbar}$, $T_{\mathrm{PbLi}} = 400\,^{\circ}\mathrm{C}$).

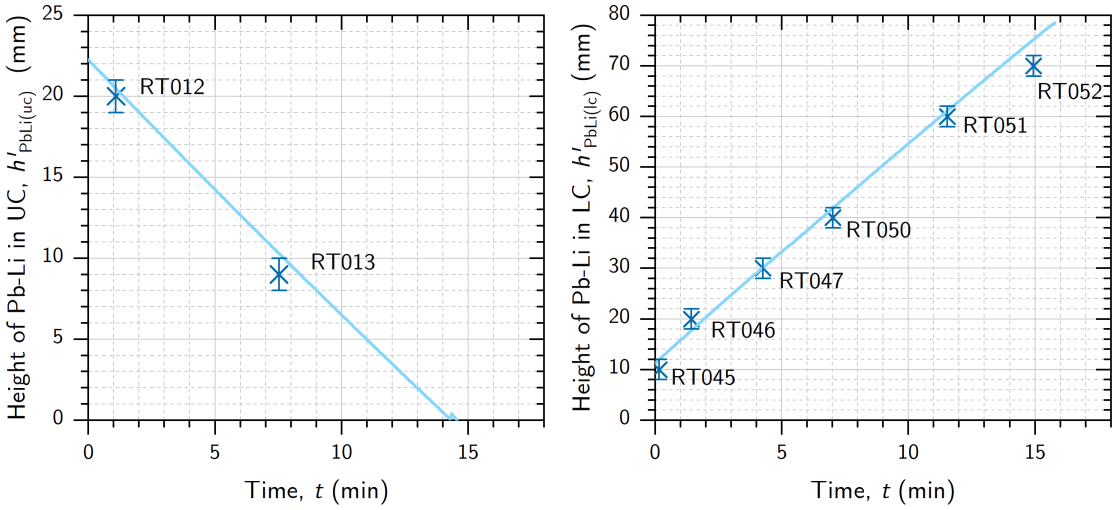

Figure F.4: Temporal evolution of Pb-Li height in the upper chamber (left) and the lower chamber (right) during run#15. Experimental data (dark blue) and simulation (light blue) with input values from fitting: $d_{\mathrm{n}} = 0.58\,\mathrm{mm}$, $V_{\mathrm{PbLi(uc)}_0} = 1.20\,\mathrm{l}$ ($p_{\mathrm{uc}_0} = 1454.0\,\mathrm{mbar}$, $T_{\mathrm{PbLi}} = 400\,^{\circ}\mathrm{C}$, $V_{\mathrm{PbLi(uc)}_f} = 0\,\mathrm{l}$).

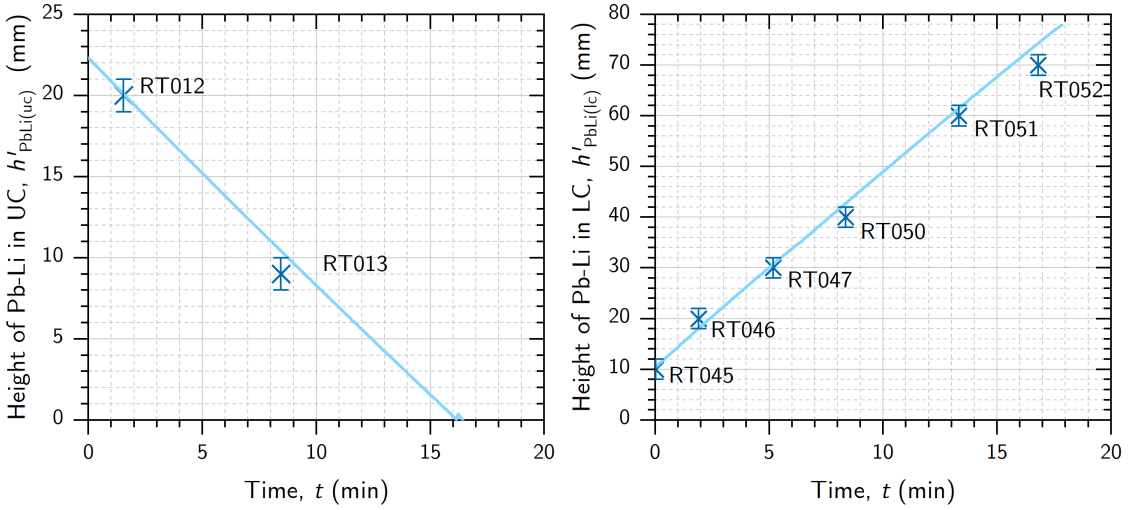

Figure F.5: Temporal evolution of Pb-Li height in the upper chamber (left) and the lower chamber (right) during run#16. Experimental data (dark blue) and simulation (light blue) with input values from fitting: $d_{\mathrm{n}} = 0.59\,\mathrm{mm}$, $V_{\mathrm{PbLi(uc)}_0} = 1.20\,\mathrm{l}$ ($p_{\mathrm{uc}_0} = 940.0\,\mathrm{mbar}$, $T_{\mathrm{PbLi}} = 400\,^{\circ}\mathrm{C}$, $V_{\mathrm{PbLi(uc)}_f} = 0\,\mathrm{l}$).

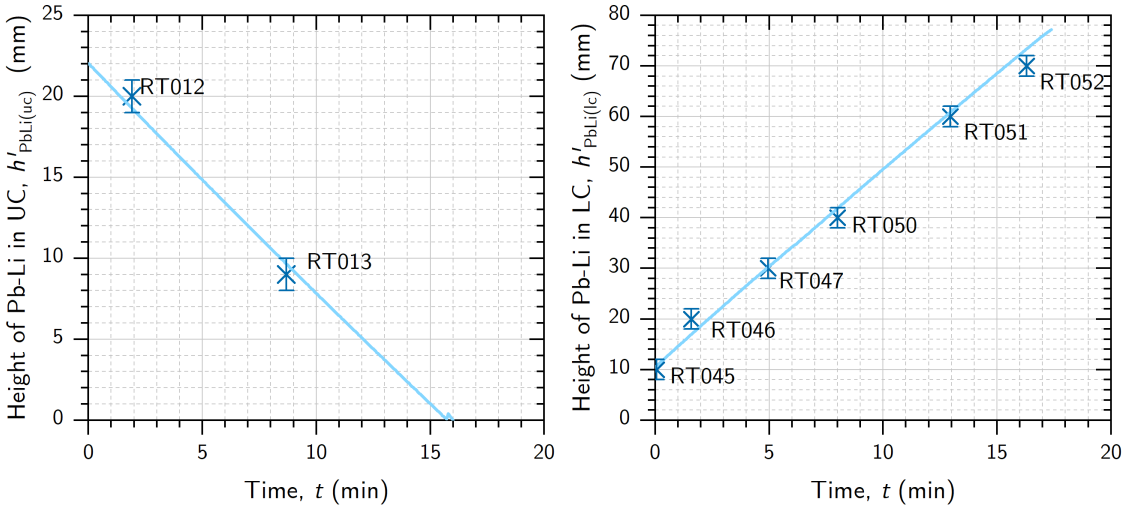

Figure F.6: Temporal evolution of Pb-Li height in the upper chamber (left) and the lower chamber (right) during run#17. Experimental data (dark blue) and simulation (light blue) with input values from fitting: $d_{\mathrm{n}} = 0.59\,\mathrm{mm}$, $V_{\mathrm{PbLi(uc)}_0} = 1.19\,\mathrm{l}$ ($p_{\mathrm{uc}_0} = 939.8\,\mathrm{mbar}$, $T_{\mathrm{PbLi}} = 400\,^{\circ}\mathrm{C}$, $V_{\mathrm{PbLi(uc)}_f} = 0\,\mathrm{l}$).

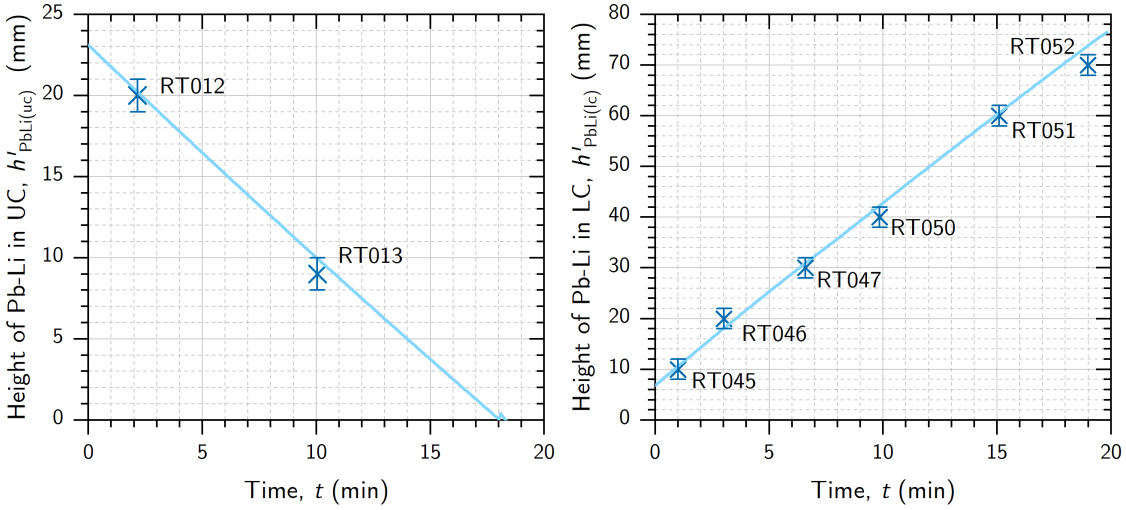

Figure F.7: Temporal evolution of Pb-Li height in the upper chamber (left) and the lower chamber (right) during run#18. Experimental data (dark blue) and simulation (light blue) with input values from fitting: $d_{\mathrm{n}} = 0.52\,\mathrm{mm}$, $V_{\mathrm{PbLi(uc)}_0} = 1.24\,\mathrm{l}$ ($p_{\mathrm{uc}_0} = 1452.5\,\mathrm{mbar}$, $T_{\mathrm{PbLi}} = 400\,^{\circ}\mathrm{C}$, $V_{\mathrm{PbLi(uc)}_f} = 0\,\mathrm{l}$).

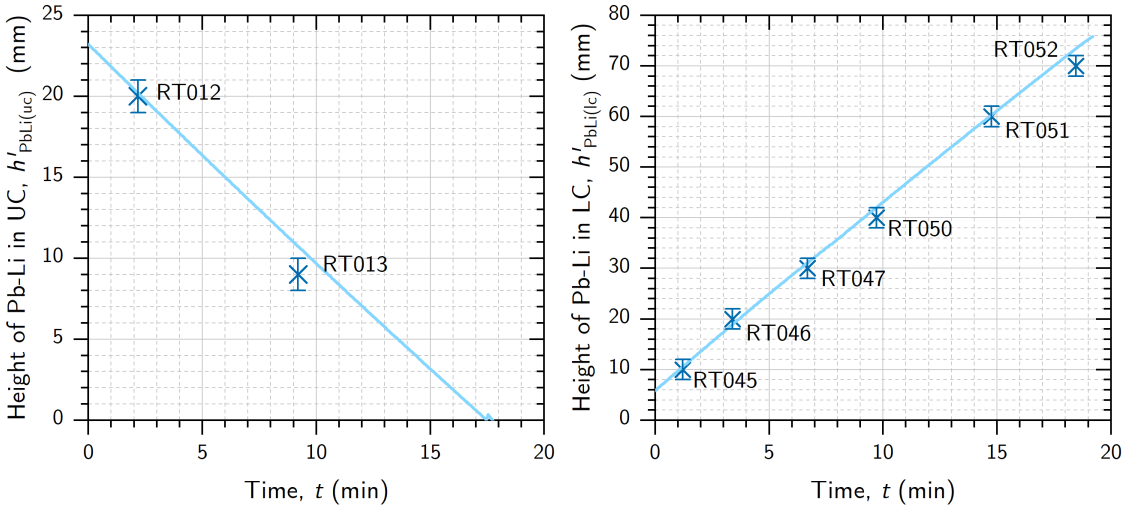

Figure F.8: Temporal evolution of Pb-Li height in the upper chamber (left) and the lower chamber (right) during run#19. Experimental data (dark blue) and simulation (light blue) with input values from fitting: $d_{\mathrm{n}} = 0.58\,\mathrm{mm}$, $V_{\mathrm{PbLi(uc)}_0} = 1.25\,\mathrm{l}$ ($p_{\mathrm{uc}_0} = 937.0\,\mathrm{mbar}$, $T_{\mathrm{PbLi}} = 400\,^{\circ}\mathrm{C}$, $V_{\mathrm{PbLi(uc)}_f} = 0\,\mathrm{l}$).

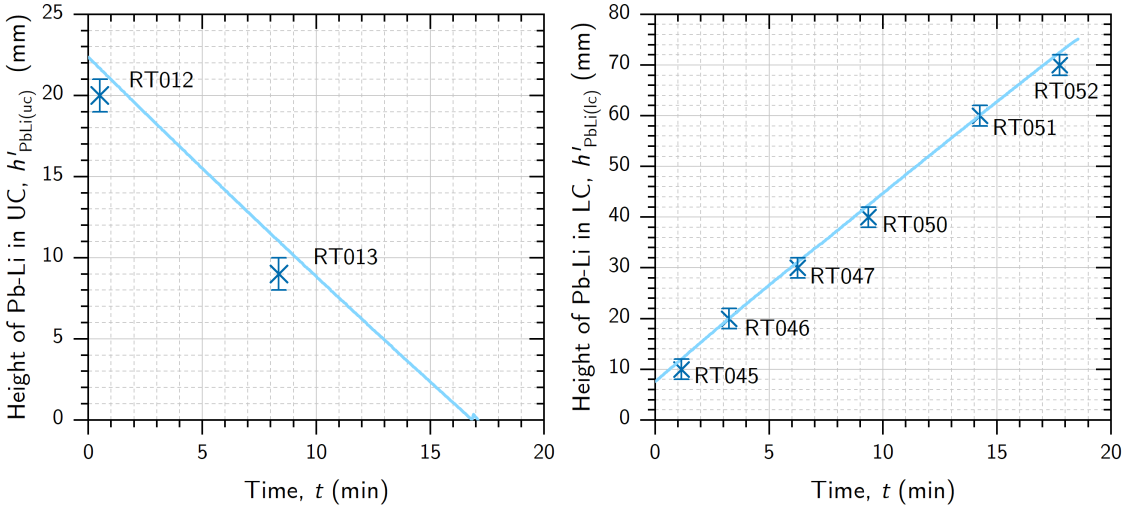

Figure F.9: Temporal evolution of Pb-Li height in the upper chamber (left) and the lower chamber (right) during run#20. Experimental data (dark blue) and simulation (light blue) with input values from fitting: $d_{\mathrm{n}} = 0.57\,\mathrm{mm}$, $V_{\mathrm{PbLi(uc)}_0} = 1.20\,\mathrm{l}$ ($p_{\mathrm{uc}_0} = 1022.0\,\mathrm{mbar}$, $T_{\mathrm{PbLi}} = 400\,^{\circ}\mathrm{C}$, $V_{\mathrm{PbLi(uc)}_f} = 0\,\mathrm{l}$).

Appendix G

Calibration of the pressure sensor in the upper chamber, RP010, with temperature

G.1 Motivation

The signal of the pressure sensor located at the upper chamber, RP010, is found to be temperature sensitive. As an example, Figure G.1 shows the measured data recorded during a long evacuation of the upper chamber, performed with the chamber at 400 °C. Since the chamber is continuously under evacuation, the pressure is constant (= zero). Neglecting the offset to zero (which is an simple correction), in this figure, one can easily see how the pressure output is varying as a function of the temperature of the sensor (given by thermocouple RT014). The uncertainty shown in the figure is calculated with the values reported by the manufacturer (given in Table G.1). This uncertainty is so large (even under normal conditions) that is un-

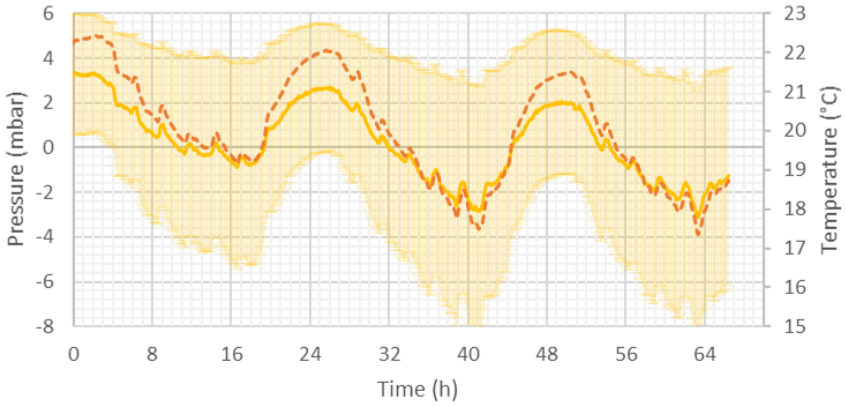

Figure G.1: Measured pressure signal from RP010 (solid yellow) and temperature at the sensor (dashed orange) recorded during constant evacuation of the upper chamber (evacuation #1). The uncertainty of the pressure signal is calculated with the data reported in Table G.1

Table G.1: Main characteristics of the pressure sensor in upper chamber, RP010 (repetition of Table 3.2)

Parameter	Value
Model:	PTA227, EFE
Full Scale (F.S.):	3 bar
Non-linearity and hysteresis:	±0.016% F.S.: 0.48 mbar
Non-repeatability:	±0.02% F.S.: 0.60 mbar
Thermal zero and sensitivity shifts:	±0.02% F.S./°C: 0.60 mbar/°C
Max. operating temperature:	125 °C

acceptable to analyse the results. Furthermore, the output pressure is so sensitive to the sensor temperature that it impedes the analysis of small pressure changes in the experiments. However, Figure G.1 also shows that the pressure signal varies linearly with the temperature at the sensor.

Therefore, an analysis is performed with data of various evacuation periods, similar to the one shown in Figure G.1, in order to find a correction factor that: (i) rectifies the deviation of the output signal due to temperature and (ii) diminishes the uncertainty of the measurements.

G.2 Temperature correction factor

Five different evacuation periods are analysed (see their relevant characteristics in Table G.2). An iteration method is used to determine the correction factor as follows:

1. A correction factor, X (mbar/°C), is given.
2. The pressure signal is corrected with X (see solid blue in Figure G.2).
3. A linear fit is applied to the corrected pressure (dotted blue in Figure G.2).
4. The iteration follows until finding the factor X that minimizes the slope of the linear fit. *Note that since the gas pressure in the chamber is constant (and zero)*[1]*, the slope of the linear fit has to be zero.*

[1]During evacuations performed in the lower chamber (whose volume is about 5 times larger than the one of the upper chamber), a vacuum in the order of $\sim 10^{-5}$ mbar is reached within the first minutes and remains constant. Therefore, the vacuum achieved in the upper chamber is assumed at least as good.

From this analysis, the correction factor **-1.2 mbar/°C** is obtained. Figure G.2 shows the resulting corrected pressure (solid blue) for the evacuation #1, with the new error bars: ±1.08 mbar (neglecting the effect of temperature). The slopes of the fits obtained with this factor for each experiment are given in Table G.2. The factor is valid for the range of temperature at the sensor: 17.4−22.4 °C.

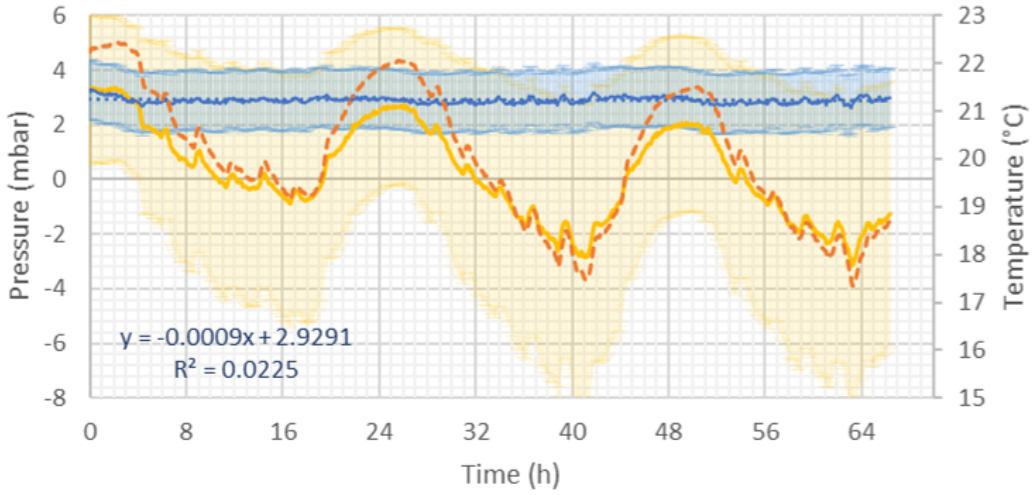

Figure G.2: Pressure output signal from RP010 (solid yellow) and temperature at the sensor (dashed orange), idem as Figure G.1. In solid blue, pressure corrected with factor -1.2 mbar/°C, with uncertainty omitting the thermal effects. In dashed blue, linear fit of the pressure corrected curve.

Table G.2: Characteristics of the evacuations periods, whose data are used for the determination of the correction factor -1.2 mbar/°C

Evacuation	Duration (h)	Temperature variation at the sensor (°C)	Slope of the linear fit after correction (mbar/min)
#1 (19.10.18)	66.4	17.4 − 22.4	-1×10^{-5}
#2 (23.10.18)	16.3	20.1 − 21.1	-3×10^{-5}
#3 (24.10.18)	16.8	20.2 − 21.1	$+8 \times 10^{-6}$
#4 (25.10.18)	17.6	20.1 − 21.5	-1×10^{-4}
#5 (26.10.18)	65.2	17.7 − 21.3	-1×10^{-5}

Appendix H

High speed camera

H.1 Settings and overview

A high-speed camera, Memrecam HX-3 (with software HXLink SP-642), is used to record the falling droplets. A LED module of 9 W (with an intermediate diffuser) lights the lower chamber from the window opposite to the camera, to maximize the contrast of the droplets. The camera can take up to 1.3×10^6 fps (frames per second). However, in practice, the maximum frequency of the frames and, more specifically, the opening of the shutter are limited by the amount of light.

For every shot, the camera is placed at 24.5 cm from its base to the surface of the window in the lower chamber (43.2 cm to the center of the lower chamber). The frames are taken with the configuration shown in Tables H.1 and H.2. Decreasing the aperture increases the range (depth) under focus, which is necessary in case the line of droplets deviate from the center. However, it also decreases the amount of light. Thus, the aperture is set to f/5.6, which maintains under focus a depth range of around one centimeter. The GXC is a function of the camera to enhance the sensitivity by combining four pixels into one, which can be seen as an equivalent to increasing the amount of light (this option affects with a factor of two the pixel-to-

Table H.1: General settings of the high-speed camera used during all shots.

Parameter	Value
Distance to window	24.5 cm
Focus	0.45
Opening	100 %
Aperture	f/5.6
GXC	on (off in run#12)

Table H.2: Configuration for each run.

Run	# of shots	Frame rate ($\mathrm{fr\,s^{-1}}$)	Shutter speed ($\mathrm{s^{-1}}$)
Run#12	Testing high-speed camera		
Run#13	14	2000	50k, 100k
Run#14	21	5000	50k, 100k
Run#15	18	5000	20k, 50k
Run#16	19	5000	10k, 20k, 50k, 100k
Run#17	21	5000	10k, 20k, 50k, 100k
Run#18	23	5000	10k, 20k, 50k, 100k
Run#19	23	5000	open, 10k, 20k, 50k
Run#20	No visibility		

mm conversion).

During each run, shots are taken at around every minute at different shutter speeds. Since the visibility inside the chamber is decreasing with time (with each run), the shutter speed is also decreased to record frames with better quality. Frames at higher speed are still taken in order to compare experiments relying on a possible later enhancement of the images.

Figure H.1 shows two frames taken at different shutter speeds: (a) 1k and (b) 2k fps. Firstly, the difference in amount of light, and contrast in the images, can be observed. In order to achieve quality images at higher shutter speed, a more powerful light is used for the next campaign and it is placed at the window opposite to the camera (in Figure H.1 the light source is placed at the left window). Secondly, a blurry effect is observed in Figure H.1 (a) with respect to (b). This is due to the time that the shutter is open capturing the image with respect to the speed of the droplets. The droplets shown in Figure H.1 (b) appear elongated along their falling line also due to this effect.

The image of a droplet falling at $v = 4\,\mathrm{m\,s^{-1}}$, recorded at $\nu_{\mathrm{sh}} = 50\mathrm{k\,s^{-1}}$, is elongated by 0.08 mm (7 % of its diameter). Therefore, $50\mathrm{k\,s^{-1}}$ is chosen as the minimum shutter speed. However, since the visibility decreases, later shots are taken at slower shutter speeds (as shown in Table H.2).

H.2 Focus and px-to-mm conversion

Since the objective of the camera cannot be focused directly on a moving object (falling droplets), previous tests are performed to record the focus on the centre of

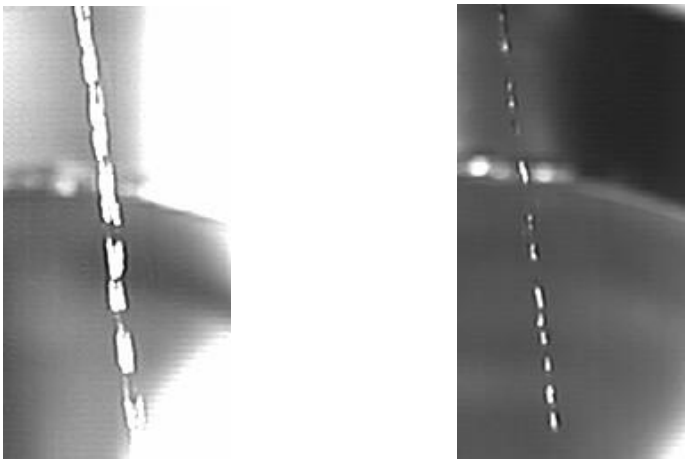

(a) $1000\,\mathrm{fr\,s^{-1}}$ **(b)** $2000\,\mathrm{fr\,s^{-1}}$

Figure H.1: Frames of run#01 in previous campaign taken at different frame rates, with the shutter speed *open* (equal to frame rate).

the chamber for different positions of the camera. This is achieved by means of a ruler placed in the centre of the lower chamber before the assembly. Pictures of the ruler are taken at various distances from the base of the camera to the window of the lower chamber, from 30 cm to 70 cm. With the pictures of the ruler not only the focus is calibrated, but also the pixel-to-millimetre conversion is obtained. Figure H.2 shows the resulting conversion factor for each distance (data points). A linear fit is performed (dashed line), to determine the pixel-to-millimetre conversion for each distance. The conversion factor for 24.5 cm is: $f = 0.1419\,\mathrm{mm\,px^{-1}}$.

The tests have been done with the GXC on and the px-to-mm conversion has been checked to be constant and equal along the horizontal and vertical lines.

The uncertainty due to error in the distance camera–droplets is calculated with the function f. The uncertainty corresponding to ± 1 cm distance is $\pm 0.0042\,\mathrm{mm\,px^{-1}}$.

H.3 Frames of the runs

Figures H.3, H.4, H.5 and H.6 show frames of runs #13–#19 at 1 and 15 min. They are a sample of each shot that has been used to evaluate the speed of the droplets in Section 4.4.3. In these figures, it is observed how the quality of the images is gradually lost due to the condensation of Pb-Li at the windows. Many of the frames shown (Figures H.4, H.5 and H.6) are processed in order to enhance the quality of the image and facilitate the analysis. The image processing consists in increasing the gain, the enhance and (in some of them) the gamma. The frames of run#19 have the maximum enhancement possible with the program used, *HX-link*,

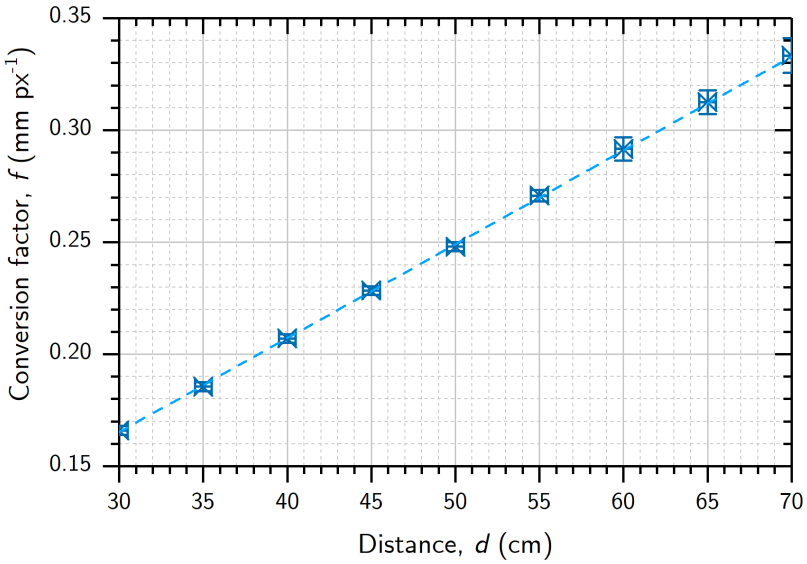

Figure H.2: Pixel-to-millimeter conversion factor as a function of the distance of the base of the camera to the surface of the window. Data points obtained from analysis of the frames (data points), linear fit (dashed line): $f = 0.0042\,d + 0.039$, $R^2 = 0.999$.

(the original pictures are completely dark). Figure H.6 (c) and (d) show the liquid jet that exits the nozzle and breaks into droplets during runs#12 and #14.

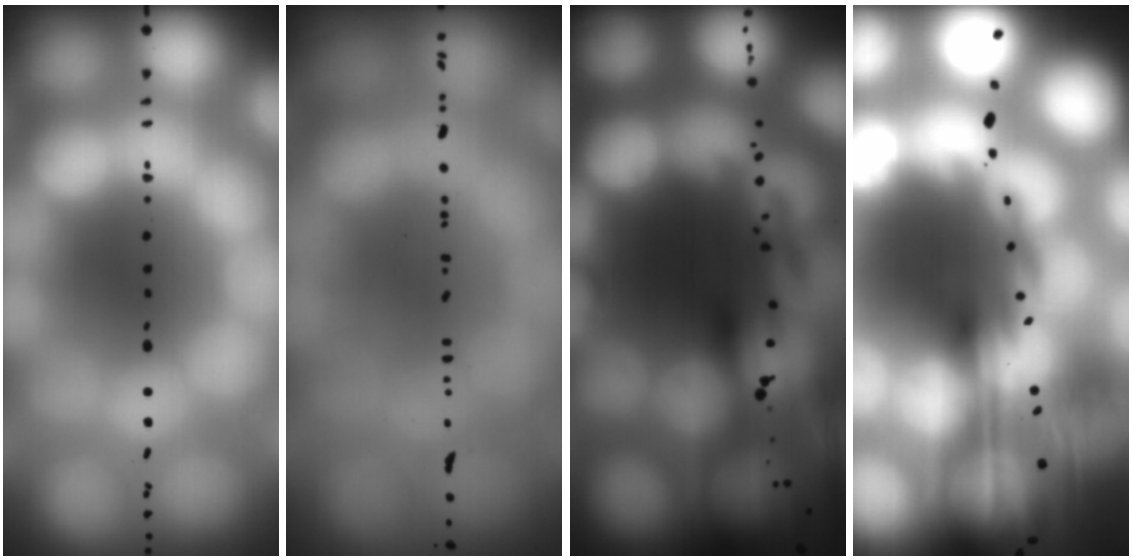

(a) Run#13 at 1 min, $\nu_{sh} = 100\text{k}\,\text{s}^{-1}$ **(b)** Run#13 at 15 min, $\nu_{sh} = 100\text{k}\,\text{s}^{-1}$ **(c)** Run#14 at 1 min, $\nu_{sh} = 100\text{k}\,\text{s}^{-1}$ **(d)** Run#14 at 15 min, $\nu_{sh} = 50\text{k}\,\text{s}^{-1}$

Figure H.3: Frames of runs #13 and #14. Original frames.

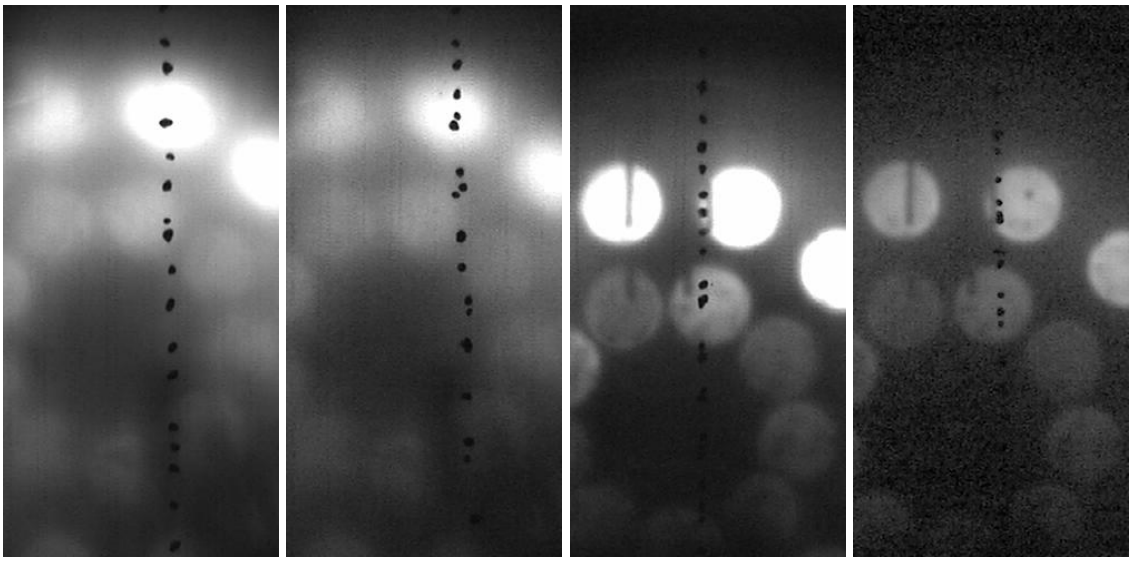

(a) Run#15 at 1 min, $\nu_{sh} = 20\text{k}\,\text{s}^{-1}$ **(b)** Run#15 at 15 min, $\nu_{sh} = 50\text{k}\,\text{s}^{-1}$ **(c)** Run#16 at 1 min, $\nu_{sh} = 20\text{k}\,\text{s}^{-1}$ **(d)** Run#16 at 15 min, $\nu_{sh} = 100\text{k}\,\text{s}^{-1}$

Figure H.4: Frames of runs #15 and #16. All frames are processed to enhance the quality of the image.

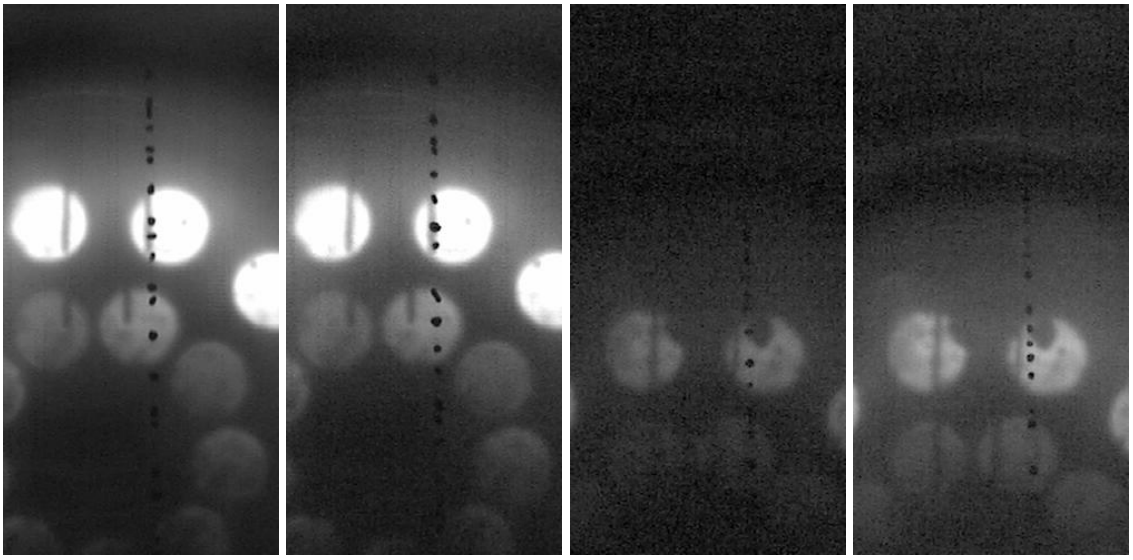

(a) Run#17 at 1 min, $\nu_{sh} = 10\text{k}\,\text{s}^{-1}$ **(b)** Run#17 at 15 min, $\nu_{sh} = 20\text{k}\,\text{s}^{-1}$ **(c)** Run#18 at 1 min, $\nu_{sh} = 50\text{k}\,\text{s}^{-1}$ **(d)** Run#18 at 15 min, $\nu_{sh} = 20\text{k}\,\text{s}^{-1}$

Figure H.5: Frames of runs #17 and #18. All frames are processed to enhance the quality of the image.

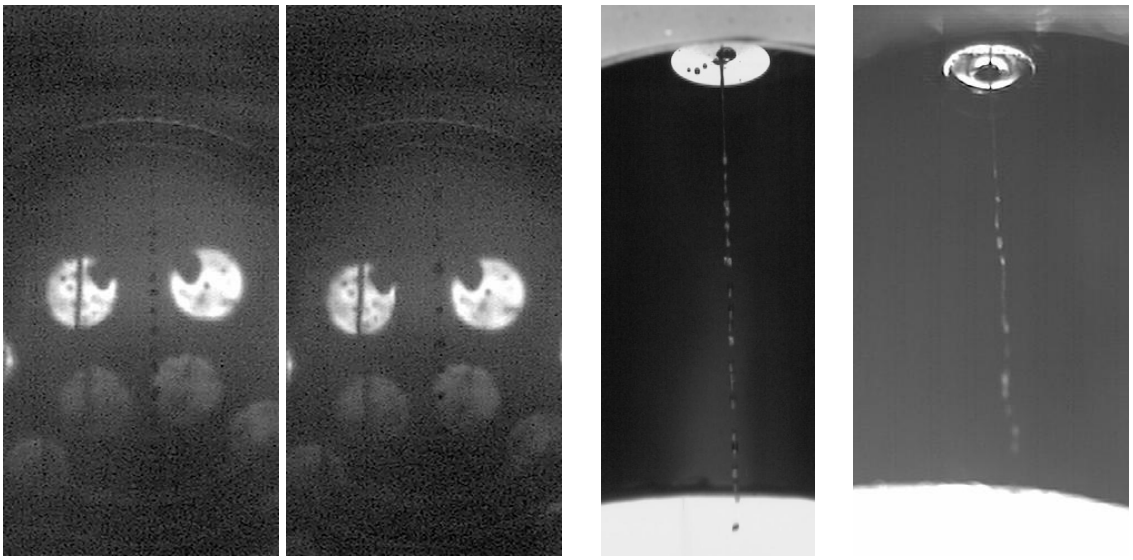

(a) Run#19 at 1 min, $\nu_{sh} = 10\text{k}\,\text{s}^{-1}$ **(b)** Run#19 at 15 min, $\nu_{sh} = 10\text{k}\,\text{s}^{-1}$ **(c)** Run#12, liquid jet, $\nu_{sh} = 2\text{k}\,\text{s}^{-1}$ **(d)** Run#14, liquid jet, $\nu_{sh} = 2\text{k}\,\text{s}^{-1}$

Figure H.6: Frames of run #19 and the liquid jet captured in runs #12 and #14. All frames are processed to enhance the quality of the image.

Appendix I

Additional experimental data of D_2 dissolution

I.1 Dissolution experiments

Figure I.1 shows the temporal evolution of pressure and temperature of the gas in the upper chamber during the dissolution phase of run#17, as representative of the two experiments with initial dissolving pressure $p_0 \approx 500\,\text{mbar}$ (runs #17 and #18). Since the temperature only varies $1.5 - 2\,\text{K}$ (within the first hours) in comparison with the uncertainty of about $\pm 8\,\text{K}$, the temperature is assumed constant.

The average values of T_{gas} for all runs are given in Table I.1. Note that the

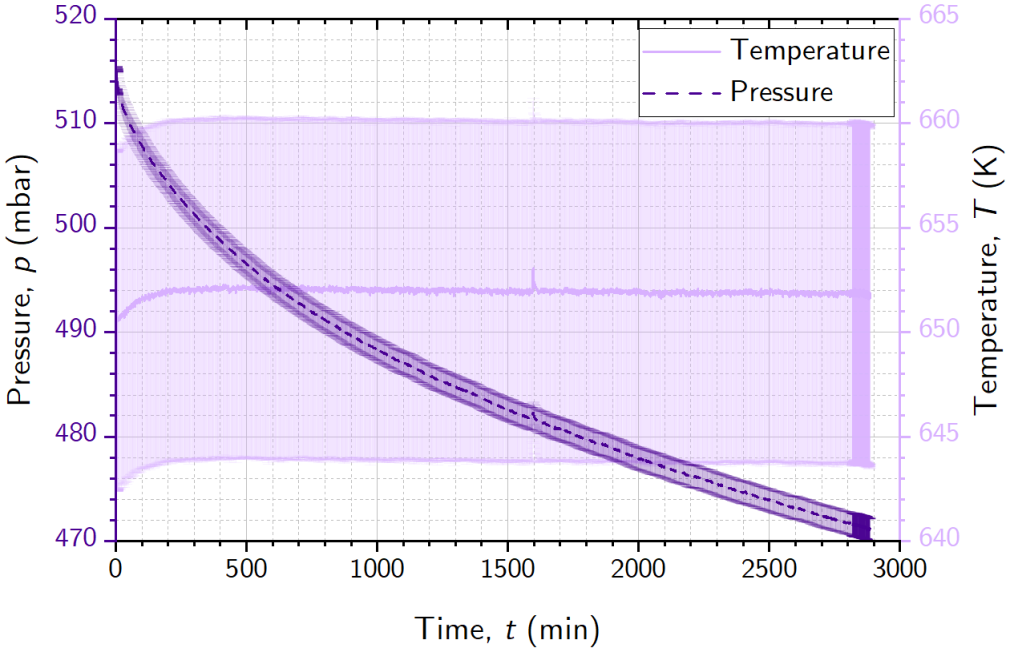

Figure I.1: Temporal evolution of gas pressure (p) and gas temperature (T) measured during the dissolution phase in run#17.

uncertainty cannot be decreased with the average, since it is of type *offset*.

The volumes of Pb-Li and gas in the upper chamber during the dissolution phase for all runs are summarized in Table I.1. Additionally, the total amount of gas diffused into the metals (Pb-Li and stainless-steel walls) is also given in Table I.1.

Figure I.2 shows the evolution of n (amount of gas) in run#13. The error bars are divided into two colours to differentiate the contribution of the error in pressure (dark purple), which is about 7 % of the total resulting error.

Table I.1: Summary of experimental values used in calculations. Volume of the Pb-Li (V_{PbLi}), volume of the gas (V_{gas}), average temperature of the gas (T_{gas}) and total amount of deuterium lost into the metals ($-\Delta n$). (See also Tables 4.3, 4.5 and 5.2.)

Run	V_{PbLi} (l)	V_{gas} (l)	T_{gas} (K)	$-\Delta n$ (mol)
Run#13	1.23 ± 0.03	3.65 ± 0.04	654.1 ± 8.2	$(5.13 \pm 0.13) \times 10^{-3}$
Run#14	1.18 ± 0.03	3.70 ± 0.03	652.8 ± 8.2	$(4.94 \pm 0.13) \times 10^{-3}$
Run#15	1.20 ± 0.04	3.68 ± 0.05	651.7 ± 8.1	$(5.29 \pm 0.14) \times 10^{-3}$
Run#17	1.19 ± 0.03	3.69 ± 0.04	651.9 ± 8.1	$(2.95 \pm 0.12) \times 10^{-3}$
Run#18	1.24 ± 0.03	3.64 ± 0.04	652.4 ± 8.1	$(2.90 \pm 0.11) \times 10^{-3}$
Run#19	1.25 ± 0.03	3.63 ± 0.04	653.5 ± 8.2	$(5.67 \pm 0.14) \times 10^{-3}$

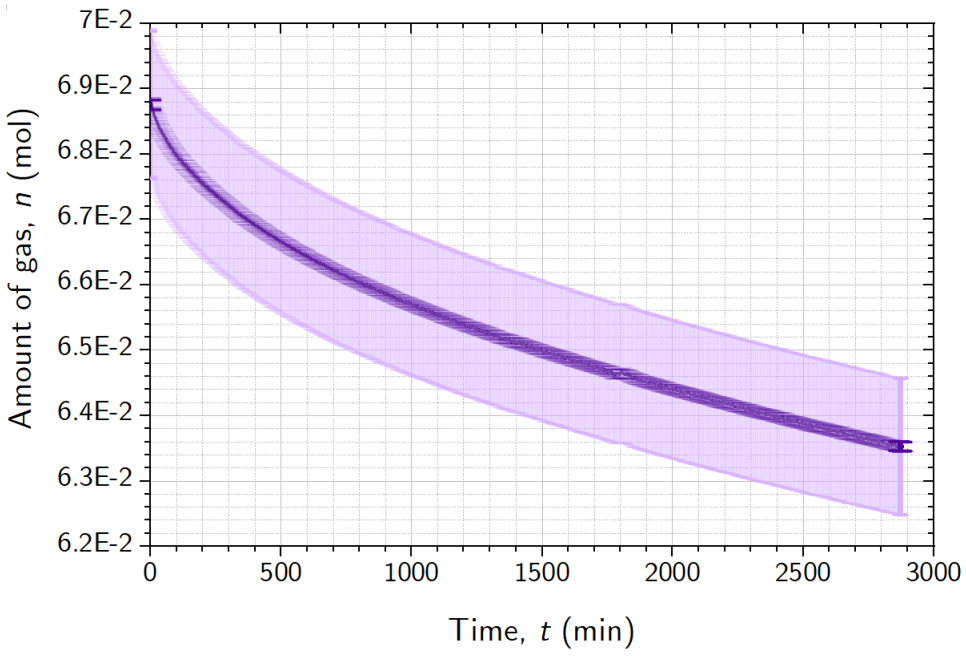

Figure I.2: Temporal evolution of amount of gas measured in the upper chamber during the dissolution phase in run#13. Error bars: contribution of p (dark error bars), contribution of V and T (depicted in lighter colour).

I.2 Permeation experiments

Figure I.3 shows the temporal evolution of pressure and temperature during the permeation experiment (without Pb-Li) perm#26 (with $p_0 \approx 500\,\text{mbar}$).

Figures I.4 and I.5 show the temperature profile of the stainless steel (ss) used in the calculations for the experiments $p_0 \approx 1000\,\text{mbar}$ and $p_0 \approx 500\,\text{mbar}$, respectively.

Figures I.6 and I.7 show the temperature of the Pb-Li free surface: T_1 (top flange) and T_2 (upper wall), respectively, as defined in Figure 5.2 (b). In Figure I.7, the values shown are in accordance between each other (permeation vs corresponding dissolution runs). However, in Figure I.6, the difference between the permeation experiments and their corresponding dissolution runs is larger than the experimental uncertainties. This is due to the different profiles, which cannot be adjusted without sacrificing the other values (T_2). The upper flange is the surface through which less deuterium permeates due to its low temperature and large thickness. Therefore, the compromise adopted is to enlarge the error bars of T_1 in the permeation experiments in the calculations. This way, the experimental results of the permeation experiments can be used to evaluate the amount of deuterium lost through the Pb-Li–free walls.

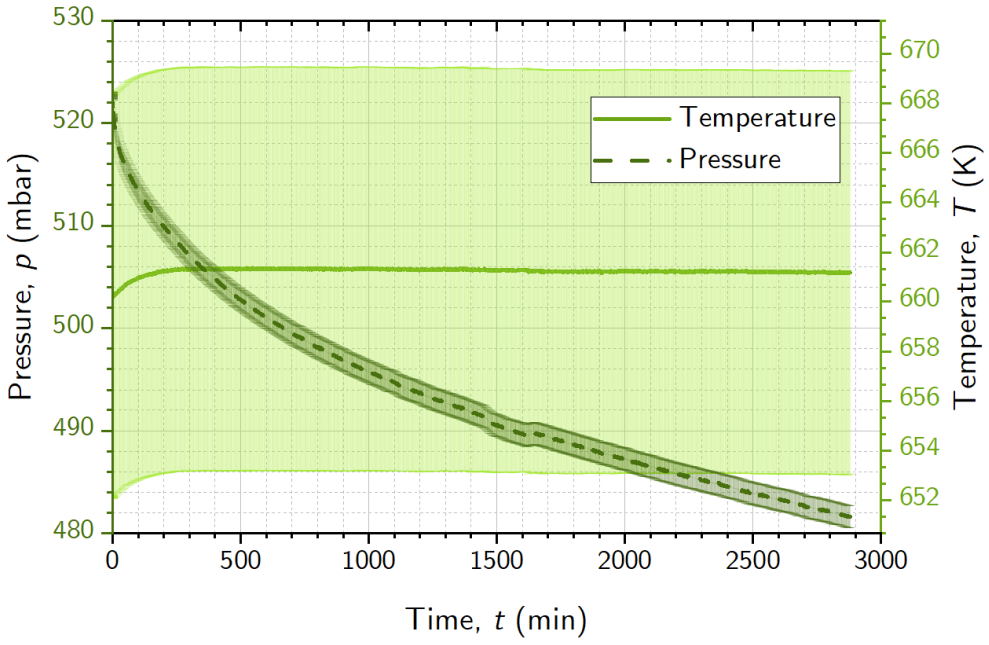

Figure I.3: Temporal evolution of gas pressure (p) and gas temperature (T) measured during the permeation experiment perm#26.

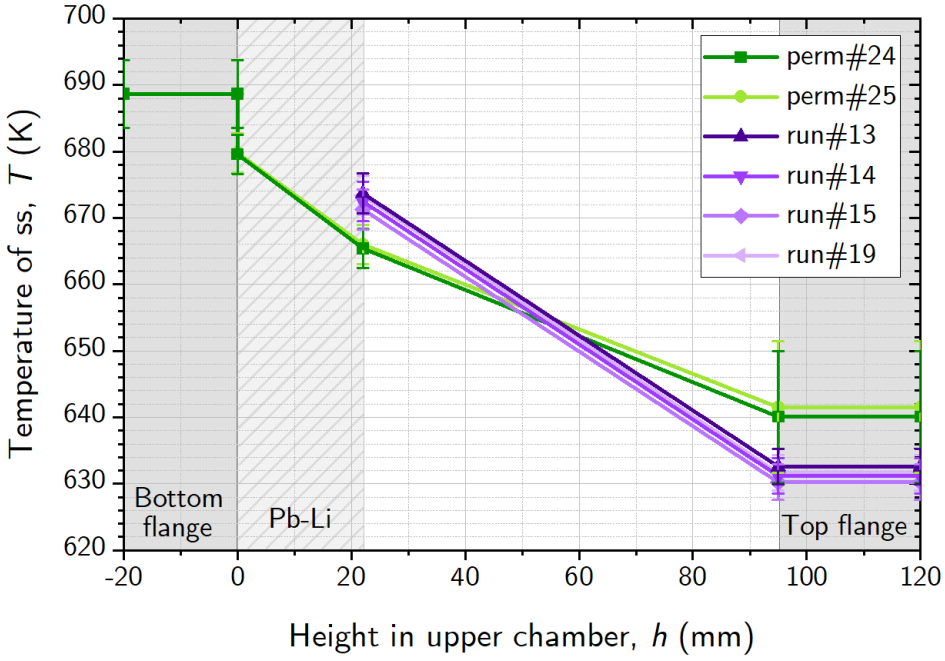

Figure I.4: Temperature profile of the stainless steel (ss) used in calculations of permeation experiments (no Pb-Li) and dissolution runs (with Pb-Li) at $p_0 \approx 1000\,\text{mbar}$. The error bars of permeation experiments at the top flange are artificially increased in order to comply with requirements (see Figure I.6).

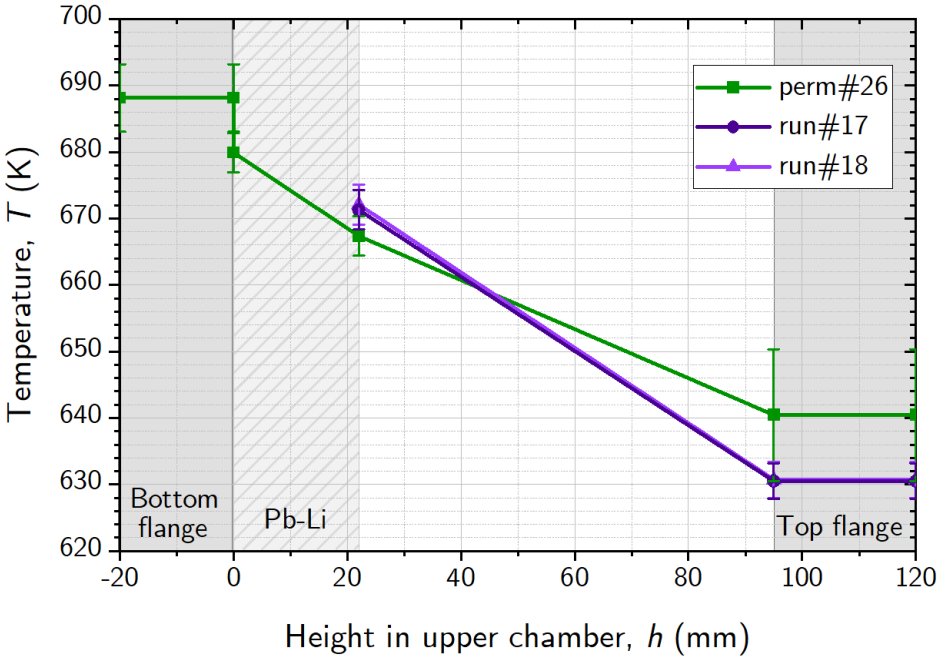

Figure I.5: Temperature profile of the stainless steel (ss) used in calculations of permeation experiments (no Pb-Li) and dissolution runs (with Pb-Li) at $p_0 \approx 500\,\text{mbar}$. The error bars of perm#26 at the top flange are artificially increased in order to comply with requirements (see Figure I.6).

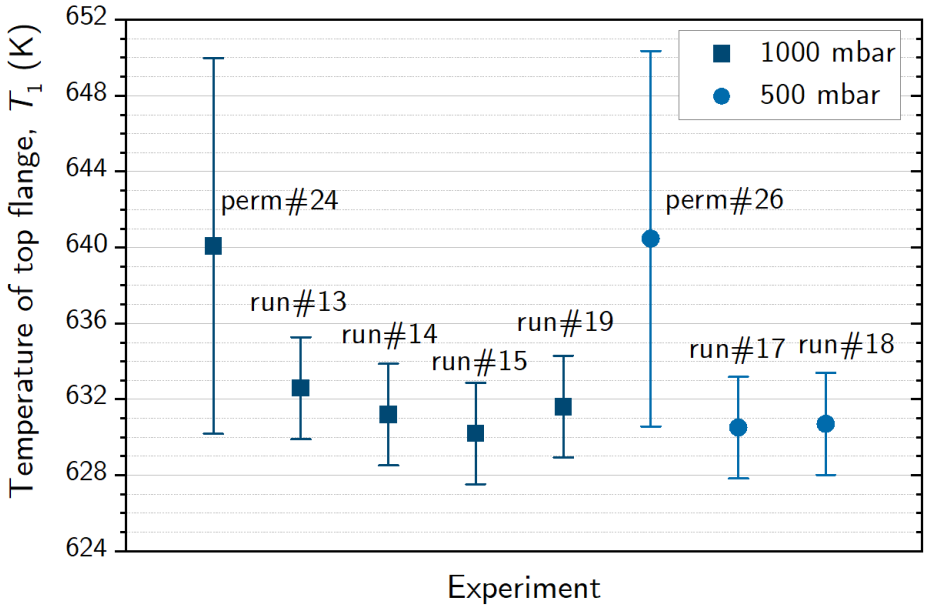

Figure I.6: Temperature of the top flange, T_1, used in the calculations (values from RT010) during experiments at 1000 mbar (squares) and experiments at 500 mbar (circles). The error bars of perm#24 and perm#26 are artificially increased in order to comply with the corresponding temperatures of the dissolution runs.

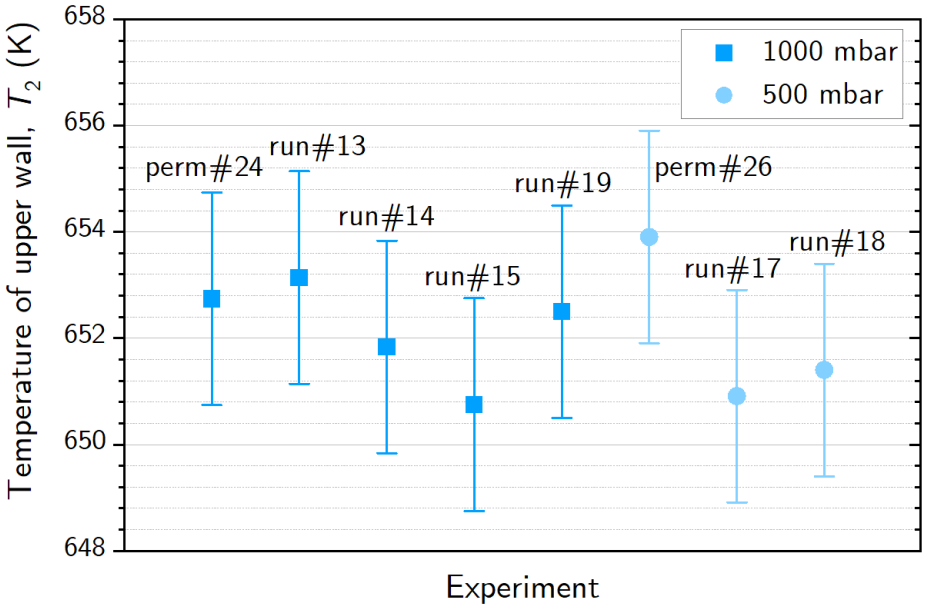

Figure I.7: Temperature of the upper wall, T_2, used in the calculations (average between RT010 and RT012) during experiments at 1000 mbar (squares) and experiments at 500 mbar (circles).

Appendix J

Additional experimental data of D_2 extraction

J.1 Gas temperature in the lower chamber

Table J.1 shows the gas temperature in each region of the lower chamber during the extraction runs. The division into regions of the lower chamber is shown in Figure 6.1.

Table J.1: Gas temperature in each region of the lower chamber during the extraction experiments. See regions in Figure 6.1.

Run	T_1 (K)	T_2 range (K)	T_3 (K)	T_{sensor} (K)
run#13	610.5 ± 11	$(545.0 - 538.6) \pm 9$	295.4 ± 2.2	301.6 ± 2.2
run#14	610.5 ± 11	$(542.8 - 539.5) \pm 9$	295.7 ± 2.2	301.5 ± 2.2
run#15	618.7 ± 11	$(544.7 - 539.7) \pm 9$	296.8 ± 2.2	302.5 ± 2.2
run#17	618.7 ± 11	$(544.9 - 539.2) \pm 9$	295.6 ± 2.2	301.5 ± 2.2
run#18	618.7 ± 11	$(544.3 - 537.9) \pm 9$	295.7 ± 2.2	302.3 ± 2.2
run#19	618.7 ± 11	$(544.6 - 538.1) \pm 9$	297.4 ± 2.2	304.0 ± 2.2
run#20	618.7 ± 11	$(545.6 - 539.7) \pm 9$	299.0 ± 2.2	305.0 ± 2.2

J.2 Evaluation of the background curves

The background curves (as shown in Figures 6.5 and 6.8) are calculated from a fit of the slope of the background data points. The slope of the background of run#13 is adjusted with a linear fit, resulting in:

$$\frac{\delta n}{\delta t} = -2.50 \times 10^{-10} t + 3.86 \times 10^{-8}, \tag{J.1}$$

with n in mol and t in min. The slope of the rest of runs (#14–#19) is fitted with a double exponential with the following form:

$$\frac{\delta n}{\delta t} = A\exp(Bt) + C\exp(Dt). \tag{J.2}$$

The coefficients A, B, C, D are given in Table J.2 (with n in mol and t in min). Run#19, as an exception, is fitted with a simple exponential ($C, D = 0$), since the double exponential does not give a physically coherent result. The uncertainty assigned to the background curves corresponds to one sigma of the residuals. I.e. the standard deviation (std) of the experimental data with respect to the background fit is calculated and assumed as the resulting error (plotted in the figures). The std (assigned uncertainty) of each background curve is given in Table J.2.

Table J.2: Coefficients of the fits of the background slopes ($\delta n/\delta t$) corresponding to equation (J.2) and standard deviation (std) of the residuals from the fit (converted to n).

Run	A (mol min^{-1})	B (min^{-1})	C (mol min^{-1})	D (min^{-1})	std (mol)
run#13		(see equation (J.1))			2.76×10^{-8}
run#14	-1.67×10^{-9}	-8.35×10^{-2}	-2.61×10^{-8}	-3.19×10^{-2}	9.67×10^{-8}
run#15	-4.28×10^{-10}	-8.70×10^{-2}	-4.51×10^{-8}	-5.70×10^{-3}	8.90×10^{-8}
run#17	-3.00×10^{-13}	-1.92×10^{-1}	-3.29×10^{-8}	-1.78×10^{-2}	9.17×10^{-8}
run#18	-1.48×10^{-9}	-7.65×10^{-2}	-3.83×10^{-8}	-1.21×10^{-2}	1.10×10^{-7}
run#19	-3.84×10^{-8}	-1.77×10^{-2}	(-)	(-)	9.60×10^{-8}

Appendix K

Error handling

K.1 Introduction: General equation for error propagation

This appendix contains the procedure followed in the error handling of the calculations of the evaluation of gas in the present work. For this, first the primary sources of error are introduced in Section K.2.

In the next sections, the assessment of uncertainty in the calculations is determined following the general equation for error propagation [80]:

$$\delta f(x_i)^2 = \sum_{i=1}^{N} \left(\frac{\partial f}{\partial x_i} \right)^2 \delta x_i^2, \tag{3.2*}$$

in which f is a function of independent variables x_i (with $i = 1, ...N$), and δ denotes uncertainty.

Note that in the sections in which all quantities clearly refer to the gas, the subscript 'gas' (or 'D_2') is omitted for simplicity and clarity.

K.2 Primary errors

K.2.1 Pressure, *p*

In the **upper chamber**, the pressure sensor RP010 is used for the pressure measurements during the dissolution and permeation experiments. The characteristics of the sensor are shown in Table 3.2. With the calibration explained in Appendix G, the uncertainty of the sensor is optimised to ± 1.08 mbar. This error is of type random, since it is due to non-linearity, hysteresis and non-repeatability. No offset error is regarded since the pressure sensor is zeroed (while the chamber is evacuated) before every experiment.

In the **lower chamber**, two vacuum sensors, RP040 and RP042, are used to measure the pressure during the extraction experiments. Their main characteristics and uncertainties are shown in Table 3.4.

K.2.2 Temperature, *T*

The **temperature sensors** have an offset uncertainty of 2.2 °C or 0.75 % (in °C), whichever is greater. This uncertainty is used for all thermocouples measuring gas.

When measuring the temperature of the **heaters**, there are always two thermocouples: one in charge of control, T_{h1}, and another one in charge of safety, T_{h2}. They normally show different temperatures because one is placed next to the heating wire and the other a bit further from it. Therefore, the temperature of the heater, T_{heater}, is taken as the mean value between the two thermocouples. Its error is calculated including the standard deviation of the two values, $\text{std}(T_{h1}, T_{h2})$, and the primary uncertainty of one thermocouple calculated over the mean value, $\delta T_{\text{mean}} = 0.75\% \, T_{\text{mean}}$, as follows:

$$\delta T_{\text{heater}} = \sqrt{\left(\frac{\text{std}(T_{h1}, T_{h2})}{\sqrt{2}}\right)^2 + {\delta T_{\text{mean}}}^2}\,. \tag{K.1}$$

For example, in the dissolution phase, the two thermocouples at the heater EH01 are normally $T_{h1} = 400\,°\text{C}$ and $T_{h2} = 408\,°\text{C}$. Then, the temperature of the heater is calculated to be: $T_{\text{heater}} = 404 \pm 5.02\,°\text{C}$.

K.2.3 Volume, *V*

The volume of the **upper chamber** is measured with a high-accuracy device [81] during the pre-commissioning of the facility. Then, the volumes of the **lower chamber**, inlet lines and rest of **sub-assemblies** are experimentally determined by gas expansions from the upper chamber. The relevant volumes and uncertainties in the error analysis are given in Table K.1.

Table K.1: Volume of the chambers and their uncertainties.

Container	Volume (l)	Uncertainty (l)
Upper chamber	4.879	± 0.02
Lower chamber	27.3	± 0.1

The uncertainties of the **Pb-Li** volumes in the upper and lower chambers that are used in the calculations are summarized in Table K.2. The values are obtained from the simulations fitting the experimental results (see Chapter 4).

Table K.2: Volume of Pb-Li in the UC during dissolution ($V_{\mathrm{PbLi(uc)\ [diss]}}$) and uncertainty of the volume of Pb-Li in the UC ($\delta V_{\mathrm{PbLi(uc)}}$) and LC ($\delta V_{\mathrm{PbLi(lc)}}$).

Run	$V_{\mathrm{PbLi(uc)\ [diss]}}$ (l)	$\delta V_{\mathrm{PbLi(uc)}}$ (l)	$\delta V_{\mathrm{PbLi(lc)}}$ (l)
Run#12	-	0.022	0.008
Run#13	1.231	0.033	0.012
Run#14	1.178	0.028	0.010
Run#15	1.198	0.043	0.016
Run#16	-	0.039	0.014
Run#17	1.187	0.034	0.012
Run#18	1.240	0.033	0.012
Run#19	1.245	0.031	0.011
Run#20	-	0.032	0.012

K.3 Amount of gas in the upper chamber

K.3.1 Gas temperature, T_{gas}

The temperature of the gas in a cylindrical chamber is calculated with:

$$T_{\mathrm{gas}} = \sqrt[4]{\frac{T_a^4 + T_b^4}{2}}, \tag{3.4*}$$

where T_a and T_b (both in K) are the temperatures of the top and bottom surfaces. This equation defines the temperature of a gas between two infinite plane surfaces (at T_a and T_b, respectively), due to radiation. The uncertainty of T_{gas} is determined by applying equation (3.2*) to (3.4*), which leads to:

$$\delta T_{\mathrm{gas}} = 2\left(\frac{T_a^4 + T_b^4}{2}\right)^{-\frac{3}{4}} \sqrt{(T_a^3 \delta T_a)^2 + (T_b^3 \delta T_b)^2}. \tag{K.2}$$

The temperature of the gas in the upper chamber is calculated with equations (3.4*) and (K.2). The values of T_a and T_b used in the different scenarios (with and without Pb-Li) are given in Table K.3. In both cases, the temperature of the top surface, T_a, is assumed to be the one given by the thermocouple RT010 (only 6 mm from the top).

The temperature of the bottom surface, T_b, is different with and without Pb-Li:

Table K.3: Experimental values of T_a and T_b used to determine T_{gas} with equations (3.4*) and (K.2) in the upper chamber (positions of thermocouples in Figure 3.3)

Scenario	T_a	T_b
Dissolution phase (with Pb-Li)	RT010	RT012
Permeation experiment (no Pb-Li)	RT010	$\frac{\text{RT013} + T_{\text{heater}}}{2}$

- In the dissolution phase, the Pb-Li level reaches RT012, therefore, in this case, T_b is given by this thermocouple.
- In the permeation experiments (without Pb-Li), the temperature of the bottom surface of the chamber is assumed to be the average between the temperature of the heater (placed at the lower part of the 20 mm-stainless-steel flange) and RT013 (which is 9 mm above the surface). In this case, the uncertainty of T_b is determined as follows:

$$\delta T_b = \sqrt{\left(\frac{\delta \text{RT013}}{2}\right)^2 + \left(\frac{\delta T_{\text{heater}}}{2}\right)^2}, \tag{K.3}$$

  which is the result of applying equation (3.2*) to the expression shown in Table K.3.

K.3.2 Gas volume, V_{gas}

The volume of the gas in the chamber is determined with:

$$V_{\text{gas}} = V_{\text{uc}} - V_{\text{PbLi(uc)}}, \tag{K.4}$$

where the subscript 'uc' refers to upper chamber. Then, the uncertainty is determined by applying equation (3.2*) to (K.4), which leads to:

$$\delta V_{\text{gas}} = \sqrt{\delta V_{\text{uc}}^2 + \delta V_{\text{PbLi(uc)}}^2}, \tag{K.5}$$

with the values δV_{uc} and $\delta V_{\text{PbLi(uc)}}$ from Tables K.1 and K.2, respectively.

K.3.3 Amount of gas, n

The amount of gas in the chamber, n, is determined with the *ideal gas law*:

$$n = \frac{pV}{RT}, \tag{3.1*}$$

where p is the pressure, V is the volume of the gas, T is the temperature of the gas and R is the *ideal gas constant*.

The application of equation (3.2*) to (3.1*) leads to:

$$\delta n = \sqrt{\left(\frac{\partial n}{\partial p}\right)^2 \delta p^2 + \left(\frac{\partial n}{\partial V}\right)^2 \delta V^2 + \left(\frac{\partial n}{\partial T}\right)^2 \delta T^2}. \tag{3.3*}$$

K.4 Amount of gas in the lower chamber

K.4.1 Gas pressure, p_{gas}

As explained in Section 6.1.2 and Appendix C, the pressure inside the lower chamber is evaluated with rarefied gas theory at the different regions depicted in Figure 6.1. With this evaluation the uncertainty of the pressure measurements is increased by $\approx 5\,\%$ of the absolute value in runs#14–#20, and $\approx 0.7\,\%$, $0.7\,\%$ and $1.1\,\%$ in regions 1, 2 and 3, respectively, in run#13. This uncertainty is estimated based on results observed in reference [109].

K.4.2 Gas temperature, T_{gas}

The temperatures of the gas in regions 1 and 2 and their uncertainties are calculated (as in the upper chamber) as follows:

$$T_{\mathrm{gas}} = \sqrt[4]{\frac{T_a^4 + T_b^4}{2}}, \tag{3.4*}$$

$$\delta T_{\mathrm{gas}} = 2\left(\frac{T_a^4 + T_b^4}{2}\right)^{-\frac{3}{4}} \sqrt{(T_a^3 \delta T_a)^2 + (T_b^3 \delta T_b)^2}, \tag{K.6}$$

where T_a and T_b (both in K) are the temperatures of the top and bottom surfaces of each region (A and B for region 1, and B and C for region 2).

K.4.3 Gas volume, V_{gas}

The uncertainty of the gas volume in region 3 (δV_3) is calculated from the creased surface of the flexible: $\delta V = 2\pi(r_{\max} - r_{\min})L/2$, with the length $L = 1.5\,\mathrm{m}$ being the length of the flexible when fully compressed (since the chamber is under high vacuum) and $r_{\max} = 0.0335\,\mathrm{m}$, $r_{\min} = 0.0295\,\mathrm{m}$ are the maximum and minimum radii of the flexible (attending to the creased surface).

The uncertainties of V_1 and V_2 are calculated with the propagation of the corresponding errors using equation (3.2*).

K.4.4 Amount of gas, n

Applying the ideal gas law, in general, the total amount of gas in the lower chamber is:

$$n = n_1 + n_2 + n_3 = \frac{p_1 V_1}{R T_1} + \frac{p_2 V_2}{R T_2} + \frac{p_3 V_3}{R T_3}. \tag{K.7}$$

Substituting $V_2 = V_1 - V_{\mathrm{PbLi(lc)}}$, in the case of **run#13**, equation (K.7) takes the form:

$$n = n_1 + n_2 + n_3 = \frac{1}{R}\left(\frac{p_1 V_1}{T_1} + \frac{p_2 (V_1 - V_{\mathrm{PbLi(lc)}})}{T_2} + \frac{p_3 V_3}{T_3}\right). \tag{K.8}$$

Additionally, in the case of **run#14** and the rest of the runs, since $p_1 = p_2 = p_3 = p$, equation (K.7) is simplified to:

$$n = n_1 + n_2 + n_3 = \frac{p}{R}\left(\frac{V_1}{T_1} + \frac{(V_1 - V_{\mathrm{PbLi(lc)}})}{T_2} + \frac{V_3}{T_3}\right). \tag{K.9}$$

The uncertainty δn is calculated by applying equation (3.2*) to equations (K.8) and (K.9).

K.5 Variation of amount of gas, n_{a} - n_{b}

This section is used to explain the calculations followed in the error propagation when subtracting two values of n. This occurs in two differentiated cases:

1. $n_0 - n_f$: In the upper chamber, both during the dissolution phase and the permeation experiments, variations of the amount of gas over time $-\Delta n = n_0 - n_f$ are calculated.

2. $n - n_{\mathrm{BG}}$: In the lower chamber, the amount of deuterium extracted is calculated by subtracting the absolute amount of gas in the chamber n minus the background curve n_{BG}.

Both cases are described in separate sections, since the calculations are different, due to the variables that are constant and the ones that are not.

K.5.1 Dissolution and permeation experiments in the upper chamber

During the dissolution phase (and also during the permeation experiments), the volume V and temperature of the gas T in the upper chamber remain constant.

Therefore, the variation of the amount of gas, using the ideal gas law, is calculated as:

$$(n_0 - n_f) = \frac{(p_0 - p_f)V}{RT}. \tag{5.2*}$$

The initial and final values of pressure, p_0 and p_f, are obtained from an average of $N = 10$ experimental data (corresponding to an interval of 10 s), as follows:

$$p_i = \sum_{j=1}^{N} \frac{p_j}{N}\,, \qquad \text{with } \; i = 1, 2. \tag{K.10}$$

Even though the error of the pressure sensor is of type *random*, the error of the average, p_i, is maintained fixed $p_i = p_j = 1.08\,\text{mbar}$ for conservative reasons. I.e., mathematically, the uncertainty of the pressure can be decreased considerably by applying equation (3.2*) to (K.10) with a large-enough number of points. However, in this case this is not physically realistic.

The propagation of error, applying (3.2*) to (5.2*), follows:

$$\delta(n_0 - n_f) = \frac{1}{R}\sqrt{\left(\frac{V}{T}\right)^2 \left(\delta p_0^2 + \delta p_f^2\right)^2 + \left(\frac{(p_0 - p_f)\delta V}{T}\right)^2 + \left(\frac{(p_0 - p_f)V\delta T}{T^2}\right)^2}. \tag{K.11}$$

K.5.2 Extraction experiments in the lower chamber

The amount of gas extracted in the lower chamber is determined by the variation of amount of gas, as follows:

$$n_{\text{ext}} = n - n_{\text{BG}} \tag{K.12}$$

where n is the calculated amount of gas in the chamber, given by equations (K.8) and (K.9), and n_{BG} is the calculated background evaluated at the same time. Then, the uncertainty of the amount of deuterium extracted is calculated with:

$$\delta n_{\text{ext}} = \sqrt{\delta n^2 - \delta n_{\text{BG}}^2}, \tag{K.13}$$

where δn_{BG} is the uncertainty of the background, which is the standard deviation of the fit.

K.6 Gas permeated through the Pb-Li–free walls in the upper chamber

K.6.1 Temperature of the metal

In the determination of the fraction of deuterium permeated through the Pb-Li–free walls, the surface of the upper chamber is divided into four sections, shown in

Table K.4: Temperature of the stainless-steel surfaces used in the calculations, corresponding to Figure 5.2 (b).

Section	Temperature
Upper flange	$T_1 = T_{\mathrm{RT010}}$
Upper wall	$T_2 = \dfrac{T_{\mathrm{RT010}} + T_{\mathrm{RT012}}}{2}$
Lower wall	$T_3 = \dfrac{T_{\mathrm{RT010}} + T_{\mathrm{heater}}}{2}$
Lower flange	$T_4 = T_{\mathrm{heater}}$

Figure 5.2 (b). The calculated temperature of each surface is shown in Table K.4.

Since T_2 and T_3 are calculated with the average between two values, their uncertainty is calculated as follows (applying equation (3.2*)):

$$\delta T_i = 0.5\sqrt{\delta T_a^2 + \delta T_b^2}, \qquad \text{with } i = 2, 3, \tag{K.14}$$

where T_a and T_b are the corresponding temperatures of each average given in Table K.4.

In the specific case of T_1, the uncertainty is artificially increased to $\pm 9.9\,\mathrm{K}$ (see explanation in Section 5.4.1 and experimental data in I.2).

K.6.2 Permeation flux

The permeation flux, $J_{i,j}$, through the section i is calculated for the four sections with

$$J_{i,j} = \mathcal{P}_j \left(\sqrt{p_{\mathrm{in}}} - \sqrt{p_{\mathrm{out}}}\right) \frac{A_i}{\delta_i}, \tag{2.10*}$$

where the subscript $i = 1, 2, 3, 4$ refers to the surface section and the subscript $j = 1, 2$ refers to the two sets of permeability coefficients given in Table 2.2.

In equation (2.10*), $p_{\mathrm{out}} \approx 0$, p_{in} is the pressure of the gas inside the chamber, A_i is the area of the permeation surface i and δ_i its thickness. The permeability, $\mathcal{P}_j$, depends on the temperature of the metal as follows:

$$\mathcal{P}_j = \mathcal{P}_{0j}\, \mathrm{e}^{-\frac{E_{\mathcal{P}j}}{RT}}. \tag{2.14*}$$

In the error propagation, the coefficients $\mathcal{P}_{0j}$ and $E_{\mathcal{P}j}$ are taken as perfect, since there is no reported uncertainty. Therefore, the error of the permeability values is calculated as follows:

$$\delta \mathcal{P}_j = \mathcal{P}_j \frac{E_{\mathcal{P}j}}{RT_i^2} \delta T_i. \tag{K.15}$$

where, as before, $i = 1, 2, 3, 4$ corresponds to the section and $j = 1, 2$ to the two permeability values.

For the calculation of the uncertainty of the permeation fluxes, $\delta J_{i,j}$, the thickness δ_i is assumed perfect. The error of p_{in} is also neglected for simplicity of the calculations, since small variations in pressure do not have a relevant impact in the permeability. The uncertainty of the surfaces A_1 and A_4 (the two flanges) are considered 0. However, A_2 and A_3 are defined as a function of the height of the Pb-Li, $h'_{\text{Pb-Li}}$, in each run, as follows:

$$A_2 = 2\pi r_{\text{uc}}(h_{\text{uc}} - h'_{\text{Pb-Li}}), \tag{K.16}$$

$$A_3 = 2\pi r_{\text{uc}} h'_{\text{Pb-Li}}, \tag{K.17}$$

where r_{uc} and h_{uc} are the radius and height of the upper chamber, respectively. Therefore, the uncertainty of each section area is:

$$\delta A_i = \begin{cases} 0 & \text{for } i = 1, 4, \\ 2\pi r_{\text{uc}}\, \delta h'_{\text{Pb-Li}} & \text{for } i = 2, 3. \end{cases} \tag{K.18}$$

Then, the uncertainty of the permeation flux follows:

$$\delta J_{i,j} = \frac{\sqrt{p_{\text{in}}}}{\delta_i} \sqrt{(\mathscr{P}_j \delta A_i)^2 + (A_i \delta \mathscr{P}_j)^2}. \tag{K.19}$$

Note that in total, eight permeation fluxes are calculated (for each experiment), which are the fluxes through each of the four sections with the two permeabilities from Table 2.2.

K.6.3 Fraction of deuterium permeated through the top surfaces

The amount of deuterium permeated through each surface is calculated with the flux as follows:

$$n_{i,j} = J_{i,j}\, \tau \qquad \text{with } i = 1, 2, 3, 4, \text{ and } j = 1, 2, \tag{K.20}$$

where $\tau = 48\,\text{h}$ is the duration of the experiment. Since during the experiment the pressure of the gas, p_{in}, varies, equation (K.20) is an integral over time. However, it has been verified that the result of an integral of 10 calculation steps gives the same result as the simplified version shown in equation (K.20). Therefore, the later is used in the propagation of error, since it decreases the obtained uncertainty considerably

(in comparison with the integral calculation). Then, the uncertainty of the amount of gas permeated through each surface is determined as follows:

$$\delta n_{i,j} = \delta J_{i,j}\,\tau \qquad \text{with } i = 1,2,3,4, \text{ and } j = 1,2, \tag{K.21}$$

assuming τ as a perfect value.

Then, the fraction that permeates through each section is calculated as follows:

$$\chi_{i,j} = \frac{n_{i,j}}{\sum_{i=1}^{4} n_{i,j}}, \tag{K.22}$$

and its uncertainty is calculated with equation (3.2*), which in the case of $i = 1$ is:

$$\delta\chi_{1,j} = \sqrt{\left(\frac{\sum_{i=1}^{4} n_{i,j} - n_{1,j}}{(\sum_{i=1}^{4} n_{i,j})^2}\right)^2 \delta n_{1,j}^2 + \left(\frac{n_{1,j}}{(\sum_{i=1}^{4} n_{i,j})^2}\right)^2 \left(\delta n_{2,j}^2 + \delta n_{3,j}^2 + \delta n_{4,j}^2\right)}, \tag{K.23}$$

The fraction of deuterium permeation through the top surfaces is:

$$\chi_{\text{top},j} = \chi_{1,j} + \chi_{2,j}, \tag{K.24}$$

whose uncertainty follows:

$$\delta\chi_{\text{top},j} = \sqrt{\delta\chi_{1,j}{}^2 + \delta\chi_{2,j}{}^2}. \tag{K.25}$$

The final value of χ_{top} is calculated with the average between the two values calculated with both permeabilities, $\mathcal{P}_1$ and $\mathcal{P}_2$ (corresponding to the subscript $j = 1,2$):

$$\chi_{\text{top}} = \frac{\chi_{\text{top},1} + \chi_{\text{top},2}}{2}. \tag{K.26}$$

Therefore, the uncertainty of the percentage fraction of deuterium permeated through the Pb-Li top walls is:

$$\delta\chi_{\text{top}} = 0.5\sqrt{\delta\chi_{\text{top},1}{}^2 + \delta\chi_{\text{top},2}{}^2}. \tag{K.27}$$

K.6.4 Gas permeated through the Pb-Li–free walls

Finally, the amount of deuterium that permeates through the Pb-Li–free walls is determined with:

$$n_{\text{D}_2[\text{ss}]} = \chi_{\text{top}}\ \ n_{\text{D}_2[\text{ss*}]}, \tag{5.3*}$$

where $n_{\text{D}_2[\text{ss*}]}$ is the total amount of deuterium permeated in the permeation experiment.

The uncertainty of $n_{\text{D}_2[\text{ss}]}$ is calculated applying equation (3.2*) as follows:

$$\delta n_{\text{D}_2[\text{ss}]} = \sqrt{\left(n_{\text{D}_2[\text{ss*}]}\,\delta\chi_{\text{top}}\right)^2 + \left(\chi_{\text{top}}\,\delta n_{\text{D}_2[\text{ss*}]}\right)^2}. \tag{K.28}$$